



HAL
open science

Assessment and mitigation of liquefaction seismic risk : numerical modeling of their effects on SSI

Silvana Montoya Noguera

► **To cite this version:**

Silvana Montoya Noguera. Assessment and mitigation of liquefaction seismic risk : numerical modeling of their effects on SSI. Civil Engineering. Université Paris Saclay (COmUE), 2016. English. NNT : 2016SACLCO23 . tel-01327934

HAL Id: tel-01327934

<https://theses.hal.science/tel-01327934>

Submitted on 7 Jun 2016

HAL is a multi-disciplinary open access archive for the deposit and dissemination of scientific research documents, whether they are published or not. The documents may come from teaching and research institutions in France or abroad, or from public or private research centers.

L'archive ouverte pluridisciplinaire **HAL**, est destinée au dépôt et à la diffusion de documents scientifiques de niveau recherche, publiés ou non, émanant des établissements d'enseignement et de recherche français ou étrangers, des laboratoires publics ou privés.

NNT : 2016SACL023

THESE DE DOCTORAT
DE
L'UNIVERSITE PARIS-SACLAY
PREPAREE A
CENTRALESUPÉLEC

ÉCOLE DOCTORALE N°579
Sciences mécaniques et énergétiques, matériaux et géosciences – SMEMAG
Spécialité de doctorat : Génie Civil

Par

Mme Silvana MONTOYA-NOGUERA

Evaluation et reduction des risques sismiques liés à la liquéfaction : Modélisation
numérique de leurs effets dans l'ISS

Thèse présentée et soutenue à Châtenay-Malabry, le 29 janvier 2016 :

Composition du Jury :

M. Alain Pecker, Professeur, Ecole Nationale des Ponts et Chaussées, Président du Jury
M. Gopal Madabhushi, Professeur, Cambridge University, Rapporteur
M. Fabian Bonilla, Directeur de recherche, Institut de Physique du Globe de Paris, Rapporteur
Mme Evelyne Foerster, Directrice du laboratoire d'études de mécanique sismique, CEA, Examinatrice
Mme Arezou Modaressi, Professeur, Université Paris-Saclay, CentraleSupélec, Directrice de thèse
M. Fernando Lopez-Caballero, Université Paris-Saclay, CentraleSupélec, Encadrant de thèse

Titre : Evaluation et réduction des risques sismiques liés à la liquéfaction : Modélisation numérique de leurs effets dans l'ISS (en anglais)

Mots clés : Liquéfaction, modèle d'éléments finis, comportement non linéaire, variabilité spatiale, champ aléatoire binaire

Résumé : La liquéfaction des sols qui est déclenchée par des mouvements sismiques forts peut modifier la réponse d'un site. Ceci occasionne des dégâts importants dans les structures comme a été mis en évidence lors des tremblements de terre récents tels que celui de Christchurch, Nouvelle-Zélande et du Tohoku, Japon. L'évaluation du risque sismique des structures nécessite une modélisation robuste du comportement non linéaire de sols et de la prise en compte de l'interaction sol-structure (ISS). En général, le risque sismique est décrit comme la convolution entre l'aléa et la vulnérabilité du système. Cette thèse se pose comme une contribution à l'étude, via une modélisation numérique, de l'apparition de la liquéfaction et à l'utilisation des méthodes pour réduire les dommages induits.

A cet effet, la méthode des éléments finis (FEM) dans le domaine temporel est utilisée comme outil numérique. Le modèle principal est composé d'un bâtiment fondé sur un sable liquéfiable. Comme la première étape de l'analyse du risque sismique, la première partie de cette thèse est consacrée à la caractérisation du comportement du sol et à sa modélisation. Une attention particulière est donnée à la sensibilité du modèle à des paramètres numériques. En suite, le modèle est validé pour le cas d'une propagation des ondes 1D avec les mesures issus du benchmark international PRENOLIN sur un site japonais. D'après la comparaison, le modèle arrive à prédire les enregistrements dans un test en aveugle.

La deuxième partie, concerne la prise en compte dans la modélisation numérique du couplage de la surpression interstitielle (Δp_w) et de la déformation du sol. Les effets favorables ou défavorables de ce type de modélisation ont été évalués sur le mouvement en surface du sol lors de la propagation des ondes et aussi sur le tassement et la performance sismique de deux structures.

Cette partie contient des éléments d'un article publié dans Acta Geotechnica (Montoya-Noguera and Lopez-Caballero, 2016). Il a été trouvé que l'applicabilité du modèle dépend à la fois du niveau de liquéfaction et des effets d'ISS.

Dans la dernière partie, une méthode est proposée pour modéliser la variabilité spatiale ajoutée au dépôt de sol dû à l'utilisation des techniques pour diminuer le degré de liquéfaction. Cette variabilité ajoutée peut différer considérablement de la variabilité inhérente ou naturelle. Dans cette thèse, elle sera modélisée par un champ aléatoire binaire. Pour évaluer l'efficacité du mélange, la performance du système a été étudiée pour différents niveaux d'efficacité, c'est-à-dire, différentes fractions spatiales en allant de non traitées jusqu'à entièrement traitées. Tout d'abord le modèle binaire a été testé sur un cas simple, tel que la capacité portante d'une fondation superficielle sur un sol cohérent. Après, il a été utilisé dans le modèle de la structure sur le sol liquéfiable. Ce dernier cas, en partie, a été publié dans la revue GeoRisk (Montoya-Noguera and Lopez-Caballero, 2015). En raison de l'interaction entre les deux types de sols du mélange, une importante variabilité est mise en évidence dans la réponse de la structure. En outre, des théories classiques et avancées d'homogénéisation ont été utilisées pour prédire la relation entre l'efficacité moyenne et l'efficacité. En raison du comportement non linéaire du sol, les théories traditionnelles ne parviennent pas à prédire la réponse alors que certaines théories avancées qui comprennent la théorie de la percolation peuvent fournir une bonne estimation. En ce qui concerne l'effet de la variabilité spatiale ajoutée sur la diminution du tassement de la structure, différents séismes ont été testés et la réponse globale semble dépendre de leur rapport de PHV et PHA.

Title: Assessment and mitigation of liquefaction seismic risk: Numerical modeling of their effects on SSI (in english)

Keywords: Liquefaction, site response, finite element model, nonlinear soil behavior, spatial variability, binary random field

Abstract: Strong ground motions can trigger soil liquefaction that will alter the propagating signal and induce ground failure. Important damage in structures and lifelines has been evidenced after recent earthquakes such as Christchurch, New Zealand and Tohoku, Japan in 2011. Accurate prediction of the structures' seismic risk requires a careful modeling of the nonlinear behavior of soil-structure interaction (SSI) systems. In general, seismic risk analysis is described as the convolution between the natural hazard and the vulnerability of the system. This thesis arises as a contribution to the numerical modeling of liquefaction evaluation and mitigation.

For this purpose, the finite element method (FEM) in time domain is used as numerical tool. The main numerical model consists of a reinforced concrete building with a shallow rigid foundation standing on saturated cohesionless soil. As the initial step on the seismic risk analysis, the first part of the thesis is consecrated to the characterization of the soil behavior and its constitutive modeling. Later on, some results of the model's validation with a real site for the 1D wave propagation in dry conditions are presented. These are issued from the participation in the international benchmark PRENOLIN and concern the PARI site Sendai in Japan. Even though very few laboratory and in-situ data were available, the model responses well with the recordings for the blind prediction.

The second part, concerns the numerical modeling of coupling excess pore pressure (Δp_w) and soil deformation. The effects were evaluated on the ground motion and on the structure's settlement and performance. This part contains material from an article published in *Acta Geotechnica* (Montoya-Noguera and Lopez-Caballero, 2015). The applicability of the models was found to depend on both the liquefaction level and the SSI effects.

In the last part, an innovative method is proposed to model spatial variability added to the deposit due to soil improvement techniques used to strengthen soft soils and mitigate liquefaction. Innovative treatment processes such as bentonite permeations and bio-grouting, among others have recently emerged. However, there remains some uncertainties concerning the degree of spatial variability introduced in the design and its effect of the system's performance.

This added variability can differ significantly from the inherent or natural variability thus, in this thesis, it is modeled by coupling FEM with a binary random field. The efficiency in improving the soil behavior related to the effectiveness of the method measured by the amount of soil changed was analyzed. Two cases were studied: the bearing capacity of a shallow foundation under cohesive soil and the liquefaction-induced settlement of a structure under cohesionless loose soil. The latter, in part, contains material published in *GeoRisk* journal (Montoya-Noguera and Lopez-Caballero, 2015). Due to the interaction between the two soils, an important variability is evidenced in the response. Additionally, traditional and advanced homogenization theories were used to predict the relation between the average efficiency and effectiveness. Because of the nonlinear soil behavior, the traditional theories fail to predict the response while some advanced theories which include the percolation theory may provide a good estimate. Concerning the effect of added spatial variability on soil liquefaction, different input motions were tested and the response of the whole was found to depend on the ratio of PHV and PHA of the input motion.

Contents

1	Introduction	1
1.1	Motivation	2
1.2	Objectives	3
1.3	Outline	4
2	Numerical modeling of dynamic soil behavior	7
2.1	Governing equations	8
2.2	Wave propagation	9
2.2.1	Motion equation simplified for 1D linear elastic material	10
2.2.2	Homogeneous deposit lying over a semi-infinite bedrock	11
2.2.3	Multi-layer soil deposit	14
2.3	Nonlinearity identification by ground motion analysis	15
2.3.1	Peak acceleration	16
2.3.2	Borehole transfer function	18
2.3.3	Time-frequency spectral functions	19
2.3.4	Seismic interferometry	25
2.4	Dynamic soil behavior characterization	27
2.4.1	Measurement errors in triaxial test	28
2.4.2	Similarities between methods to calculate the deformation properties	30
2.4.3	Differences between laboratory and <i>in-situ</i> measurements	34
2.4.4	Summary of the proposed procedure	36
2.4.5	Comparison of the proposed procedure with that of Ishihara (1996)	36
2.4.6	Empirical models for nonlinearity curves	37
2.5	Modeling dynamic soil behavior	41
2.5.1	Equivalent linear analysis	41

2.5.2	Nonlinear models	43
2.5.3	Comparisons between models	43
3	Numerical tools used in this study	45
3.1	Finite Element Model	46
3.2	Numerical integration	47
3.2.1	Numerical damping	49
3.2.2	Discretization	54
3.3	Soil behavior model	56
3.3.1	Model description	57
3.3.2	Model Parameters identification	63
3.4	Sensibility of the numerical model parameters	66
3.4.1	Soil profiles	67
3.4.2	Input motions	70
3.4.3	Effect of some model parameters	71
3.5	Numerical model validation	80
3.5.1	PARI Sendai	81
3.5.2	Model parameters	83
3.5.3	Input motions	83
3.5.4	Comparison between recorded and numerical results	84
3.5.5	Partial conclusions	90
4	Effect of coupling pressure and deformation	91
4.1	Introduction	93
4.1.1	Summary of previous findings	93
4.2	Coupled and Decoupled dynamic approach	97
4.3	Free field response	98
4.3.1	Soil behavior	98
4.3.2	Input earthquake motions	100
4.3.3	Initial soil response	100
4.3.4	Nonlinear soil response	102
4.3.5	Peak surface acceleration	103
4.3.6	Acceleration profile	107
4.3.7	Acceleration response spectra	111

4.3.8	Partial conclusions	119
4.4	Soil structure interaction response	121
4.4.1	Structure model	121
4.4.2	Input earthquake motions	125
4.4.3	Initial SSI model response	125
4.4.4	Seismic soil behavior	126
4.4.5	SSI effects on a 2D model	130
4.4.6	Surface acceleration	135
4.4.7	Structure relative settlement	137
4.4.8	Structure seismic demand	139
4.4.9	Partial conclusions	143
5	Effect of the spatial variability	145
5.1	Introduction	147
5.2	Previous studies on soil heterogeneity	149
5.2.1	Inherent spatial variability	150
5.2.2	Added spatial variability	156
5.3	Discrete random field model	158
5.3.1	Correlation structure	160
5.3.2	Homogenization theories	162
5.4	Bearing capacity model	167
5.4.1	Coupling binary random field with FEM	169
5.4.2	Homogeneous equivalent models	174
5.4.3	Partial conclusions	183
5.5	Settlement induced by seismic liquefaction	184
5.5.1	Input earthquake motion	186
5.5.2	Non-treated soil deposit response	186
5.5.3	Liquefaction mitigation analysis	187
5.5.4	Heterogeneous models	190
5.5.5	Permeability and soil type effect	200
5.5.6	Random field discretization	203
5.5.7	Homogenization theories and other input motions	203
5.5.8	Other EDPs	207

5.5.9	Partial conclusions	209
6	Conclusions	211
A	Soil model parameters	215
A.1	LMS	216
A.1.1	Drained triaxial test	216
A.1.2	Consolidation test	218
A.1.3	Drained cyclic strain-controlled shear test	218
A.1.4	Undrained cyclic stress-controlled shear test	219
A.2	MDS	220
A.2.1	Drained triaxial test	220
A.2.2	Consolidation test	222
A.2.3	Drained cyclic strain-controlled shear test	223
A.2.4	Undrained cyclic stress-controlled shear test	224
A.3	Soils used in chapter 2	225
A.4	General conclusions	226
B	Nonlinear soil behavior in 2D models	229
B.0.1	Shear stress and strain	231
B.0.2	Liquefaction ratio	232
B.0.3	Acceleration	233
C	Signal tools and processing	241
C.1	Signal processing	242
C.2	Earthquake parameters	245
C.3	Anderson criteria	250
C.4	Coherency	251
C.5	Ground motion database	252

List of Figures

1.1	Schema of the thesis framework	4
2.1	Homogeneous deposit lying over a semi-infinite bedrock : 1D analysis	11
2.2	Theoretical transfer function for different material damping and amplification ratio for different Impedance ratios	14
2.3	Shear wave velocity profile and the theoretical transfer function for varying layers number	16
2.4	Recorded and estimated peak ground acceleration (<i>PGA</i>) as a function of peak horizontal acceleration at outcropping (<i>PHA</i>)	17
2.5	Borehole transfer function for Tohoku earthquake	19
2.6	Time-frequency spectral functions	21
2.7	Surface acceleration and normalized S-transform for Tohoku earthquake	22
2.8	Temporal changes on the $ TF $ for Tohoku earthquake on station FKSH10	22
2.9	STFT for the Tohoku earthquake	23
2.10	Shear modulus degradation and damping evolution with shear strain by transfer function analysis	24
2.11	Seismic interferometry example	25
2.12	Shear modulus degradation and damping evolution with shear strain by interferometry analysis	27
2.13	Effect of bedding error in cyclic triaxial tests	29
2.14	Comparison of deformation properties	31
2.15	Shear modulus degradation and Damping evolution comparison between tests	33
2.16	Hyperbolic fit for shear modulus degradation of cyclic triaxial (TX) test results	34
2.17	Normalized shear modulus degradation curves for different tests	34
2.18	Correction factor $C_r(\gamma)$ for different degrees of sample disturbance	37
2.19	Applied correction factor (C_r) to the normalized shear modulus degradation curves	38

2.20	Kokusho (1980) nonlinearity curves	38
2.21	Vucetic and Dobry (1991) nonlinearity curves	39
2.22	Darendeli (2001) nonlinearity curves	40
2.23	Menq (2003) nonlinearity curves	41
3.1	Spectral radii as a function of normalized frequency for different sets of Newmark parameters	49
3.2	Surface displacement time history for the different spectral radius (ρ_∞)	51
3.3	Induced numerical damping of a soil deposit over a rigid bedrock	52
3.4	Induced numerical damping of a soil deposit over an elastic bedrock	54
3.5	Effect of the time step in the transfer function and in the surface acceleration	56
3.6	Shear modulus (G) degradation and damping (D) evolution with shear strain (γ) for profile P1	69
3.7	Shear modulus (G) degradation and damping (D) evolution with shear strain (γ) for profile P2	69
3.8	Acceleration, velocity and displacement time histories of the sinusoidal motions	70
3.9	Acceleration, velocity and displacement time histories of the real motions	71
3.10	Shear stress-strain plots near the base for the profile P1 with elastic bedrock	72
3.11	Surface displacement and acceleration for the profile P1 with elastic bedrock and the sinus 1 motion	72
3.12	Anderson criteria for the surface acceleration of profile P1 with elastic bedrock	73
3.13	Shear stress-strain plots near the base for the profile P1 with elastic bedrock	74
3.14	Wave propagation for the profile P1 with elastic bedrock and the sinus 1 motion	74
3.15	Model of equivalent response for borehole boundaries	76
3.16	Comparison between PHA at the bedrock and at the outcropping	77
3.17	Maximum acceleration profile for the P1 and the real 0 LF motion	78
3.18	Pseudo spectra of acceleration at surface (PSA)	79
3.19	Shear-wave velocity (V_s) profile for P2 with different n values	80
3.20	Maximum acceleration profile for the P2 with the real 1 HF	80
3.21	Shear wave velocity (V_s) profile and Transfer Function for profile P1 - Validation	82
3.22	Nonlinearity curves for P1 - Validation	83
3.23	Acceleration spectra of the input motions - Validation - EW component	85
3.24	Surface acceleration time history	85

3.25	Surface acceleration spectra	86
3.26	Transfer function between surface and recorded borehole acceleration	86
3.27	Summary for NS and EW components of all input motions	87
3.28	Mean Anderson criteria for surface acceleration	88
3.29	Anderson criteria for surface acceleration at each frequency band	88
3.30	Transfer function for all motions with EW component	89
3.31	Profiles for maximum acceleration and maximum shear stress	90
4.1	Response spectral ratio (RSR= PSA^{CPD}/PSA^{DPD})	94
4.2	Relation between CPD and DPD analyses	95
4.3	Proposed model of the amplification function for each GMPE	96
4.4	Simulated laboratory tests for LMS and MDS	99
4.5	Response spectra of acceleration for the outcropping motions	101
4.6	Initial behavior of CPD and DPD	101
4.7	Acceleration time history at outcropping and obtained at surface with both analyses for LMS	102
4.8	Normalized response spectra for the LMS	103
4.9	PGA and PHA relationship for LMS and MDS deposits	104
4.10	PGA and PHA relationship for CPD and DPD models	105
4.11	CPD/DPD ratios as a function of PHA	106
4.12	PGA of the DPD and CPD models grouped by the liquefaction index for LMS	107
4.13	Time history of r_u profile and outcropping input motion	108
4.14	Comparing profiles for CPD and DPD	109
4.15	Shear stress and strain plots with the coupled (CPD) and the decoupled (DPD) model for case C3	110
4.16	Time histories of the surface acceleration and mean and maximum r_u throughout the profile	111
4.17	u_z time evolution at surface for the three cases	112
4.18	I_A time evolution at surface for the three cases	113
4.19	PSA at surface for different time windows and for different cases	114
4.20	Mean and standard deviation RSR for both soils	115
4.21	Mean RSR of each $Q_{H=10m}$ level for both soils	116
4.22	Mean NRSR of each $Q_{H=10m}$ level for both soils	117

4.23	Mean NRSR values ranged by Q levels for LMS	118
4.24	Mean NRSR values ranged by Q levels for MDS	119
4.25	Schema of the numerical model for soil structure interaction response	122
4.26	Force and Moment diagram for beam elements in B01	122
4.27	Increment of the horizontal stress ($\Delta\sigma_{yy}$) before shaking	123
4.28	Degree of mobilized friction (r_k) before shaking	124
4.29	Transfer function of the free-field and the structure	125
4.30	Input motions used for the SSI model	126
4.31	Degree of mobilized friction (r_k) before shaking for both analyses	127
4.32	Time history liquefaction ratio at free-field	128
4.33	Time history analysis for one motion tested	129
4.34	Liquefaction ratio at the end of shaking for one motion tested in the SSI with T040	129
4.35	Maximum shear strains for one motion tested in the SSI with T040	130
4.36	SSI effect on PGA	131
4.37	SSI effect on settlement	131
4.38	SSI effect on $Q_{H.L}$	132
4.39	SSI effect on r_u with and without structure	134
4.40	SSI effect on r_u with and without structure	134
4.41	Relation between PHA, $T_{V/A}$ and Q_{FEM}	135
4.42	Mean peak ground acceleration (PGA) at structures base for CPD and DPD analyses	136
4.43	Comparison of CPD and DPD results for the response spectra of acceleration at structures base evaluated at the predominant structure period	137
4.44	RSR at structure's base	138
4.45	Comparison of CPD and DPD results for the relative settlement with respect to free-field	138
4.46	Static and dynamic capacity curves	139
4.47	Nonlinearity evolution at the structure's $ TF $ (Top/FF) for B01	140
4.48	Cross-correlation at the structure's top of three acceleration levels for B01	141
4.49	Maximum shear strain level in the CPD analysis with the three acceleration levels for B01	141
4.50	Nonlinearity evolution at the structure's $ TF $ (Top/FF) for T040	142

4.51	Relation of $ TF $ (Top/FF) with the liquefaction index (Q_{FF}) for the CPD analysis	142
4.52	Comparison of CPD and DPD results for the maximum inter story drift (ISD)	143
5.1	Uncertainty in geotechnical soil properties (adapted from Jones et al., 2002)	149
5.2	Examples of added heterogeneity after soil treatment	157
5.3	Procedure scheme for the auto-regressive discretization model	160
5.4	Simulations of a binary random field for different correlations	161
5.5	Correlation structure of the binary random field for $\beta_1=\beta_2$	162
5.6	Example of the percolation types	166
5.7	Schema of the numerical model	167
5.8	Relative difference of the Finite Element model with respect to the Prandtl solution (δ_{FE}) as a function of the undrained shear strength (c_u) of a homogeneous soil deposit	169
5.9	Binary mixture for 2 distributions with $\gamma = 0.5$ and $\beta_1 = \beta_2 = 0.9$	170
5.10	Convergence of the mean and standard deviation of the bearing capacity (q_u)	170
5.11	Normalized settlement as a function of the normalized bearing capacity for different spatial fractions	171
5.12	Models with different heterogeneity surface fraction γ and different auto-regressive coefficients	172
5.13	Coefficient of variation (CV) of the bearing capacity (q_u) as a function of the spatial fraction (γ)	173
5.14	Anisotropic correlation effect on the bearing capacity	175
5.15	Experimental cumulative density function of the bearing capacity	176
5.16	Input and Output of the homogeneous equivalent model	177
5.17	Heterogeneous mean normalized q_u values compared to homogenization theories	177
5.18	Different soils c_u ratios tested	178
5.19	Mean normalized q_u for different soils with the same c_u ratio	179
5.20	BEM equation for different c_u ratios	180
5.21	Bearing capacity as a function of γ^{eff} for $\beta = 0.9$	181
5.22	Bearing capacity as a function of γ^{eff} for $\gamma = 0.5$ and $\beta = 0.9$	182
5.23	Optimization summary results for the coefficient of determination R^2 values of varying LA area	183
5.24	CV decrease due to the optimization on LA area	183

5.25	Schema of the numerical model	185
5.26	Simulated liquefaction curves for both soils	185
5.27	Zoom on the heterogeneous zone for 2 distributions with $\gamma = 0.5$ and $\beta_1 = \beta_2 = 0.4$	186
5.28	Input earthquake motions acceleration time histories, response and Fourier spectra	188
5.29	Liquefaction ratio (r_u) at the end of shaking for EQ1 before and after soil treatment	188
5.30	Time histories of the relative settlement ($ u_z $) and the liquefaction ratio (r_u) before and after soil treatment	189
5.31	Box-and-whiskers plot for the relative settlement ($ u_z $) of the structure with respect to free-field for EQ1	192
5.32	Convergence of the mean and standard deviation of $ u_z $ with EQ1 and $\beta_1 = \beta_2 =$ 0.4	193
5.33	Shear stress (τ) distribution for the homogeneous cases before shaking	194
5.34	Degree of mobilized friction (r_k) in the model before shaking	196
5.35	Liquefaction ratio evolution with time for LMS and MDS elements	197
5.36	Liquefaction ratio evolution with time for a LMS element surrounded by MDS elements	198
5.37	Settlement and Arias intensity profile below the structure	199
5.38	Difference between the heterogeneous with maximum $ u_z $ and the homogeneous LMS model	200
5.39	Effect of the spatial variability of different soil parameters on $ u_z $	201
5.40	Time evolution of liquefaction ratio and settlement for different soil parameters .	202
5.41	Effect of the mesh size of the binary random field on $ u_z $	203
5.42	Homogenization theories for the original LMS - MDS soil mixture	204
5.43	Homogenization theories for the different motions	205
5.44	Relation of the relative difference for $\gamma=0.5$ and different IM	207
5.45	Box-and-whiskers plot for different EDPs	208
5.46	Other EDPs relation with γ for all input motions	209
A.1	Simulated drained triaxial tests for LMS: a) $q - \varepsilon_1$ and b) $\varepsilon_v - \varepsilon_1$	218
A.2	Simulated drained triaxial tests for LMS: a) $\varepsilon_v - p$ and b) $\eta - \varepsilon_1$	218
A.3	Simulated consolidation tests for LMS: a) isotropic and b) oedometric	219
A.4	Simulated drained cyclic shear test for LMS: a) normalized shear modulus degra- dation (G/G_{max}) and b) damping (D) curves as a function of γ	219

A.5	Simulated drained cyclic shear test for LMS: a) $G - \gamma$ and b) $D - G/G_{max}$. . .	220
A.6	Simulated undrained cyclic shear test for LMS: $SR - N$	220
A.7	Simulated drained triaxial tests for MDS: a) $q - \varepsilon_1$ and b) $\varepsilon_v - \varepsilon_1$	222
A.8	Simulated drained triaxial tests for MDS: a) $\varepsilon_v - p$ and b) $\eta - \varepsilon_1$	222
A.9	Simulated consolidation tests for MDS: a) isotropic and b) oedometric	223
A.10	Simulated drained cyclic shear test for MDS: a) normalized shear modulus degradation (G/G_{max}) and b) damping (D) curves as a function of γ	223
A.11	Simulated drained cyclic shear test for MDS: a) $G - \gamma$ and b) $D - G/G_{max}$. . .	224
A.12	Simulated undrained cyclic shear test for MDS: $SR - N$	224
B.1	Horizontal and vertical waves	230
B.2	a) Shear modulus profile and b) TF - surface/bedrock - quasi-elastic behavior .	231
B.3	a) Maximum shear stress and b) strain for a strong motion - Nonlinear behavior	232
B.4	Time history of shear stress and strain: a) and c) at 8.5m and b) and d) at 9m	233
B.5	Profile of liquefaction ratio r_u at the end of shaking for 1D and 2D centerline . .	234
B.6	Liquefaction ratio time evolution at : a) 8.5m and b) 9m	234
B.7	Differences in the Peak acceleration profile : a) horizontal and b) vertical	235
B.8	Response spectra of the horizontal acceleration : a) at surface and b) at 8m . .	235
B.9	Coherency between 1D and 2D models with incremental time windows : a) at surface and b) at z=9m (liquefied area)	236
B.10	Signal coherence between 1D and 2D centerline with depth	236
B.11	Anderson signal similarity between 1D and 2D models : a) at surface and b) at z=9m (liquefied area)	237
B.12	Signal similarity between 1D and 2D centerline with depth : a) mean of all criteria, b) PGD and c) Fs	238
B.13	Interferometry with strong ground motion - Nonlinear behavior : a) 1D and b) 2D centreline	238
B.14	Particle trajectory : a) at surface and b) at z=8m (liquefied area)	239
C.1	Signal processing scheme	245
C.2	Signal processing scheme	246
C.3	Magnitude, Distance and Shear-wave velocity	252

List of Tables

3.1	Material elastic properties for numerical damping evaluation	51
3.2	Newmark parameters tested	51
3.3	Classification of the ECP model parameters as proposed by Lopez-Caballero (2003)	63
3.4	Input motion parameters for SENDAI - Validation - EW component	84
4.1	Input motions intensity measures for free field response analysis	100
4.2	Earthquakes used for detailed analysis	108
4.3	Structures properties	123
5.1	Theoretical autocorrelation functions	152
5.2	Mean values and standard deviations of the lognormally distributed horizontal and vertical correlation lengths of CPT data	153
5.3	Sets of soil model parameters tested	179
5.4	Input motions' identification and some intensity measures	187
5.5	Cases tested for permeability and soil type	201
5.6	Calibration of GEM parameters	205
A.1	ECP model parameters for loose-to-medium sand (LMS)	217
A.2	ECP model parameters for medium-to-dense sand (MDS)	221
A.3	ECP model parameters for P1 - Verification phase	225
A.4	ECP model parameters for P2 - Verification phase	226
A.5	ECP model parameters for P1 - Validation	227
C.1	Anderson criteria for accelerogram similarity (Anderson, 2004)	250
C.2	Frequency bands used for Anderson criteria. Modified from (Anderson, 2004) . .	251
C.3	Selected Ground motion records from NGA database	252

Notations and abbreviations

For the sake of brevity, the notations and abbreviations are described by its most common meaning in the present thesis, however, some symbols were not included in this list because they concern single cases. We shall use boldface symbol (e.g. \mathbf{u} , $\boldsymbol{\sigma}$) for vector and tensor fields, and subscripts (e.g. \mathbf{p}_k , $\boldsymbol{\varepsilon}_v$) to designate vector and tensor components in a Cartesian coordinate system or additional information. Overdots are used to indicate time derivatives (e.g., $\dot{\mathbf{u}} = \partial\mathbf{u}/\partial t$, $\ddot{\mathbf{u}} = \partial^2\mathbf{u}/\partial t^2$).

Latin alphabet

\mathbf{a}	acceleration
\mathbf{a}_{out}	outcropping rock acceleration
\mathbf{a}_{rel}	relative acceleration
a_1, a_2	deviatoric hardening (ECP model parameters)
B	base width
b	yield surface shape (ECP model parameters)
\mathbf{C}_c	Autocovariance function
C_S	Anderson criteria of similarity
c_u	undrained shear strength
c_1, c_2	isotropic hardening (ECP model parameters)
D	soil damping
D_1, D_2	property of material 1 and 2
D_{5-95}	predominant duration
D_{eff}	effective property
D_r	relative density
d	distance between CSL and ICL (ECP model parameters)

Continued on next page...

d_{BEM}	dimensionality BEM parameter
E	Young modulus
e	void ratio
F	global applied loads
\mathbf{F}_k	isotropic hardening function (ECP model)
f	frequency
f_0	fundamental frequency
f_c	central frequency
f_k, f_{iso}	deviatoric and isotropic yield surfaces (ECP model)
\mathbf{g}	gravity acceleration vector
G_{aux}	auxiliary shear modulus (ECP model)
G_{max}	maximum shear modulus
G_{ref}	shear modulus at reference pressure (ECP model parameter)
I	Impedance ratio (inverse of α_z)
I_{JMA}	instrumental seismic intensity
I_{RMS}	root-mean-square intensity
I_A	Arias Intensity
ISD	maximum inter-story drift
k	complex wave number
\mathbf{K}	permeability tensor
K_{ref}	bulk modulus at reference pressure (ECP model parameter)
K_s	solid compressibility
K_w	fluid compressibility
L	Loading parameter (inverse of FS)
l_c	correlation length
L_y, L_z	mesh length in horizontal and vertical direction
m	cyclic loading path (ECP model parameters)
M	Moment
M_w	moment magnitude
n	soil porosity
N	Number of cycles or number of simulations

Continued on next page...

N_c	dimensionless bearing capacity factor
n_e	degree of nonlinearity (ECP model parameter)
\mathbf{p}	confinement pressure or mean stress
p_{c0}	initial critical mean stress (ECP model parameter)
\mathbf{p}_c	critical mean stress (ECP model parameter)
p_f	failure probability
p_w	pore pressure
p'_{ref}	mean effective reference stress (ECP model parameter)
Q	compressibility parameter
\mathbf{q}	deviatoric stress
Q_A	liquefaction index evaluated at area A
Q_i	nodal forces
q_u	bearing capacity
$r_{ela}, r_{hys}, r_{mob}, r_{iso}^{ela}$	threshold domain (ECP model parameters)
R_{JB}	Joyner-Boore source-to-site distance
R_{tol}	Convergence criteria for RHS linearization (ECP model)
\mathbf{r}_k	friction mobilization degree (ECP model)
\mathbf{r}_u	liquefaction ratio
R^2	Coefficient of determination
\mathbf{S}_a	spectra of acceleration at the top of the building
t	time
T	period
$T_{V/A}$	period of equivalent harmonic wave
T_0	Fundamental fixed base period
t_5, t_{95}	time for I_A of 5% and 95%
T_m	mean period
T_p	predominant period
T_s	fundamental period of the soil
\mathbf{u}	displacement
\mathbf{u}_{rw}	fluid displacement with respect to the solid skeleton
U_{tol}	Convergence criteria for unknown variables (ECP model)

Continued on next page...

u_d	maximum drift at the top of the building
\mathbf{u}_s	solid displacement
\mathbf{u}_w	water displacement
\mathbf{u}_z	relative settlement of the structure
\mathbf{v}_{rw}	fluid movement with respect to the solid skeleton
V_{s30}	average shear wave velocity in the upper 30 meters
V_p	p-wave velocity
V_s	shear wave velocity

Greek alphabet

α_k	hardening evolution function (ECP model)
α_{psi}	volumetric constant (ECP model parameter)
β	plastic compressibility modulus (ECP model parameter)
β_N	Newmark integration parameter
β_1, β_2	correlation coefficients (Chapter 5)
Δp_w	excess pore pressure
δ_{FE}	Relative difference of FEM with respect to the Prandtl solution
γ	shear strain
γ	spatial fraction of material 2 (Chapter 5)
γ_c	critical spatial fraction
γ_N	Newmark integration parameter
γ^{eff}	effective spatial fraction
κ	kinematic permeability tensor or hydraulic conductivity
λ	compressibility index in plane $e - \ln p'$
$\dot{\lambda}^p$	plastic multiplier
μ	arithmetic mean (in statistics)
ν	Poisson ratio

Continued on next page...

ω	angular frequency
ϕ_{pp}	friction angle at the critical state (ECP model parameter)
ϕ'_{apt}	apparent friction angle
ψ	characteristic friction angle (ECP model parameter)
ρ	total average unit mass
ρ	autocorrelation function (Chapter 5)
ρ_{∞}	spectral radius at infinity
ρ_s	soil particle mass
ρ_w	fluid mass
$\boldsymbol{\sigma}$	total stress tensor
$\boldsymbol{\sigma}'$	effective stress tensor
σ^2	variance (in statistics)
$\boldsymbol{\tau}$	shear stress
τ	lag separation (Chapter 5)
θ	scale of fluctuation
$\boldsymbol{\varepsilon}$	strain
$\boldsymbol{\varepsilon}_1$	axial strain
$\boldsymbol{\varepsilon}_v$	volumetric strain
$\boldsymbol{\varepsilon}^e$	elastic strain
$\boldsymbol{\varepsilon}^p$	plastic strain
ξ	damping
ξ_N	Newmark integration damping
ζ	logarithmic standard deviation (in statistics)

Abbreviations

AR	Amplification Ratio
BEM	Bruggeman Effective Medium
CDF	Cumulative Density Functions

Continued on next page...

CPD	Coupled pore Pressure and Deformation
CSL	Critical State Line
CU	Coefficient of Uniformity
CV	Coefficient of Variation
DPD	Decoupled pore Pressure and Deformation
ECP	École Centrale Paris
EDP	Engineering Demand Parameters
EMT	Effective Medium Theories
EQL	Equivalent Linear
FEM	Finite Elements Model
FF	Free Field
FFT	Fast Fourier Transform
FS	factor of safety
<i>GEFDyn</i>	Géomécanique Eléments Finis DYNamique
GEM	Generalized Effective Medium
GMPE	Ground Motion Prediction Equations
HS	Hashin and Shtrikman
ICL	Isotropic Consolidation Line
IM	Intensity measures
IP	Plasticity Index
IQR	Inter-Quartile Range
LA	Local Average
LMS	Loose-to-Medium Sand
MDS	Medium-to-Dense Sand
NGA	Next Generation Attenuation
NRSR	Normalized Response Spectra Ratio
OCR	Over-Consolidation Ratio
PBEE	Performance-Based Earthquake Engineering
PDF	Probability Density Function
PEER	Pacific Earthquake Engineering Research Center
PGA	Peak Ground Acceleration

Continued on next page...

PGD	Peak Ground Displacement
PGV	Peak Ground Velocity
PHA	Peak horizontal acceleration at outcropping rock
PRENOLIN	PREdiction of NOnLINear effects
PSA	Pseudo-Spectra of Acceleration (or acceleration response spectra)
PSV	Pseudo-Spectra of Velocity
RC	Resonant Column
RSN	Record Sequence Number
RSR	Response Spectral Ratio
SB	Structure's base
SDOF	Single Degree-Of-Freedom
SED	Strain Energy Density
SGLMM	Spatial Generalized Linear Mixed Models
SI	Spectral Intensity
SR	Stress Ratio
SSI	Soil-Structure Interaction
STFT	Short-Time Fourier Transform
TF	Transfer Function

Chapter 1

Introduction

1.1 Motivation

Recent ground motions such as the Christchurch, New Zealand and Tohoku, Japan earthquakes, both in 2011, evidence the need to account for the effects of the site geology and the nonlinear soil behavior on the seismic risk analysis of structures. Although these so-called site effects have been accepted and studied for more than 30 years by the engineering and seismological communities; in modern building codes, they are only addressed by site amplification factors depending on the intensity of the motion, the period of interest and some information of the soil deposit, often limited to the average shear wave velocity in the upper 30 meters (V_{s30}). These factors embedded on the ground motion prediction equations (GMPEs) are derived from mostly empirical functions and as a result, represent a blended average site amplification effect.

Liquefaction is described as the loss of soil strength due to the rapid increase in pore water pressure and consequent reduction of effective stress. Seismically-induced soil liquefaction can alter the characteristics of ground shaking at a site, however, at present these effects are not included in current site amplification factors and building codes. In some contemporary building codes, when a soil deposit is likely to be susceptible to liquefaction, effective stress site response analysis is required to accurately assess the seismic risk. In general, this risk is the convolution of the seismic hazard and the vulnerability of the site. A thorough characterization of the possible input motions and the soil behavior is required for a reliable assessment of seismic risk. Additionally, special attention is required to properly quantifying it, for example via advanced numerical modeling. Lastly, if the risk is above a certain threshold, soil improvement may be desired. Then again, a proper evaluation followed by the consequences to the original soil characterization is needed.

Concerning liquefaction evaluation, a number of procedures have been developed in the last 40 years. These range from simplified procedures based on empirical relationships and correlations to advanced procedures based on site-specific, nonlinear ground response analyses. Effective stress analysis accounting for the excess pore water pressure generation is necessary if maximum shear strain becomes several percent. However, effective stress analysis is more time consuming and less known than total stress analysis hence the latter is frequently carried out even when shear strains become very large. Moreover, protocols for nonlinear code usage are not very well established especially for liquefaction cases, and this has restricted their use in practice. Moreover, it is not clear in which cases the use of effective stress is required.

Furthermore for a robust seismic risk assessment, the effect of the soil-structure interac-

tion (SSI) on the structure's performance as well as in that of the soil deposit have to be addressed. The SSI effects have been the subject of numerous investigations assuming linearity of both, structure and soil foundation. Nevertheless, to take into account the modeling of soil liquefaction, the soil behavior must be nonlinear. In every-day engineering practice, nonlinear structural seismic analysis procedures become more and more frequent. In contrast, the addition of soil nonlinearity in the dynamic SSI analysis is still out of the usual practice, and is restricted because of the high computational cost. As a general rule, the SSI effects are assumed beneficial and ignored. However, a more precise knowledge of the expected structural seismic response including both liquefaction and SSI effects could allow to reduce the cost of new structures with the same reliability and improve the earthquake engineering practice.

1.2 Objectives

The main objective of this thesis is to be a contribution to the numerical modeling of soil nonlinearity and, in particular, liquefaction evaluation and mitigation. In pursuit of the main objective, several subordinate objectives are also addressed:

- Validate the numerical model for taking into account realistically the physical phenomena of wave propagation and nonlinear soil behavior.
- Quantitatively assess the effects of pore-water pressure generation by using objective and effective engineering demand parameters (EDPs) of the seismic site response and the structure's performance.
- Develop a procedure to model the uncertainty due to soil improvement techniques in terms of spatial variability added with the treated soil.

This work aims to show how realistic finite element models (FEM) can be constructed and applied in a practical way to deal with practical engineering issues associated to nonlinear SSI and liquefaction effects. Several EDPs for both structure and soil responses are analyzed in order to summarize their behavior under seismic loading. Different soils and structures are tested and to a certain extent, conclusions and general tendencies are identified. The ultimate goal is to encourage practice of coupled analysis, nonlinear soil modeling and SSI effects in order to improve the assessment of the seismic risk analysis. Generally, the evaluation of the seismic risk is related to the combined probability of attaining a threshold of a particular damage

measure. However, the final calculation of this probability, often shown in the form of fragility curves, has been intentionally excluded from the scope of the present work.

1.3 Outline

A schema of the thesis framework is shown in Figure 1.1. This thesis is organized in three main chapters that are delineated with dashed boxes in the figure.

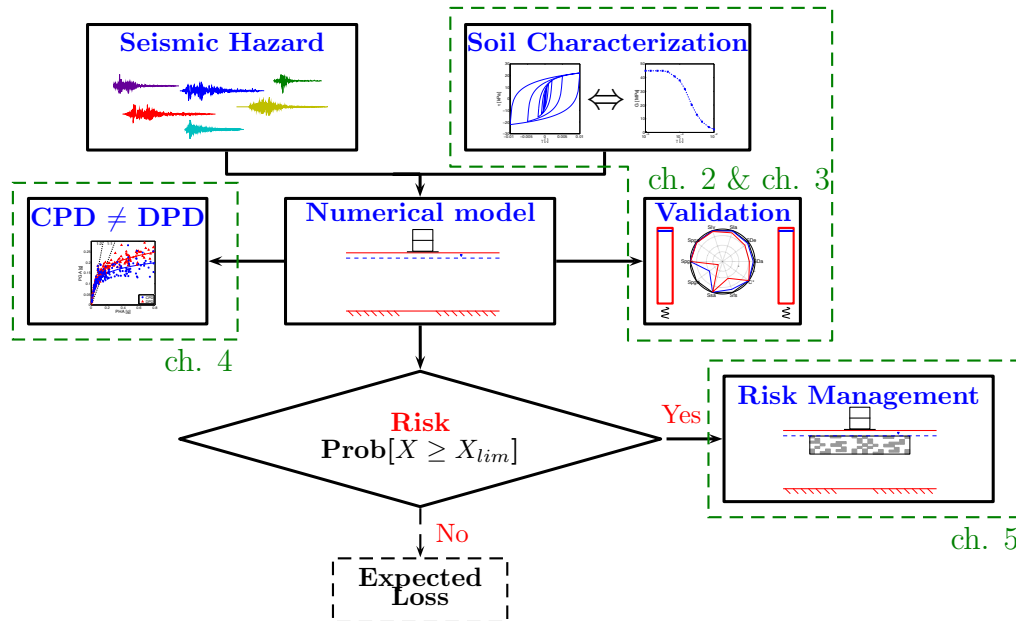


Figure 1.1 – Schema of the thesis framework

As part of the initial step on the seismic risk analysis, **chapters 2 and 3** are consecrated to the characterization of the soil behavior and its constitutive modeling, respectively. **Chapter 2** starts with a brief literature review on the numerical modeling of nonlinear soil behavior. First the governing equations are established for both the dynamic behavior of saturated soils and for the wave propagation. Some recent techniques to identify nonlinear soil behavior by ground motion analysis are presented followed by an overview of nonlinearity characterization via laboratory testing. A procedure is proposed to account for the error due to the external measurements in cyclic triaxial testing.

Further on, **chapter 3** presents the numerical tools used in this study. The finite element method (FEM) in time domain and the constitutive soil model used for the numerical simulations are described. Special attention is given to the model's sensibility to the numerical parameters and the validation of the model for nonlinear behavior and 1D wave propagation. Different numerical aspects developed within the model are discussed and some guidelines are

provided for the time integration scheme and the boundary conditions.

Chapter 4, explores the effect of coupling excess pore pressure (Δp_w) and soil deformation on seismic site response analysis. With this purpose, a coupled (CPD) model is compared to a fully drained (DPD) one where initial conditions are identical and differences are only due to the generation of Δp_w . First, the effect on the surface motion is analyzed by 1D wave propagation for two types of soils: loose-to-medium (LMS) and medium-to-dense (MDS) sands. This part contains material from an article published in *Acta Geotechnica* ([Montoya-Noguera and Lopez-Caballero, 2016](#)). Afterwards, a 2D soil-structure interaction (SSI) model is studied and the effect of coupling is then evaluated in the structure's settlement and seismic performance. At this stage, only the LMS deposit is used and two structures with different predominant periods are tested.

In **chapter 5**, an innovative method is proposed to model spatial variability added to the deposit due to soil improvement techniques used to strengthen soft soils and mitigate liquefaction. The method consists in coupling FEM with a binary random field in order to account for the interactions between the natural soil and the treated one. First the method is tested in a simple case, which is the bearing capacity evaluation of a shallow foundation under purely cohesive soil. Afterwards, it is used to assess the liquefaction-induced settlement of a structure under cohesionless loose soil. The latter, in part, contains material published in *GeoRisk* journal ([Montoya-Noguera and Lopez-Caballero, 2015](#)).

Conclusions arising from this work and suggestions for future research are presented in the last chapter. Three appendices are used to give more details on the signal motions, the soil model parameters and the 2D modeling.

Chapter 2

Numerical modeling of dynamic soil behavior

This section aims to link wave propagation analysis with the dynamic behavior of soils. Firstly the governing equations of dynamic soil behavior are presented. Then an introduction to wave propagation in homogeneous and layered systems is followed by an overview of the soil behavior under dynamic loading. Highlight is given to the soil properties that describe or control the wave propagation and the relationship between field and laboratory measurements.

2.1 Governing equations

Concerning the dynamic behavior of saturated soils, the state of the system is described by the displacement and pressure quantities. However, strains and stresses will appear in the conservation equations. The relation between these two sets is done by the soil constitutive laws.

For fully saturated soils, the behavior of the solid skeleton is derived assuming the principle of effective stress proposed by [Terzaghi \(1943\)](#). The total stress tensor ($\boldsymbol{\sigma}$) is separated into two components: the effective stress tensor ($\boldsymbol{\sigma}'$) and the pore pressure (p_w). That is:

$$\boldsymbol{\sigma} = \boldsymbol{\sigma}' - p_w \cdot \mathbf{I} \quad (2.1)$$

where \mathbf{I} is the second-order identity tensor. In equation 2.1 the continuum mechanics sign convention is assumed, i.e. tractions and fluid pressures are positive. This decomposition is strictly correct only if the increment of pore pressure for a constant effective stress does not deforms the soil skeleton.

The set of governing equations for the system is the following:

- Overall equilibrium for the soil-fluid mixture:

The momentum equation for a system subjected to a displacement \mathbf{u} is:

$$\mathbf{div} \boldsymbol{\sigma}' - \nabla p_w + \rho \cdot \mathbf{g} = \rho \cdot \ddot{\mathbf{u}} \quad (2.2)$$

where ρ is the total average unit mass ($\rho = n \cdot \rho_w + (1 - n) \cdot \rho_s$); n is the soil porosity; ρ_w , the fluid mass; ρ_s , the soil particle mass; \mathbf{g} , the gravity acceleration vector and $\ddot{\mathbf{u}}$ is the solid skeleton acceleration.

- Equilibrium of water and flow conservation equation using generalized Darcy's law:

Assuming each phase as homogeneous, the fluid movement with respect to the solid skeleton (\mathbf{v}_{rw}) is:

$$\mathbf{v}_{rw} = \mathbf{K} \cdot [-\nabla p_w + \rho_w \cdot (\mathbf{g} - \rho \cdot \ddot{\mathbf{u}})] \quad (2.3)$$

where \mathbf{K} is the permeability tensor:

$$\mathbf{K} = \frac{\boldsymbol{\kappa}}{\rho_w \cdot \mathbf{g}} \quad (2.4)$$

with $\boldsymbol{\kappa}$ being the kinematic permeability tensor, also known as the hydraulic conductivity and measured in m/s.

Then, the combination of the mass conservation in both phases is:

$$\mathbf{div} \dot{\mathbf{u}} + \mathbf{div} \mathbf{v}_{rw} = -n \frac{\dot{p}_w}{\mathbf{K}_w} - (1 - n) \frac{\dot{p}_w}{\mathbf{K}_s} \quad (2.5)$$

where \mathbf{K}_w and \mathbf{K}_s are respectively the fluid and solid bulk compressibility. These are related by the compressibility parameter Q :

$$\frac{1}{Q} = \frac{n}{\mathbf{K}_w} + \frac{1 - n}{\mathbf{K}_s} \quad (2.6)$$

By replacing equations 2.3 and 2.6 in equation 2.5, the mass conservation is finally described by the following expression:

$$\mathbf{div} \dot{\mathbf{u}} - \mathbf{div}(\mathbf{K} \cdot (\nabla p_w - \rho_w \cdot \mathbf{g})) - \mathbf{div}(\mathbf{K} \cdot \rho_w \cdot \ddot{\mathbf{u}}) + \frac{\dot{p}_w}{Q} = 0 \quad (2.7)$$

2.2 Wave propagation

The case of SH-wave propagation in the vertical direction will be presented for a homogeneous elastic media. Afterwards, the results will be extended for a multi-layer media and for soil nonlinearity.

Theoretically, only body waves exist in an unbounded media. These waves can be decomposed in two: primary (p) and secondary (s) waves. As the name hints, p-waves have a higher velocity and reach the surface faster. The energy in these waves travels by compressing and dilating the material in the direction of propagation. In contrast, the s-waves move by shearing the material in a transverse plane to the propagation direction. Considering that more

than 90% of the energy radiated from an earthquake is carried by the s-waves (Boatwright and Fletcher, 1984), this section will focus on these waves. Additionally, as only the shallow soil layers will be modeled, a reasonable hypothesis is that the waves are purely vertical. Hence, the analysis will consist of the SH wave propagation along the vertical direction. In order to simplify the equations, in this section, the soil will be considered as homogeneous, isotropic and elastic. These hypotheses will only be valid for very small levels of strains (i.e. $\gamma < 1 \cdot 10^{-7}$ according to Ishihara, 1993), but will be useful as reference to evaluate the level of non linearity in other cases.

2.2.1 Motion equation simplified for 1D linear elastic material

If no body forces are considered, pore-water pressure is neglected and only horizontal displacements (u_y) are introduced, the equation of motion (2.2), in partial differences, is reduced to:

$$\frac{\partial \sigma_{yz}}{\partial z} = \rho \frac{\partial^2 u_y}{\partial t^2} \quad (2.8)$$

In the case of linear elastic behavior, the shear stress is related to the shear strain by the shear modulus (i.e. $\sigma_{yz} = 2G \cdot \varepsilon_{yz}$) and the strain - displacement relationship simplified by the SH wave propagation is $\varepsilon_{yz} = 0.5 \partial u_y / \partial z$. Replacing these two definitions in equation 2.8, gives:

$$\frac{G}{\rho} \frac{\partial^2 u_y}{\partial z^2} = \frac{\partial^2 u_y}{\partial t^2} \quad (2.9)$$

where $G/\rho = V_s^2$, the square of the shear-wave velocity. Further on, the shear stress (σ_{yz}) will be referred to as τ and the shear strain ($2\varepsilon_{yz}$), as γ ; which are of common use in laboratory testing.

When vertical displacements are introduced, the propagation of compressive waves is given by the p wave velocity (V_p) which is related by the following expression:

$$\frac{V_p}{V_s} = \sqrt{\frac{2 - 2\nu}{1 - 2\nu}} \quad (2.10)$$

For a typical Poisson's ratio (ν) of 0.3, the V_p is $1.87V_s$. As the stiffness of the material with respect to deformation increases, ν approaches 0.5, and the V_p approaches infinity, though seismic recordings in stiff rock stations present clearer p and s arrivals.

The simplest case of a bounded media is a semi-infinite deposit where a condition of free-field is imposed in one end, for example at $z=0$ (see Figure 2.1). Hence, two main boundary

conditions are imposed: (1) at the surface no shear nor normal stresses are possible and (2) at infinite depth induced displacement approaches zero. When these conditions are applied to the body waves, surface waves appear. Mainly two types can be identified: Rayleigh and Love waves. The former are present in any homogeneous elastic half-space and the latter are only due to superficial layers of lower stiffness.

On one hand, Rayleigh waves can be thought of a combination of p- and s-waves with a velocity slightly smaller than V_s for all ν less than 0.5 (Kramer, 1996). One important characteristic is that the horizontal and vertical components are out of phase by $\pi/2$; thus their identification is possible by evaluating the rotational phase between the two components. Regarding particle motion, Rayleigh waves are identified by retrograde elliptic shapes at shallow depths. Additionally, these waves are dispersive, which means that at higher frequencies, their velocity is lower. This property is of key importance for geophysics evaluation of subsurface stiffness profiles.

In the other hand, the Love waves are essentially SH waves that are trapped by multiple reflections within the surficial layer. Their velocity varies from the V_s of the deeper layer at low frequencies to that of the shallow layer at very high frequencies. Surface waves have very low attenuation, thus at distances greater than about twice the thickness of the earth's crust, the peak ground motion will be produced by the surface rather than by the body waves (Kramer, 1996).

2.2.2 Homogeneous deposit lying over a semi-infinite bedrock

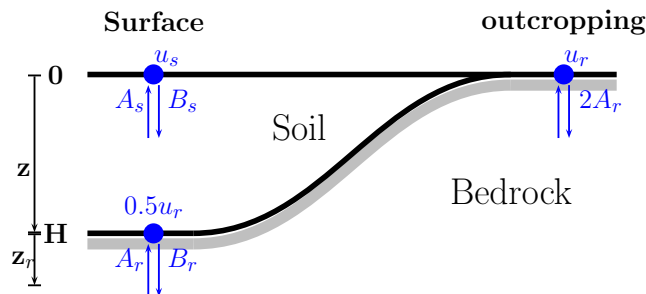


Figure 2.1 – Homogeneous deposit lying over a semi-infinite bedrock : 1D analysis

For the first case, a uniform layer lying over a flexible rock is shown in Figure 2.1. In the bedrock, the displacement field is the sum of the up-going (incident) and down-going (reflected) waves:

$$u_r(z_r, \omega) = \exp(i \cdot \omega \cdot t) [A_r \cdot \exp(i \cdot k_r \cdot z_r) + B_r \cdot \exp(-i \cdot k_r \cdot z_r)] \quad (2.11)$$

where z_r is the depth of the reference in the bedrock - in the Figure 2.1 equal to H - and k_r is the complex wave number. In the elastic case, k_r is the ratio between the angular frequency and the shear wave velocity, i.e. $k = \omega/V_s$. Lastly, A_r and B_r are the amplitudes associated to the upward and downward propagating waves, respectively.

Similarly, in the soil deposit, the displacement field is given by:

$$u_s(z, \omega) = \exp(i \cdot \omega \cdot t) [A_s \cdot \exp(i \cdot k_s \cdot z) + B_s \cdot \exp(-i \cdot k_s \cdot z)] \quad (2.12)$$

The coefficients A_r , B_r , A_s and B_s , depend on the boundary conditions. In the interface (i.e. $z_r = 0$ and $z = H$), the continuity of the displacements and stresses has to be assured. This gives:

$$A_r + B_r = A_s \cdot \exp(i \cdot k_s \cdot H) + B_s \cdot \exp(-i \cdot k_s \cdot H) \quad (2.13)$$

$$A_r - B_r = \frac{k_s \cdot G_s}{k_r \cdot G_r} [A_s \cdot \exp(i \cdot k_s \cdot H) + B_s \cdot \exp(-i \cdot k_s \cdot H)] \quad (2.14)$$

The coefficient $(k_s \cdot G_s)/(k_r \cdot G_r)$ is the complex impedance contrast (C) and it can be simplified to $(V_s \cdot \rho_s)/(V_r \cdot \rho_r)$, which is known as α_z . Additionally, the inverse of α_z is referred to the impedance ratio (I), which will be used in this study. Note that when the rock is infinitely rigid with respect to the soil deposit, I tends to ∞ and the upward and downward waves in the rock are equal (i.e. $A_r = B_r$).

Finally, as in the free surface ($z = 0$), no stresses are possible:

$$B_s = A_s \quad (2.15)$$

Leaving A_r and B_r as a function of A_s , it gives:

$$A_r = \frac{1}{2} A_s \cdot \left[\left(\frac{I+1}{I} \right) \cdot \exp(i \cdot k_s \cdot H) + \left(\frac{I-1}{I} \right) \exp(-i k_s H) \right] \quad (2.16)$$

$$B_r = \frac{1}{2} A_s \cdot \left[\left(\frac{I-1}{I} \right) \cdot \exp(i \cdot k_s \cdot H) + \left(\frac{I+1}{I} \right) \cdot \exp(-i \cdot k_s \cdot H) \right] \quad (2.17)$$

The transfer function (TF) is the ratio between two wave fields in frequency domain and it gives information solely of the soil between the 2 points. Thus, if the TF is computed between

the displacements of the soil surface and the base (or bedrock) the response of only the soil deposit will be seen. However, if the reference is taken at the outcropping bedrock (i.e. at rock surface), the response will take into account the effect of the soil-base interface. The latter is also known as the amplification ratio (Dobry et al., 1982), as it characterizes how much the soil amplifies the rock energy. These functions can be expressed as:

$$TF_{surf/bd} = \frac{2A_s}{Ar + B_r} = \frac{1}{\cos(k_s \cdot H)} \quad (2.18)$$

$$AR_{surf/out} = \frac{2A_s}{Ar} = \frac{1}{\cos(k_s \cdot H) + i \sin(k_s \cdot H)/I} \quad (2.19)$$

Regarding equation 2.18, two important aspects can be highlighted. Considering elastic materials, the amplitude of the surface displacement will be at least equal to that of the bedrock, i.e. only amplification is allowed. Additionally, when the cosine approaches nullity (i.e. when $\omega \cdot H/V_s \rightarrow \pi \cdot n - \pi/2$), the amplification tends to infinity. That is, for frequencies (f) equal to $(2n - 1) \cdot V_s/(4H)$, n being the modes of the system. The response of the elastic wave propagation is therefore highly dependent on the frequency of the input motion and it will be strongly amplified depending on the geometry (depth) and the material properties (s wave velocity). If a small damping (ξ) is present, the complex number will then be $k_s^* = k_s \cdot (1 - i \cdot \xi)$, and the modulus of equation 2.18 turns to:

$$|TF|_{surf/bd} = \frac{1}{\sqrt{\cos^2(k_s \cdot H) + \sinh^2(\xi \cdot k_s \cdot H)}} \approx \frac{1}{\sqrt{\cos^2(k_s \cdot H) + (\xi \cdot k_s \cdot H)^2}} \quad (2.20)$$

Hence the amplification will have a local maximum when $f = (2n - 1) \cdot V_s/(4H)$ but will not reach infinity. Additionally, the amplitude for each mode will decrease with frequency. The greatest amplification corresponds to the fundamental frequency (f_0) evaluated at the first mode ($n = 1$).

In contrast, equation 2.19 is related to the impedance ratio. Hence, the radiation damping is due to the elasticity of the bedrock and it also prevents the amplification reaching infinity. At resonance, the amplification is equal to the impedance ratio at all modes. But at the presence of a small damping, the amplitude of the transfer function for mode n is:

$$|AR|_{surf/out n} = \frac{I}{1 + 0.5 \cdot (2n - 1) \cdot \pi \cdot \xi \cdot I} \quad (2.21)$$

This equation will be useful in the next chapter to evaluate the damping introduced by the

numerical integration. Figure 2.2 shows the theoretical transfer function and amplification ratio for an elastic deposit. The effect of material damping and radiation damping induced by the impedance ratio is shown. As expected, material damping increases with frequency, hence short wavelengths are more affected by small scale heterogeneities (more attenuated), compared to larger wavelengths. In contrast, radiation damping is frequency-independent and depends solely in the impedance ratio.

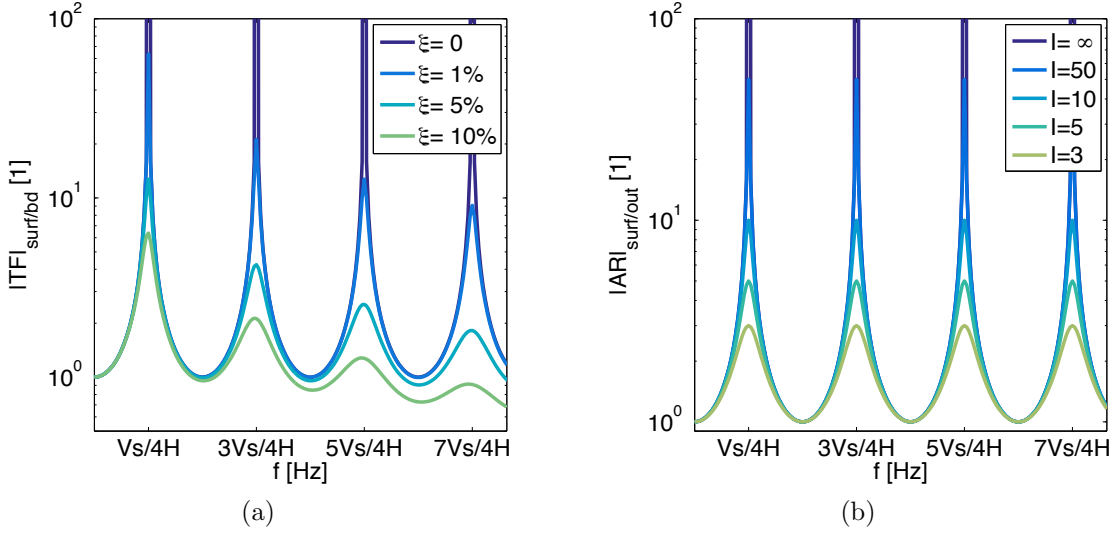


Figure 2.2 – Theoretical a) transfer function for different material damping and b) amplification ratio for an elastic deposit for different Impedance ratios (hence different radiation damping)

2.2.3 Multi-layer soil deposit

Finally, it is important to generalize the previous calculations for the case of multi-layer soil deposit. The theoretical transfer function can be deduced from the mono-layer case (Kramer, 1996). The equations 2.16 and 2.17 can be generalized for amplitudes A_m and B_m of the layer m , as follows:

$$A_{m+1} = \frac{1}{2}A_m \left(\frac{I_m^* + 1}{I_m^*} \right) \exp(i \cdot k_m^* \cdot h_m) + \frac{1}{2}B_m \left(\frac{I_m^* - 1}{I_m^*} \right) \exp(-i \cdot k_m^* \cdot h_m) \quad (2.22)$$

$$B_{m+1} = \frac{1}{2}A_m \left(\frac{I_m^* - 1}{I_m^*} \right) \exp(i \cdot k_m^* \cdot h_m) + \frac{1}{2}B_m \left(\frac{I_m^* + 1}{I_m^*} \right) \exp(-i \cdot k_m^* \cdot h_m) \quad (2.23)$$

where I_m^* is the impedance ratio between the layers m and $m + 1$:

$$I_m^* = \frac{\rho_{m+1} \cdot (V_s^*)_{m+1}}{\rho_m \cdot (V_s^*)_m} = \frac{\rho_{m+1} \cdot (V_s)_{m+1}(1 + i \cdot \xi_{m+1})}{\rho_m \cdot (V_s)_m(1 + i \cdot \xi_m)} \quad (2.24)$$

Additionally, k_m^* is the complex number taking into account the damping of the layer m :

$k_m^* = k_m(1 - i \cdot \xi_m)$ and h_m is the height of the layer. In order to find the amplitudes of all the layers, equations 2.22 and 2.23 are successively solved starting from the surface to the bottom, given that at the surface (i.e. $m = 1$) the shear stresses must be equal to zero and the amplitudes of the upward and downward waves must be equal ($A_1 = B_1$). The calculations are then performed by setting $A_1 = B_1 = 1.0$. The transfer function between the surface and the bedrock will then depend on the properties and height of each layer.

This function is the key formula for 1D wave propagation along borehole sensors since, if the layer parameters are known via deconvolution, it allows theoretical computation of the free surface waveform when the downhole waveform is given or vice-versa. It is also appealing to resolve the inverse problem, then the objective will be to come back to the layer parameters knowing the free surface and downhole waveform. Several algorithms can be found in the literature, such as those proposed by De Martin (2010) and by Regnier (2013), to identify the soil parameters by inversion methods. As long as the soil behavior is still elastic and small damping is present, these methods are very useful. However, there are multiple solutions for combinations of number of layers, their heights and properties and these will be affected differently by stronger loadings and nonlinear behavior. As an example the theoretical transfer function of the gradient profile presented in the verification section as P2 is shown in Figure 2.3b. Different number of layers - i.e. different discretization steps (Δz) - were tested and their effect on the transfer function can be identified. It is interesting to note that while the first two predominant frequencies are very similar, a great difference is presented for the third peak and specially for the highest Δz . In general, as the Δz decreases, the high predominant frequencies shift to the right. Additionally, it appears that the response arrives to a threshold for very low Δz as values of 1 and 5m are very similar for all frequencies.

2.3 Nonlinearity identification by ground motion analysis

Laboratory tests consistently indicate that the stress-strain relationship of soils is nonlinear, especially at shear strains larger than about $1 \cdot 10^{-5}$, however, nonlinearity identification by ground motion analysis is still challenging because the site effect itself is poorly isolated. The source and path effects are individual for every earthquake and tend to dominate the spectra of ground motions. In the late 80s and 90s, several strong motion recordings such as the 1985

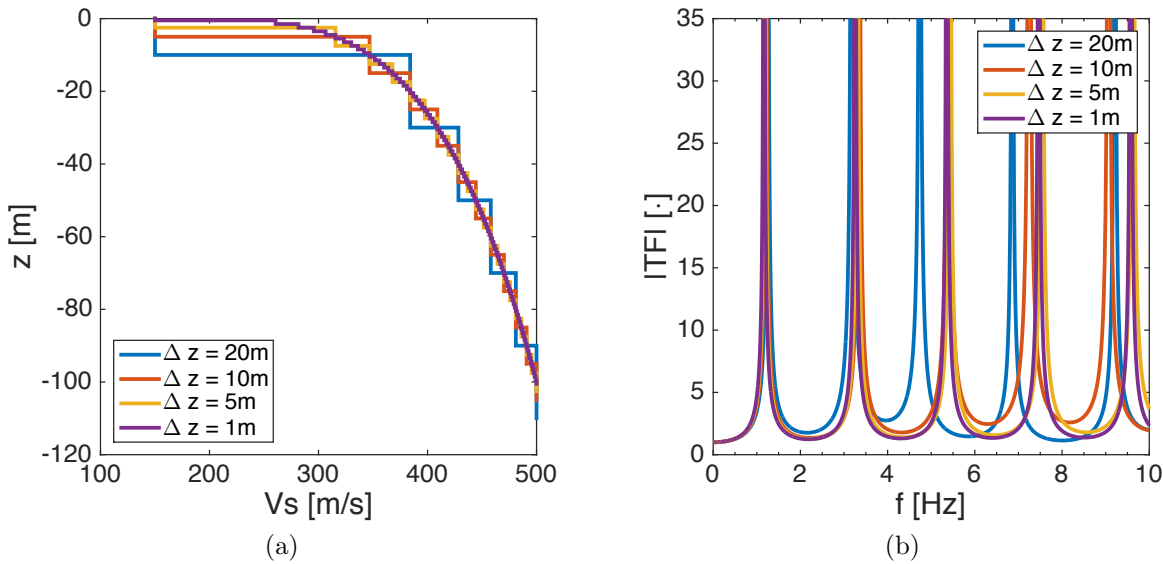


Figure 2.3 – An example of a) a shear wave velocity profile and the consequent b) theoretical transfer function for different number of layers - case of P2 profile on the verification section.

Michoacan earthquake, the 1989 Loma Prieta earthquake, the 1994 Northridge earthquake, the 1995 Kobe earthquake and the 1999 Chi-Chi earthquake, provided substantial evidence of soil nonlinearity. The paper by [Beresnev and Wen \(1996\)](#) comprehends a state of the art on this subject. In the last 25 years, the amount of available good-quality digital recordings of strong motions at surface and at vertical arrays has provided additional techniques to identify and measure soil nonlinearity in the wave propagation. Some of these techniques and results will be presented and later applied if possible in this study.

2.3.1 Peak acceleration

Concerning soft soil amplification, [Seed et al. \(1976\)](#) presented site factors which are still being used as reference nowadays. These amplitude dependent amplifications for different soil types were issued from the mean values of several surface recordings of eight earthquakes with magnitudes of about 6.5, occurring in the western part of the United States. The factors were given as ratios between the peak surface acceleration of a soft deposit (PGA) and the peak horizontal acceleration at outcropping rock (PHA) as shown in Figure 2.4a. The relationship of motions recorded at different stations (in different site conditions) were used to calculate the curve for stiff soil conditions and the curve of deep cohesionless soils. Values for PHA above 0.3g are extrapolations as no data was available. Additionally, an estimated curve for soft to medium stiff clay and sand was provided by the authors based on experience of the few peak accelerations recorded on soft to medium clay deposits. These curves correspond to the average behavior,

however no information was given in the original curves accounting for data dispersion. This indicates that some caution should be exercised in interpreting site-response characteristics as source and path effects could be also involved. Note that the threshold beyond which nonlinearity becomes perceptible is between 0.1 and 0.2g, however, according to [Beresnev and Wen \(1996\)](#), in the laboratory, the soil behavior is slightly more nonlinear.

Using data of distant sites from the 1985 Michoacan earthquake and the 1989 Loma Prieta earthquake, [Idriss \(1991\)](#) performed site response calculations for PHA values above 0.2g and developed a median factor curve for soft sites. In comparison with the estimated curve by [Seed et al. \(1976\)](#), higher amplifications for small PHA values are presented. For instance, for PHA between 0.05g and 0.10g, PGA are 1.5 to 4 times greater. Additionally, the threshold for nonlinearity is at 0.4g, more than twice the one estimated by [Seed et al. \(1976\)](#).

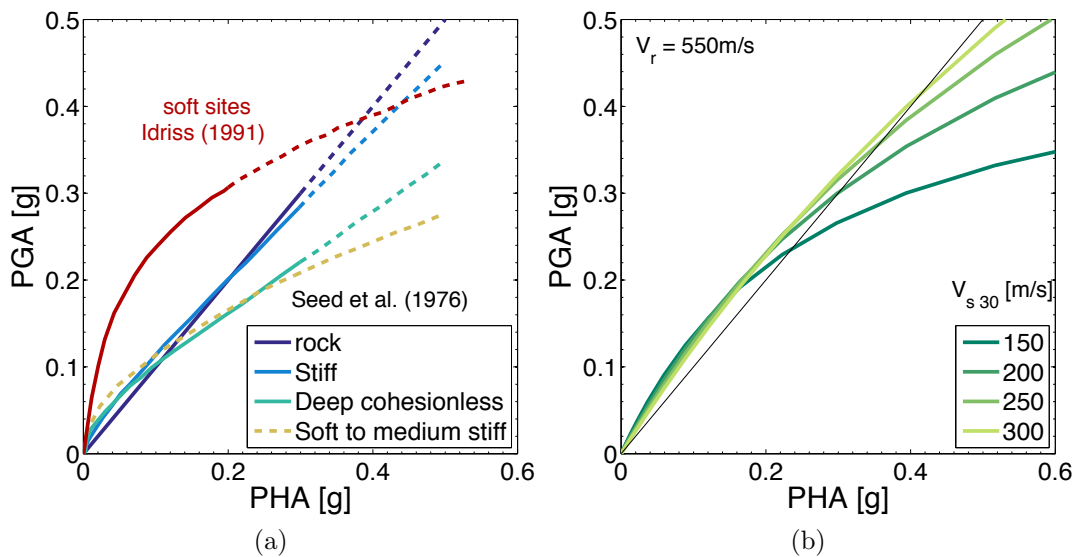


Figure 2.4 – Peak ground acceleration (PGA) as a function of peak horizontal acceleration at outcropping (PHA) a) estimations based on recordings and extrapolations (after [Seed et al., 1976](#); [Idriss, 1991](#)) and b) GMPE from [Abrahamson et al. \(2013\)](#)

In modern building codes, this amplification or deamplification is taken into account via the ground motion prediction equations (GMPEs), which provide estimates of spectral accelerations depending on the earthquake magnitude and focal mechanism, site-source distance, and site characteristics. These equations are essentially a combination of regression analysis of recorded seismograms and calibration of analytic models. Some modern GMPEs account for shallow soil site conditions through V_{s30} , hence a similar PGA - PHA relationship can be established if PHA is calculated with a much higher V_{s30} . Concerning PGA at soft soil deposits, most equations show a deamplification with respect to PHA. Figure 2.4b shows results for the GMPE developed

by [Abrahamson et al. \(2013\)](#) as part of the next generation attenuation (NGA) project. The PHA values correspond to the GMPE PSA evaluated at the minimum period (i.e. $T=0.01s$), with V_{s30} of 550m/s (i.e. V_r) and varying magnitude. As for PGA, the same parameters were used except for varying V_{s30} . It can be seen that the threshold for nonlinearity increases from about 0.2g to 0.4g as V_{s30} increases. This threshold increases slightly as V_r increases. Compared to the curve given by [Idriss \(1991\)](#) with the given V_r the threshold is similar for $V_{s30}=300m/s$. However the amplification for values below the threshold is much smaller.

2.3.2 Borehole transfer function

Borehole vertical arrays are useful to identify the nonlinearity in a soil deposit. If the downhole instrument is installed in the bedrock, the surface-to-bedrock Fourier spectral ratio gives a pure (borehole) transfer function of the soil, nearly isolated from source and path effects. Recent studies have focused on the analysis of these arrays and some examples will be presented.

[Bonilla et al. \(2011a\)](#) used recordings from the Tohoku earthquake, Japan 2011, with magnitude (M_w) of 9, to evidence nonlinear site response. This event is one of the largest events recorded in the near-field by numerous stations in borehole -i.e. in surface and at depth- (KiK-net) and only at surface (K-net). The average shift to lower frequencies depending on the soil conditions was evaluated by comparing the borehole transfer function ($|TF|$) evaluated for weak motions (i.e. $PGA < 0.02g$) were compared to the one computed for the Tohoku earthquake.

Figure 2.5a shows examples for four stations with very different average shear-wave velocity in the top 30m (V_{s30}). The Tohoku $|TF|$ (in black) presents a deamplification for high frequencies and a shift of the predominant frequency to lower values compared to the linear $|TF|$ confidence limits of 95% (light gray area) and 68% (dark gray area). It can be noted that the frequency for the shift of deamplification between the linear and nonlinear increases with the V_{s30} . To better identify this nonlinear shift, [Bonilla et al. \(2011a\)](#) followed the procedure by [Field et al. \(1997\)](#) and computed the average ratio between linear and nonlinear amplification functions for 73 sites ranged in different V_{s30} classes as shown in Figure 2.5b. If this ratio is larger than one, nonlinear behavior is suspected at a given frequency band. Nonlinear soil effects appear to increase with decreasing V_{s30} , but even at stiff sites ($V_{s30} > 800m/s$), nonlinearity can be evidenced. In this case, a clear separation is observed between classes and the nonlinearity spreads through a large band. For example, for soils having $V_{s30} < 400m/s$ the nonlinearity is present from 3 to 30Hz.

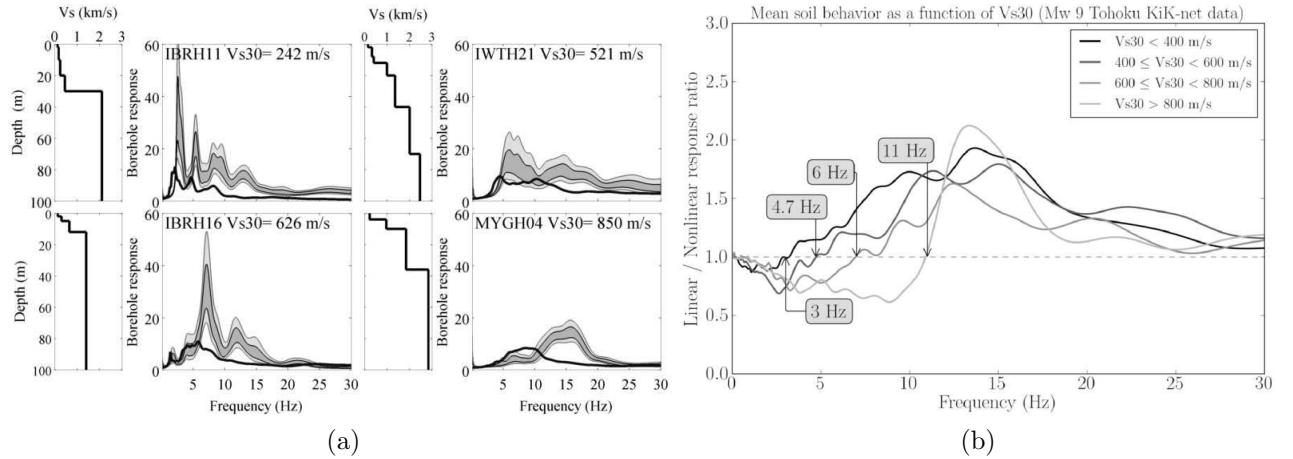


Figure 2.5 – Borehole transfer function: a) for weak motions - linear behavior- confidence limits of 95% (light gray area) and 68% (dark gray area) and for Tohoku earthquake - nonlinear - (black line) and b) average ratio between linear and nonlinear $|TF|$ for V_{s30} classes (after [Bonilla et al., 2011a](#))

An effort to quantify this nonlinearity was presented by [Regnier \(2013\)](#), by which two types of parameters were defined: the frequency shift (Sh) and the percentage of non-linearity (PNL). The former is the frequency lag of the cross-correlation between the mean linear and nonlinear $|TF|$ and the latter is the normalized area between the nonlinear $|TF|$ and the 95% confidence limit of the linear $|TF|$. The normalization is made by the mean linear $|TF|$. These parameters were tested in more than 200 KiK-net sites with more than 45000 events, of which less than 1% was above 0.05g. Nonlinearity was primarily identified at the superficial layers, as the shallowest velocity contrasts are more affected by this soil behavior. As the use of H/V spectral ratios gave similar results as those with $|TF|$, these parameters could be calculated without the downhole sensors. In this type of sites, the nonlinearity can be triggered at lower PGA values hence, above a PGA threshold of 0.075g there is a probability above 40% that nonlinear soil behavior takes place. The borehole sensor in KiK-net stations is generally located about 100m from the surface though, V_s at 40m is in most cases above 500m/s. Hence, the $|TF|$ at KiK-net stations takes into account an elastic amplification from 100m to at least 40m and the nonlinearity of the superficial less stiff soil.

2.3.3 Time-frequency spectral functions

In order to see the spectral changes, time-frequency transforms are useful, as they produce a spectral estimate centered at each time element of the data ([Reine et al., 2009](#)). In this respect,

a 1D frequency data trace is mapped into a 2D spectrogram, which has dimensions of time and frequency. Mainly two types of time-frequency transforms can be used to compute the spectral function: (1) those with fixed time-windows and (2) those with frequency-dependent time-windows. The most recognized time-frequency transform is the short-time Fourier transform - STFT - (Hauge, 1981 and Dasgupta and Clark, 1998), in which the Fourier transform is applied to a time data trace which is gated by a sliding window function. This window can be described by, among other, a rectangular, a Hamming or a Gaussian window. When using the latter, the STFT is called a Gabor transform. In the work of Wu et al. (2009) and Wu and Peng (2011) a 5% Hanning window is used. Concerning the second type, the S-transform (Stockwell et al., 1996) and the wavelet transform (Rioul and Vetterli, 1991; Chakraborty and Okaya, 1995) are becoming more popular as they can better localize the time extent of the energy at high frequencies (i.e. $f > 50\text{Hz}$). The S-transform uses a Gaussian window function with a fractional distribution width equal to the inverse of the center frequency (i.e. $\sigma = 1/f$), hence it analyzes shorter data segments as the frequency increases. Lastly for the wavelet transform a modulated Gaussian, or Morlet, wavelet is used. Once the type of wavelet is chosen, a time-scale decomposition is obtained, where increasing scale corresponds to decreasing frequency.

Reine et al. (2009) compared time-frequency transforms precision and accuracy to estimate attenuation. One example is shown in Figure 2.6. Relative amplitudes are shown for each case where the highest values (shown in red) are for the primary arrival. As expected, frequency-dependent transforms present broader frequency ranges of stability while using fixed-time windows will result in peaks and notches in the natural log spectral ratio for very high or very low frequencies, respectively. Moreover, concerning the frequency-dependent transforms, the use of shorter time windows for higher frequencies helps to isolate the primary arrival from the coda and to reduce the influence of spectral fluctuations by averaging. While for the fixed-time window transforms, the stability range and the spectral averaging at high frequencies will depend on the size of the time-window specified. Hence a careful decision of this time window size for the STFT could give comparable results with the S-transform in a chosen frequency range.

Studies by Iai et al. (1995) and Bonilla et al. (2005) among others, have identified cyclic mobility by the presence of large acceleration peak values riding over a low frequency carrier. The soil behavior under this phenomena will be addressed in the next chapter, yet it can be briefly explained by the apparent stiffness recovery when the soil is in the phase transformation between contractancy and dilatancy. In this phase, the spikes in acceleration are due to spikes

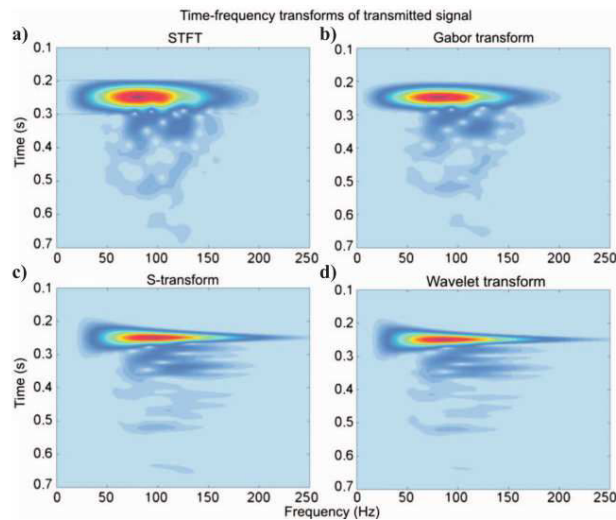


Figure 2.6 – Time-frequency spectral functions : a) STFT, b) Gabor transform, c) S-transform and d) wavelet transform (after [Reine et al., 2009](#)). Only relative amplitudes are shown where red depicts the highest values.

in stress and pore pressure generation. Time-frequency spectral functions are useful to identify the evolution of energy in these two domains.

[Bonilla et al. \(2011a\)](#) used the S-transform of the two horizontal components at surface of the Tohoku earthquake to identify the cyclic mobility on station MYG013 and the liquefaction on station CHB024 as shown in Figure 2.7. The highlighted regions on the acceleration indicate the high frequency spikes on a predominantly low frequency motion, characteristic of cyclic mobility. Furthermore, the S-transform shows shifts of energy to lower frequencies in these same time windows. However, for CHB024 station, the energy for frequencies higher than 0.5 Hz after around 125s is almost zero (dashed line in bottom panel of Figure 2.7b). Hence, it is possible that true liquefaction was triggered at this moment. [Bonilla et al. \(2011a\)](#) noted that field surveys close to the location of CHB024 station observed liquefaction; however, no information was provided on this subject for MYG013 station.

Similar to the borehole transfer function, the ratio between the time-frequency transforms at surface and at borehole provides information solely of the soil behavior by removing source and path effects of the input motion. Studies by [Wu et al. \(2009\)](#) and [Wu and Peng \(2011\)](#) analyze the temporal changes in the site response of various boreholes at different levels of peak ground acceleration (PGA). The shift to lower values of the resonant frequency and the acceleration deamplification is identified by using the sliding-window technique to compute the time-history spectral ratios by STFT from a pair of surface and borehole stations. This procedure was used with the EW component recording of Tohoku earthquake on station FKSH10 and results are

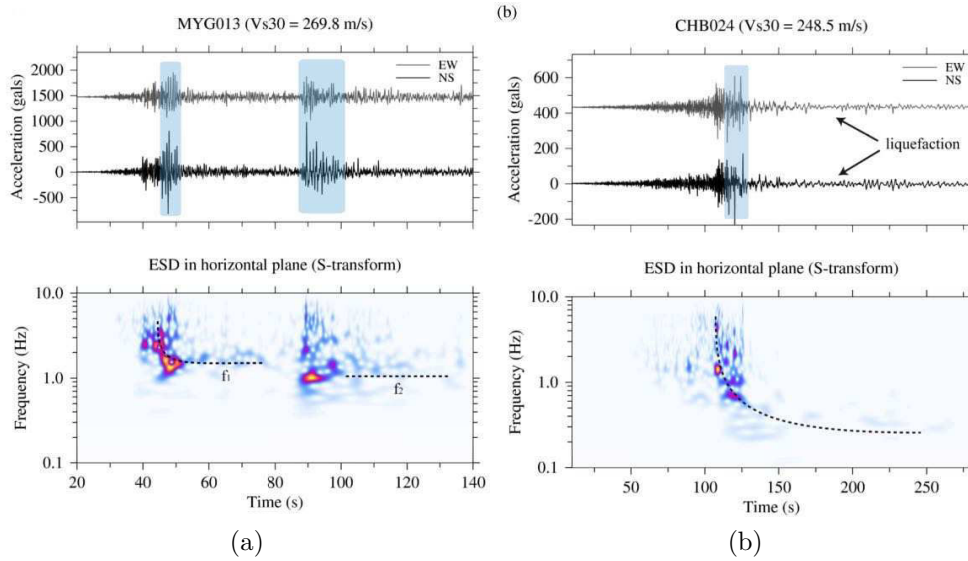


Figure 2.7 – Surface acceleration and normalized S-transform evaluated at surface acceleration for both components of the Tohoku earthquake recorded at two stations: a) MYG013 and b) CHB024 (after [Bonilla et al., 2011a](#))

shown in Figure 2.8. The first two traces show similar peaks in frequency but for the main shock, in the third trace, the frequency dropped almost 3Hz. For the last trace, the frequency is again increased hence a soil recovery can be evidenced.

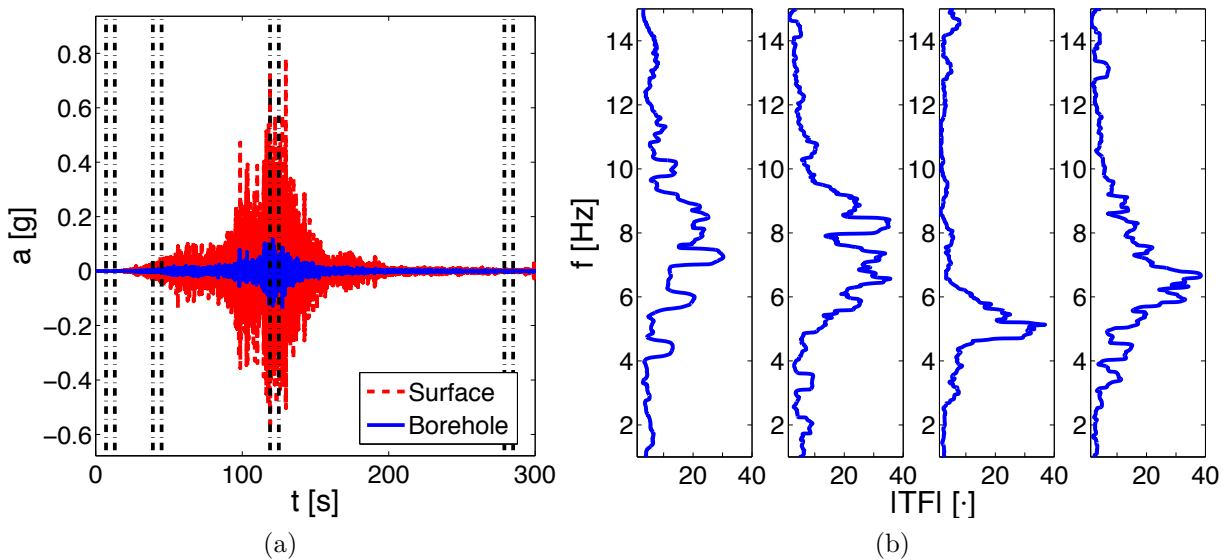


Figure 2.8 – Temporal changes on the $|TF|$ calculated for the EW component recording of Tohoku earthquake on station FKSH10: a) time history of acceleration and windows for the $|TF|$ evaluation and b) $|TF|$ for each time window (following procedure by [Wu et al. \(2009\)](#))

The computed STFT for FKSH10 and MYGH04 are shown in Figure 2.9. Above the STFT, the surface and borehole recordings are shown in white and black, respectively. Below, the

measure peak frequencies for each time window are shown with red dots and the least-squares logarithmic fitting after the PGA is the blue dashed curve. Finally, at the panel on the bottom, the measured peak spectral ratios are shown. Coseismic frequency and amplitude recovery after the mainshock reached to at least 90% of the reference value.

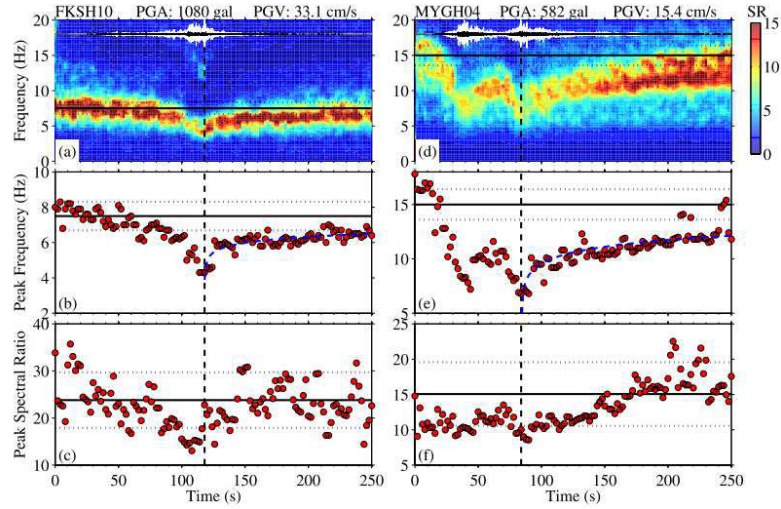


Figure 2.9 – STFT for the Tohoku earthquake recorded at stations (a) FKSH10 and (d) MYGH04. Below, are the peak frequencies (b and e) and the peak spectral ratios (c and f). The vertical dashed line denotes the PGA value and horizontal black solid and dashed lines show the reference value and uncertainties of the peak frequency obtained by averaging all the spectral ratios for the windows before the p-arrivals of all the earthquakes between 2011/01/01 and 2011/03/28 (after [Wu and Peng, 2011](#))

The reductions in the amplitude of the spectral ratios and in the peak frequency correspond to a reduction in soil strength and an increase in soil damping observed during laboratory studies and presented in Section 2.4. Assuming a homogeneous elastic soil layer of depth H with a constant shear wave velocity (V_s) over a half-space bedrock with large impedance contrast, recalling equation 2.20 presented at the beginning of the section, the fundamental frequency (f_0) of the soil layer can be computed by:

$$f_0 = \frac{V_s}{4H} = \frac{\sqrt{G/\rho}}{4H} \quad (2.25)$$

where G is the shear modulus and ρ is the soil density. Hence as frequency decreases, G decreases. Additionally, the soil damping (D) can be related to the deamplification of the spectral ratio by taking the amplification ratio as was shown in equation 2.21, thus with the

assumption of large impedance contrast, [Wu et al. \(2009\)](#) simplified the equation to:

$$|TF| = \frac{4}{\pi D} \quad (2.26)$$

Finally, [Wu et al. \(2009\)](#) used the displacement-based shear strain firstly introduced by [Hill et al. \(1993\)](#) defined as:

$$\gamma_{DB} = \frac{du}{dz} = \frac{du/dt}{dz/dt} = \frac{PGV}{V_s} \quad (2.27)$$

Figure 2.10 shows the mean and one standard deviation G/G_{max} degradation and D evolution, called ξ in the figure, with γ_{DB} as presented by [Hill et al. \(1993\)](#) for the 2004 M_w 6.6 Mid-Niigata Earthquake Sequences in Japan. G_{max} was evaluated as the average shear modulus before the earthquake. The results although with great variation, agree with the shear degradation reference curves for clay from [Vucetic and Dobry \(1991\)](#) and the damping evolution from [EPRI \(1993\)](#). The major drawback is the low level of strains. Unfortunately, the authors did not present similar curves for the Tohoku earthquake in the previously addressed article ([Wu and Peng, 2011](#)).

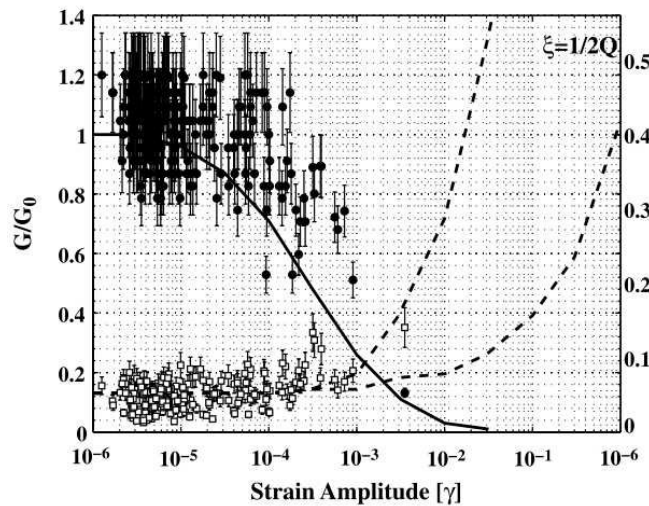


Figure 2.10 – Normalized shear modulus degradation and damping evolution with shear strain. Mean values are shown in solid circles and open squares, respectively. Vertical solid bars show one standard deviation. The solid and dashed lines show the modulus reduction curve for clay ([Vucetic and Dobry, 1991](#)) and the typical range of damping ratio for clay ([EPRI, 1993](#)), respectively. (after [Wu et al., 2009](#))

2.3.4 Seismic interferometry

Another technique to measure nonlinearity evolution is the seismic interferometry. It is a technique based on the correlation of waves recorded at different receivers with the advantage that it does not need a source at one of the locations and is independent of the behavior beyond the receivers. Two methods can be distinguished to perform interferometry: cross-correlation and (more recently) deconvolution. The primary difference between them is that the latter eliminates the characteristics of the incoherent excitation more effectively than does correlation. However, since the deconvolution is unstable due to the zeros in the denominator, a conjugation is used instead and a corrector parameter (ε) is added to the denominator, as follows:

$$D(\omega) = \frac{u_j(\omega)u_k^*(\omega)}{|u_k^*(\omega)|^2 + \varepsilon} \quad (2.28)$$

Interferometry is widely used for the identification of equivalent or homogenized mechanical properties of a geotechnical structure (e.g. shear wave velocity and attenuation or damping) under the condition of one-dimensional wave propagation. Figure 2.11 shows a clear example of identifying the shear wave velocity of the soil deposit for the initial part of a ground motion.

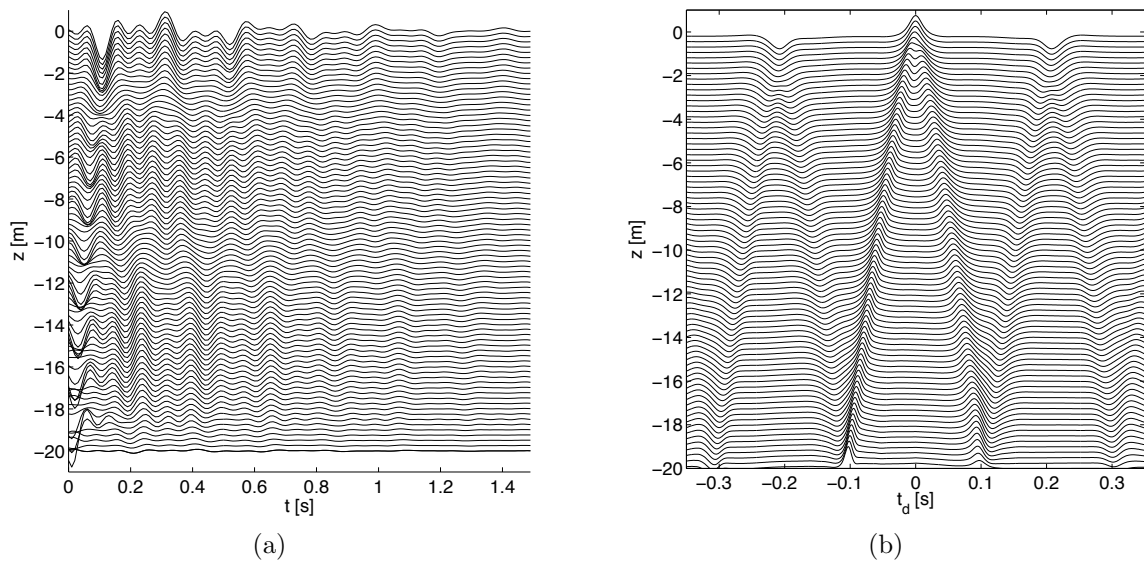


Figure 2.11 – Seismic interferometry example: a) time history of horizontal acceleration and b) interferometry with surface (acausal)

[Snieder and Safak \(2006\)](#) used seismic interferometry by deconvolution to extract the Mikkan library building response and for separating intrinsic attenuation from radiation damping. Two applications were identified: on one hand, when the deconvolution is performed with the signal recorded at the top floor, the upgoing and downgoing propagating waves are clearly

separated and the shear-wave velocity of the building can be identified. On the other hand, when the deconvolution is done with the waveform recorded in the basement, only the upward wave is visible and it provides information on the fundamental mode of the building. The advantage of interferometry is that it separates the mechanical properties of the media from the excitation and the surrounding soil (Curtis et al., 2006). Deconvolution is often used, rather than correlation, because it eliminates the characteristics of the incoherent excitation more effectively; however an additional parameter is needed to avoid instabilities near the notches in the spectrum. As only the deconvolved waves are independent of the excitation when the building response is linear; the nonlinearity of the system can be identified by comparing the deconvolved waveforms for events with different strengths.

Hence, if interferometry is used for strong ground motions and at different stages, i.e. for different time windows with different amplitudes, the evolution on the nonlinear behavior can be identified, namely decrease of shear modulus and increase of damping with shear strain. Recently, great advancements have been made concerning this subject. Besides the classical elastic shear-wave velocity (V_s) profiles inversion by deconvolution, Chandra et al. (2015) presented *in-situ* estimations of the shear modulus degradation curves for soils between sensors from two sites: the Garner Valley Downhole Array (GVDA) and the Wildlife Liquefaction Array (WLA). More than 5000 events with magnitudes (M_L) up to 5.5 were used for each array, however the maximum PGA value was 0.12g and 0.3g for GVDA and WLA respectively. Figure 2.12 shows some examples of the results corresponding to the WLA and the motions with NS direction. For the superficial layer, the average results fit well the laboratory measurements performed by Cox (2006) although a great dispersion is present. As not many strong ground motions were recorded, minimum normalized shear degradation found was 0.8, for deformations about $2 \cdot 10^{-4}$; however, nonlinearity was identified at very low deformations (e.g. $1 \cdot 10^{-6}$) and was satisfactorily fitted by a hyperbolic model. Surprisingly, some degradation was also presented between 7.7 and 30m.

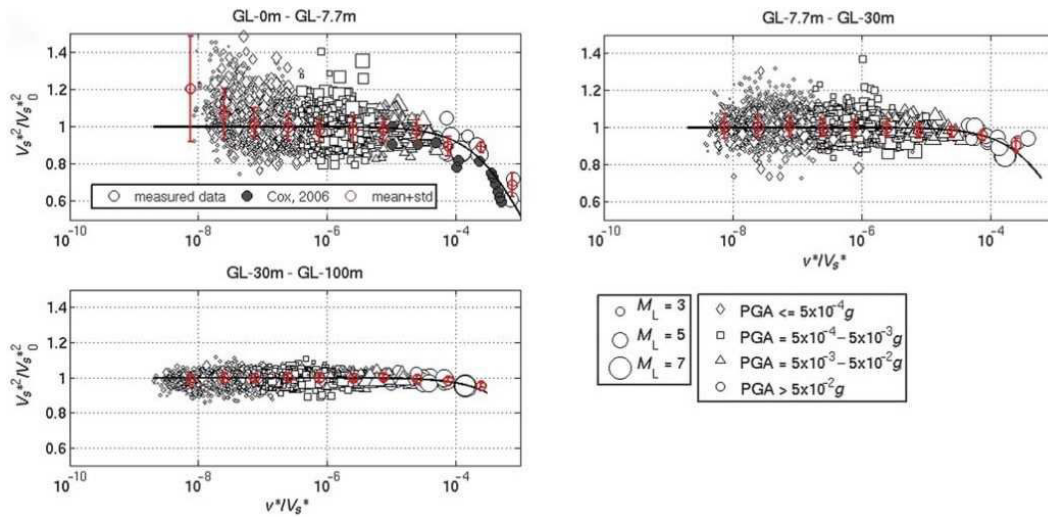


Figure 2.12 – Normalized shear modulus degradation and damping evolution with shear strain. NS direction. The solid black curve corresponds to the hyperbolic model and the gray-filled circles represent the results from Cox (2006). In red are shown the mean and one standard deviation for different bands of strain (after Chandra et al., 2015)

2.4 Dynamic soil behavior characterization

When a seismic wave is propagated through a soil deposit, the energy is felt by the soil as a series of shear loading and reloading that will affect both the media and the propagation of the wave. The behavior of soils under dynamic loading is mainly characterized by (1) the elastic - or maximum- stiffness represented by the Young modulus(E_{max}) in compression tests or shear modulus (G_{max}) in shear tests; and (2) the degradation of the secant shear modulus (G) and the evolution of damping (D) with respect to shear strain (γ), known as the nonlinearity curves.

The decrease of G involves the decrease of the shear wave velocity (V_s) and hence a shift to low frequencies, as was shown earlier. Additionally, the increase in D causes a deamplification of the amplitude of the propagating motion. Finally at high levels of strain, other phenomena appear related to the evolution of volume change and of pore water pressure generation, in the case of saturated media.

An accurate characterization of soils is of key importance for site-response-analysis. This characterization can be performed by laboratory testing or via *in-situ* measurements. A large variety of tests are available, each with different advantages and limitations mainly related to the level of strains tested. While efforts can be made to reduce the errors in the interpretation, testing equipment and sampling disturbance; uncertainties related to the inherent variability of soils resulting by natural geologic formations and inherent or induced anisotropy should not be neglected (Kramer, 1996).

Element laboratory tests use small specimens that are assumed to be representative of a larger body of soil. The most common element test used for low levels of strain is the resonant column (RC), while as for high levels of strain three cyclic shear tests are generally used: triaxial (TX), direct (CDS) and torsional (CT). When using the conventional triaxial testing system, that has the load and the displacement transducer outside the cell, [Tatsuoka et al. \(1995\)](#) found that the Young modulus (E) will be underestimated and the damping (D) value, overestimated.

A procedure to use laboratory data from cyclic triaxial test where strains are measured externally is proposed in order to use it for nonlinear modeling of dynamic soil behavior.

2.4.1 Measurement errors in triaxial test

[Tatsuoka et al. \(1995\)](#) presented data from numerous laboratory tests, performed by them and by other researchers, to illustrate the importance of measuring deformation characteristics accurately. Concerning the conventional triaxial testing system, three errors can be identified:

- Because of the piston friction, the measured load will be greater than the load applied; hence, both E and D can be overestimated.
- However, due to the deformation of the loading piston measured by the external transducer, E may be underestimated.
- Additionally, due to the frictional forces developed at the sample ends, known as bedding, the specimen deformation adjacent to the platens is restrained resulting in non-uniform loading and deformation that will cause an underestimation of E and an overestimation of D .

Globally, these errors will result in an underestimation of the Young modulus (E) and an overestimation of the damping (D) value, the latter being more important.

Figure 2.13 shows the effect of bedding error in cyclic triaxial tests on undisturbed Pleistocene clay performed by [Mukabi \(1994\)](#) and presented by [Tatsuoka et al. \(1995\)](#). Figure 2.13a shows the stress-strain relation obtained for the 10th cycle from one undrained cyclic TX test. The axial strain was measured both locally using a pair of local deformation transducers (LDTs) and externally from the axial displacement of the specimen cap with a proximeter. For this case, the E value measured externally is 60% of the one measured locally (i.e. $E_{ext} = 0.6E_{loc}$). Additionally, the D value from the strains measured with the proximeter is more than twice the one measured locally. Figures 2.13b and 2.13c show a comparison of E and D values, respectively,

based on locally and external measured axial strains for undrained and drained conditions and for two different single amplitude axial strains (ε_a). In all cases, the E_{ext} are smaller than E_{loc} and it seems that the difference increases with decreasing modulus and with increasing strain level. Concerning the damping values, no clear tendency can be seen between the bedding error and the measured damping. However, for the lower level of strain (i.e. $\varepsilon_a = 5 \cdot 10^{-6}$), the damping external and local ratio shows more dispersion and higher values. Furthermore, the drainage conditions do not show a clear effect on the bedding error.

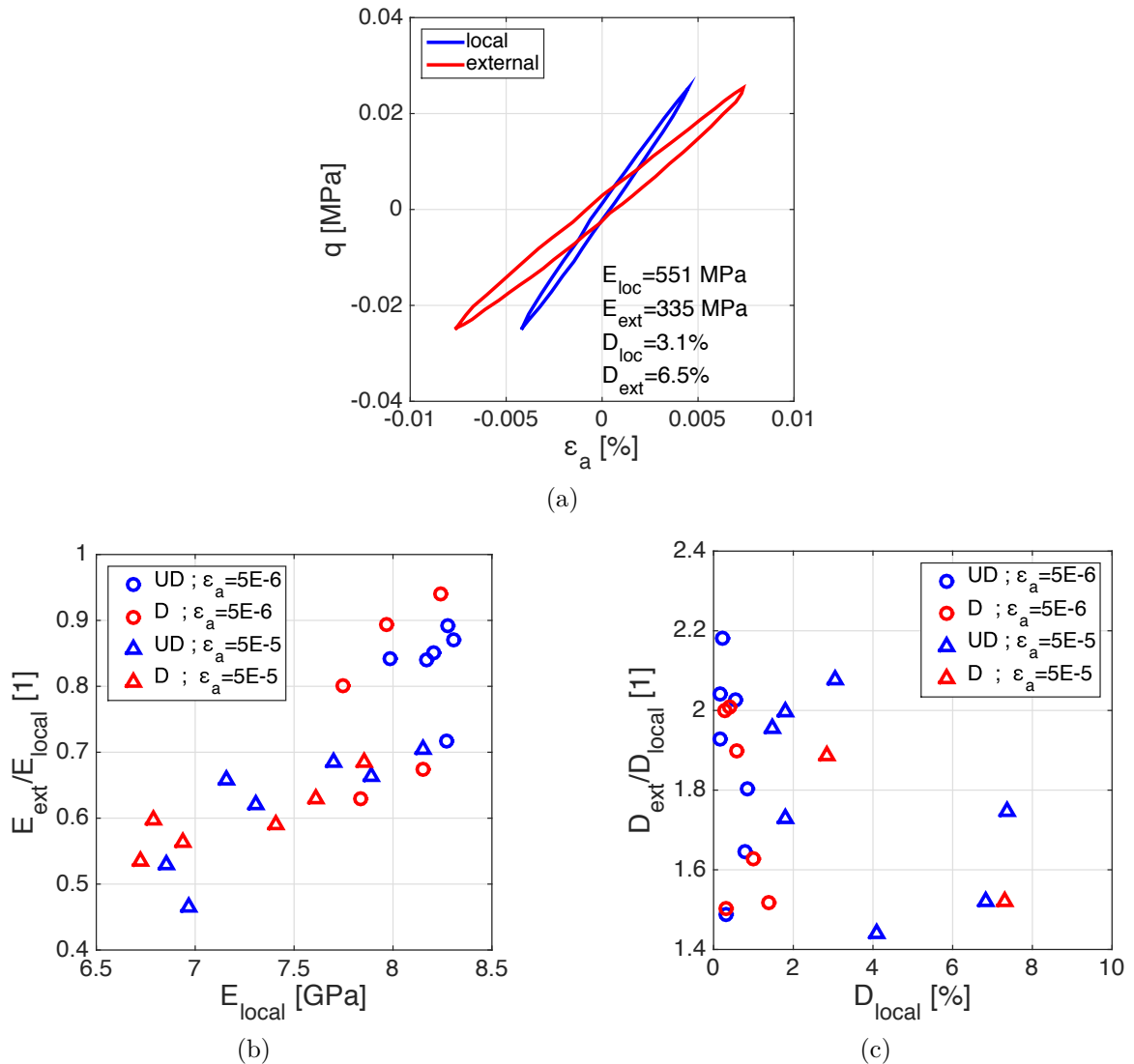


Figure 2.13 – Effect of bedding error in cyclic triaxial tests: a) typical stress-strain relation, and comparison of b) E and c) D values based on local and external measures of axial strains for undrained and drained conditions and for two strain levels on undisturbed OAP clay (modified from [Tatsuoka et al., 1995](#))

In addition, [Tatsuoka et al. \(1995\)](#) compared local and external deformation measurements for 46 CD triaxial compression tests in three different sands and found that E values measured

externally were always smaller and down to 55% those measured locally. Unfortunately, even if these differences decrease with strain, the high scatter of the data was not systematic nor related to each test. Therefore the authors judged that a precise correction of the bedding error for externally measured axial strains is not feasible. However, some attempts have been made to theoretically explain differences in E and D values and will be presented in shortly.

2.4.2 Similarities between methods to calculate the deformation properties

Provided that the measurements of the deformation properties are sufficiently accurate, statically -monotonic and cyclic- determined G_{max} and shear modulus degradation curves can be compared with those obtained by the corresponding dynamic tests (such as resonant column) or evaluated by wave propagation -e.g. field interferometry.

[Tatsuoka et al. \(1995\)](#) presented a comparison between the maximum shear modulus (G_{max}^{TX}) from triaxial (TX) tests and the corresponding elastic shear modulus ($G_{max}^{in-situ}$) obtained from field shear wave velocity. In the laboratory tests, the shear modulus was defined at strains less than $1 \cdot 10^{-5}$. Mostly CU monotonic triaxial compression tests were performed but also some cyclic triaxial tests were used. Each data point was obtained by averaging the tests under a similar condition. Concerning field data, the shear modulus was measured at a depth for which the concerned undisturbed samples for the triaxial tests were retrieved. Five different types of soil were tested: sedimentary soft rock (mudstone and sandstone), cement-treated sandy soil (slurry and dry) and deep mixing methods treated soils. Three different sampling methods were used: rotary core tube (RCT), block sampling and direct coring. The former is more commonly used but it produces more sample disturbance.

Figure 2.14a shows the results for G_{max} from TX tests as a function of the G_{max} measured *in-situ* divided in two categories: those measured locally and those measured externally. It can be observed that all G_{max} obtained based on externally measured axial strains are much lower than the corresponding $G_{in-situ}$, with values down to 10 times smaller. These difference is primarily due to bedding error and not to sample disturbance. The later however can explain the differences between G_{max} based on local strain measures and $G_{in-situ}$; which is significantly lower. Mostly samples obtained by RCT presented these G_{max} of half the *in-situ* corresponding.

Concerning shear modulus degradation curves, Figure 2.14b shows a comparison between five laboratory tests: the dynamic resonant column (RC) test and four static tests: monotonic

triaxial compression (MTX), cyclic triaxial (CTX), monotonic torsional shear test (MTS) and cyclic (CTS) performed on Ticinio sand at the same confinement pressure ($p'=49$ kPa). Even if some differences were presented in the initial shear modulus, there were never above 20%; thus, suggesting that even by using monotonic loading the elastic stiffness can be evaluated accurately. Concerning the decay curves, differences can be observed between the monotonic and cyclic tests, specially for the triaxial one. Tatsuoka et al. (1995) explained this by the differences in extension and compression maximum and minimum stress ratio in the CTX test. These differences will increase when less stiff soils are tested. Lastly, in Figure 2.14b, a very good agreement can be found between the cyclic tests and the resonant column, even for medium levels of strain, due principally to the small -or lack of- increase in the pore water pressure hence low level of softening. However, differences in the decay between static and dynamic tests becomes more complicated due to the effects of variable strain rates in the latter.

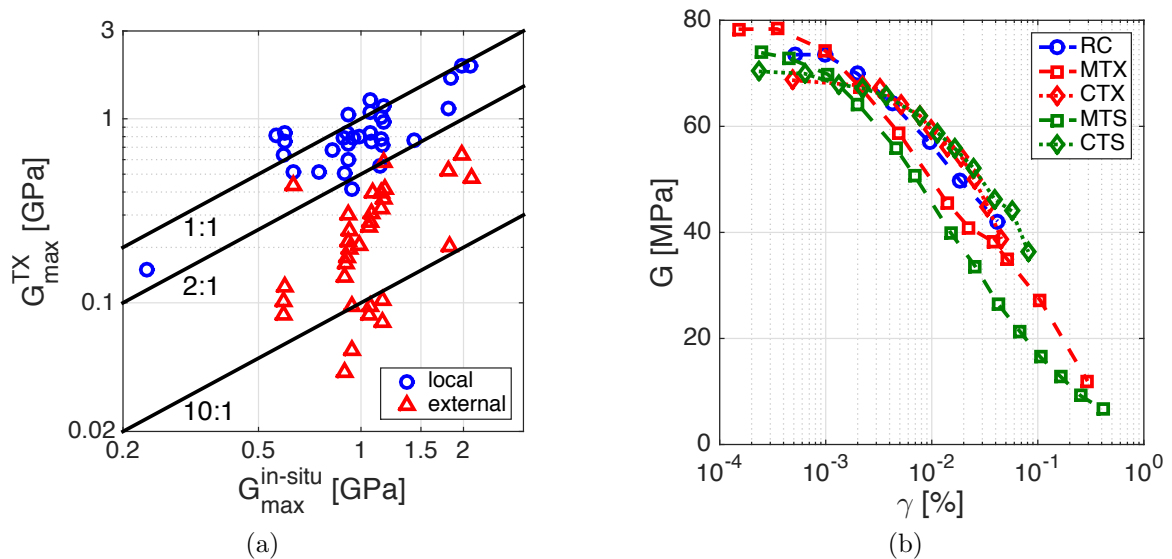


Figure 2.14 – Comparison of deformation properties: a) G_{max} from field shear wave velocity and from triaxial tests for sedimentary soft rocks and cement-mixed soils and b) G degradation with shear strain curves from different laboratory tests (strain was measured locally in the triaxial test) (modified from Tatsuoka et al., 1995)

When strains are measured externally, discrepancies can be found when using different laboratory tests. As an example, Figure 2.15 shows the shear degradation and damping evolution curves based on resonant column (RC) and cyclic triaxial (TX) test - with external strain measurement- for two different soils from the work of Pitilakis and Anastasiadis (1998). The black line also present in the figure will be addressed later. The soils tested were a silty-clay with $PI=23\%$ and confining pressure $\sigma'_0=160$ kPa; and a sand with $e=0.575$ and $\sigma'_0=100$ kPa.

Three important aspects can be highlighted from their results. Firstly, in TX the G_{max} value measured was lower than that from RC, i.e. 25% for the silty-clay and 70% for the sand. Nevertheless, both tests seem to follow the same degradation curve of G with strain as the G_{max}^{TX} were attained for higher strains. In contrast, there are some differences in the evolution of damping with strain for the clay specimen. This can be due to three main aspects: mainly, as discussed before, the bedding error in the TX if the strains were measured externally, the stress path used - i.e. the initial conditions, the stress ratio and the strain rates - and the drainage conditions (specially for higher levels of strain). For the TX, an initial isotropic state is then modified by cyclically loading the vertical stress while keeping the lateral stress constant. In contrast, for the RC the initial state is triaxial and the lateral and vertical stresses are kept constant while a cyclic shear stress is imposed.

A methodology is proposed in order to estimate the real G_{max} value (i.e. for lower levels of strain of about $1 \cdot 10^{-6}$) from the cyclic triaxial tests (TX) with external strain measurements, that have a minimum strain of $1 \cdot 10^{-4}$. The TX data for strains where no stabilization of modulus is present are fitted to the hyperbolic equation of [Nakagawa and Soga \(1995\)](#):

$$\frac{G}{G_{max}} = \frac{1}{1 + \alpha \cdot \gamma^\beta} \quad (2.29)$$

where α and β are the geometric parameters (i.e. the intercept and the slope of the logarithmic fit), γ is the shear strain - not in percentage - and G_{max} is the unknown variable. In order to find this value, a linear regression is fitted to the data plotted in $\log(G_{max}/G - 1)$ as a function of $\log(\gamma)$ and the coefficient of determination (R^2) is optimized by changing the value of G_{max} . Figure 2.16 shows the best hyperbolic fit for both soils. The G_{max} values found were 72kPa for the silty-clay and 52kPa for the sand, similar to those found with the RC. These values correspond to 0.6 and 0.8 external-to-local ratios, which are reasonable values according to those presented by [Tatsuoka et al. \(1995\)](#) and shown in Figure 2.13b. The corresponding R^2 values were 0.99 and 1.00, respectively. The proposed models are compared to the G vs. γ curves shown in figures 2.15a and 2.15b and agree with both tests.

Finally, the normalized shear modulus degradation curves are shown in Figure 2.17 for both tests and for the proposed model. Additionally the model given by [Darendeli \(2001\)](#) is shown. It is interesting to note that the normalized curve for TX data are 10 times stiffer for the clay and 5 times for the sand than the RC ones. In contrast, those with the proposed model are between both tests for the clay and slightly less stiffer than the RC for the sand. Concerning

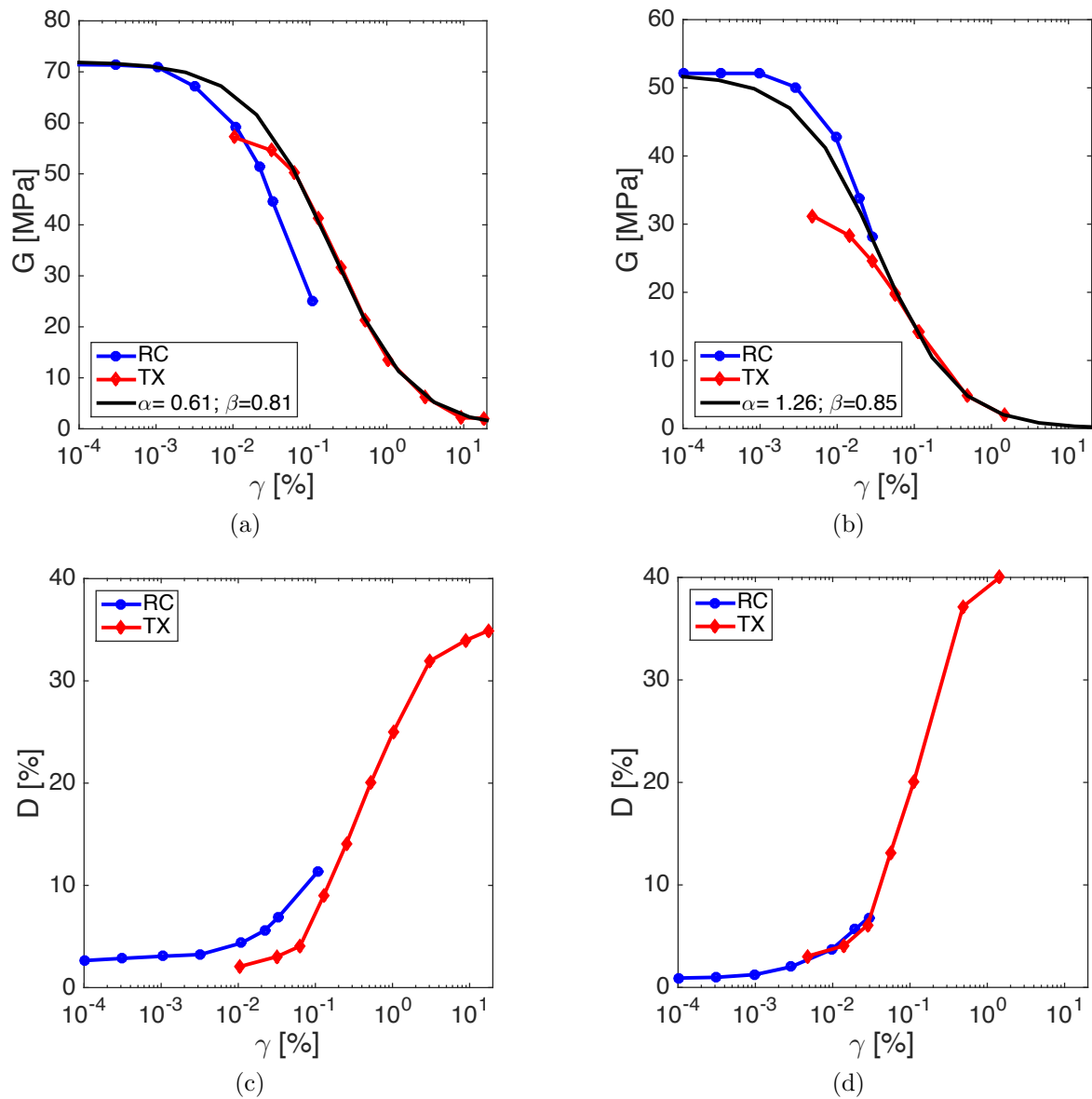


Figure 2.15 – Shear modulus degradation and Damping evolution comparison between resonant column (RC) and cyclic triaxial (TX) tests for a) and c) Silty-clay with $PI=23\%$ and confining pressure $\sigma'_0=160$ kPa; and b) and d) sand with $e=0.575$ and $\sigma'_0 = 100$ kPa (modified from [Pitilakis and Anastasiadis, 1998](#))

the Darendeli curves, for the clay it agrees more with the RC curve but with the sand it has a better agreement with the proposed model.

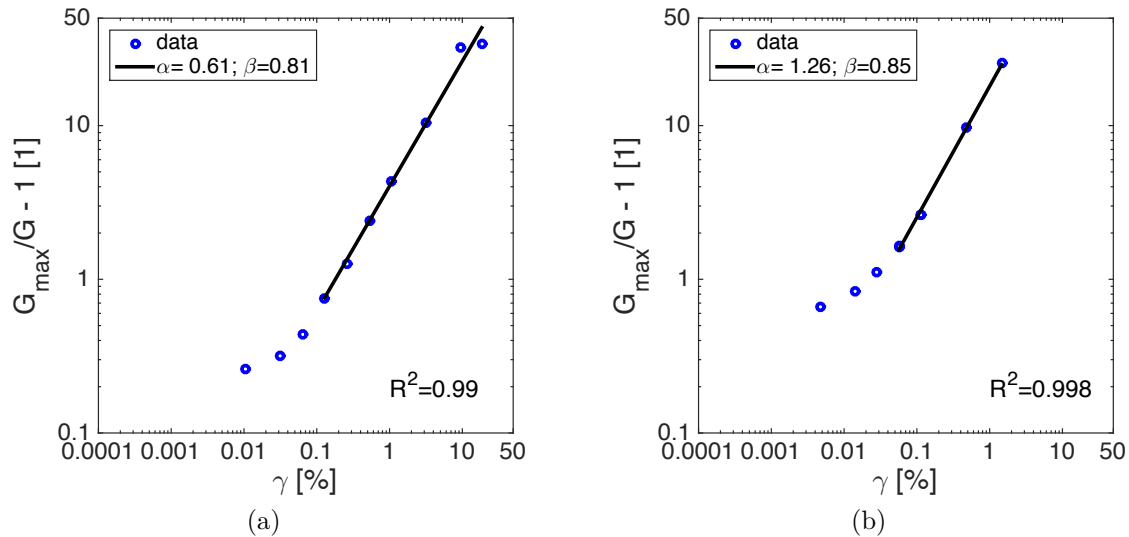


Figure 2.16 – Shear modulus degradation : hyperbolic fit of cyclic triaxial (TX) test results for a) Silty-clay with $PI=23\%$ and confining pressure $\sigma'_0=160\text{kPa}$; and b) sand with $e=0.575$ and $\sigma'_0=100\text{kPa}$ (from Pitilakis and Anastasiadis, 1998)

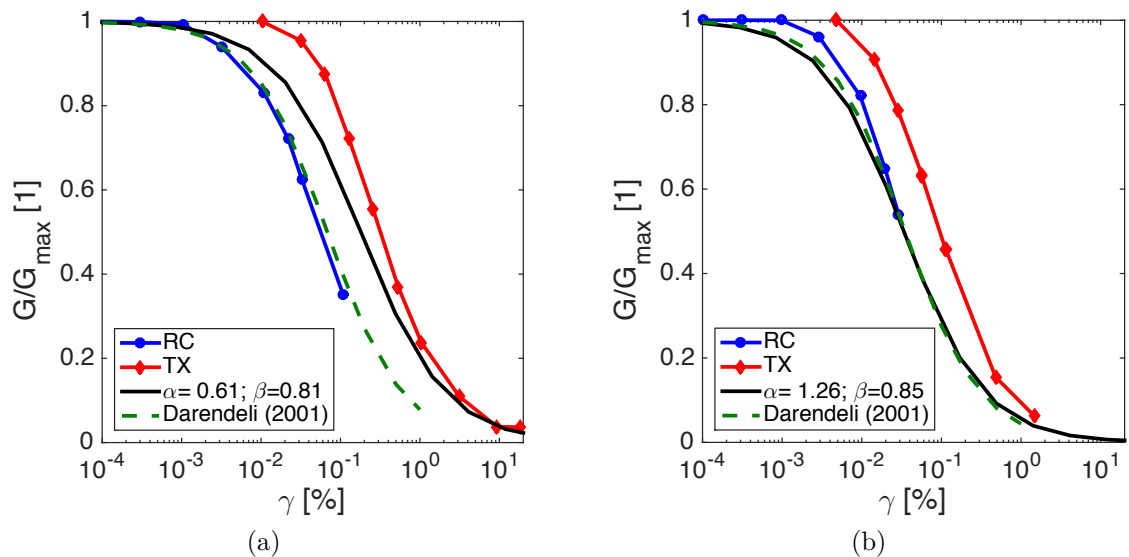


Figure 2.17 – Normalized shear modulus degradation curves for resonant column (RC) and cyclic triaxial (TX) tests for a) Silty-clay with $PI=23\%$ and confining pressure $\sigma'_0=160\text{kPa}$; and b) sand with $e=0.575$ and $\sigma'_0=100\text{kPa}$ (from Pitilakis and Anastasiadis, 1998)

2.4.3 Differences between laboratory and *in-situ* measurements

As discussed above, even considering that the laboratory tests were sufficiently accurate, some differences between the G_{max} values can still be present between those obtained in the laboratory and by field shear wave velocity. Stokoe and Richart (1973) compared measurements in the field by the cross-hole (CH) seismic method and in the laboratory by the resonant column (RC) method for different soils. Good agreement was found for the silty sand and the shale (i.e.

relative differences of less than 10%); but for the sandy silt and the clayey silt, the laboratory values were 30% smaller than the field values. Ptilakis and Anastasiadis (1998) comparisons of V_s from CH and RC methods, present similar results; although, variations of 30% are also present for some sands, silts and soft clays. Recall that Tatsuoka et al. (1995) presented values 50% smaller corresponding to sample disturbances for accurate local strain measurements in cyclic TX test (refer to Figure 2.14a). Other than this source of differences, Stokoe and Richart (1973) mentions the importance of selecting the appropriate confining pressure and evaluating secondary time effects, i.e. the increase of V_s with time which is inversely proportional to the particle size. In addition, other reasons have been identified by Ptilakis and Anastasiadis (1998), for example: aging, anisotropy, representative volume and inherent variability.

Tatsuoka et al. (1995) and Ptilakis and Anastasiadis (1998), among others, agree that the initial or maximum stiffness (G_{max}) is better estimated from field seismic surveys. However the question remains on how should the shear degradation curve, measured at the laboratory, is to be fitted to the field G_{max} value.

A 1D equivalent linear seismic response analysis was performed by Ptilakis and Anastasiadis (1998) in order to test different procedures. Among them:

1. $G(\gamma)^{in-situ} = G(\gamma)^{lab}$: The maximum shear modulus and degradation curve measured in the laboratory;
2. $G(\gamma) = G(\gamma)^{lab} + \Delta(G_{max}^{in-situ} - G_{max}^{lab})$: The same degradation curve but translated to the in-situ G_{max} value;
3. $G(\gamma) = G(\gamma)^{lab} / G_{max}^{lab} \cdot G_{max}^{in-situ}$: Normalize the laboratory degradation curve and multiply it by the in-situ G_{max} value.

The first option will not only affect the soil degradation but will modify the wave propagation as it will shift the natural frequency of the deposit to lower values and will deamplify the acceleration amplitude. The second option has the same normalized shear degradation curve as in the laboratory but applied to a stiffer initial value will result in stiffer decay for all shear strains; hence at strong accelerations, the response will be amplified for higher frequencies and deamplified for lower ones. The third procedure was also suggested by Tatsuoka et al. (1995) as it takes into account the strain level-dependency and the stress path during loading. Compared to the normalized curve in laboratory, this procedure will give a steeper degradation (or higher decay) which will result in less deamplifications for weak motions and higher deamplifications

for stronger ones. The third procedure gave the best and more reasonable results according to [Pitilakis and Anastasiadis \(1998\)](#) and is therefore recommended by the authors.

2.4.4 Summary of the proposed procedure

The proposed procedure to use laboratory data from cyclic triaxial test where strains are measured externally for nonlinear modeling of dynamic soil behavior can be summarized in three steps:

1. Find the maximum shear modulus (G_{max}) by fitting the logarithmic equation [2.29](#) proposed by [Nakagawa and Soga \(1995\)](#).
2. Compare the G_{max} values found with those in the literature or available from other tests. Note that this value should not be more than twice the measured one as it only accounts for the external-to-local strain measurement error.
3. Normalize the fitted degradation curve and multiply it by the in-situ G_{max} value.

2.4.5 Comparison of the proposed procedure with that of [Ishihara \(1996\)](#)

Instead of fitting a logarithmic equation to the shear modulus reduction curve, [Ishihara \(1996\)](#) proposed an empirically based correction factor (C_r) as a function of the shear strain to be applied to the normalized curve. This correction is expressed as $C_r(\gamma) = (G/G_{max})^{in-situ} / (G/G_{max})^{TX}$ and depends on the degree of sample disturbance. It is to be applied to the normalized shear modulus degradation curve of the laboratory. Four degrees of disturbance were identified:

- A** Highly undisturbed;
- B** Block sampling;
- C** Tube sampling;
- D** Reconstituted samples.

The C_r values for each degree are given in [Figure 2.18](#). The C_r values for degree D correspond to the mean values of results of highly undisturbed samples recovered by the ground freezing

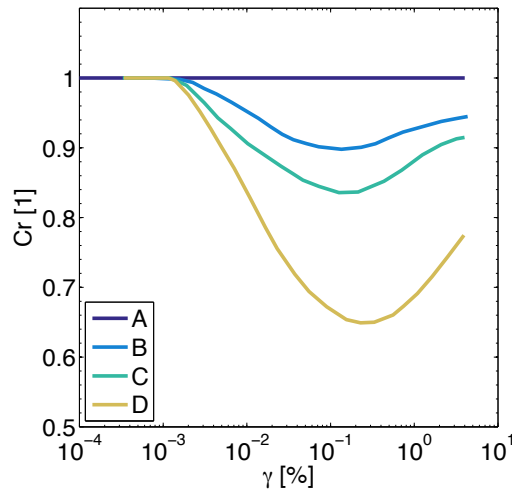


Figure 2.18 – Correction factor $C_r(\gamma)$ for different degrees of sample disturbance from [Ishihara \(1996\)](#)

technique and reconstituted samples. The curves B and C were then suggested based mainly on interpolation. For degree D, C_r presents the lowest value of 0.65 for a shear strain of 1%.

Figure 2.19 shows the tests presented by [Pitilakis and Anastasiadis \(1998\)](#) with the corrections of [Ishihara \(1996\)](#) applied to the TX data. It can be noted that if C_r for degree D is used, the corrected curves are in agreement with the RC normalized curve. The proposed fitted curve is similar to the corrections C for the silty clay and D for the sand, which is accordance with the differences of G_{max} shown between the tests. Concerning the damping values, [Ishihara \(1996\)](#) stated that “the influence of sample disturbance has been shown to be inconsequential and therefore the value determined from the tests on any sample may be used for the analysis purposes”.

2.4.6 Empirical models for the shear degradation and damping evolution curves

Several authors have proposed shear degradation and damping evolution curves based on empirical data. Figures 2.20 and 2.21 shows some examples. In Figure 2.20 are shown the ranges presented by [Kokusho \(1980\)](#) for different confining pressures (p') from cyclic triaxial tests in dense Toyoura sand and the ranges for sand resulting from data of four different sites in the United States presented by [Seed et al. \(1986\)](#). As expected, less nonlinearity and damping is expected as p' increases, hence less degradation is presented for a same level of γ and less energy is dissipated. Comparing with [Seed et al. \(1986\)](#) curves for sands, a similar behavior in

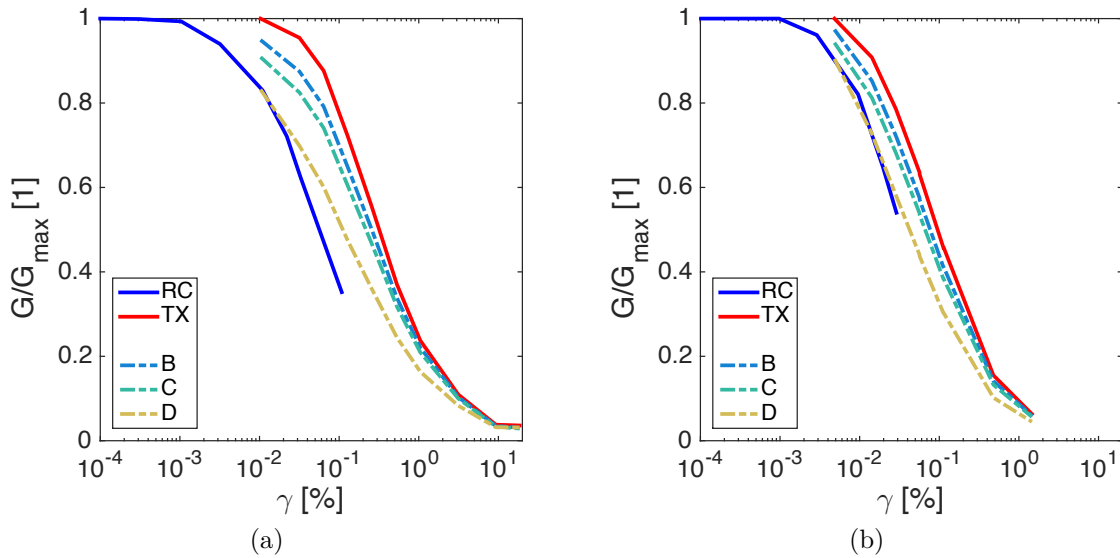


Figure 2.19 – Applied correction factor (C_r) from [Ishihara \(1996\)](#) to the normalized shear modulus degradation curves for cyclic triaxial (TX) tests performed by [Pitilakis and Anastasiadis \(1998\)](#) for a) Silty-clay with $PI=23\%$ and confining pressure $\sigma'_0=160\text{kPa}$; and b) sand with $e=0.575$ and $\sigma'_0 = 100\text{kPa}$.

both shear degradation and damping evolution is presented even if the sand type is different.

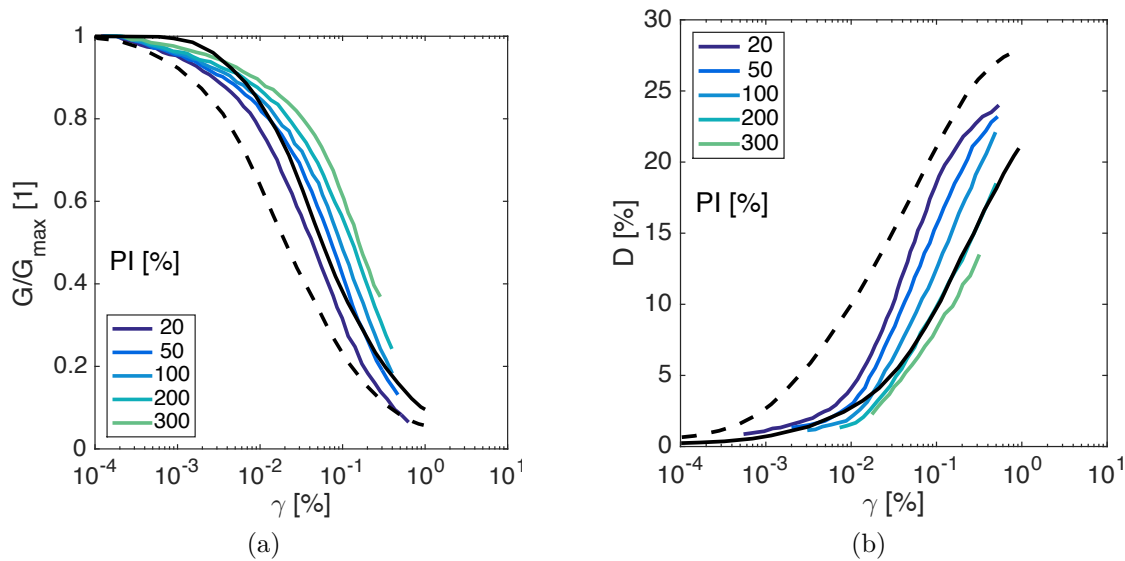


Figure 2.20 – [Kokusho \(1980\)](#) curves of a) normalized shear modulus degradation and b) damping evolution as a function of shear strain for dense Toyoura sand at different confining pressures (p'). The ranges for sand (black solid and dashed curves) given by [Seed et al. \(1986\)](#) are also shown.

Concerning clayey-silty soils, [Vucetic and Dobry \(1991\)](#) presented mean curves for varying plasticity index (PI) as shown in [Figure 2.21](#). The effect of PI in clays is similar to the effect of p' in sands that is, for higher PI , less nonlinearity and damping. Compared to the references

of Seed et al. (1986), the variation in these curves is more important. All these curves are, in general, used as reference and compared to other laboratory data and to numerical simulations. However, as limited data was used for each set of curves, these are only valid for limited cases.

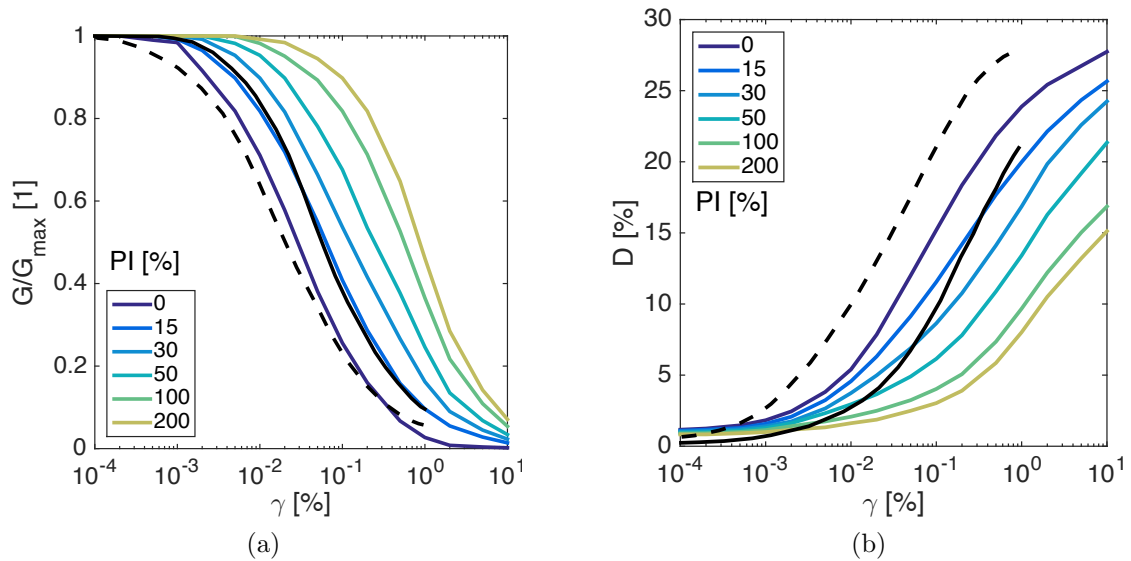


Figure 2.21 – Vucetic and Dobry (1991) curves of a) normalized shear modulus degradation and b) damping evolution as a function of shear strain for different plasticity index. The ranges presented by Seed et al. (1986) for sand are also shown.

In contrast, Darendeli (2001) used data from various research projects of resonant column and torsional shear tests performed on more than 20 sand sites to develop a model for the estimation of normalized modulus reduction (G/G_{max}) and damping (D) curves as a function of shear strain depending on several variables. The tests were sequentially performed on intact samples from soils described as having low void ratio and not liquefiable during seismic activity. The tested soil samples ranged from natural clean sands to clays, characterised by broad intervals of sampling depth (3-263 m), effective confining pressure (p') ranging from 30-2750kPa, plasticity index (PI) from 0-132%, and over-consolidation ratio (OCR) ranging from 1 to 8. Additionally, D curves were found to depend also, but not as important, on the excitation frequency (f_{exc}) and the cycles of loading (N). The model was calibrated using a first-order, second-moment Bayesian technique. An interesting aspect of the proposed model is that not only the mean value is given for each shear strain but also the standard deviation. Figure 2.22 shows an example for these curves with different effective confining pressures. The used parameters are: $PI=0$, $OCR=1$, $f_{exc}=1$ and $N=10$. Additionally, plus and minus one standard deviation is given for $p'=500kPa$. It is noted how this variability is important compared to the variation due to the effective confining pressure. As expected, the soil is stiffer for higher

p' i.e. the shear modulus degradation shifts to higher strains.

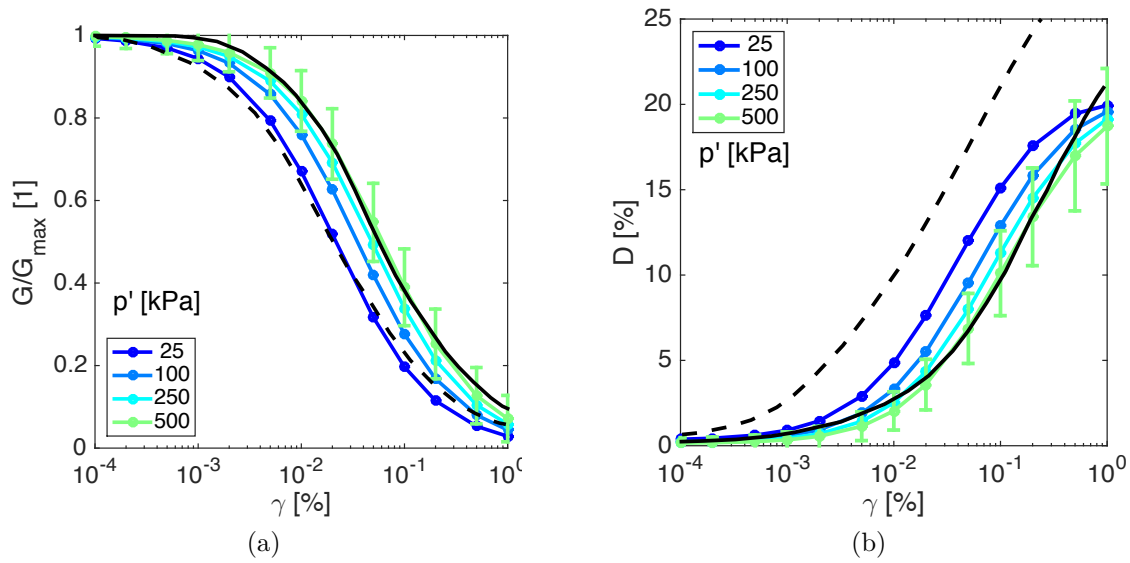


Figure 2.22 – Darendeli (2001) curves of a) Normalized Shear modulus degradation and b) Damping evolution as a function of shear strain for different effective confining pressures. With $PI=0$, $OCR=1$, $f_{exc}=1$ and $N=10$. The \pm standard deviation is given for $p'=500kPa$

A similar behavior is presented for an increase in PI , not shown here, with the exception that for higher PI values, the damping at low strains slightly increases. It is important to note that due to test data collection limitations, the equations are recommended by the author only for strains below 1%. Additionally, the PI lacks representativeness for values above 30% as less than 9% of samples where in this range. According to Guerreiro et al. (2012), this could have introduced a bias in the development of the curves, as they exhibit a narrower breath for varying values of PI , when compared with the proposals by Vucetic and Dobry (1991). Darendeli (2001) curves propose a reduction of damping ratio at very large strains, specially marked at low confining pressures and low plasticity index that has never been captured so far in laboratory tests nor seen in other proposed curves. Similarly, the OCR values are also not very well represented above 2 (9 samples against 101 samples for $OCR \leq 2$).

In the same laboratory, Menq (2003) performed resonant column and torsional shear tests on solely sand sites and presented some modifications to the curves proposed by Darendeli (2001), which apply for more coarser material. The main differences is that G/G_{max} as well as the D curves are now dependent on the uniformity coefficient (CU) and the 50% diameter size ($D50$), in addition to the effective confining pressure (p') and that the D curves depend only on the N value. Figure 2.23 shows an example for these curves with different effective confining pressures and different CU . $D50$ was set to 1mm and N to 10. When CU is equal to 8, the

G/G_{max} curves are inside the ranges given by Seed et al. (1986) and are similar to those given by Darendeli (2001) and they shift to the right as the CU decreases. Concerning the damping curves, values are below all other values presented. The effect of $D50$ is the opposite of that of CU , in fact, an increase in $D50$ will give an increase in nonlinearity and a decrease in damping.

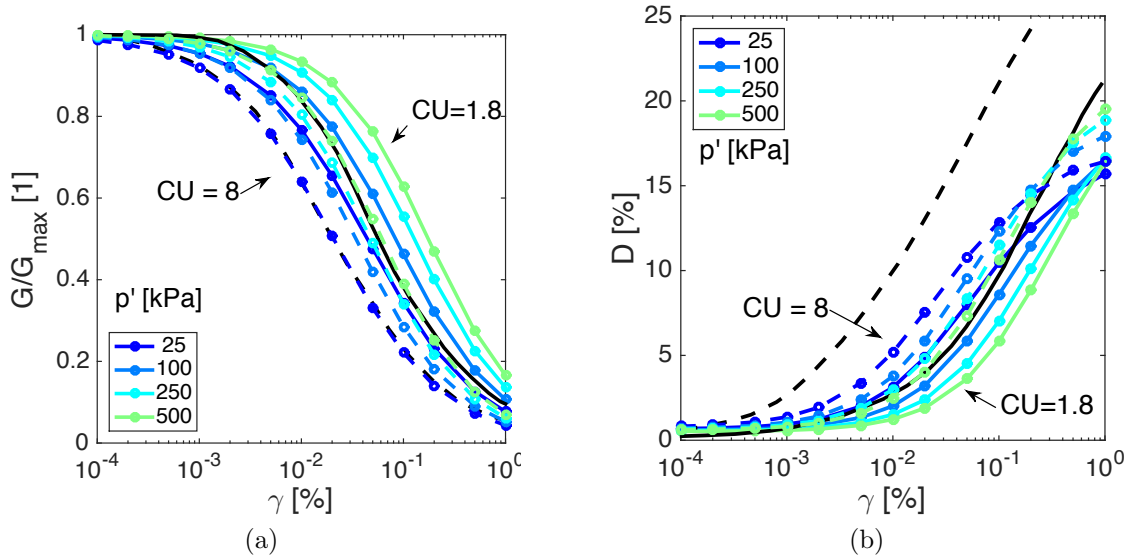


Figure 2.23 – Menq (2003) curves of a) Normalized Shear modulus degradation and b) Damping evolution as a function of shear strain for different effective confining pressures. With $CU = 1.8$ (solid lines) and 8 (dashed lines), $D50 = 1\text{mm}$ and $N = 10$

2.5 Modeling dynamic soil behavior

2.5.1 Equivalent linear analysis

Equivalent-linear (EQL) analysis is probably the most commonly used procedure in practice to simulate nonlinear soil behavior because of the small computational effort and few input parameters. Most of its popularity is related to its implementation in the computer code SHAKE developed by Schnabel et al. (1972) for one-dimensional ground response analysis of layered sites. Later modifications were implemented in the versions SHAKE91 (Idriss and Sun, 1992) and SHAKE04 (Youngs, 2004).

EQL modeling is based on a total stress representation of soil behavior and in the visco-elastic concept. The only input parameters in addition to the unit mass, are the maximum shear modulus (G_{max}) and the nonlinearity curves: normalized modulus (G/G_{max}) reduction and damping (D) evolution as functions of shear strain (γ). The equivalent linear properties are then corresponding to couples of G and D for a determined effective shear strain level (γ_{eff}),

usually taken as 65% of the peak strain calculated from the input motion. This coefficient controls the nonlinearity and can be reduced to improve high-frequency response.

Since the computed strain level depends on the values of the equivalent linear properties, an iterative procedure is required to ensure the compatibility with the evolution of the nonlinearity curves at each layer. In other words, to ensure that the strain-compatible properties are consistent with the properties used to perform the dynamic response analysis. Although convergence is not absolutely guaranteed, differences of less than 10% are usually achieved in less than 5 iterations (Schnabel et al., 1972).

Two main limitations have been identified in the EQL analysis: (1) overestimation of the maximum acceleration and (2) underestimation of high frequencies amplification. The former is related to the overestimation of stresses as the relationship between maximum stress and strain is simplified as linear. This overestimation increases with strain, as the nonlinearity increases. The reason for the latter is the overestimation of damping ratio for small amplitude (high cycle) vibration. This effect is more important for the small to medium earthquakes.

Even though the iterative process allows the nonlinear soil behavior to be approximated, the response method is still linear. Hence, the strain compatible properties are constant throughout the duration of the earthquake, regardless of whether the strains at a particular time are small or large (Yoshida and Iai, 1998). Additionally, the method is incapable of representing the changes in soil stiffness that actually occur during the earthquake as no strain accumulation neither softening due to pore-water pressure generation is possible (Kramer, 1996).

Ishihara (1993) suggests that equivalent linear methods can be used as long as no hysteresis degradation is present. That is when no progressive change is evidenced in the shear modulus and damping ratio due to cycles of load application. This strain-dependent but cycle-independent behavior is present for medium strains (i.e. approximately $10^{-5} < \gamma < 10^{-3}$). Above this level, the soil properties change not only with strain but with the progression of cycles. This change depends on the shear stress loading and its effective confining stress evaluation. The use of constitutive laws, in which the stress-strain relation is described for each step of loading, unloading and reloading, becomes necessary. This type of response analysis was termed by Ishihara (1993) as step-by-step integration method and are employed in history-tracing type models.

2.5.2 Nonlinear models

Two types of nonlinear models can be identified: those that rely on the description of the backbone and hysteretic curves and advanced constitutive models based on the plasticity framework and can take into account the initial and critical state, volume deformations and drainage conditions, among others.

The backbone - or skeleton - curve is the nonlinear shear stress-strain relationship for monotonic loading. The hysteretic curves are the nonlinear energy dissipating scheme that are usually related to the backbone curve by a series of rules. The most common are the [Masing \(1926\)](#) rules by which unloading of any cycle starts with a shape that is identical to that of the negative part of the initial loading (backbone curve) enlarged by a factor of two; and, for reloading the positive part of the initial loading backbone curve is used. Two additional rules called the extended Masing rules are also very popular. The first one concerns the maximum strain history; thus, if the unloading or loading curve exceeds the maximum past strain and intersects the backbone curve, it follows the backbone curve until the next stress reversal. The second one consists in the cycle history; hence, if an unloading or loading curve crosses an unloading or loading curve from a previous cycle, the stress-strain curve follows that of the previous cycle.

In contrast, advanced constitutive models are described by intrinsic soil properties and geometric parameters and are capable of simulating complex soil behavior under a variety of loading conditions. The key components of such models include a yield surface, flow rules, and hardening (or softening) laws.

2.5.3 Comparisons between models

The geotechnical literature provides numerous examples of ground response modeling using an equivalent-linear code with total stress analyses or true nonlinear methods ([Chin and Aki, 1991](#); [Yu et al., 1993](#); [Kramer et al., 2011](#); [Yoshida, 2013](#), among others). For weak ground motions, when the soil behavior is still not substantially modified, equivalent-linear analysis (e.g. SHAKE) can provide similar results. However, for large accelerations and soft soils, this method notably differs from true nonlinear techniques.

As SHAKE is based on an equivalent-linear shear-stress relationship, the maximum shear strain and the corresponding maximum acceleration are some times overestimated, which can result in a conservative design. However, the underestimation of the high frequency energy at large strains causes the underestimation of accelerations for the corresponding frequencies.

In other words, acceleration amplification for long periods is underestimated. This underestimation could be highly prejudicial for flexible buildings. In addition, peak displacements and shear strains are often underestimated which will result in damages on the structure above them. As these factors depend on the frequency content as well as in the degree of nonlinearity, the evaluations of SHAKE scatter. Hence, true nonlinear models which track the exact form of stress-strain relationship, like the one used in this study, are suggested for dynamic response analysis in the most general case ([Beresnev and Wen, 1996](#)).

[Foerster and Modaressi \(2007b\)](#) simulated the wave propagation of two earthquake arrays (Loma Prieta 1989 and Kobe 1995) with the 1D version of the ECP model, known as CyberQuake ([Modaressi and Foerster, 2000](#)), and with SHAKE. In general, the response of the studied sites was better reproduced with the effective-stress nonlinear constitutive model than with the equivalent linear approach. Both the overestimation of maximum accelerations and the underestimation for high frequencies were attested.

The equivalent-linear and the nonlinear models have different formulations and underlying assumptions thus differences in their results are expected. For instance, the implementation of empirical dependencies of shear modulus and damping on strain, the use of effective strains and the inability to represent the development of permanent and shear-induced volumetric strains ([Kramer, 1996](#)). One of the limitations of the equivalent-linear models is the inability to model the generation, redistribution and eventual dissipation of excess pore-pressure during and after earthquake shaking; which is of key importance in the behavior of liquefiable soils. To account for this particular capability, the nonlinear models can be formulated in terms of effective stresses. In chapter [4.2](#), the comparison is made between the total and effective stress analyzes in the interest of solely evaluating the effect of coupling excess pore-pressure generation and deformation.

Chapter 3

Numerical tools used in this study:

GEFDyn and ECP models

This chapter describes the numerical tools used in this thesis. Special attention is given to the numerical integration, the evaluation of the added damping due to the dissipative Newmark scheme and the discretization in time. The nonlinear constitutive model is briefly described and its sensibility to some of the numerical parameters is shown. Lastly, some results of the model's validation for the 1D site response analysis are presented.

3.1 Finite Element Model

The finite element code used throughout the analyses is GEFDyn. It was created at Ecole Centrale Paris on the early 80s as a program for the analysis of static and dynamic soil behavior with coupling soil, water and air (Aubry et al., 1985). Thereafter, it has been continuously improved by, among others, Aubry and Modaressi (1985); Modaressi (1987); Aubry and Modaressi (1989). In this study, 2D coupled pore pressure and soil deformation finite element computations with plane-strain assumption will be performed. The soil is modeled using quadrilateral isoparametric elements with eight nodes for both solid displacements and fluid pressures.

For the case studies of chapters 4 and 5, the numerical model is divided into two steps: first, the initial stress state is obtained by the conservation equations in static conditions and then, the dynamic behavior is analyzed starting from the previously found stress state. The initialization step is important to correctly model the consolidation process or the construction by layers, for example.

To take into account the coupling of pore pressure and soil deformation, Biot (1941) equations for the dynamic behavior of saturated porous media were introduced in GEFDyn by Modaressi (1987). Three formulations exist: in terms of (1) absolute displacements of the solid, the fluid and the pore pressure ($\mathbf{u}_s - \mathbf{u}_w - p_w$) (Zienkiewicz and Shiomi, 1984), (2) absolute displacement of the solid, relative displacement of the fluid and the pore pressure ($\mathbf{u}_s - \mathbf{u}_{rw} - p_w$); and (3) absolute displacement of the solid and the pore pressure ($\mathbf{u}_s - p_w$) (Zienkiewicz and Taylor, 1991). The first two are useful for high frequency range, but when these are low, the relative displacement of the fluid can be neglected and the simplified $\mathbf{u}_s - p_w$ formulation can be used. As further simplifications, soil grain compressibility is assumed to be null and thermal effects are ignored.

Note that the pore water pressure generation and dissipation will depend on the permeability tensor and the compressibility bulk parameter. The main advantage of the simplified model is related to the reduction of the numerical cost, due to the reduction of the degrees of freedom.

The inaccuracies of this approach are seen only in high-frequency, short-duration phenomena which are presented in the work of [Zienkiewicz et al. \(1999\)](#).

3.2 Numerical integration

An implicit Newmark numerical integration scheme is used in the dynamic analysis for the discretization in time. The step-by-step integration uses a predictor-corrector scheme [Modaressi \(1987\)](#). The Newmark method is one of the most popular classical numerical time-integration algorithm and guarantees accuracy of first order ([Kuhl and Crisfield, 1999](#)).

Disregarding the iterative algorithm which handles the nonlinearity, the governing finite element equation of a viscoelastic media at time $t_{n+1} = t_n + \Delta t$, commonly known as the equation of motion is:

$$\mathbf{M} \cdot \ddot{\mathbf{u}}(t_{n+1}) + \mathbf{C} \cdot \dot{\mathbf{u}}(t_{n+1}) + \mathbf{K} \cdot \mathbf{u}(t_{n+1}) = \mathbf{F}(t_{n+1}) \quad (3.1)$$

where \mathbf{M} , \mathbf{C} , and \mathbf{K} are the global mass, damping and stiffness matrices, respectively, \mathbf{F} is the vector of the global applied loads, and \mathbf{u} , $\dot{\mathbf{u}}$ and $\ddot{\mathbf{u}}$ are the vectors of displacement, velocity and acceleration, respectively.

Newmark method approximate solution consists in assuming that \mathbf{u} , $\dot{\mathbf{u}}$ and $\ddot{\mathbf{u}}$ are known variables at the time t_n and are related to those of time t_{n+1} by the finite difference formula describing their evolution with equations 3.2 and 3.3 :

$$\mathbf{u}(t_{n+1}) = \mathbf{u}(t_n) + \Delta t \cdot \dot{\mathbf{u}}(t_n) + \left(\frac{1}{2} - \beta_N\right) \cdot \Delta t^2 \cdot \ddot{\mathbf{u}}(t_n) + \beta_N \cdot \Delta t^2 \cdot \ddot{\mathbf{u}}(t_{n+1}) \quad (3.2)$$

$$\dot{\mathbf{u}}(t_{n+1}) = \dot{\mathbf{u}}(t_n) + (1 - \gamma_N) \cdot \Delta t \cdot \ddot{\mathbf{u}}(t_n) + \gamma_N \cdot \Delta t \cdot \ddot{\mathbf{u}}(t_{n+1}) \quad (3.3)$$

where β_N and γ_N are the numerical parameters that assure precision and stability of the algorithm. The higher modes of semi-discrete equations are artifacts of the discretization process and they are not representative of the behavior of the governing partial differential equations. Hence, it is generally desired to introduce some algorithmic damping to remove the participation of the high-frequency modal components even if second-order accuracy is lost ([Hughes, 2000](#)). For a damping ξ_N , less than unity, the Newmark method is unconditionally stable when the equations 3.4 are satisfied:

$$\gamma_N \geq \frac{1}{2} \text{ and } \beta_N \geq \frac{(\gamma_N + 1/2)^2}{4} \quad (3.4)$$

Otherwise the stability can be conditional to the period (T) and the time step (Δt), as follows:

$$\begin{aligned} \gamma_N &\geq \frac{1}{2} \\ \frac{\Delta t}{T} &\leq \frac{\xi_N \cdot (\gamma_N - \frac{1}{2})/2 + [(\gamma_N + \frac{1}{2})^2/4 - \beta_N + \xi_N^2 \cdot (\beta_N - \frac{\gamma_N}{2})]^{1/2}}{2\pi \cdot [(\gamma_N + \frac{1}{2})^2/4 - \beta_N]} \end{aligned} \quad (3.5)$$

Thus, to assure stability of higher modes (i.e. lower periods), either the time step should be reduced or the damping should be increased. When $\gamma_N > \frac{1}{2}$ and $\beta_N = (\gamma_N + \frac{1}{2})^2/4$, the stability is unconditional but the numerical damping depends on T and Δt as follows:

$$\xi_N = \pi \left(\gamma_N - \frac{1}{2} \right) \frac{\Delta t}{T} + O \left(\frac{\Delta t}{T} \right)^2 \quad (3.6)$$

Note that in this equation, the first derivative with respect to the normalized frequency ($\Delta t/T$) is positive for $\Delta t/T=0$, an indication of first-order accuracy. Additionally the numerical dissipation of low modes (i.e. $\Delta t/T < 0.1$) is more important compared to other numerical algorithms that present zero slopes hence second-order accuracy (Hughes, 2000).

The modes of the system can be considered independently in order to investigate the stability and accuracy characteristics of the integration scheme in the linear regime (Kontoe et al., 2008). The governing equation is then a single-degree-of-freedom (SDOF) model and the solution leads to the set of equations 3.7:

$$\begin{Bmatrix} u \\ \dot{u} \\ \ddot{u} \end{Bmatrix}_{n+1} = [\mathbf{A}] \cdot \begin{Bmatrix} u \\ \dot{u} \\ \ddot{u} \end{Bmatrix}_n \quad (3.7)$$

where \mathbf{A} is the amplification matrix that determines algorithmic characteristics such as stability, accuracy and numerical dissipation. The spectral radius at infinity (ρ_∞) is the maximum eigenvalue of the amplification matrix. The algorithm is conditionally stable when $\rho_\infty \leq 1$. For ρ_∞ equal to 1, the dissipation is equal to zero, but as ρ_∞ decreases, the algorithmic dissipation increases for the higher modes.

Kuhl and Crisfield (1999), among others, propose to calculate γ_N and β_N as a function of the spectral radius at infinity (ρ_∞) to achieve an ‘‘optimal high-frequency dissipation with

minimal low-frequency impact”, i.e. to decrease amplitude with time when the response is near to free-oscillations. Figure 3.1 shows the spectral radii as a function of normalized frequency for different sets of Newmark parameters. The minimum value of β_N that retains unconditional stability is $\gamma_N/2$. However as may be seen from the black dashed lines in Figure 3.1, for values of β_N such that $\gamma_N/2 \geq \beta_N < (\gamma_N + \frac{1}{2})^2/4$, the eigenvalues of \mathbf{A} bifurcate and become real beyond some $\Delta t/T$. Thus, the high frequencies are not effectively damped. In the other hand, as it can be seen with the color lines, when the Newmark parameters are related by ρ_∞ , i.e. $\beta_N = (\gamma_N + \frac{1}{2})^2/4$, the spurious high frequencies are the most effectively filtered.

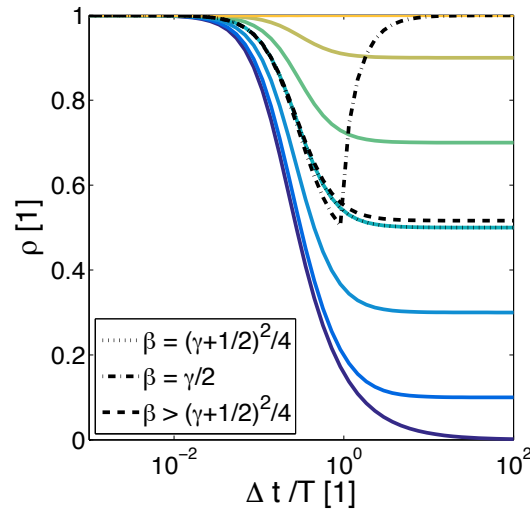


Figure 3.1 – Spectral radii as a function of normalized frequency for different sets of Newmark parameters. Color lines show parameters related by ρ_∞ and dashed lines show an example for $\gamma_N=0.83$ and different β values.

The relations are:

$$\beta_N = \frac{1}{(\rho_\infty + 1)^2} \text{ and } \gamma_N = \frac{3 - \rho_\infty}{2\rho_\infty + 2} \quad (3.8)$$

Note that these equations satisfy the equation 3.4 of unconditional stability; thus, the solution’s stability is independent of the frequency and time step. When ρ_∞ is equal to 1.0 ($\beta_N = 0.25$, $\gamma_N = 0.5$), there is no dissipation and therefore no numerical damping is added. On the other hand, the algorithm with $\rho_\infty = 0$ leads to the strongest possible high-frequency dissipation but achieves very poor accuracy in the low modes. Thus, it is not useful for most applications.

3.2.1 Numerical damping

Theoretically, below the elastic shear strain threshold, no hysteretic dissipation of energy takes place. However, even if the mechanism is not well understood, there is experimental evidence of

such dissipation (Darendeli, 2001). Some advanced constitutive models, as the one used in this study, require the addition of a small amount of low strain damping to avoid spurious response at very low strain levels. This damping is introduced by the numerical algorithm of the dynamic equilibrium solution in the time domain and is applicable for strains less than 0.01%. In this section, two ways to quantify the numerical damping (ξ_N) induced by the dissipative integration scheme in the case of elastic soil behavior are presented. The first one is by analyzing the time domain of the surface displacement of a soil deposit over a rigid bedrock; and the second one is by calculating the deamplification of the transfer function of a deposit over an elastic bedrock. As no material damping should be present, a scaled motion with a maximum acceleration (PHA) of approximately $1 \cdot 10^{-5}g$ is applied to the bottom of a soil deposit. With a very small PHA, the behavior is assured to be elastic.

The first method consists in comparing the wave propagation of the soil deposit with a single degree-of-freedom (SDOF) model. This is done under the hypothesis that the response is near to free oscillation and the damping is small (i.e. less than 1%) (Ruiz and Saragoni, 2009). For a homogeneous case, the exact solution of the displacement is:

$$\mathbf{u}(\mathbf{t}, \mathbf{z}) = \exp(-2\xi_N \cdot \pi \cdot \omega^h \cdot \mathbf{t}) [d_0 \cos(\omega_d^h \cdot \mathbf{t}) + c \sin(\omega_d^h \cdot \mathbf{t})] \quad (3.9)$$

with

$$\begin{aligned} c &= \frac{v_0 + \xi_N \cdot \omega^h \cdot d_0}{\omega_d^h} \\ \omega_d^h &= (1 - \xi_N^2)^{1/2} \cdot \omega^h \end{aligned} \quad (3.10)$$

where ω_d^h is the damped natural angular frequency for mode h . Recall that $f_d^h = 2\pi \cdot \omega_d^h$. Hughes (2000) derived the discrete solution and arrived to the conclusion that after one period, for small ξ_N , the amplitude decay is:

$$AD \cong 2\pi \cdot \xi_N \quad (3.11)$$

In order to evaluate the numerical damping added, different spectral radii were tested in a simple one dimensional wave propagation test of a 20m homogeneous elastic soil overlying a rigid bedrock. The material properties are shown in Table 3.1 and correspond to profile P1 that will be used to test the model parameter's sensibility in section 3.4. Likewise, the input motion used corresponds to a japanese recording at a KiK-net station and is shown in section

3.4, Figure 3.9a. The spectral radii tested are listed in Table 3.2. The time step (Δt) is constant for all simulations and set to $1 \cdot 10^{-3}$ s and the element size is 25cm.

Material	ρ [kg/m ³]	ν [1]	V_s [m/s]
Soil	2000	0.4	300
Rock	2500	0.3	1000

Table 3.1 – Material elastic properties for numerical damping evaluation for P1 profile.

ρ_∞	β_N	γ_N
1	0.25	0.50
0.9	0.28	0.55
0.7	0.35	0.68
0.5	0.44	0.83
0.3	0.59	1.04
0.0	1.00	1.50

Table 3.2 – Newmark parameters tested and calculated by equation 3.8

Figure 3.2 shows the surface displacement (\mathbf{u}) as a function of time (\mathbf{t}) for the different spectral radii. It evidence the effect of the numerical damping for the different cases shown as the rate for the amplitude decay after the peak acceleration. However, it can be noted that this decay is not linear with respect to the spectral radius.

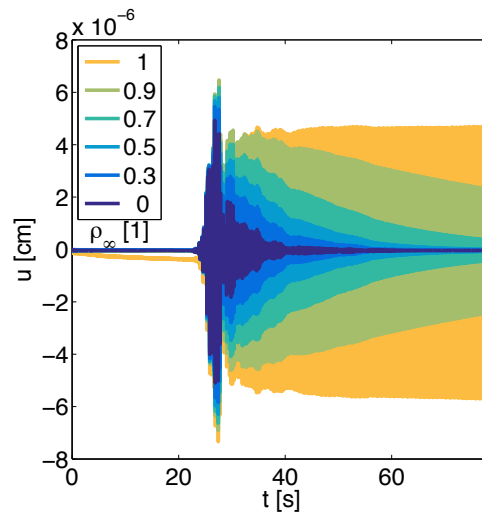


Figure 3.2 – Surface displacement time history for the different spectral radius (ρ_∞)

The numerical damping was evaluated by simplifying equation 3.9, as done by Ruiz and

Saragoni (2009), as follows:

$$\frac{u}{u_{max}} = \mathbf{y} \cdot \exp(-2\pi \cdot f_0 \cdot \xi_N \cdot \mathbf{t}) \quad (3.12)$$

where u_{max} is the maximum displacement and f_0 is the predominant frequency. Figure 3.3a shows an example of the displacement normalized by the maximum value as a function of time normalized by the natural angular frequency ($\omega_0 = 2\pi \cdot f_0$). The envelope after the peak is then fitted by an exponential function where the slope coefficient is equal to the damping value. Note that the exponential decay is best analyzed at the end of the signal while the initial part is more related to the vector \mathbf{y} which describes the second part of equation 3.9. This procedure was performed for all the values tested. Additionally, other soil columns were tested which will be used in Chapters 4 and 5. Figure 3.3b shows the numerical damping (ξ_N) as a function of the spectral radius (ρ_∞) for all the soil profiles. It can be seen that even for the smallest ρ_∞ the damping is less than 1%. This damping is independent of the soil and the motion properties. Additionally, the theoretical equation 3.6 is evaluated for the predominant frequency ($f_0=3.75\text{Hz}$) and the time step ($\Delta t = 1 \cdot 10^{-3}\text{s}$) and shown in Figure 3.3b. Neglecting the quadratic terms, the results agree well with the computed values for the different soils and with ρ_∞ above 0.2. When ρ_∞ equals 0, the ξ_N varies for the different cases possibly due to the high value of damping that is approaching unity.

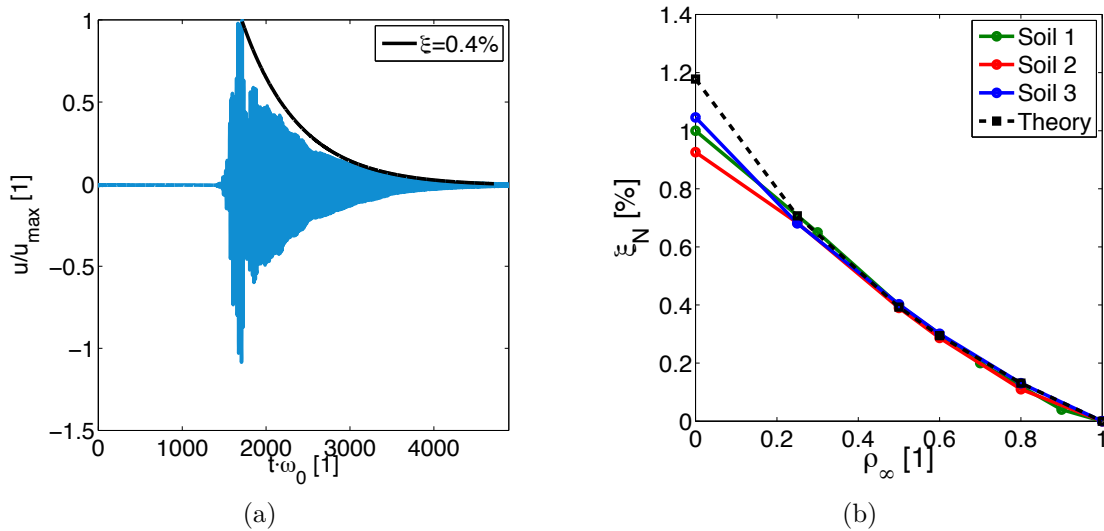


Figure 3.3 – Induced numerical damping of a soil deposit over a rigid bedrock: a) Normalized surface displacement as a function of the normalized time history and b) ξ_N as a function of the spectral radius (ρ_∞) calculated by exponential decay and by equation 3.6 in dashed line.

The second method consists in measuring the amplitude of the transfer function between

the surface and the outcropping displacement known as the amplification ratio ($|AR|$) at the different modes (Dobry et al., 1982). When no damping is present, the amplitude of all modes is equal to the impedance ratio (I) between the rock (r) and the soil (s). Which is defined as: $I = \frac{\rho_r \cdot V_{sr}}{\rho_s \cdot V_{ss}}$. Otherwise, when no material damping exist, the deamplification is due to the numerical damping, thus it can be evaluated as follows:

$$\xi_N(\omega) = \frac{\frac{I}{|AR|} - 1}{(2n - 1)\pi \cdot I/2} \quad (3.13)$$

Figure 3.4a shows the $|AR|$ for the different spectral radii without any kind of smoothing. Note that for the undamped case, the maximum amplitude for all modes is approximately equal to the impedance ratio (i.e. $I = 4.16$ for this model); although as no dissipation is allowed some spurious peaks are present. However, these peaks are not visible for the other spectral radii. Additionally, it can be seen how the deamplification is greater for the second and third modes, hence this numerical damping is shown to be frequency dependent. The damping is quantified for each mode using equation 3.13 and it is shown in Figure 3.4b as a function of spectral radius. In the figure, the damping evaluated with the first approach is also shown. Note that it is similar to that of the first mode, thus both approaches are useful to quantify the numerical damping induced in the model. Once more, the theoretical equation 3.6 is evaluated for the first three modal frequencies and the time step ($\Delta t = 1 \cdot 10^{-3}$ s) used. Results are shown in Figure 3.3b as black dashed lines. Neglecting the quadratic terms, the results agree well with the computed values for the first mode; however differences increase for higher modes and for higher damping. The second method is more reliable as it is measured in the response and allows to quantify the damping for different frequencies without any approximations.

As high-frequency dissipation is advisable, a ρ_∞ equal to 0.8 (i.e. $\gamma_N=0.611$ and $\beta_N=0.301$) will be used, unless it is mentioned different. The corresponding ξ_N is approximately 0.1% for the frequencies close to 5Hz. It is important to remark that this numerical damping affects principally the elastic response of the model (i.e. for shear strains (γ) lower than 10^{-5}) and for greater values of γ the damping is provided by the material degradation as will be shown in the next section.

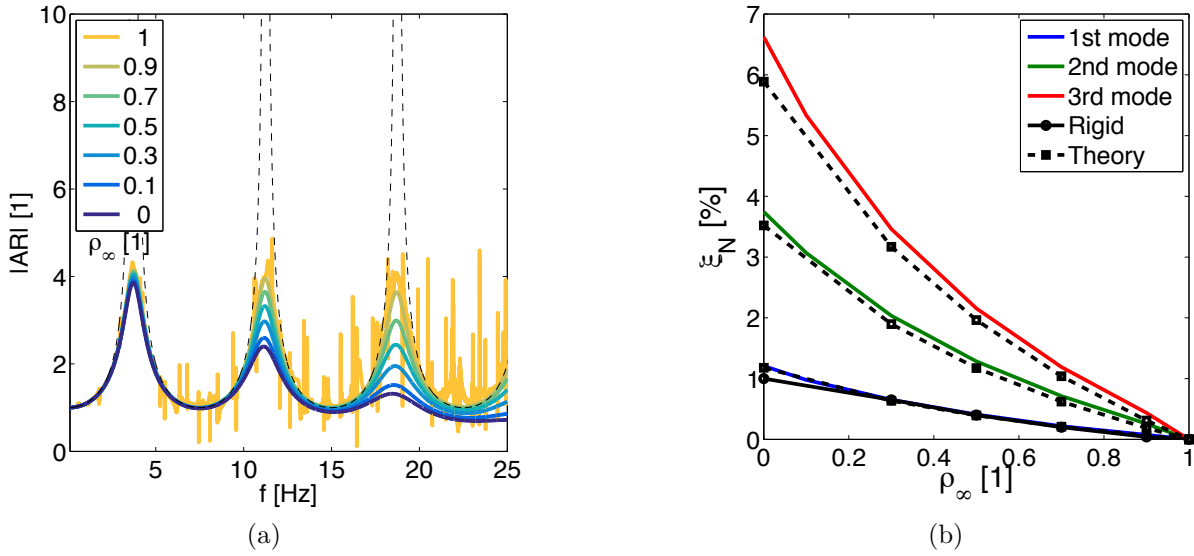


Figure 3.4 – Induced numerical damping of a soil deposit over an elastic bedrock: a) Amplification ratio ($|AR|$) between the surface and the outcropping displacement and b) ξ_N as a function of the spectral radius (ρ_∞) for the first three modes. No smoothing was used for the $|AR|$.

3.2.2 Discretization

3.2.2.1 Mesh size

In dynamic modeling, the discretization in space is given by the minimum shear wave velocity ($V_{s\min}$), the highest frequency (f_{\max}) of interest in the analysis and the maximum number of points per wavelength (n). The minimum wavelength (λ) visible to the soil is directly proportional to $V_{s\min}$ and inversely proportional to f_{\max} , i.e. $\lambda = V_{s\min}/f_{\max}$. Hence, the element size is bounded by:

$$\Delta z \leq \frac{V_{s\min}}{n \cdot f_{\max}} \quad (3.14)$$

It is usually admitted that 10 points per wavelength are sufficient to obtain good numerical results, hence $n = 10 \cdot (N_e - 1)$, where N_e is the number of integration points per element defined by the integration order. In this study, a quadratic approximation is used, hence N_e equals 3, i.e. 9 integration points per element. However, it is important to remark that for non-linear models, the shear-wave velocity will decrease with the shear-strain amplitude; thus more points per wavelength should be used. In general for this study, Δz is 0.5m; that, for a f_{\max} of 20Hz and n of 10, a minimum $V_{s\min}$ of 50m/s will still be feasible.

3.2.2.2 Time step

The discretization in time depends on the element size (Δz) and the shear wave velocity (V_s), but also on the mass matrix determination, the damping used and the fundamental period of the system. The use of finite element methods imposes a basic stability criterion. In other words, as a wave propagates in space it reaches one point after the other; but if the time step in the analysis is too large the wave front can reach two consecutive elements at the same moment. This would violate a fundamental property of wave propagation and can lead to instability. The time step therefore needs to be limited. Foerster and Modaressi (2007a) derived the critical time step for a series of cases for 1D isoparametric elements and nodal quadrature. The most restrictive case tested was that of a rigid bedrock used for explicit schemes; which gives:

$$\Delta t < \frac{\Delta z}{V_s} \sqrt{\frac{3A \cdot B}{8\beta_N}} \quad (3.15)$$

where $A = (23 + \sqrt{345})/120$ and $B = (37 - \sqrt{345})/60$ when the diagonal consistent scheme is used to diagonalize the mass matrices. If the traditional lumping scheme is used instead $A = 1/6$ and $B = 2/3$. Foerster and Modaressi (2007a) showed some advantages of using the diagonal consistent scheme as it gives smoother results specially avoiding the high frequency spurious oscillations in acceleration, which are due to numerical instabilities. It is important to highlight that these coefficients are only valid for the 1D case whereas for 2D or 3D cases, coefficients will change.

In the present case the time step should be smaller than $3 \cdot 10^{-3}$ s. An additional stability criterion results from the nonlinear implementation of the numerical solution of wave propagation. Similar to the spatial discretization, the smallest fundamental period of the system (T_n) chosen, should be represented by 10 time steps (Preisig and Jeremic, 2005) - equal to $5 \cdot 10^{-3}$ s in this case if 3 modes are used. Lastly a third criterium is related to the dynamic analysis, by which the numerical time step is also affected by that of the input motion. In general, the numerical time step should be 5 times smaller than the latter (Preisig and Jeremic, 2005). All of these criteria should be respected in order to avoid stability and convergency problems.

Furthermore, the time step will affect the attenuation at high frequencies, due to the dissipative scheme of the Newmark method chosen. As an example, the elastic model for profile P1, used above for the numerical damping calculation, is tested with different time steps. The numerical parameters used are $\beta_N=0.28$ and $\gamma_N=0.55$, which correspond to ρ_∞ of 0.9 and ξ_N about 0.06% when $\Delta t = 1 \cdot 10^{-3}$ s. The same input motion is used and is applied to a rigid

bedrock. Figure 3.5a shows the transfer function between the acceleration at surface and the one used as input. For a given set of Newmark parameters, the damping increases with the time step; specially for the second and third modes. However, if the time step is below the one calculated with equation 3.15, the damping is only slightly increased. Note that the time steps were changed by a factor of 5 thus the damping is increased when the highest value is used, which corresponds to the motions time step $5 \cdot 10^{-3}$ s-. In fact, the peak acceleration at surface is very similar for the other values, refer to Figure 3.5b, whereas for the highest time step some differences can be seen even before the maximum amplitude. Referring to the approximation of numerical damping given by equation 3.6, by neglecting quadratic terms, ξ_N is described by a linear function directly proportional to the time step and inversely proportional to the period. In this case, damping is given by : $\xi_N \approx 0.16\Delta t/T$. Thus, for the smallest time step tested, ξ_N is about 0.03% and it is ten times fold for the highest time step used.

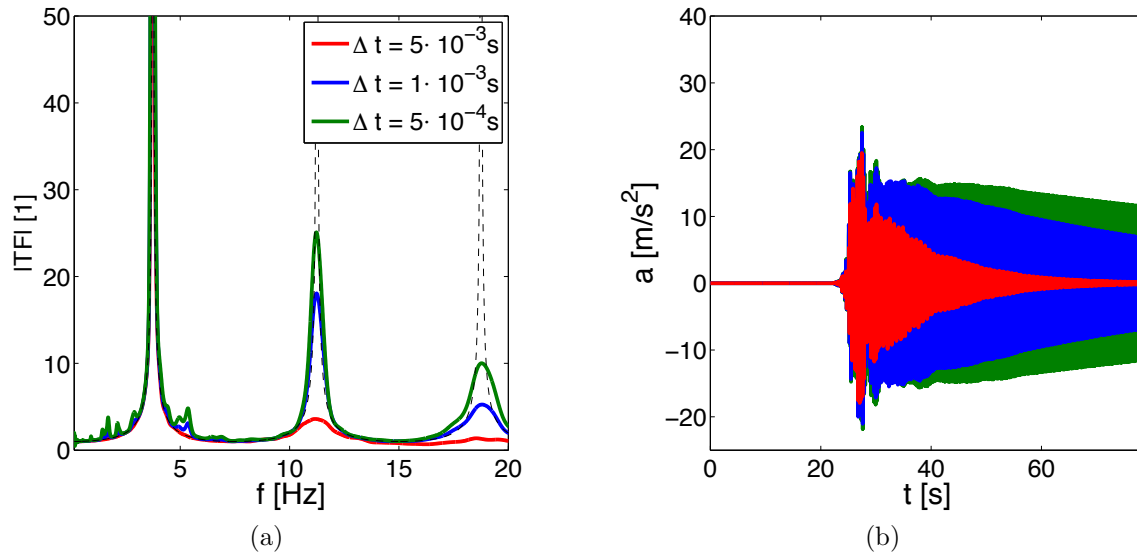


Figure 3.5 – Effect of the time step in a) the transfer function and in b) the surface acceleration. Results for P1 and the elastic model.

3.3 Soil behavior model

Previously the numerical model was debriefed and some aspects of the integration of the system of equations were introduced. However, embedded on these equations is the constitutive model of the soil behavior which relates the stresses due to the loads imposed in the system to the strains in the material. The soil behavior is simulated in this analysis with the elastoplastic multi-mechanism model developed at *École Centrale Paris* and known as ECP model. In this

section a synthesis of the mechanical behavior of soils will be presented, followed by a brief description of the soil model and the calibration of its parameters.

The model is written in terms of effective stresses of [Terzaghi \(1943\)](#), as it was already mentioned in the beginning of this chapter, because when water is present, the soil mechanical behavior is determined by the contact forces between grains which depend on the total stresses but also on the pore-water pressure. One important remark of this approach is that the *true cohesion* will not be used. That is, the shear strength for a zero mean effective stress will be null for saturated soils.

The ECP model can take into account a large range of deformations due to its decomposition into pseudo-elastic, hysteretic and mobilized domains. According to the critical-state concept, the macroscopic behavior of sands and clays is similar and is related to the proximity of its initial state to the critical state or steady-state rather than to the absolute measurements of density ([Roscoe and Pooroshab, 1963](#); [Been and Jefferies, 1985](#); [Ishihara, 1993](#)). The critical state is defined as the state defined by the mean stress (\mathbf{p}') and the void ratio (e) where there is constant deviatoric stress (\mathbf{q}) for increasing strain and no volumetric strain and is shown as a curve at the space $e - \mathbf{p}' - \mathbf{q}$. Hence the contractant or dilatant behavior is given by the initial position with respect to this curve. Three hardening evolutions are used for the different mechanisms. For monotonic mechanisms: (1) the deviatoric, which is based on the plastic strain and is dependent on deviatoric and volumetric strains, and (2) the isotropic, where only volumetric strains are involved; and for cyclic loading: (3) the kinematic hardening that relies on the state variables at the last load reversal. A brief description of the model will be given; however for more details, refer to [Aubry et al. \(1982\)](#), [Hujeux \(1985\)](#) and [Lopez-Caballero and Modaressi-Farahmand-Razavi \(2010\)](#) among others.

3.3.1 Model description

Following the incremental plasticity theory, the strains ($\boldsymbol{\varepsilon}$) and the strain-rate ($\dot{\boldsymbol{\varepsilon}}$) can be decomposed into an elastic (reversible) and a plastic (irreversible) part:

$$\boldsymbol{\varepsilon} = \boldsymbol{\varepsilon}^e + \boldsymbol{\varepsilon}^p \quad (3.16)$$

$$\dot{\boldsymbol{\varepsilon}} = \dot{\boldsymbol{\varepsilon}}^e + \dot{\boldsymbol{\varepsilon}}^p \quad (3.17)$$

The elasticity behavior is isotropic and nonlinear, where the maximum bulk (\mathbf{K}_{max}) and

the maximum shear (\mathbf{G}_{max}) moduli are functions of the mean effective stress (\mathbf{p}'), as follows:

$$\mathbf{K}_{max} = K_{ref} \left(\frac{\mathbf{p}'}{p'_{ref}} \right)^{n_e} \quad (3.18)$$

$$\mathbf{G}_{max} = G_{ref} \left(\frac{\mathbf{p}'}{p'_{ref}} \right)^{n_e} \quad (3.19)$$

with K_{ref} and G_{ref} being the bulk and shear moduli at the reference stress (p'_{ref}) and n_e , the degree of nonlinearity. The relation of the stiffness with the confinement pressure is derived from the Hertz theory of elastic spheres under isotropic stresses and its applications in granular soils have been studied by many authors as [Hardin \(1978\)](#); [Biarez and Hicher \(1994\)](#); [Tatsuoka \(2001\)](#), among others. In most cases, n_e is near 0.5 for sands and is higher for clays. Its value can be calibrated with in-situ measurements of \mathbf{G} or \mathbf{V}_s which increase with depth.

For the multi-mechanism model three deviatoric mechanisms in three perpendicular planes are taken into account. Adopting the soil mechanics sign convention (i.e. compression positive), the deviatoric primary yield surface on the k plane is:

$$\mathbf{f}_k = \mathbf{q}_k - \mathbf{p}'_k \cdot \mathbf{F}_k \cdot \mathbf{r}_k \cdot \sin \phi'_{pp} \quad (3.20)$$

where ϕ'_{pp} is the friction angle at the critical state, \mathbf{p}'_k is the mean stress and \mathbf{q}_k is the second invariant of the deviatoric stress tensor defined on the k plane as follows:

$$\mathbf{p}'_k = \frac{\sigma_{ii} + \sigma_{jj}}{2} \quad (3.21)$$

$$\mathbf{q}_k = (\mathbf{s}_{k1}^2 + \mathbf{s}_{k2}^2)^{1/2} \quad (3.22)$$

with:

$$\mathbf{s}_{k1} = \frac{\sigma_{ii} - \sigma_{jj}}{2} \quad (3.23)$$

$$\mathbf{s}_{k2} = \sigma_{ij} \quad (3.24)$$

Note that equation 3.20 is an evolution of Cam-Clay model where 2 new variables are added: b and \mathbf{r}_k . The parameter b controls the effect of the density and overconsolidation in the shape of the yield surface in the $\mathbf{p}' - \mathbf{q}$ plane. It is embedded in the isotropic hardening associated

with the volumetric strain by:

$$\mathbf{F}_k = 1 - b \cdot \ln \left(\frac{\mathbf{p}'_k}{\mathbf{p}_c} \right) \quad (3.25)$$

The effect of density is also present in the variable \mathbf{p}_c , which is the mean stress at the critical state and is defined as:

$$\mathbf{p}_c = p_{c0} \cdot \exp(\beta \cdot \boldsymbol{\varepsilon}_v^p) \quad (3.26)$$

where p_{c0} is the stress corresponding to the critical state of the initial density and initial void ratio and $\boldsymbol{\varepsilon}_v^p$ is the volumetric plastic strain. The parameter β is the plastic compressibility modulus which is related to the evolution of void ratio with respect to the increase in mean stress.

Lastly, the isotropic hardening generated by plastic shearing is controlled by the degree of mobilized friction \mathbf{r}_k . It allows the decomposition of the behavior into pseudo-elastic, hysteretic and mobilized domains and therefore, allows simulations ranging from loads inducing small strains to very strong earthquake motions. \mathbf{r}_k is described by:

$$\mathbf{r}_k = r_k^{ela} + \left(\frac{\bar{\boldsymbol{\varepsilon}}_k^p}{\mathbf{a} + \bar{\boldsymbol{\varepsilon}}_k^p} \right) \quad (3.27)$$

that varies from the size of the elastic deviatoric domain where no hardening is produced (r_k^{ela}), to the unit value at the perfect plasticity. Lopez-Caballero and Modaressi-Farahmand-Razavi (2013) defined an apparent friction angle (ϕ'_{apt}) as follows:

$$\sin \phi'_{apt} = \frac{\mathbf{q}_k}{\mathbf{p}'_k \cdot \mathbf{F}_k} \quad (3.28)$$

Thus, \mathbf{r}_k is useful for evaluating the state of the soil in the deposit by representing the “distance to reach the critical state” as:

$$\mathbf{r}_k = \frac{\sin \phi'_{apt}}{\sin \phi'_{pp}} \quad (3.29)$$

The hardening evolution is given by the following law:

$$\dot{\mathbf{r}}_k = \dot{\boldsymbol{\lambda}}_k^p \frac{(1 - \mathbf{r}_k)^2}{\mathbf{a}} \quad (3.30)$$

where $\dot{\boldsymbol{\lambda}}_k^p$ is the plastic multiplier of the k mechanism. The variable \mathbf{a} is of key importance as it controls the stiffness in the plastic domain. It is divided in two components, known as the

plastic stiffness parameters related by the following equation:

$$\mathbf{a} = a_1 + (a_2 - a_1) \cdot \alpha_k(\mathbf{r}_k) \quad (3.31)$$

where:

$$\alpha_k(\mathbf{r}_k) = \begin{cases} 0 & \text{if } r_{ela} < \mathbf{r}_k < r_{hys} \\ \left(\frac{r_k - r_{hys}}{r_{mob} - r_{hys}} \right)^m & \text{if } r_{hys} < \mathbf{r}_k < r_{mob} \\ 1 & \text{if } r_{mob} < \mathbf{r}_k < 1 \end{cases}$$

The parameter m controls the response of the cyclic loading path and is best when equal to 1 (Kordjani, 1995). The parameters r_{ela} , r_{hys} and r_{mob} designate the hardening threshold of the pseudo-elastic, hysteretic and mobilized domains, respectively. These parameters are very important in liquefaction modeling as they control the degradation hysteresis and the pore-water pressure change in undrained conditions or the volume change in drained conditions. Concerning α_k , a physical interpretation was given by Hujeux (1985), where $\alpha_k \cdot \boldsymbol{\varepsilon}_k^p$ represents the fraction of the plastic shear strain increment due to relative tangent displacement between grains, with total mobilization of the shear strength. This displacement induces the rearrangement of grains hence the evolution of plastic volumetric strains. The remaining fraction, i.e. $(1 - \alpha_k) \cdot \boldsymbol{\varepsilon}_k^p$ corresponds to the displacement with partial mobilization; thus, since no grain rearrangement is present, no volumetric plastic strains are produced. The parameter α_k controls that until a certain level of shearing, no volume variations are allowed, in drained conditions, and that in undrained conditions, the pore pressure evolution will depend, among others, on the level of deformations, specially at cycle accumulation (Modaressi, 2003).

The plastic potential has the form of the original Cam-clay surface, and the flow rule can be non-associated (i.e. the characteristic angle (ψ), that limits the dilating and contracting domain, is different to the critical friction angle ϕ). The evolution of the volumetric plastic strain is given by the flow rule based on Roscoe's dilatancy, as follows:

$$(\dot{\boldsymbol{\varepsilon}}_v^p)_k = (\dot{\boldsymbol{\varepsilon}}_d^p)_k \cdot \alpha_k(\mathbf{r}_k) \cdot \alpha_\psi \cdot \left(\sin \psi - \frac{\mathbf{q}_k}{\mathbf{p}'_k} \right) \quad (3.32)$$

where α_ψ is a parameter that can control the volumetric behavior. Note that these mechanisms can not account for the isotropic behavior of soils. In other words, an isotropic consolidation can not be modeled except if it is at the critical state. Therefore a fourth mechanism is added to account for isotropic stress paths.

Concerning the isotropic mechanism, only volumetric strains are produced. The yield surface is then:

$$\mathbf{f}_{iso} = |\mathbf{p}'| - d \cdot \mathbf{p}_c \cdot r_{iso} \quad (3.33)$$

where:

$$r_{iso} = r_{iso}^{ela} + \frac{\varepsilon_{v iso}^p}{c_1 \frac{\mathbf{p}_c}{p_{ref}} + \varepsilon_{v iso}^p} \quad (3.34)$$

$$\dot{r}_{iso} = \varepsilon_{v iso}^p \frac{(1 - r_{iso})^2}{c_1 \frac{\mathbf{p}_c}{p_{ref}}} \quad (3.35)$$

The parameter d is the mean stress difference in a logarithmic scale between the isotropic consolidation line and the critical state line and c_1 is the isotropic hardening parameter which controls the isotropic evolution in a similar manner as a_1 and a_2 do in the deviatoric mechanism. Camoes (2014) analyzed the effect of c_1 in the $\varepsilon_v - \mathbf{p}'$ plane for an isotropic compression test. Results showed that for higher c_1 , the stiffness rate decreases; hence, the volumetric strain increases for small \mathbf{p}' values. However at low c_1 values, the mechanism will evolve faster and the transition between pre-consolidation and virgin states is more abrupt.

The parameter r_{iso}^{ela} designates the extension of the elastic domain for the isotropic mechanism and is usually ten times smaller than the deviatoric counterpart. Note that the equation 3.33 describes a vertical line that cuts the deviatoric yield surface of equation 3.20 at a mean stress given by the ε_v^p .

To couple the four mechanisms, the plastic volumetric strains of each mechanism are summed and the critical stress (\mathbf{p}_c), which is common for all the mechanisms, is changed. For a general case, where all mechanisms are active, the plastic multiplier is the solution of a 4×4 non linear system where the hardening modulus matrix is composed of deviatoric terms in the diagonal and volumetric hardening in all terms. Then, softening is related to a global dilative state, where $\dot{\mathbf{p}}_c < 0$ and $\mathbf{p} > \mathbf{p}_c$; while, hardening is related to a global contractive state, i.e. $\dot{\mathbf{p}}_c > 0$ and $\mathbf{p} < \mathbf{p}_c$.

For the cyclic yielding surface, it is necessary to take into account the stress state and its direction for each mechanism. Hence, two historic state variables are introduced: (1) the nor-

malized deviatoric stress tensor at the last load reversal (\mathbf{T}_k^h) and (2) its direction. Respectively,

$$\mathbf{T}_k^h = \frac{\mathbf{s}_k^h}{\mathbf{p}_k'^h \cdot \mathbf{F}_k^h \cdot \sin \phi_{pp}} \quad (3.36)$$

$$\mathbf{t}_k^h = \frac{\mathbf{s}_k^h}{\mathbf{q}_k^h} \quad (3.37)$$

where \mathbf{s}_k^h is the deviatoric stress tensor and the index h denotes the historic variable. On that account the cyclic yielding surface can be written as:

$$\mathbf{f}_k^c = \mathbf{q}_k^c - \mathbf{p}_k' \cdot \mathbf{F}_k \cdot \mathbf{r}_k^c \cdot \sin \phi_{pp}' \quad (3.38)$$

with

$$\mathbf{q}_k^c = \left(\frac{1}{2} \text{Tr}(\mathbf{s}_k^c \cdot \mathbf{s}_k^c) \right)^{1/2} \quad (3.39)$$

$$\mathbf{s}_k^c = \mathbf{s}_k - (\mathbf{T}_k^h - \mathbf{t}_k^h \cdot \mathbf{r}_k^c) \cdot \mathbf{p}_k' \cdot \mathbf{F}_k \cdot \sin \phi_{pp} \quad (3.40)$$

Like in the monotonic case, the mobilization of the cyclic mechanism is controlled by the variable \mathbf{r}_k^c . When the stress state is inside of the yield surface, i.e. the circle defined by \mathbf{r}_k of equation 3.20, the cyclic mechanism is deactivated and the monotonic mechanism is activated. Then, \mathbf{r}_k^c is set to r_{ela} at each change of direction. Introducing the position of the last load reversal, the equation 3.27 applied for the evolution of \mathbf{r}_k^c can be expressed by:

$$\mathbf{r}_k^c = r_{ela} + \frac{|\boldsymbol{\varepsilon}_k^p - \boldsymbol{\varepsilon}_k^{p^h}|}{\mathbf{a} + |\boldsymbol{\varepsilon}_k^p - \boldsymbol{\varepsilon}_k^{p^h}|} \quad (3.41)$$

where $\boldsymbol{\varepsilon}_k^{p^h}$ is the plastic distortion of the mechanism k at the last load reversal h . Note that the variable \mathbf{a} is the same for the monotonic and the cyclic loading.

For the isotropic mechanism, the successive consolidation thresholds are orthogonal planes to the mean stress axis at a distance \mathbf{r}_{iso}^c . The equation 3.33 derives to:

$$\mathbf{f}_{iso}^c = |\mathbf{p}_k'^h| - d \cdot \mathbf{p}_c \cdot \mathbf{r}_{iso}^c \quad (3.42)$$

where:

$$\mathbf{p}'_k{}^h = \mathbf{p}'_k - d \cdot \mathbf{p}_c \cdot r_{iso}^h \quad (3.43)$$

$$r_{iso}^h = \frac{\mathbf{p}'_k}{d \cdot \mathbf{p}_c} \quad (3.44)$$

The evolution of the isotropic hardening variable r_{iso}^c is given by equation 3.34; however the parameter c changes for the cyclic case and is called c_2 .

3.3.2 Model Parameters identification

In the literature, a series of publications can be found concerning the identification of ECP model parameters. They differ principally in the applications and the lab tests available for calibration. Lopez-Caballero (2003), Lopez-Caballero and Modaressi (2011a) and Carrilho Gomes et al. (2015) propose some methodologies focused in seismic analysis. The twenty model parameters were classified by the former according to the different mechanisms and are divided in two groups: whether they can be directly measured or not.

	Elasticity	Critical State and Plasticity	Flow Rule and Isotropic Hardening	Threshold Domains
Directly measured	G_{ref} , K_{ref} , n_e and p_{ref}	ϕ'_{pp} , p_{co} , d and β	ψ	
Undirectly measured		b	a_1 , a_2 , c_1 , c_2 , α_ψ , and m	r^{ela} , r^{hys} , r^{mob} and r_{iso}^{ela}

Table 3.3 – Classification of the ECP model parameters as proposed by Lopez-Caballero (2003)

The model parameters shown in Table 3.3 as undirectly measured are geometric parameters that allow the calibration of different lab tests. In lack of experimental data, a library of different types of soils can be found in the model website (GEFDyn, 2009).

1. Elasticity

The elasticity domain is described by the shear (\mathbf{G}) and bulk moduli (\mathbf{K}) and can be related to the mean stress (\mathbf{p}) with the parameter n_e . These parameters are related to the shear and compression wave velocity (\mathbf{V}_s and \mathbf{V}_p) measured with geophysical tests. The Poisson coefficient (ν), the shear and the bulk modulus are defined as follows:

$$\nu = \frac{1}{2} \left[\frac{(\mathbf{V}_p/\mathbf{V}_s)^2 - 2}{(\mathbf{V}_p/\mathbf{V}_s)^2 - 1} \right] ; \quad \mathbf{G} = \rho \cdot \mathbf{V}_s^2 \quad \text{and} \quad \mathbf{K} = \frac{2\mathbf{G} \cdot (1 + \nu)}{3 \cdot (1 - 2\nu)} \quad (3.45)$$

As the vertical stress increases with depth (i.e. $\sigma_v = \rho \cdot \mathbf{g} \cdot z$), the stiffness moduli are also generally increasing with depth. This relation is possible in the ECP model via the mean stress $\mathbf{p} = \sigma_v(1 + 2k_0)/3$ and n_e as following:

$$\mathbf{K}_{max} = K_{ref} \left(\frac{\mathbf{p}'}{p'_{ref}} \right)^{n_e} \quad \text{and} \quad \mathbf{G}_{max} = G_{ref} \left(\frac{\mathbf{p}'}{p'_{ref}} \right)^{n_e} \quad (3.46)$$

with K_{ref} and G_{ref} being the bulk and shear moduli at the reference stress (p'_{ref}) usually taken as 1MPa and n_e , the degree of nonlinearity. Therefore, a gradient shear wave profile can be used to find the parameter n_e . However, for constant profiles, this value is set to zero.

2. Critical State and Plasticity

The friction angle at the perfect plasticity (ϕ'_{pp}) is measured via the triaxial test and corresponds to:

$$\sin(\phi'_{pp}) = \frac{3M}{6 + M} \quad (3.47)$$

where M is the slope of the perfect plasticity line in the stress plane $\mathbf{q}-\mathbf{p}'$.

The initial critical mean stress (p_{c0}) defines the distance from the initial state to the critical state line in the plane $\mathbf{e}-\ln(\mathbf{p})$ as it does the state parameter of [Been and Jefferies \(1985\)](#) (ψ_{BJ}), with the distinction that the latter is defined as the void ratio difference between the initial state and the critical state line. The triaxial compression test at the same initial mean stress in the deposit is used to calculate this value. On the absence of this test, empirical correlations for clays and sands can be found in the literature with respect to the over consolidation ratio (OCR) and the relative density (D_r), respectively. The parameter d defines the distance between the isotropic consolidation line and that of the perfect plasticity in the plane $\mathbf{e}-\ln(\mathbf{p})$. As following:

$$d = \exp \left(\frac{\Delta e}{\lambda} \right) \quad (3.48)$$

When no consolidation has been performed before the test, experimental results performed

by Saim (1997) show that Δe can be assumed as 0.1 for all types of sands and clays. In this analysis, d was set constant and equal to 2.0, hence the value of Δe will be function of λ .

The compressibility modulus (β) is the inverse of the critical state slope at the plane ($\epsilon_v^p - \ln p'_c$) and it depends on the initial void ratio (e_0) and the compressibility index (λ), as follows:

$$\beta \simeq \frac{1 + e_0}{\lambda} \quad (3.49)$$

Hence for the same soil, at higher density, β decreases and less ϵ_v^p is developed. Note that the previous equation is given for the plane $e - \ln p'$, if the plane were to be $e - \log p'$, the slopes are related by the natural number: i.e. $C_c = 2.3 \cdot \lambda$.

Lastly, the geometric parameter b controls the shape of the yield surface. For clays, this value is near 1, which will mean a Cam-Clay yield surface and for sands it approaches 0 (Coulomb type surface). In this study, clays take a value of 0.8 and sands a value of 0.2.

3. Flow Rule and Isotropic Hardening

The characteristic friction angle (ψ) is also issued from the triaxial tests and corresponds to the limit of contractant / dilatant behavior. It is often known as transformation phase state and, is supposed equal to ϕ'_{pp} in most cases. Additionally, it is of key importance for the cyclic behavior of sands.

Additionally, a total of 6 geometric parameters control the hardening and softening in the monotonic and cyclic loading paths: a_1 , a_2 , c_1 , c_2 , α_ψ , and m . Of these, special attention is given only to the first four parameters and their calibration will be explained in the next section. The remaining two parameters are usually kept constant: α_ψ , that control the evolution of the volumetric plastic strain, and the parameter m , which is the exponential of the evolution of α_k for the cyclic loading, are taken equal to unity (Kordjani, 1995).

4. Threshold domains

The hardening thresholds (r^{ela} , r^{hys} , r^{mob} and r^{iso}) are related to strain thresholds of the shear stiffness degradation curves ($\mathbf{G}/G_{max} - \gamma$). In general as \mathbf{a} increases, the rate of stiffness degradation and damping evolution decreases hence lower stiffness and higher damping are present for small strains. However, as this variable depends on 6 parameters (i.e. the 3 hardening thresholds, m , a_1 and a_2), the degradation curves can be adjusted.

It is important to remark that these curves, very popular in soil dynamics, are not an input of the model, instead they are the consequence of the evolution of hardening due to plastic strains.

Carrilho Gomes et al. (2015) proposed a methodology to calibrate these parameters. Firstly, the pseudo-elastic threshold is related to the maximum shear modulus (G_{max}) and the strain threshold for elasticity (γ^{ela}) by the ratio between the shear stress at elasticity (τ^{ela}) and at perfect plasticity (τ^{pp}) as follows:

$$r^{ela} = \frac{\tau^{ela}}{\tau^{pp}} = \frac{G_{max} \cdot \gamma^{ela}}{p' \cdot \sin \phi'_{pp} \cdot F} \quad (3.50)$$

Similarly, the hysteretic threshold is related to the threshold strain $\gamma_{0.7}$, for which $G = 0.7G_{max}$, by the following equation:

$$r^{hys} = \frac{\tau_{0.7}}{\tau^{pp}} = \frac{0.7G_{max} \cdot \gamma_{0.7}}{p' \cdot \sin \phi'_{pp} \cdot F} \quad (3.51)$$

At this domain, the total threshold strain can be decomposed in an elastic and a plastic part. Knowing that the elastic part is described by the ratio between the shear stress and the maximum shear modulus and the total strain is approximated to the ratio between the shear stress and the linear equivalent shear modulus, the plastic strain at threshold is equal to $0.3\gamma_{0.7}$.

Finally, the isotropic hardening parameters at monotonic and cyclic loading, c_1 and c_2 are calibrated with undrained triaxial tests. The monotonic isotropic hardening evolution is the rate in the plane $(\eta/M - \varepsilon_1)$, where $\eta = q/p'$. In addition, the cyclic parameter is taken as half of the monotonic one, i.e. $c_2 = 0.5c_1$.

3.4 Sensibility of the numerical model parameters

The results presented in this section form part of the international benchmark PRENOLIN (Improvement of PREdiction of NONLINEar effects caused by strong seismic motion) which started at april 2013 and ended on october 2015. The main objective of the project is to assess the epistemic uncertainties between nonlinear codes in simple 1D conditions and with respect to real recordings. Additionally, it aims to develop guidelines for deterministic, physic-based, nonlinearity predictions for use in seismic hazard assessments. These guidelines are divided in 2

categories: required geotechnical/ geophysical measurements and quality control for nonlinear computations (Régnier et al., 2014).

The research program was divided into two parts: verification (i.e. comparison between different codes) and validation (i.e. comparison between simulations and real recorded signals). The analyses were done in simple conditions : no pore-pressure generation and only one-component vertically incident shear waves. The verification phase was performed in canonical (i.e. really simple) sites; while for the validation phase, three japanese sites were chosen. Some of the results for the second phase will be shown in the next section.

For the first phase, two constitutive models were used in the GEFDyn program: an isotropic elastic (EL) and the *École Centrale Paris* (ECP) elastoplastic multi-mechanism model. For very low acceleration amplitudes, the response is in the elastic domain and the ECP model matches the EL model's behavior and the exact (or analytic) solution. For stronger excitations, an exact solution is not available; although, the ECP model provides results that are in reasonable agreement with the majority of the other nonlinear codes used in the PRENOLIN benchmark. As a whole, two profiles were subjected to one impulse, two sinusoidal motions and two real accelerograms with three different scaling factors. Additionally, three bedrock conditions have been analyzed: elastic (deformable), rigid and elastic-rigid (i.e. very high impedance between soil and bedrock).

In this section, the canonical sites of the verification phase are used to analyze the sensibility of some numerical model parameters. For the sake of brevity only some cases are shown and focus is given on the effect of the parameters in the seismic site response. For more information concerning the results of this phase refer to Régnier et al. (2014).

3.4.1 Soil profiles

The soil profiles used were called canonical sites which are idealistic (or unrealistically simple) cases that should have identical results between codes or should exhibit explainable differences. Two profiles were used: P1, a shallow mono-layer of constant shear velocity (V_s) and P2, a deep mono-layer of gradient V_s . The former has the bedrock at 20m depth while for the latter, the bedrock is at 100m. The soil V_s for P1 is 300m/s and for P2 is an exponential function from 150m/s in the surface to 500m/s at 100m with a coefficient of 0.25. The bedrock V_s is equal to 1000m/s for P1 while is doubled for P2.

The material is assumed as a cohesionless soil and the water is located at 100m depth. The

poisson coefficient for the sediment is 0.4 and for the rock is 0.3. The density for the sediment is taken as 2000 kg/m^3 while for the rock is 2500 kg/m^3 . The attenuation quality factor was set to be equal to 5000, thus a damping (ξ) equal to $1 \cdot 10^{-4}$. For other models, this value is used as input for the calculations; whereas, for the ECP model, the damping was provided by the numerical integration as seen in section 3.2. Thus a ρ_∞ equal to 0.9 (i.e. $\gamma_N=0.55$ and $\beta_N=0.28$) was used, which was proofed in section 3.2 to present a numerical damping (ξ_N) of $6 \cdot 10^{-4}$ with a time step (Δt) of $1 \cdot 10^{-3}$ s. Although it is slightly higher than the one prescribed it is judged to be acceptable for stability reasons.

Concerning the nonlinear soil properties, only the shear modulus (G) and damping (D) curves as a function of the shear strain (γ) were provided. For the P1, only one curve was provided; and for the P2, five curves were given corresponding to different depths. It is important to remark that in other constitutive models these curves do not depend on the confinement pressure; although, this relationship has been evidenced by laboratory tests, e.g. in the work of [Darendeli \(2001\)](#). Therefore, for the ECP model, the soil parameters that define these curves had to be calibrated for smaller sublayers; however, the behavior will be always influenced by the confinement pressure. The other soil parameters required in the ECP model were found by the use of empirical correlations following the methodology defined by [Lopez-Caballero \(2003\)](#) and a set of hypothesis that were necessary due to the lack of information.

Regarding the hypothesis, it was assumed that the soil was a clay (i.e. $b = 0.8$). Therefore, the mean stress ratio between the initial critical state and the actual state (p_{c0}/p) is constant and the overconsolidation ratio (OCR) is equal to unity, i.e. the soil is normally consolidated. As the friction angle at the perfect plasticity (ϕ'_{pp}) was given, the plasticity index (I_p) was found with the correlation given by [Lopez-Caballero \(2003\)](#). The simulated normalized shear modulus (G/G_{max}) and damping (D) curves with respect to the shear strain (γ) at different depths are shown in Figures 3.6 and 3.7 for the two soils, respectively. The reference curves given by the PRENOLIN organizers are shown in solid black lines and the sand ranges presented by [Seed et al. \(1986\)](#) are shown in dashed lines. Most of the reference curves are in the sand ranges for both G/G_{max} and damping; however, for P2 deep layers the curves are stiffer and present less nonlinearity as it to be expected due to the high confinement pressure. It is to be noted that the calibration was focused on the normalized modulus decay while for the damping evolution, high overestimations are present. [Carrilho Gomes et al. \(2015\)](#) introduced in the ECP model an additional parameter to control damping at high strains. In sands, the reduction achieved in damping curves produced no significant influence on the seismic soil response, since the profiles

of maximum shear strain, peak ground acceleration (PGA) at surface and normalized response spectra (PSA) were similar for both the modified and the standard model. For clays, however, a small effect was seen caused by an increase in stiffness. The model parameters of both profiles defined for each soil layer can be found in the appendix A.

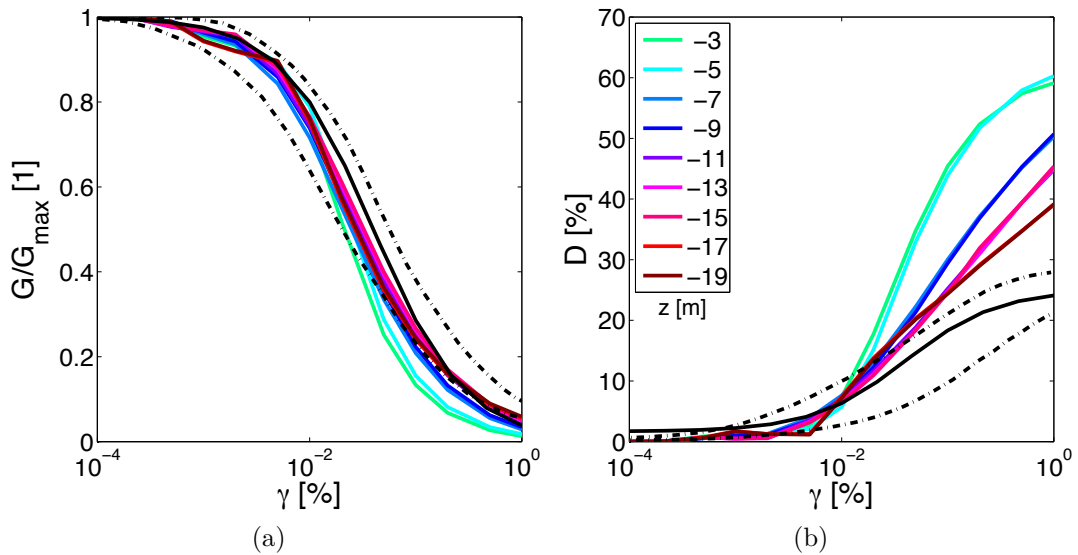


Figure 3.6 – Shear modulus (G) degradation and damping (D) evolution with shear strain (γ) for profile P1. The PRENOLIN reference curves are shown in solid black lines and the ranges by Seed et al. (1986) are shown in dashed lines.

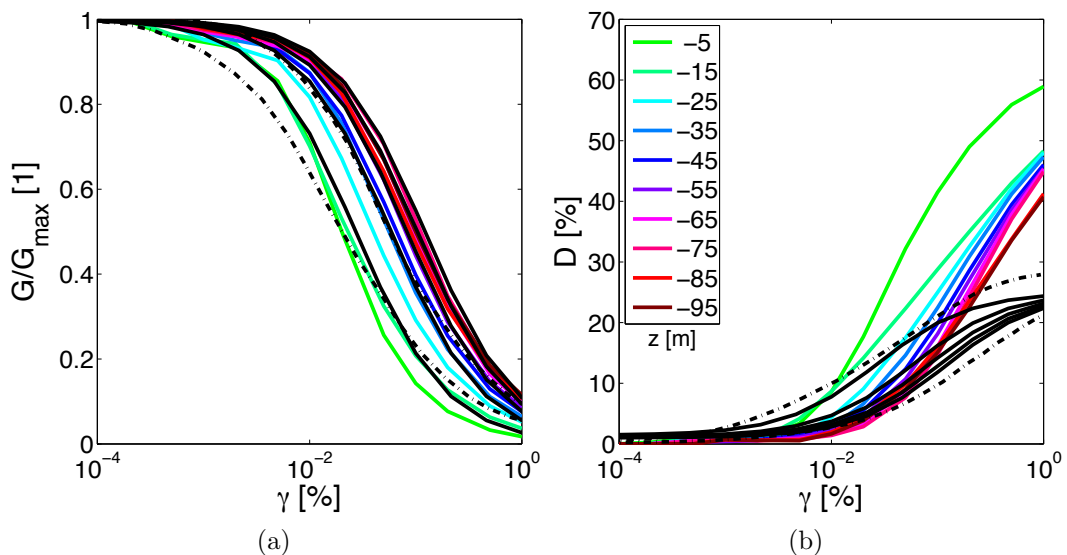


Figure 3.7 – Shear modulus (G) degradation and damping (D) evolution with shear strain (γ) for profile P2. The PRENOLIN reference curves are shown in solid black lines and the ranges by Seed et al. (1986) are shown in dashed lines.

3.4.2 Input motions

The input motions were selected to analyze different aspects of the nonlinear soil behavior. Firstly, two sinusoidal motions shown in Figure 3.8 were tested: (1) A monotonic signal with increasing amplitude and (2) the same motion with an additional linear trend. The first one is intended to analyze the mobilization of large-strain resistance; and the second, the development of permanent deformations. These analyses permit to test the constitutive model. Therefore, the effect of some numerical parameters can be evaluated. In general, the wave propagation and the acceleration amplification is not affected; although the strain evolution at the integration points can be drastically modified.

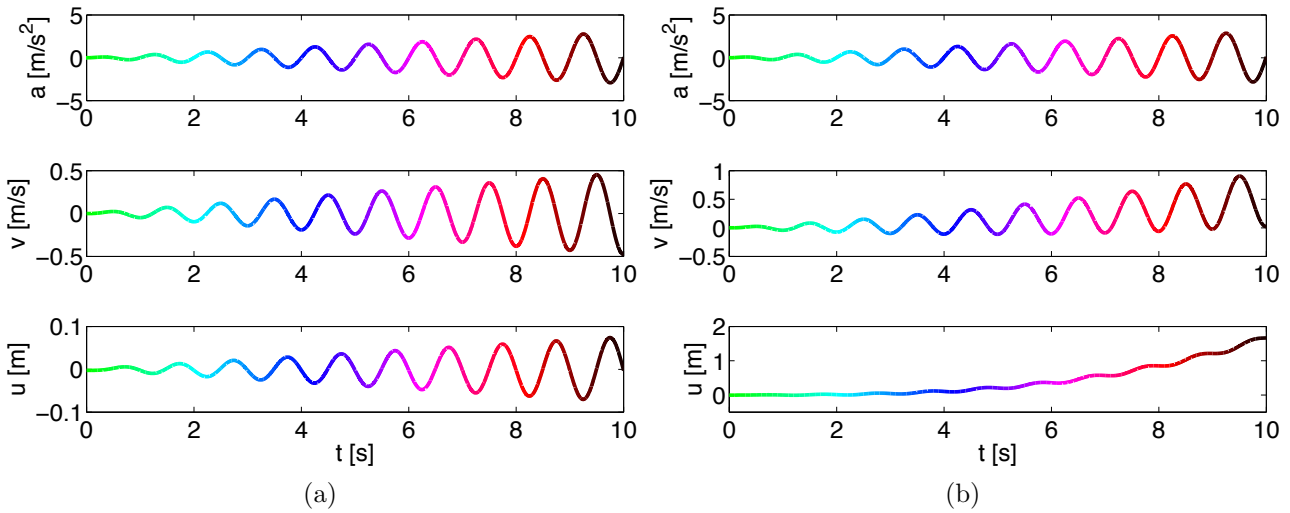


Figure 3.8 – Acceleration, velocity and displacement time histories of the sinusoidal motions a) 1 and b) 2

Additionally, two real motions were tested with different frequency content. In this study, they will be called: real HF (for the one with mostly high frequency content) and real LF (with predominantly amplitudes at low frequencies). Both models were tested with 4 scale factors in order to test different levels of nonlinearity: 1) 0.5 m/s^2 , 2) 2 m/s^2 , 3) 5 m/s^2 and 4) 0.05 m/s^2 (which was added after). The real HF has a magnitude (M_w) of 6.4, with depth (D) of 122 km and epicentral distance (R_e) of 39 km, recorded at the Japanese KiKnet station IWTH15, which has a $V_{s,30}=1200\text{m/s}$. The other motion, real LF, has a M_w of 6.6, D of 10 km and R_e of 20 km; recorded at Flagbjarnarholt (ESMD iceland station). Only the EW component was used for the model. The acceleration, velocity and displacement time histories for both motions are shown in Figure 3.9. The color code will be helpful for the evolution of shear stress-strain curves.

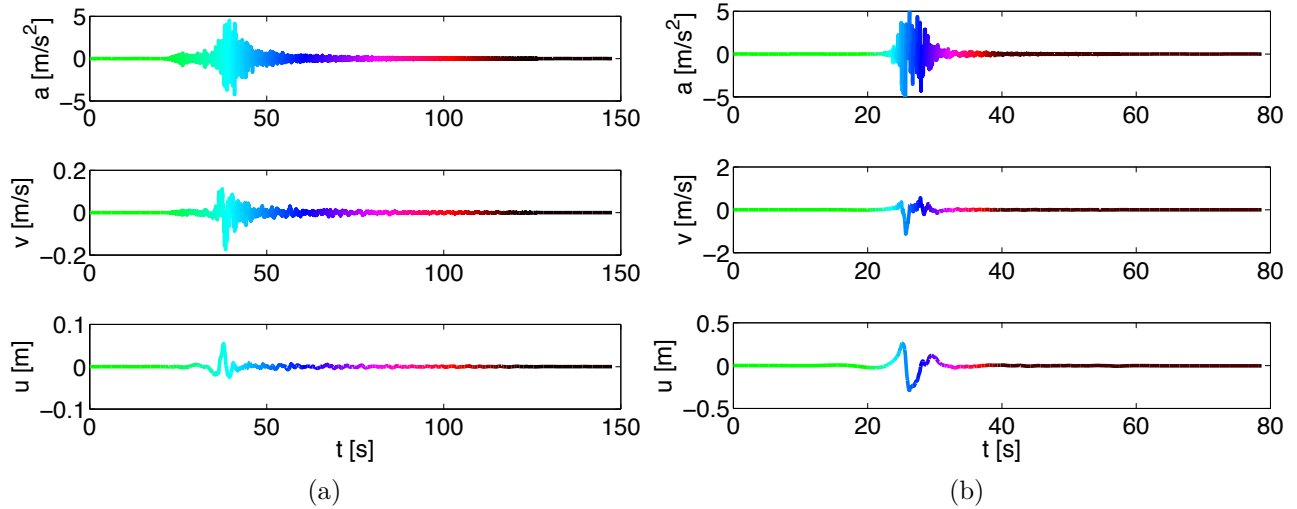


Figure 3.9 – Acceleration, velocity and displacement time histories of the real motions a) HF and b) LF with scale factor 3 (PHA=5m/s²)

3.4.3 Effect of some model parameters

3.4.3.1 Auxiliary shear and bulk moduli

The system of equations to be solved is linearized as a first-order Taylor series and an iterative method is used. It consists of a Newton-Raphson simplified solution in which a corrector for each variable is used to calculate the new approximation. In fact, for each step in time, a number of iterations are performed until the convergence criteria is attained. The simplification consists of using an auxiliary (or initial) matrix for all the iterations; thus, avoiding to recalculate, assemble and triangularize the matrix for each iteration. This technique is useful for coupled analysis and specially for big systems. However, if the auxiliary value is too small, the result can diverge from the first iterations and the evaluation of the constitutive equations can be affected. [Modaressi \(2003\)](#) proposed values of three or five times the real value; although, it was intended for monotonic cases. For the present study, two cases were tested: (a) $G_{aux} = G_{ref}$ and (b) $G_{aux} = 10G_{ref}$ (where G_{ref} is described by equation 3.19). Figure 3.10 shows the shear stress-strain plots at 19m (i.e. near the base) for the profile P1 with elastic bedrock and the sinus 1 motion. As it is seen for the first case, some jumps in the loops evidence a numerical problem. By simply adjusting the auxiliary value, the loops are fixed and the shear behavior seems to follow the Masing rules.

Even though the shear stress-strain plots shown vary greatly; it has a small effect on the obtained displacement and acceleration. The surface displacement time history and acceleration response spectrum are shown in Figure 3.11. As it can be seen, differences are due to high

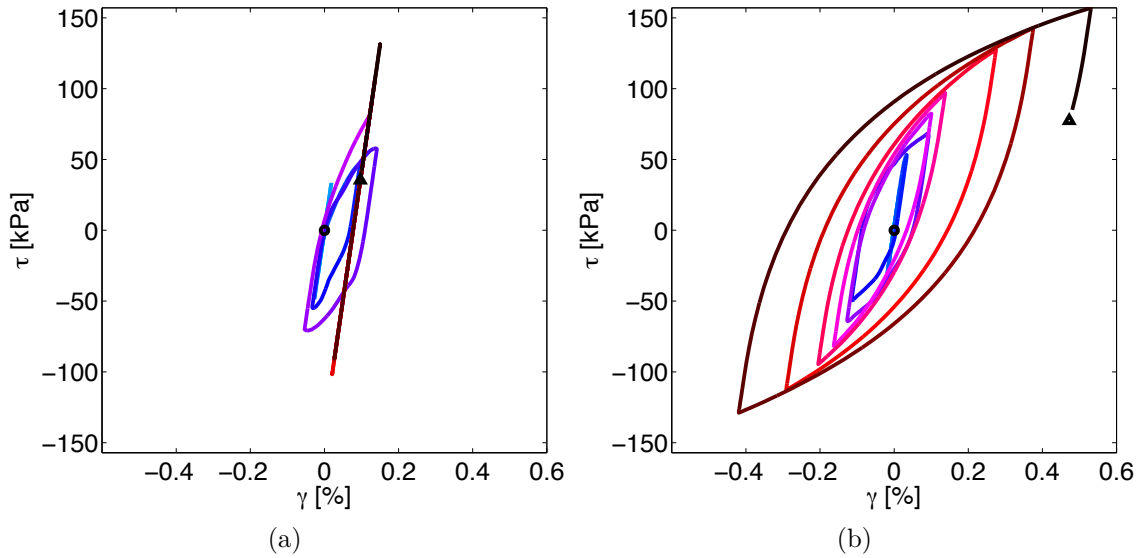


Figure 3.10 – Shear stress-strain plots near the base for the profile P1 with elastic bedrock and the sinus 1 motion: (a) $G_{aux} = G_{ref}$ and (b) $G_{aux} = 10G_{ref}$ at 19m.

frequency peaks presented in the second case and reflected at the higher amplitudes near the end of shaking.

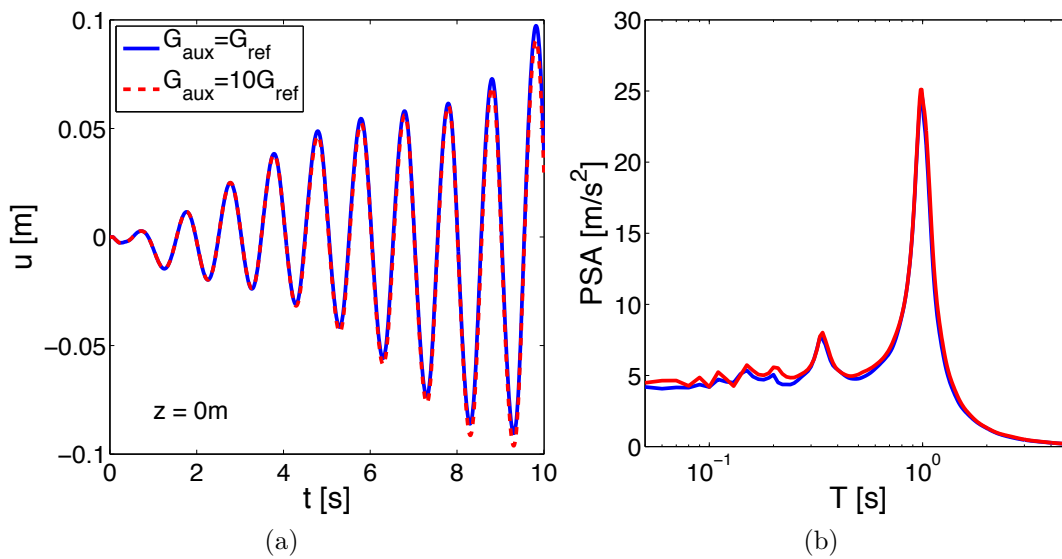


Figure 3.11 – Surface displacement and acceleration for the profile P1 with elastic bedrock and the sinus 1 motion: (a) time history displacement and (b) acceleration response spectrum

The mean and extreme values of the goodness-of-fit criteria proposed by [Anderson \(2004\)](#) are evaluated at the surface for the two cases and are shown in [Figure 3.12](#). The Anderson criteria is a quantitative analysis that consists in comparing ten intensity measures (IM) computed for the two signals in different frequency bands. Refer to [Appendix C.3](#) for further details on these criteria. In [Figure 3.12](#), the bigger the circles, the higher the score. This representation intends

to highlight the best and the worse criteria; although, it lacks the information of the different frequencies. In this case, the lower values correspond to those of the highest frequencies or for the first frequency band (i.e. very low frequencies). One of the IM with the lowest score is the displacement, as it is computed by the double integration of the acceleration time vectors and can introduce non-realistic residuals. If available, the time history of velocity and displacement should be used to evaluate the criteria. In this case, as seen in Figure 3.11a the displacement time histories are very similar. The IM with the lowest score is in this case the Fourier spectra that presented some differences at high frequencies.

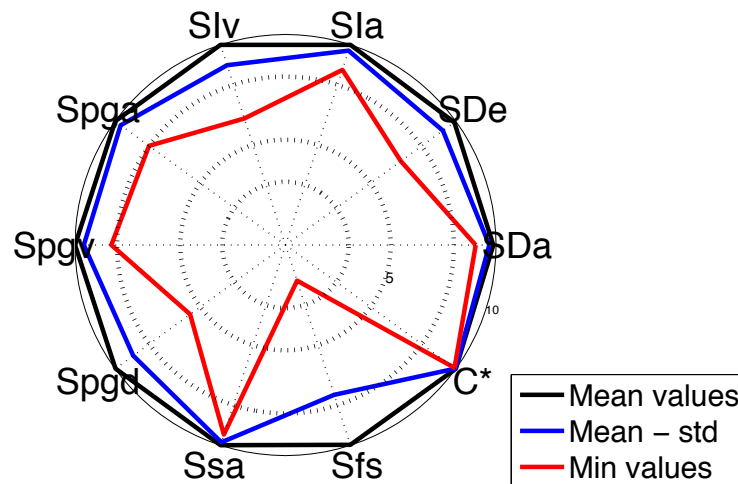


Figure 3.12 – Anderson criteria average mean and extreme values for the surface acceleration of profile P1 with elastic bedrock and the sinus 1 motion in the two cases of auxiliary moduli

3.4.3.2 Error tolerance

The convergence criteria consists of two sets of error tolerances. The first set is called U_{tol} and corresponds to the value of the unknown variables. The second, R_{tol} , fits the inequality given by the right-hand-side (RHS) vector of the linearization. For the present case, the variables are the displacements (\mathbf{u}) and the pressures (\mathbf{p}). These values depend on the auxiliary moduli and the analysis type. In general, the first criterium is easier to attain; while, in some analyses, the second one is not fulfilled. [Modaressi \(2003\)](#) proposed again some values: U_{tol} equal to 10^{-3} and R_{tol} , 10^{-2} . For the present study, the effect of R_{tol} is evaluated. Two values were tested: (a) 10^{-2} and (b) 10^{-3} . For both cases, the auxiliary moduli are ten times the actual one. Some effects of the R_{tol} value can be observed in the shear stress-strain plots and in the high-frequency peak amplitudes on acceleration; although the average solution is not drastically changed. As before, Figure 3.13 shows the shear stress-strain plots at 19m (i.e. near the base)

for the profile P1 with elastic bedrock and the sinus 1 motion. It is noted that both the shear strain and stress are reduced thus the damping is lower.

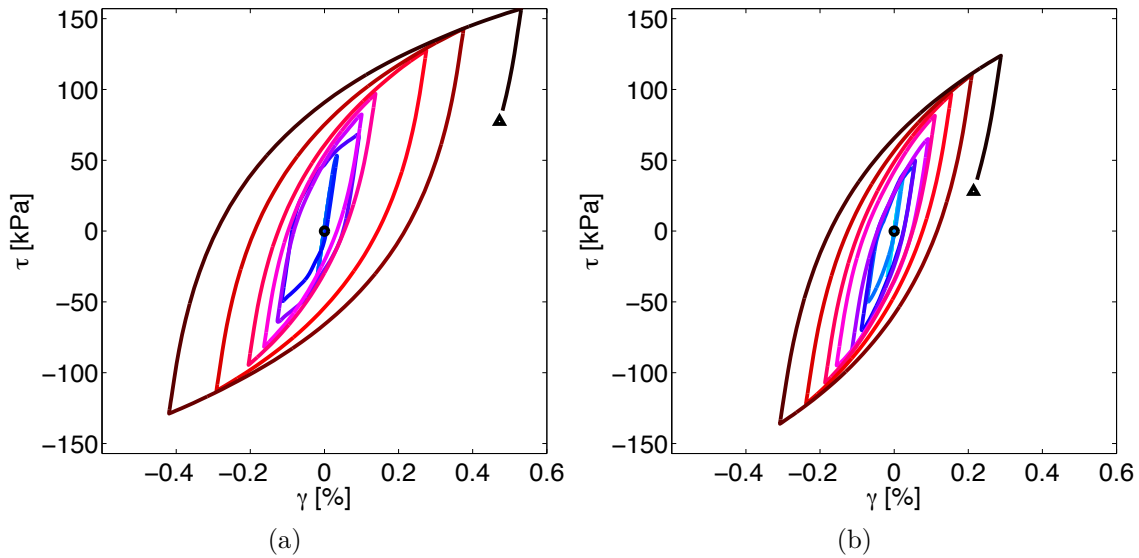


Figure 3.13 – Shear stress-strain plots near the base for the profile P1 with elastic bedrock and the sinus 1 motion: (a) $R_{tol} = 10^{-2}$ and (b) $R_{tol} = 10^{-3}$ at 19m.

Concerning the wave propagation, the surface displacement time history and acceleration spectrum are shown in Figure 3.14. The high frequency peaks presented for the response spectrum with $R_{tol} = 10^{-2}$ have been smoothed out. Though their existence was a problem of error tolerance on the analysis. Concerning, the displacement time history only a slight difference can be identified at the end of the motion.

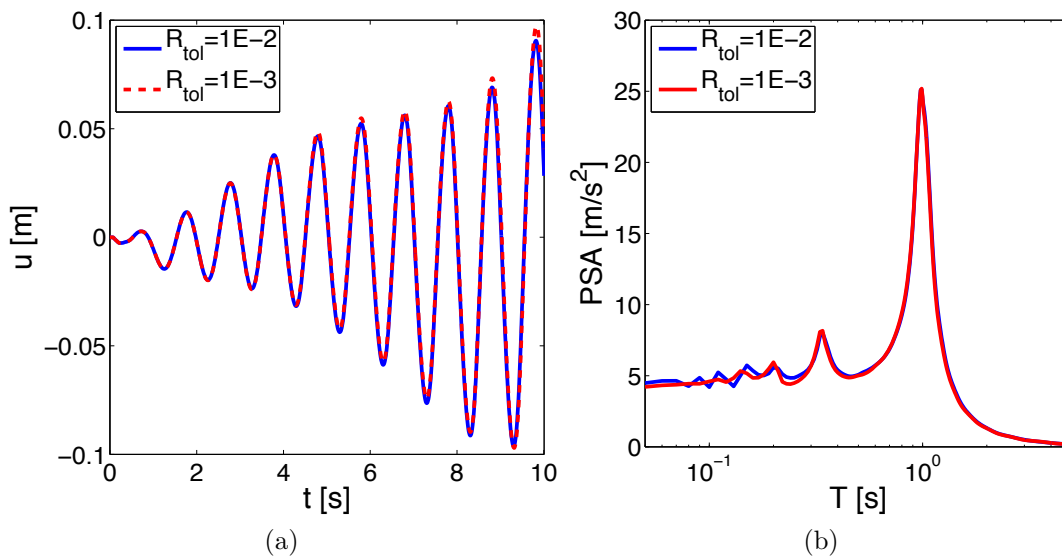


Figure 3.14 – Wave propagation for the profile P1 with elastic bedrock and the sinus 1 motion: (a) surface displacement time history and (b) acceleration response spectrum

It is important to highlight that these results depend on the input parameters: the discretization in time and space, the input motion and the soil model parameters. Hence, the sensibility of these parameters on the global response will vary in other cases.

3.4.3.3 Boundary conditions

Lateral boundaries

Concerning lateral boundary conditions, as the signal propagation is one-dimensional and as the response of an infinite semi-space is modeled, equivalent boundaries have been imposed on the lateral nodes (i.e. the displacements of nodes at the same depth in two opposite sides are the same in all directions and if 1D columns are used - and only one element is used in the horizontal direction- the normal stress on these boundaries remains constant) (Lopez-Caballero and Modaressi, 2011b). As the lateral limits of the problem are considered to be far enough from the structure in the middle of the model, periodic conditions are verified.

Bedrock's boundaries

For the bedrock's boundary, the pore pressure conditions are assumed to be impervious. Therefore, no flux occurs across the interface boundary between the studied domain and the underlying semi-infinite space. Concerning the mechanical conditions, three approaches will be analyzed in this section: rigid, elastic and borehole. The former is relative to the bedrock, hence displacements and forces are relative to those at the input as a uniform excitation. This condition is used to model vibrating tables or centrifuge tests, as the base is infinitely rigid compared to the soil deposit. Thus, the very strong mechanical characteristics bind the total motion to be the incident plus the reflected wave; which is what is normally registered at surface stations under rock conditions (i.e. outcropping bedrock). As the motion on the overlying bedrock is equal to that of the outcropping bedrock, the response on the deposit is given as relative to the input motion (\mathbf{a}_{rel}). Hence, the acceleration at a depth z is given by: $\mathbf{a}(z) = \mathbf{a}_{rel}(z) + \mathbf{a}_{out}$, where $\mathbf{a}_{out}(z)$ is the outcropping motion.

On the other hand, the elastic bedrock is modeled with paraxial elements simulating “deformable unbounded elastic bedrock” (Modaressi and Benzenati, 1994). This condition, often called absorbing boundaries, is used when the deformability and the transient evolution of the motion have to be taken into account. As an unbounded medium is simulated, the obtained

movement at the bedrock is composed of only the incident waves while no input from the infinite domain exist. The paraxial elements efficiently evacuate outgoing (diffracting) waves in a local domain. Additionally, they introduce the vertically incident shear waves, defined at the outcropping bedrock, after deconvolution. This type of bedrock will be used in the model analyzed in chapters 4 and 5. The rigid and borehole conditions will be only used in this chapter and precisely in section 3.5.

Although the wave propagation and the equations that describe it have already been addressed in section 2.2, the system will be rewritten in other terms in order to properly define the equivalent response for the borehole boundaries. The schema shown in Figure 3.15 is taken as reference. According to Bielak and Christiano (1984); Bielak et al. (2003), the problem consists

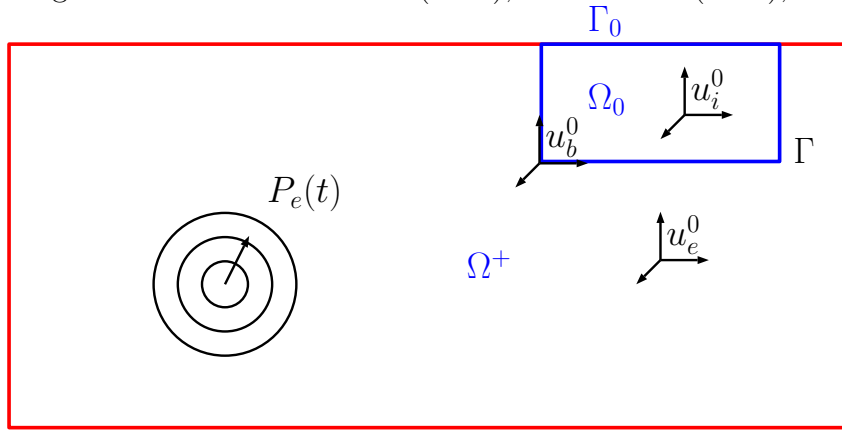


Figure 3.15 – Model of equivalent response for borehole boundaries (inspired by the Domain Reduction Model by Bielak et al., 2003)

in determining the scattered wave (\mathbf{u}) and the total stress tensor ($\boldsymbol{\sigma}$) in Ω_0 and Ω^+ due to a driving field \mathbf{u}^0 , satisfying a suitable radiation condition at infinity such that :

$$\operatorname{div} \boldsymbol{\sigma} - \rho \cdot \ddot{\mathbf{u}} = \mathbf{0} \quad \text{in } \Omega_0 \cup \Omega^+ \quad (3.52)$$

$$\boldsymbol{\sigma} = \lambda \cdot (\operatorname{Tr} \cdot \boldsymbol{\varepsilon}) \cdot \mathbf{I} + 2\mu \cdot \boldsymbol{\varepsilon} \quad (3.53)$$

$$\boldsymbol{\sigma} \cdot \mathbf{n} = \mathbf{0} \quad \text{in } \Gamma_0 \quad (3.54)$$

$$\mathbf{u}(0) = \mathbf{0} = \dot{\mathbf{u}}(0) \quad \text{in } \Omega^+ \quad (3.55)$$

$$\mathbf{u}^- = \mathbf{u}^+ + \mathbf{u}^0 \quad \text{in } \Gamma \quad (3.56)$$

$$\boldsymbol{\sigma}^- \cdot \mathbf{n} = \boldsymbol{\sigma}^+ \cdot \mathbf{n} + \boldsymbol{\sigma}^0 \cdot \mathbf{n} \quad \text{in } \Gamma \quad (3.57)$$

In this case, the driving field (\mathbf{u}^0) consists of an incoming wave defined in all of Ω plus its reflection from the free surface. As long as the relative motion (\mathbf{u}) satisfies the preceding

set of equations, it is also applicable for problems where \mathbf{u}^0 and $\boldsymbol{\sigma}^0$ are related by a nonlinear constitutive equation. Considering the 1D wave propagation, the incident SH-wave of unit amplitude can be defined at the bottom of a soil deposit of depth H by:

$$w^i = \exp(i \cdot [\omega t - k_L \cdot H]) \quad (3.58)$$

where ω is the excitation frequency and $k_L = \omega/V_s$ is the wave number of layer L . The radiation condition for this problem simply states that, in Ω_L , $w^t - w^i$ must consist of outgoing waves only. Hence a solution of equation 3.58 at interface Ω_L is given by:

$$w^t = \frac{2 \cdot \cos(k_N \cdot H) \cdot \exp(i(\omega t + k_L H))}{\cos(k_N \cdot H) + i \cdot \alpha_z \cdot \sin(k_N \cdot H)} \quad (3.59)$$

Recall that α_z is the inverse of the impedance ratio (I) and is defined as $\alpha_z = 1/I = (V_{sN} \cdot \rho_N)/(V_{sL} \cdot \rho_L)$. When the bedrock is infinitely rigid with respect to the soil deposit, $V_{sL} \gg V_{sN}$ hence $\alpha_z \approx 0$. Regarding equation 3.59, the second part of the denominator can then be neglected and the cosines cancel out, resulting in two times the equation 3.58. In other words, the amplitude of the total wave will be twice the incident wave as it will be in an outcropping recording. The difference in this case is that the absorbing boundary then needs only to satisfy a radiation condition for the incompatible outgoing waves. Hence, the motion arriving from any given location may be specified in the interface of the computation region (Γ) rather than through an artificial boundary outside the model (Bielak et al., 2003).

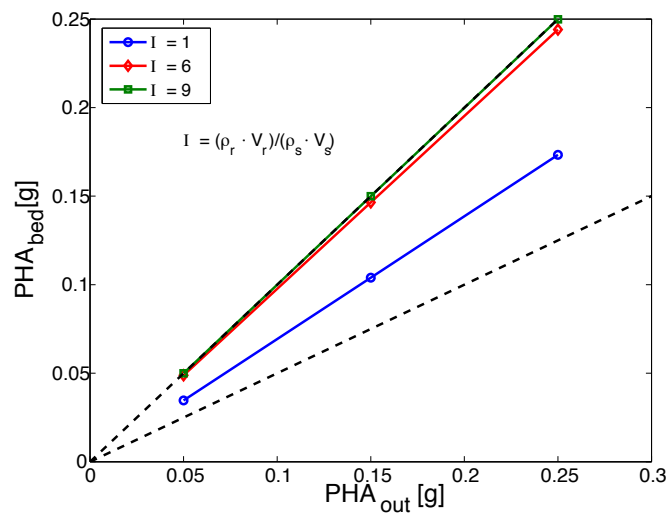


Figure 3.16 – Comparison between PHA at the bedrock and at the outcropping as a function of the impedance ratio

It is clear that if the same outcropping motion is used and only the boundary conditions

are modified, the soil response is different. As an example, the three boundary conditions were used for the P1 profile and for the real 0 LF motion. The response of elastic and nonlinear soil behavior is shown in the following Figures 3.17 and 3.18. Concerning the maximum acceleration profile, Figure 3.17 shows a gradual amplification with wave propagation for the elastic case, as was seen in section 2.2; in contrast, nonlinearity produces peaks of acceleration and deamplifications at different depths. Although these profiles show some discrepancies between the three boundaries, the pseudo spectra of acceleration at surface (PSA) is only slightly modified between the elastic and the borehole conditions, as shown in Figure 3.18.

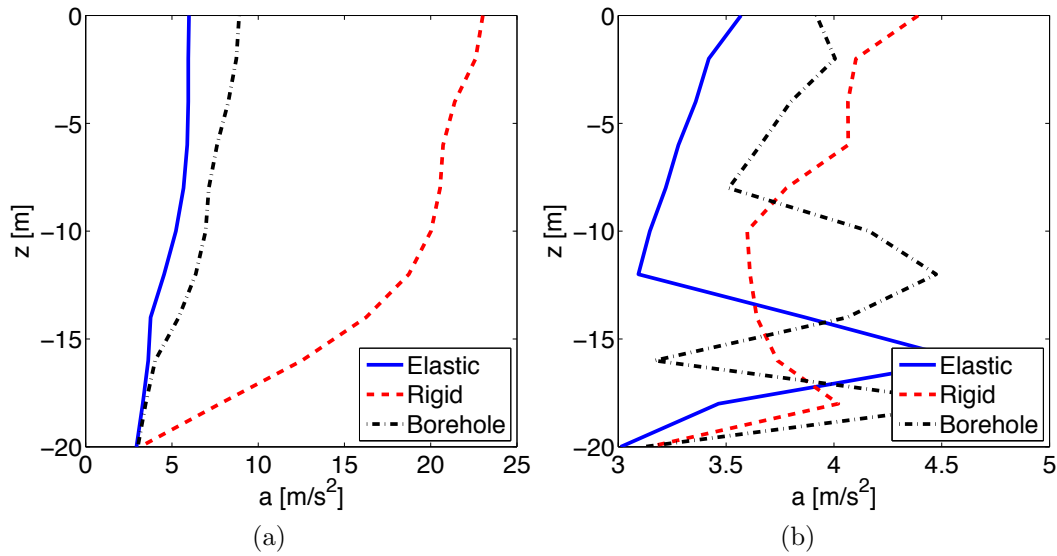


Figure 3.17 – Maximum acceleration profile for the P1 and the real 0 LF motion with (a) an elastic and (b) a nonlinear behavior

3.4.3.4 Gradient moduli: effect of n_e

The P2 profile, as said earlier, has a gradient shear-wave velocity (V_s) with depth. Hence the shear and bulk modulus too. This gradient can be related to the confinement stress with an exponential function like the following:

$$K_{max} = K_{ref} \left(\frac{p'}{p'_{ref}} \right)^{n_e} \quad \text{and} \quad G_{max} = G_{ref} \left(\frac{p'}{p'_{ref}} \right)^{n_e} \quad (3.60)$$

where K_{max} and G_{max} are the moduli at the effective mean stress (p') and are described by a reference (K_{ref} and G_{ref} evaluated at p'_{ref}) and an exponential value n_e . When this value is zero, the moduli will have no dependence on stress.

Results of geophysics test and inversions are commonly expressed by layers of non-dependent

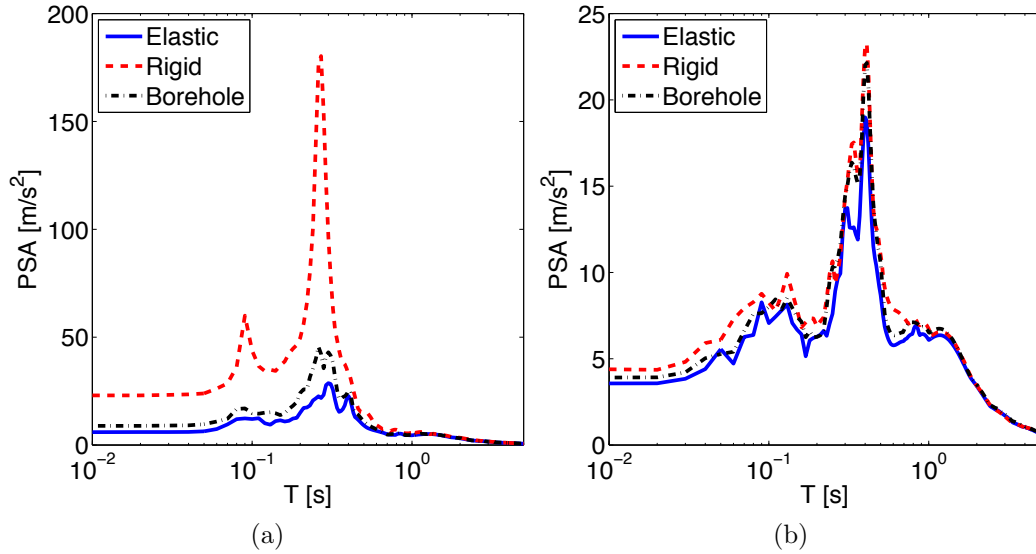


Figure 3.18 – Pseudo spectra of acceleration at surface (PSA) with (a) an elastic and (b) a nonlinear behavior

moduli (i.e. $n_e = 0$) that increase with depth as steps with jumps between values. Hence many site-specific-analysis programs are not capable of relating the moduli with stress in a continuous matter. In order to verify the same non linear computations, within the scope of the PRENOLIN benchmark, the effect of considering these steps rather than the gradient curve is evaluated for the P2 profile. As the number of steps increases, the two approaches should present less differences. Thus, a very small distance between steps is used (i.e. 1m per step) and a regression analysis was performed to find one pair of values for G_{ref} and n_e that best fit the profile with p'_{ref} constant. It is important to remark that, even though the maximum moduli will not change with depth in each step; its degradation due to shear strain will depend on stress. The V_s profile for both cases is shown in Figure 3.19.

The profile of maximum acceleration is shown in Figure 3.20 for motion real 1 HF with elastic and rigid base. Interestingly, the differences are negligible for the former case; however, they increase when a rigid base is used. For this case, the multilayer profile presents, in general, much higher accelerations at depth and its evolution is less smooth. This could be due to the differences in the evolution of nonlinearity and shear modulus degradation in each of the layers that would cause an increase in the impedance ratio between the layers and the amplification of the acceleration.

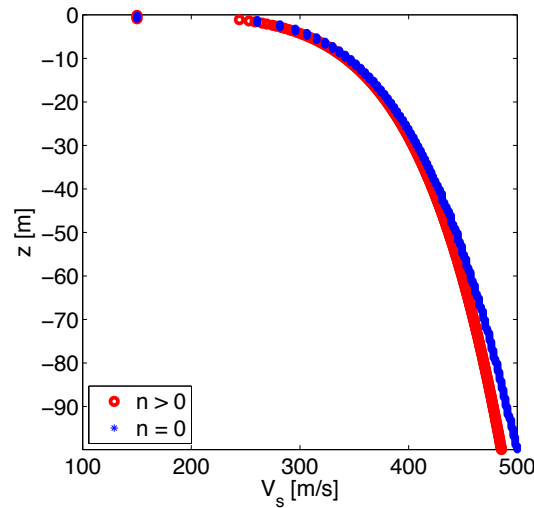


Figure 3.19 – Shear-wave velocity (V_s) profile for P2 with different n values

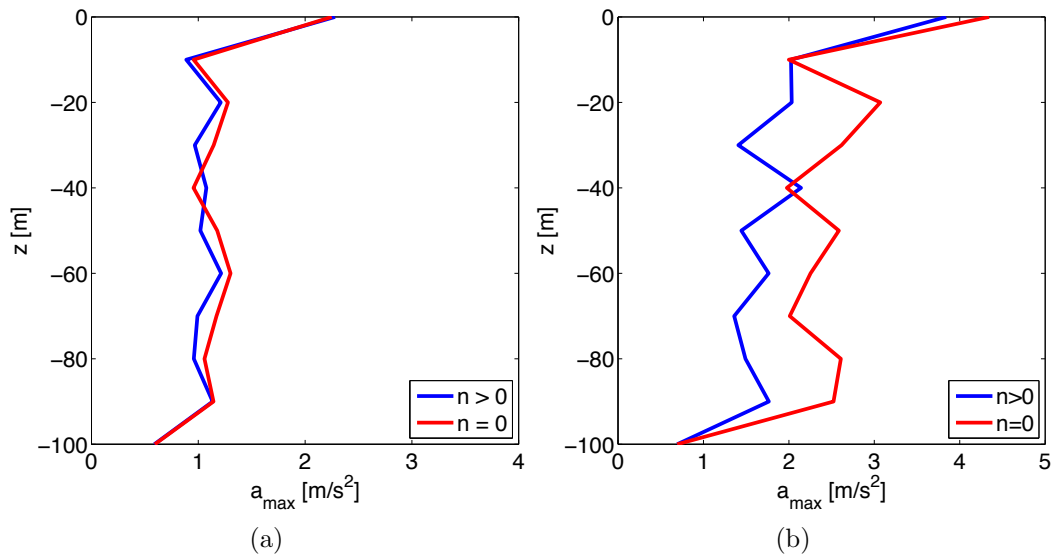


Figure 3.20 – Maximum acceleration profile for the P2 with the real 1 HF for a) elastic and b) rigid base

3.5 Numerical model validation

In present, a variety of surface and borehole pair recordings from downhole arrays are available. For instance, the Kiban-Kyoshin Network (KiK-net), in Japan, is composed of 688 stations with high-quality surface and downhole digital 3-component accelerometers. While the stations are located in a variety of site conditions (i.e. $200 < V_{s,30} < 800$); in most, only velocity profiles obtained from downhole PS logging measurements are available. Additionally, most of the borehole stations are located at depths higher than 100 m which will add more complexity to the model. Furthermore, even if a large database is available; only a small fraction are strong ground motions, e.g. from more than 46000 recordings between 1996 to 2009, only 370 (i.e.

less than 1%) had a PGA above $0.5\text{m}/\text{s}^2$ at borehole (Regnier, 2013). In fact, there are limited available and complete vertical array data for the validation of nonlinear soil behavior in 1D wave propagation. Additionally, for a successful validation of nonlinear soil behavior a series of conditions have to be present in order to be appropriate for the model simplifications.

As part of the international benchmark PRENOLIN, three Japanese sites were chosen for the validation of the numerical model. The selection criteria were in part followed from the work of Regnier (2013). The input motion selection was done by the organizers of the benchmark PRENOLIN. Laboratory tests and *in-situ* measurements were performed to properly characterize the soil deposit. Lastly, the adjustments of the site profile by transfer function inversion was performed by the PRENOLIN organizers.

The basic assumptions for these sites were:

- waves essentially propagating vertically;
- 1D soil configuration is possible, i.e. no lateral velocity variations;
- evidence of strong nonlinearity;
- existence of strong ground motion recordings;
- low probability of liquefaction nor cyclic mobility in the area.

Two sites were taken from the Port and Airport Research Institute (PARI) and are called Sendai and Onohama. The latter was rejected as the site characterization evidenced a high spatial variability of soil parameters and therefore violated the second of the basic assumptions previously stated. The other site corresponds to the KiK-net station KSRH10. In this study, results will be shown only for the PARI station Sendai because at the time of writing the other sites were not fully analyzed.

In the following, the site properties and model parameters will be presented. Afterwards, the input motions recorded and calculated with the ECP model will be compared and the evolution of nonlinearity will be shown.

3.5.1 PARI Sendai

P1 is a shallow stiff site of 7m of fine sand with slightly gradient V_s profile followed by rock. The borehole is at 10.4m depth and the water-table is placed at 1.45m. After the soil characterization, 2 layers were identified. The first 3m are considered as moderated compacted sand

with a density (ρ) of 1850kg/m^3 ; followed by 4m of stiffer sand ($\rho=1890\text{kg/m}^3$). The shear wave velocity (V_s) profile and the theoretical transfer function between surface and borehole are shown in Figure 3.21.

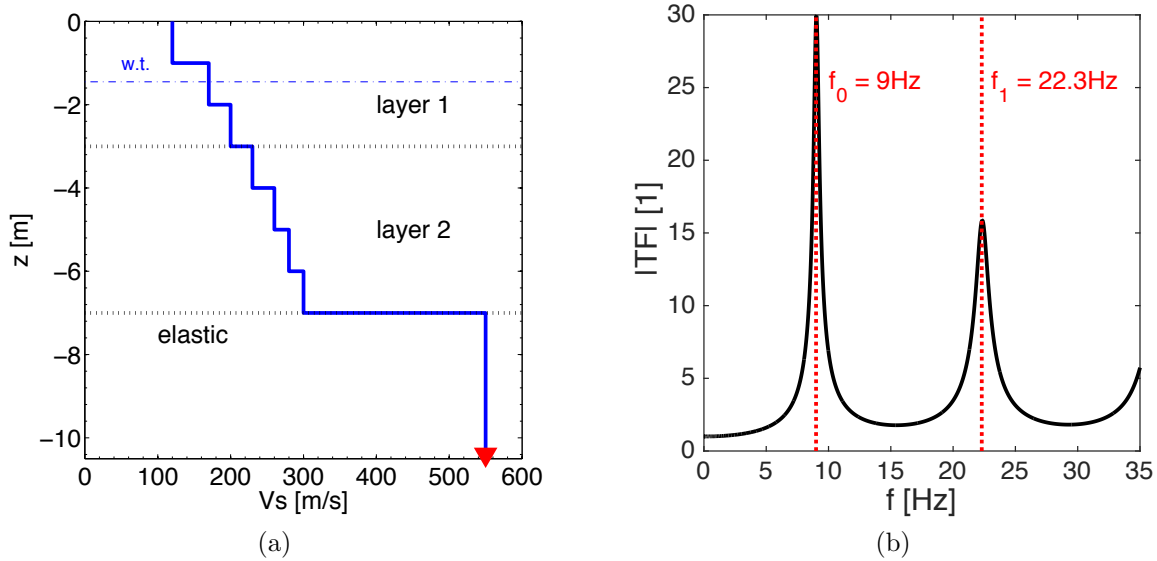


Figure 3.21 – Elastic properties: a) Shear wave velocity (V_s) profile and b) Transfer Function for Profile P1 - Validation

As the soil is assumed to be horizontally homogeneous, a 2D finite element computation with plane-strain assumption was performed. The soil was modeled using quadrilateral isoparametric elements with nine integration points per element. The width of the elements is 1m and the thickness is 0.25m, which is in agreement with the suggestions made by Foerster and Modaressi (2007a) to prevent numerical dispersion for strong ground motions. For a maximum frequency of 25Hz (of engineering interest in this study) and a minimum initial V_s of 120m/s (at the surface), a minimum of 38 points per wavelength is allowed in the elastic domain. The number of points is high, although it will decrease as the soil softens and the V_s decreases. As in the previous models, the time step (Δt) is $1 \cdot 10^{-3}\text{s}$ and a dissipative Newmark integration scheme is used with ρ_∞ equal to 0.9 (i.e. $\gamma_N=0.55$ and $\beta_N=0.28$).

Concerning the lateral boundary conditions, equivalent - or periodic - boundaries have been imposed on the lateral nodes. These conditions are valid because the response of an infinite semi-space is modeled and is assumed that the wave propagation is purely one-dimensional and vertical. Also referred as tied-nodes, they consist in linking the nodes at opposite sides at the same depth to constant horizontal stress and equal displacements in all directions. For the bedrock's boundary, the borehole condition described above is used. Different impedance ratios were tested in order to confirm that the motion at the bottom of the model was the

same as the recorded at borehole. Lastly, as the *in-situ* measurements attested that the soil above 1.45m was saturated a special condition was used for the numerical modeling. Thus, the mass of the water was taken into account for the correct calculation of the initial effective stress state, however, as one of the constraints of the PRENOLIN project, no excess pore-pressure generation (Δp_w) was allowed. The GEFDyn model was therefore used by decoupling Δp_w of the soil deformation as if the soil would be fully drained. This kind of analysis will be called DPD and will be further explained in chapter 4.

3.5.2 Model parameters

Each layer had a set of shear degradation and damping curves -known as the nonlinearity curves-, hence 2 sets of model parameters were calibrated. Besides these curves and the elasticity parameters, no other information was given concerning the other parameters for soil characterization. The ECP model parameters for each layer can be found in appendix A. The nonlinearity curves are presented for P1 at each meter in Figure 3.22, the given curves are shown in black. As it can be noted, the damping at large strains is overpredicted; although focus was given to calibrate mostly the shear degradation at low and moderate shear strains.

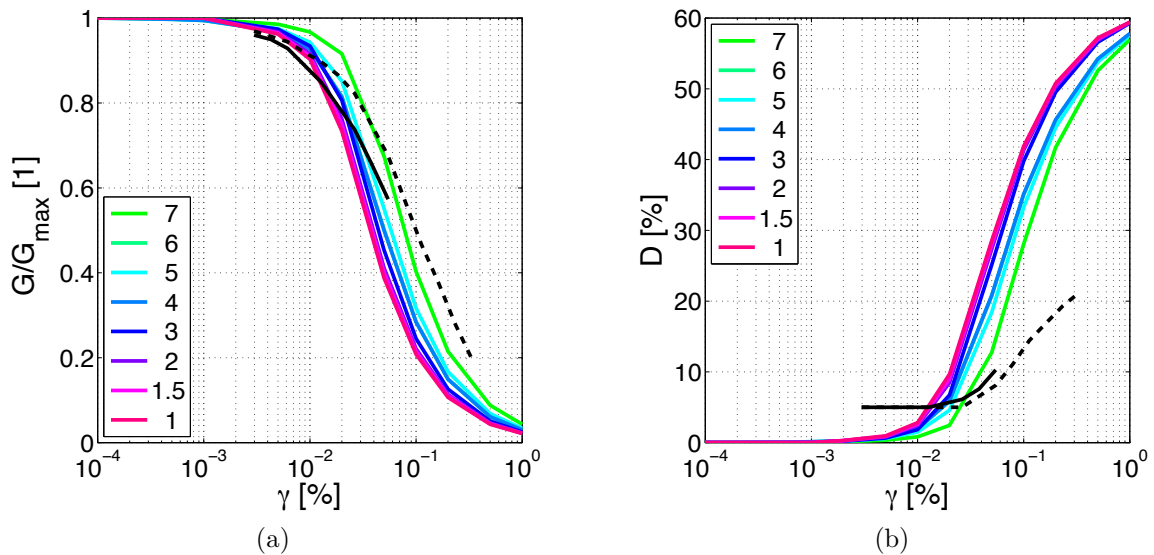


Figure 3.22 – Shear modulus (G) degradation and damping (D) evolution with shear strain (γ)

3.5.3 Input motions

The input motions correspond to the borehole recordings. Three time series (TS) with different frequency contents were selected for each of the 3 levels of peak horizontal acceleration at

TS	M_w	R [km]	PHA [m/s ²]	PGV [cm/s]	I_A [m/s]	D_{5-95} [s]	CAV_5 [m/s]	f_c [Hz]
1	9.0	162.7	2.46	16.50	1.204	100	20.9	5.9
2	7.1	81.3	0.62	3.93	0.074	23	2.33	6.9
3	6.4	19.1	0.61	2.50	0.032	12	0.99	8.5
4	6.8	169.4	0.25	2.13	0.011	26	0.48	5.1
5	5.9	96.4	0.25	1.63	0.003	8	0.14	5.7
6	7.2	83.4	0.35	2.47	0.015	26	0.64	4.6
7	5.9	94.7	0.12	0.66	0.001	15	0.034	5.7
8	6.4	208	0.05	0.34	3e-4	18	0.001	2.5
9	5.8	175.9	0.03	0.22	2e-4	19	1e-4	4.6

Table 3.4 – Input motion parameters for SENDAI - Validation - EW component recorded at borehole

borehole: (1) $PHA > 0.6 \text{ m/s}^2$, $0.2 < PHA < 0.4 \text{ m/s}^2$ and $PHA < 0.15 \text{ m/s}^2$. Some of the input motion parameters are shown in Table 3.4 and correspond to the EW component of the borehole recordings. The moment magnitude (M_w) and the epicentral distance (R) were reported by the PRENOLIN organizers. As it can be observed, in each acceleration level, the motions have different central frequencies (f_c). Note that all have f_c below the fundamental site frequency ($f_0=9\text{Hz}$), but TS 3 value is very near to it and could have caused some resonance. The first input motion corresponds to the 2011 Tohoku earthquake and is almost six times stronger than the second one, with respect to PHA. Unfortunately, no other input motion with high acceleration was recorded that fitted the criteria; hence, only strong nonlinearity could be analyzed for TS 1.

Figure 3.23 shows the acceleration response spectra of the EW component motion recorded at borehole. It is interesting to note that while the peak acceleration (shown for minimum period - $T=0.01\text{s}$) is decreasing with the input motions, the frequency content varies for each motion. For instance, TS 2 and TS 3 have similar PHA values but the latter has less energy in higher periods (or lower frequencies). Additionally, TS 8, which has the highest epicentral distance has most of the energy concentrated at high periods and presented the lowest f_c .

3.5.4 Comparison between recorded and numerical results

Given the complexity of the seismic signals, different parameters with respect to amplitude, frequency content, duration and energy could be analyzed; however, in this study only some examples will be given. First, individual cases of acceleration time histories, Fourier and response spectra will be shown for TS 1, 6 and 9, one of each amplitude level. Then, a summary

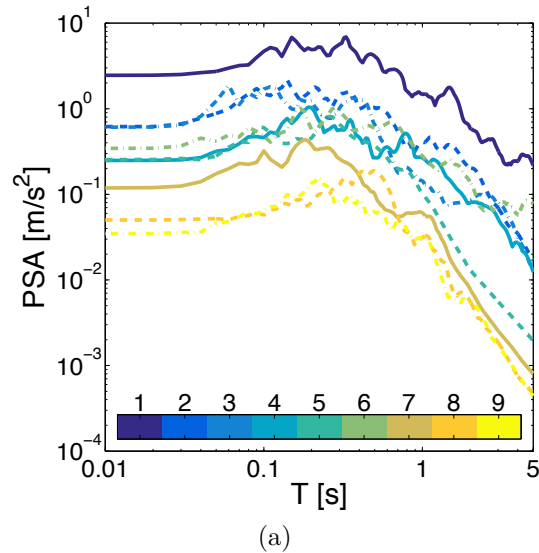


Figure 3.23 – Acceleration spectra of the input motions - Validation - EW component recorded at borehole

of the peak acceleration and the Anderson criteria will follow. The surface acceleration time history for TS 1, 6 and 9 is shown in Figure 3.24. Real recorded and numerical results show very good agreement at almost all instants, except for the peak value overestimated for TS 1, and some amplitudes for TS 9. As the motions are long and the frequency content is difficult to observe in these figures, other representations are needed.

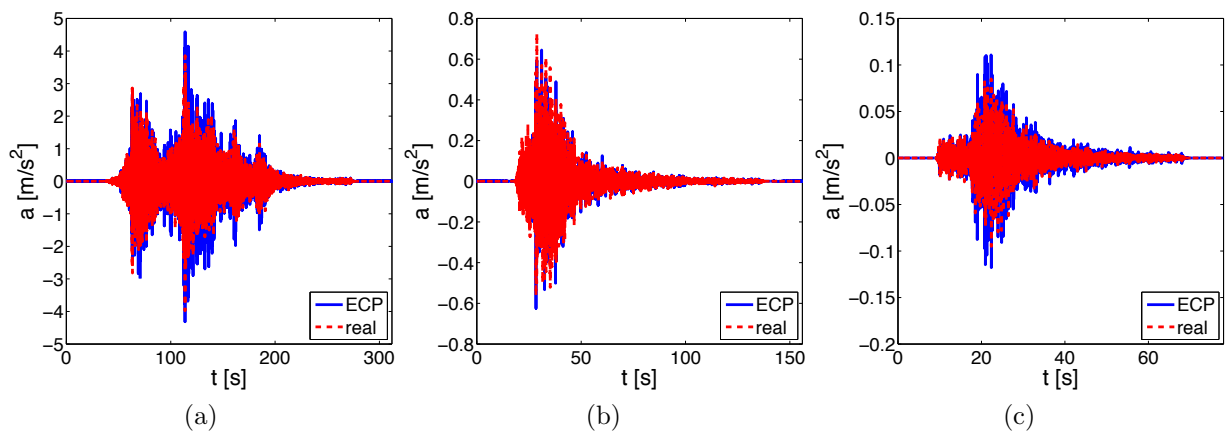


Figure 3.24 – Surface acceleration time history for a) TS 1, b) TS 6 and c) TS 9. EW component.

The response spectra of the surface acceleration and the transfer function for TS 1, 6 and 9 are shown in Figures 3.25 and 3.26, respectively. All present fair agreements between the recorded and the modeled motion, specially at low frequencies. Concerning TS 1, a higher deamplification and a greater shift to low frequencies can be observed in the recordings. Even though this motion had a high PHA value, the nonlinearity evidenced in both the recordings

and the modeled response was low. Still, the model response presented even lower nonlinearity. Moreover at high frequencies ($f > 15\text{Hz}$) another peak in the Transfer function is evidenced, specially for TS 9. For the latter, the amplification is also overestimated.

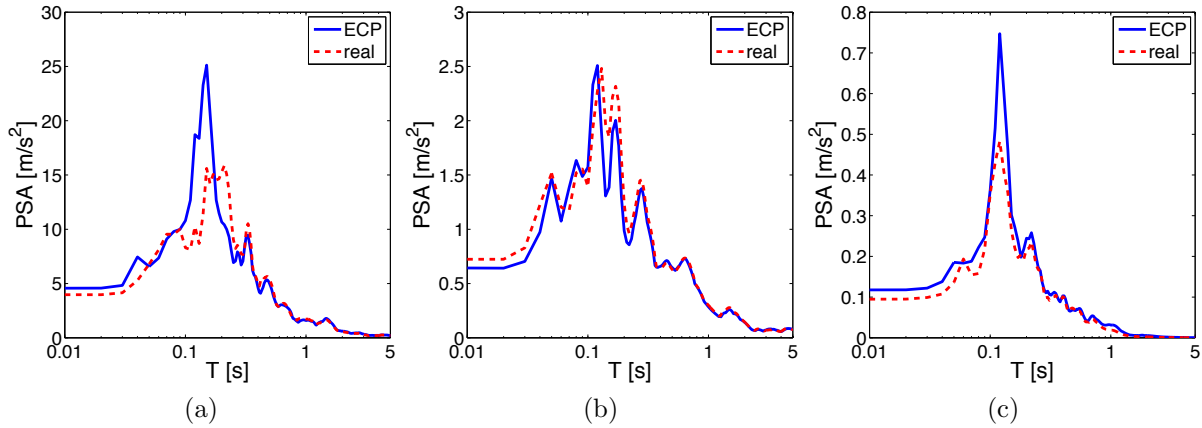


Figure 3.25 – Surface acceleration spectra for a) TS 1, b) TS 6 and c) TS 9. EW component.

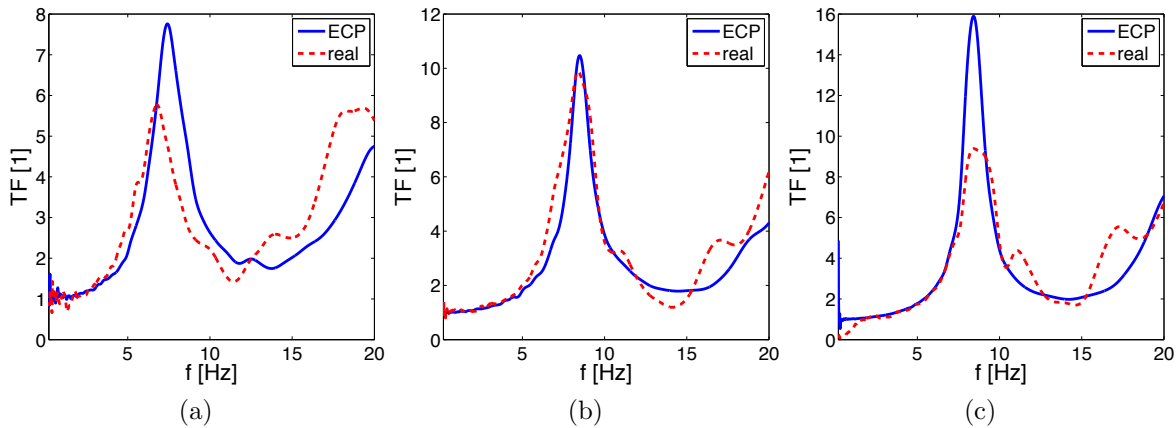


Figure 3.26 – Transfer function between surface and recorded borehole acceleration for a) TS 1, b) TS 6 and c) TS 9. EW component.

The relationship between the maximum acceleration at surface (PGA) and at borehole (PHA) is shown in Figure 3.27a for the real recordings and for the numerical model. For most of the motions, the numerical results match well the measured ones. For TS 1, Tohoku motion, the differences are more important but while for the EW component, the real recordings evidence more nonlinearity than that observed in the model, for the NS component, the response is inverted. However, the analysis of only the maximum acceleration is very limited as it does not account for other aspects of the input motion, as for example the frequency content and energy duration. Hence the goodness-of-fit criteria defined by Anderson (2004) was applied to the nine motions and each horizontal component recorded and modeled at the surface. Details of this

criteria are provided in Appendix C. Results are shown in Figure 3.27b as a function of PHA. Two values are presented: the average of all frequency bands -known as S1 - and the average of a low pass frequency band ($0.05 < f < 15\text{Hz}$) - S2. In general, all time series presented good similarity, even TS 1. Regarding S1, it seems that the match is better for stronger motions; while for S2 values there appears to be no dependency with PHA.

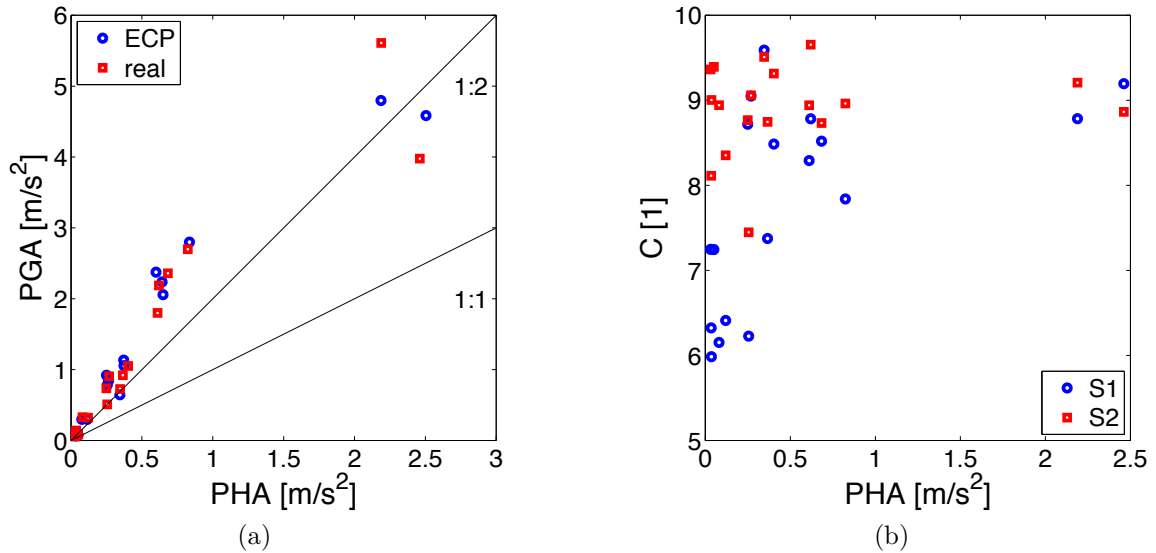


Figure 3.27 – Summary for NS and EW components of all input motions: a) Peak ground acceleration (PGA) as a function of peak horizontal acceleration at borehole (PHA) and b) Anderson criteria for surface acceleration (mean of all frequency bands and mean for frequencies between 0.05 and 15Hz)

Figure 3.28 shows the average values of each Anderson criteria. Concerning both averages : S1, mean of all frequency bands, shown in Figure 3.28a, and S2, mean for frequencies between 0.05 and 15Hz, shown in Figure 3.28b, the least similar parameter is the Fourier spectra; however, for the S1 value, other parameters, such as the Response Spectra (S_a), the peak values (PGA and PGD) and the intensities (I_A and I_V) presented also smaller values for the weakest motions (i.e. TS 7, 8, 9) and TS 5.

Differences in the weak motions are principally presented for low frequencies and therefore results are better without comparing these frequencies. For example, Figures 3.29a and 3.29b show the values for each frequency band for the similarity in PGA and I_A , respectively. Both criteria present zero values in the low frequencies for almost all motions, except for motions 1 and 6 where there is still energy (as shown in the response spectra of Figure 3.23). Except for TS 5 where other causes of error are identified, the level of similarity is very good for frequencies above 1Hz. Possible causes of differences can be the non-verticality and the component orientation not taken into account in the model.

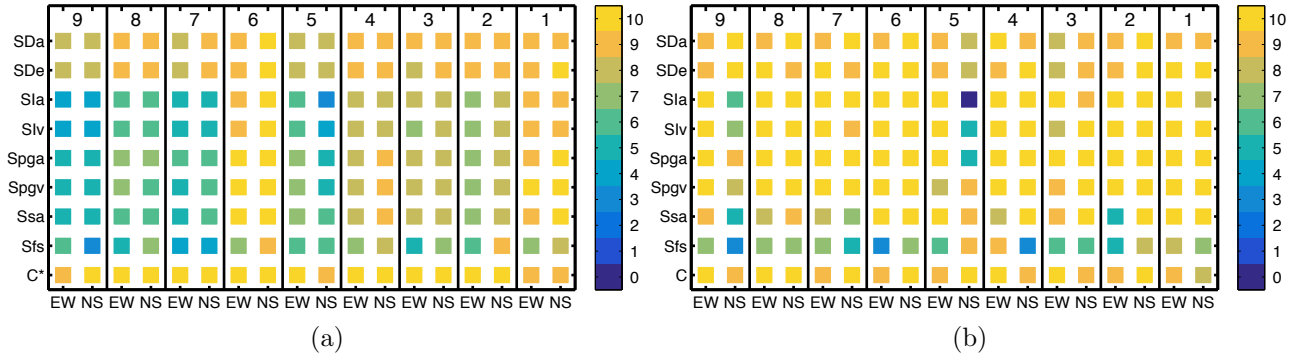


Figure 3.28 – Anderson criteria for surface acceleration: a) C_{S1} : mean of all frequency bands and b) C_{S2} : mean for frequencies between 0.05 and 15Hz

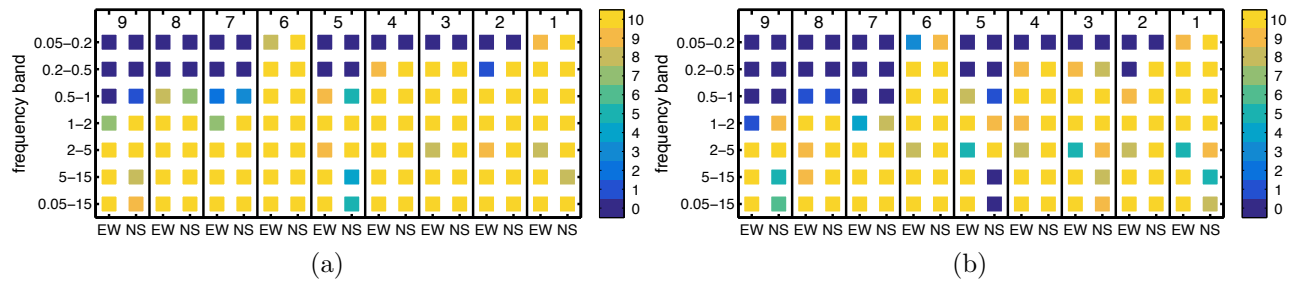


Figure 3.29 – Anderson criteria for surface acceleration at each frequency band: a) PGA and b) Ia

Concerning the component orientation, additional analyses were made with the rotated motion (ROT), finding the axes for the highest intensity (measured in this case as maximum PHA or I_A) which is supposed to be horizontal and aligned with the earthquake source direction (Penzien and Watabe, 1974). In theory, using the ROT will produce higher nonlinearity as it has a higher intensity. However, calculating the transfer function with the similar ROT of the recorded surface acceleration, the amplification is generally higher and the shift in frequency is less important. Comparing with numerical results, the ROT motion seems to give similar results at surface, specially for TS 5 that presented the highest dependence between components and are not shown here for the sake of brevity.

3.5.4.1 Evolution of nonlinearity

The evolution of nonlinearity for the different PHA can be analysed by observing the deamplification and frequency shift in the transfer function ($|TF|$) shown in Figure 3.30 for the modeled and the recorded motions. The first peak amplification for the weak motions was in general overestimated by the model; however, for the strong motions -i.e. TS 1, 2 and 3- the

model gave satisfactory results. Only these motions, present clear nonlinear behavior: with deamplifications of almost half the elastic value and a frequency shift of approximately 1Hz; in contrast, TS 4 and 6 do not show any shift in frequency. For both modeled and recorded motions, $|TF|$ of TS 6 presented the deamplification but without the shift to lower frequencies. Whereas for TS 5, while the amplitude of the modeled motion's $|TF|$ is above the weakest motion; for the recorded motions, the amplitude is below TS 2 and 3. This motion presented the lowest similarity according to Anderson criteria which is probably due to the simplifications of the model; however, in general, the similarity was very high for all the motions even if it consisted entirely in a blind test and no modifications were done to the model parameters.

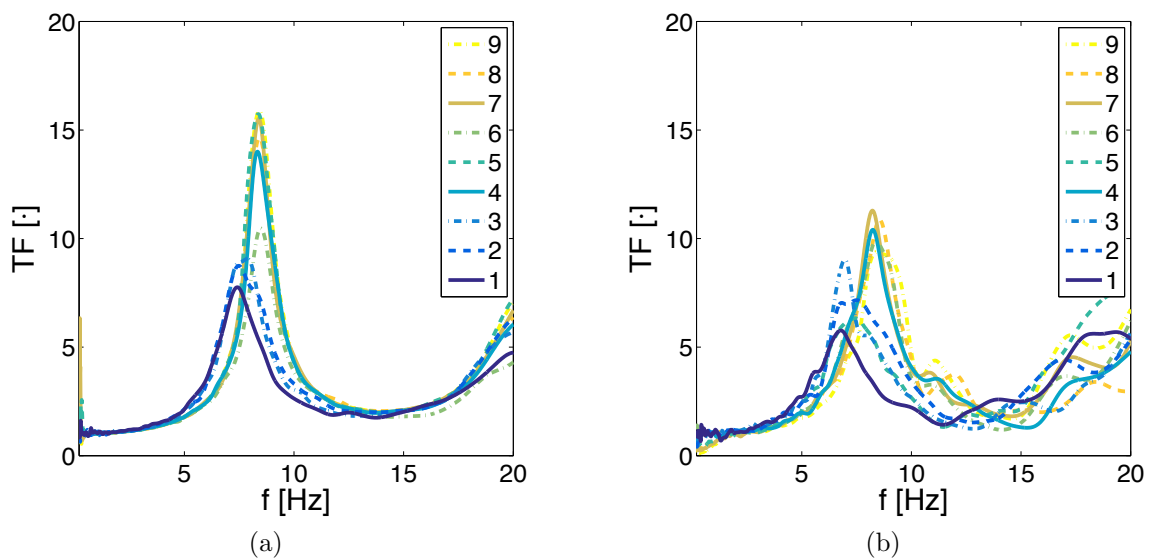


Figure 3.30 – Transfer function for all motions with EW component: a) modeled and b) recorded

3.5.4.2 Profile analysis

Whereas for the real recordings, only the borehole and surface motions are available, for the numerical model the evolution of maximum shear stresses and maximum accelerations can be analyzed with depth and are shown in Figure 3.31. Concerning the profile of maximum acceleration, all motions present generally a gradual increase in amplification as it arrives to the surface. Note that almost all motions, except for TS 5 and 7, present an initial acceleration amplification in the bottom elastic layer followed by a sudden deamplification and a smooth amplification to the surface. With respect to the maximum shear stress (τ_{max}) profile, note that for the weakest motions the increase with depth is in general smooth. In contrast for TS 1, 2 and 3, the τ_{max} changes for each depth. It is interesting to note how the soil behavior is modified for each input motion and introduces heterogeneities on the profile.

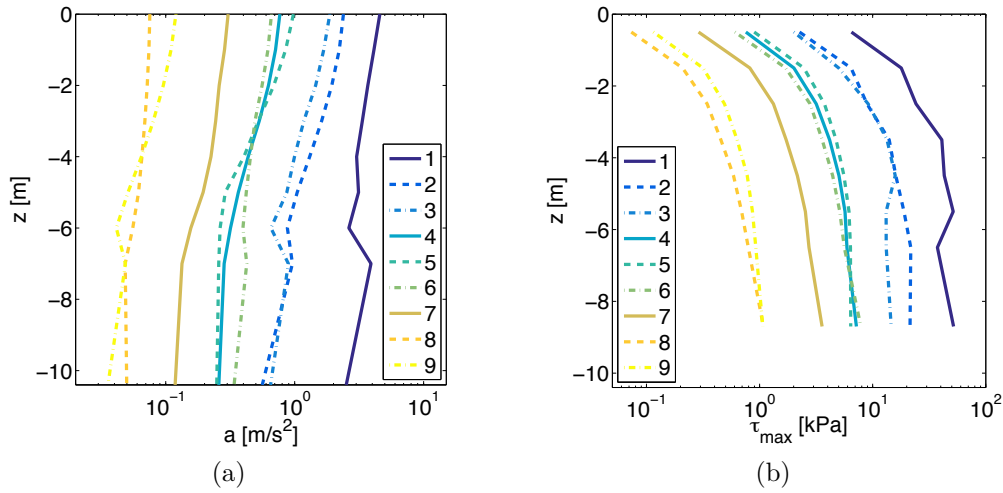


Figure 3.31 – Profiles for a) maximum acceleration and b) maximum shear stress

3.5.5 Partial conclusions

While very limited information was provided for the soil characterization and the validation was entirely a blind test, results are very satisfactory, specially for the nonlinear behavior of the strong ground motions. Concerning, frequencies below 1Hz, the similarity was lower however this is a known limitation of the numerical analysis and finite element models. The limited number of input motions tested, specially concerning high levels of nonlinearity, was a drawback of the analysis; however, considering the simplifications of the model -i.e. homogeneous, 1D wave propagation, no pore-pressure, etc.- results were close to the recordings.

In general, the present case provides results to validate the site response analysis of the 1D wave propagation. The finite element code as well as the constitutive soil model were satisfactorily validated for nonlinear dynamic behavior; however, this case presented some differences with respect to the general framework of this study. For instance, the soil was a very stiff sand and no laboratory test data was available concerning the liquefaction resistance or porosity of the material. Additionally, the homogeneity of the deposit and consequent condition of 1D soil configuration can be faulting while surface waves are hardly negligible.

Chapter 4

Effect of coupling excess pore-water pressure and soil deformation

The excess pore pressure (Δp_w) generation and consequent reduction in effective stress leads to the softening of a liquefiable soil deposit that can alter ground motions in terms of amplitude, frequency content and duration. However, total stress analyses, which are the most currently used, do not take into account coupling of excess pore pressures and soil deformations. To assess this effect two models were tested: i) A Biot hydraulic and mechanical computation of a saturated soil deposit with coupling pore pressures and soil deformations (CPD) and ii) a mechanical computation of a decoupled model (DPD) with the same initial state. Both analyses were performed with the ECP model. First, the 1D wave propagation on a 20m soil column is modeled with the two analyses and focus is given to the modifications of the surface signal in terms of peak values and response spectra (Section 4.3). This part contains material from an article published in *Acta Geotechnica* (Montoya-Noguera and Lopez-Caballero, 2016). Afterwards, a 2D soil-structure model is studied in Section 4.4. The effect of coupling is then evaluated in the soil-structure interaction (SSI), the structure settlement with respect to free field and the structure seismic performance.

As Δp_w depends on the soil properties, two sands were analyzed for the 1D analysis : loose-to-medium (LMS) and medium-to-dense (MDS). The results regarding the profile of maximum accelerations and shear strains, the surface accelerations and their corresponding response spectra are discussed. The mean values of the normalized response spectra ratio of surface accelerations between CPD and DPD analyses show a deamplification of low and high frequencies (i.e. at frequencies lower than 1.0Hz and higher than 10Hz) that tend to increase with the liquefaction zone size. When LMS deposits are subjected to strong ground motions, the coupling of Δp_w and soil deformation is of great importance in order to accurately model the free field response. On the contrary if for such cases DPD models are used, while peak acceleration predictions could be conservative, the amplification on the low frequencies could be largely underestimated which might be prejudicial for flexible buildings.

To evaluate the effect on the structure's performance, two structures lying on an LMS deposit were tested. Higher differential settlements were obtained with the CPD model for both structures and most motions tested. In this regard, the use of DPD models will not be recommended for structure design when dealing with strong earthquakes and LMS deposits. In contrast, due to the SSI effect in the structure for which the predominant period was near to that of the soil, the maximum inter-story drift (ISD) was consistently overestimated by the DPD models.

4.1 Introduction

The performance of structures during earthquakes is strongly influenced by the behavior of the soils that support them. Local site effects can influence structures' performance in two primary ways: by imposing additional deformations on the structure through ground failure and by influencing the ground motions that excite them. The reliable and economical seismic design of structures requires that local site effects on the ground motions be accurately predicted ([Bird and Bommer, 2004](#); [Kramer et al., 2011](#)).

Liquefaction is a phenomenon commonly observed in earthquakes in which the strength and stiffness are significantly reduced by the generation of excess pore water pressure in saturated cohesionless soils. In loose sands, the tendency of densification causes the excess pore water pressure to increase and the effective stresses to decrease. Some consequences are excessive vertical settlement, lateral spreading, flooding of low-lying land and even soil failure. Additionally, liquefaction also affects the dynamic response of soil deposits. As the soil stiffness decreases so does the shear-wave velocity and the predominant frequency shifts to lower values. Similarly, as the strains increase, the energy dissipation increases and the soil amplification will be reduced causing a "strong-motion deamplification effect" ([Beresnev and Wen, 1996](#)).

Advanced nonlinear models can be formulated in terms of effective stresses to account for the generation, redistribution and eventual dissipation of excess pore-pressure (Δp_w) during and after earthquake shaking; which is of key importance in the behavior of liquefiable soils. In this work, the comparison is made between analyses with and without Δp_w in the interest of evaluating the effect of coupling excess pore-pressure generation and deformation. To address this subject, only a limited number of studies have been published and are presented in the following section. Each study used a different technique but in all the fundamental variation is in the presence or lack of Δp_w ; thus for clarity the two analyzes will be referred to: coupled pore-pressure and deformation (CPD) and decoupled (DPD).

4.1.1 Summary of previous findings

[Hartvigsen \(2007\)](#) performed a series of CPD and DPD analyses of 1D wave propagation in different soil columns and subjected to a variety of earthquake motions. The main conclusions of the parametric study were also published by [Kramer et al. \(2011\)](#). In total, nine 20-m thick soil profiles were subjected to 139 input motions. The nonlinear site response program PSNL written by S. Kramer (more information in [Anderson et al., 2011](#)) was used to perform both the

CPD and DPD analyses. The program is written in effective stress but for the former, the bulk modulus of the pore fluid was reduced to a very low value. Thus, while the weight of the water contributes to the dynamic soil response (i.e. the inertial effect), there is no generation of excess pore-water pressure. As a result, they presented a correction function for the response spectra (PSA) obtained by the ratio of CPD and DPD analyses. This correction, called the response spectra ratio ($RSR = PSA^{CPD}/PSA^{DPD}$), is a function of period and of the loading parameter (L) that is the inverse of the factor of safety (FS) defined by the cyclic stress approach (Seed and Idriss, 1971) and is shown in Figure 4.1a.

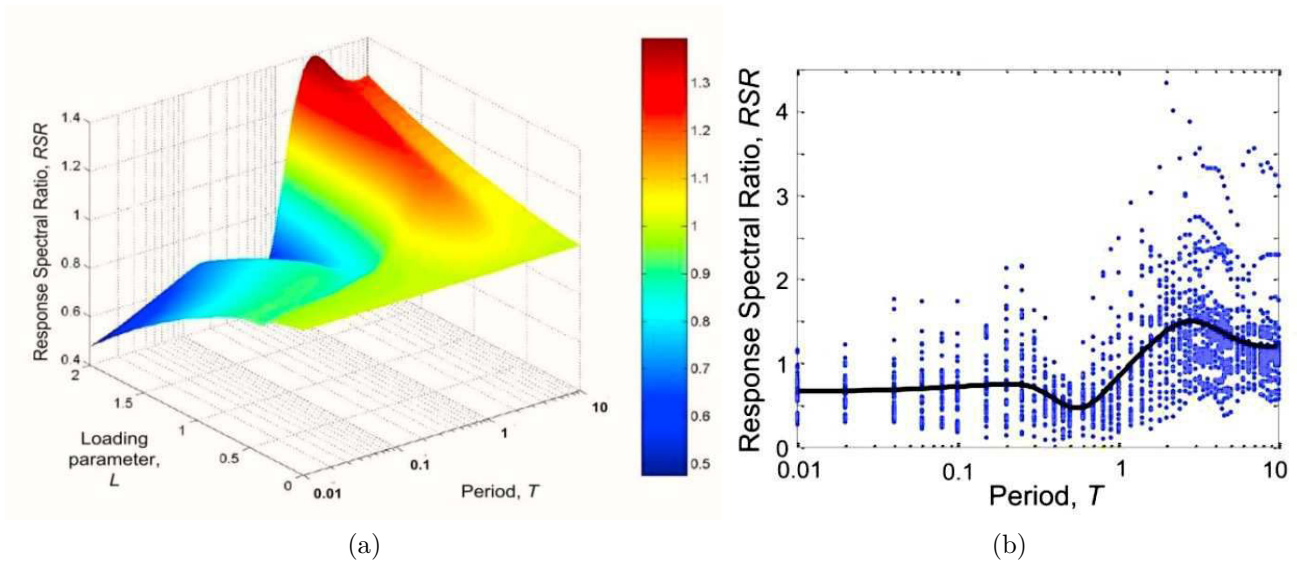


Figure 4.1 – Response spectral ratio ($RSR=PSA^{CPD}/PSA^{DPD}$): a) Mean values and b) Variation with period for $1.8 < L < 2.0$ (after Kramer et al., 2011)

The RSR can then be applied to a total stress analysis to obtain a more accurate response spectrum for liquefiable soils. Among the main features of this factor is that even for very low L, an amplification is evidenced -i.e. $RSR > 1$ - above a certain period (T_a). This period increases with L (from about 0.13s at L= 0.5 to about 1.7s at L=2). Additionally, for L above 1, values of RSR below 1 are obtained for periods around 0.1s, whereas for shorter periods, RSR is again increased (up to a maximum of about 0.7). The combination of the mid-period deamplification trough and long period amplification evidences the shift to low frequencies that occurs as a result of soft-site amplification (Beresnev and Wen, 1996). For the lowest liquefaction resistance shown (L=2), maximum RSR is approximately 1.4 at $T \approx 3$ s and the minimum is about 0.5 at $T \approx 0.5$ s. A regression analysis was used to obtain the RSR but the correlation between the residuals was low as shown in Figure 4.1b for the highest L range, hence the applicability of the function is unlikely. Additionally, the use of a loading parameter reduces

the analysis to a simplified procedure where the input motion variability is only expressed by the peak acceleration and the magnitude scaling factor while the soil response is only described by the SPT blow count and the reduction factor.

Similarly, [Yoshida \(2013\)](#) used the YUSAYUSA program ([Yoshida and Towhata, 2003](#)) for the CPD and the DPD analyses and compared results also with SHAKE ([Schnabel et al., 1972](#)). A total of 268 sites were subjected to eleven earthquake motions. Again the only difference between the analyses is consideration of excess pore water pressure generation or not; however, no information on how this was performed was stated. The comparison was focused on five frequently used intensity measures of the surface time history: the peak acceleration (PGA), peak velocity (PGV), peak displacement (PGD), instrumental seismic intensity (I_{JMA}) and spectral intensity (SI). All intensity measures evaluated with SHAKE were in general higher than with DPD analyses, except for PGD. The highest difference of more than 1.5 to 1 was seen for PGA values. Concerning the comparison between CPD and DPD analyses, the differences are consistently higher and for most cases DPD presented higher values. Once more, PGA difference was the highest of up to 1 to 4 as shown in [Figure 4.2a](#).

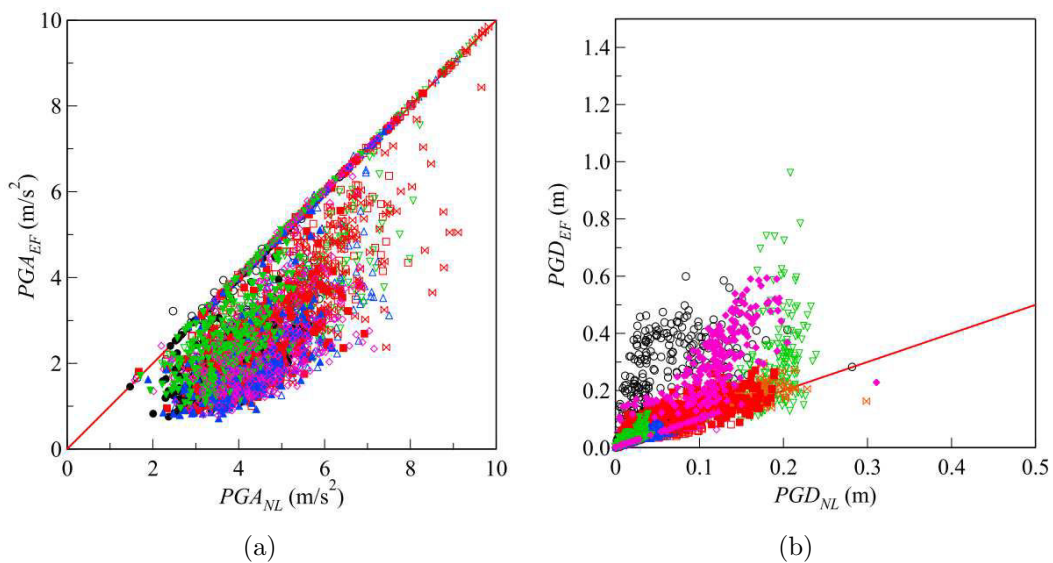


Figure 4.2 – Relation between CPD (EF) and DPD (NL) analyses : a) PGA and b) PGD. Colors define the different earthquake motions used. (after [Yoshida, 2013](#))

Whereas for PGD shown in [Figure 4.2b](#), the CPD values were greater than with the DPD which could affect the design of underground structures such as piles and pipelines. Once more, the program used for these analyses only took into account the SPT blow count to describe soil behavior. In contrast with [Hartvigsen \(2007\)](#) results, no clear trend between the two

analyses was identified, possibly due to the great variability of sites tested, some of those with no liquefiable soil.

A similar procedure from [Hartvigsen \(2007\)](#) was performed by [Gingery et al. \(2014\)](#) but applied to ground motion prediction equations (GMPEs) that do not account for liquefaction. The four GMPEs used were the updated attenuation relationships for the western U.S. from the Next Generation Attenuation (NGA) project ([Chiou and Youngs, 2008](#)) that accounted for soil conditions. An amplification function (AF) for each of the GMPEs was calculated from the logarithmic ratio of PSA from recorded motions in 19 liquefiable soil deposits and the evaluated NGA GMPE, i.e. $\ln(AF) = \ln(PSA^{rec}/PSA^{NGA})$. The correction functions presented in general a similar trend as the RSR proposed by [Hartvigsen \(2007\)](#) but with higher maximums and minimums; although these factors are hard to compare, as they are applied to different analyses (i.e. CPD vs DPD and measured vs. GMPEs). However, an interesting aspect of these results is that added to the known long period amplification, a second amplification can be observed in [Figure 4.3](#) for short periods (around $T \leq 0.05$ seconds) which could be the result of acceleration spikes that occur in association with the dilatational part of liquefaction phase transformation behavior.

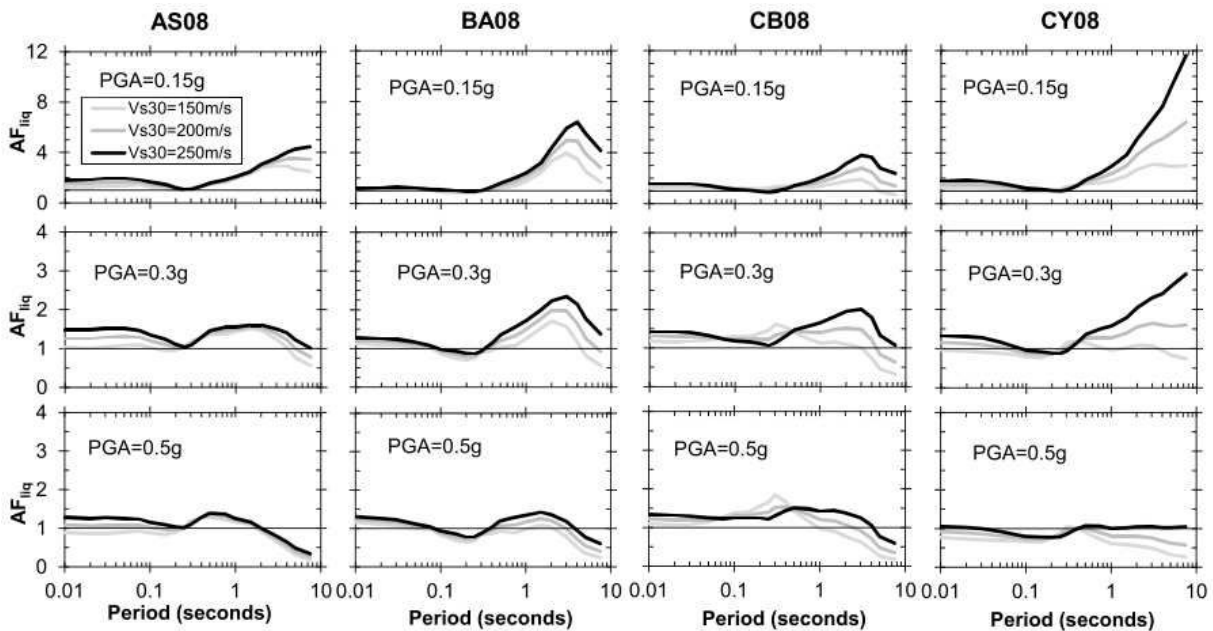


Figure 4.3 – Proposed model of the amplification function ($\ln(AF) = \ln(PSA^{rec}/PSA^{NGA})$) for each GMPE and varying PGA and V_{s30} (after [Gingery et al., 2014](#))

4.2 Coupled and Decoupled dynamic approach

The dynamic behavior of saturated porous media is described by the governing equations initially proposed by [Biot \(1941\)](#). When the absolute displacement of the fluid and soil grain compressibility can be neglected the simplified $\mathbf{u}_s - p_w$ formulation given by [Zienkiewicz and Taylor \(1991\)](#) might be used. This formulation and the set of equations were presented in sections [2.1](#) and [3.3](#) and will only be briefly recalled.

The coupling of excess pore water pressures and deformations on the soil behavior involves the effective stress principle, the mass conservation and the Darcy's laws. Following the principle of effective stress proposed by [Terzaghi \(1943\)](#), the effective stress ($\boldsymbol{\sigma}'$) which is applied to the solid skeleton is the sum of the total stress ($\boldsymbol{\sigma}$) and the pore pressure (p_w). [Biot \(1941\)](#) performed the extension to three dimensional consolidation and arbitrary loads variable with time and is expressed by two main equations:

- The momentum equation for the soil-fluid system is given by :

$$\mathbf{div}\boldsymbol{\sigma}' - \nabla p_w + \rho \cdot \mathbf{g} = \rho \cdot \ddot{\mathbf{u}} \quad (4.1)$$

where ρ is the total average unit mass ($\rho = n \cdot \rho_w + (1 - n) \cdot \rho_s$); n is the soil porosity; ρ_w , the fluid mass; ρ_s , the soil particle mass; \mathbf{g} , the gravity acceleration vector and \mathbf{u} is the solid skeleton displacement.

- The equilibrium of water and flow conservation equation using the generalized Darcy's laws is as follows:

$$\mathbf{div}\dot{\mathbf{u}} - \mathbf{div}(\mathbf{K} \cdot (\nabla p_w - \rho_w \cdot \mathbf{g})) - \mathbf{div}(\mathbf{K} \cdot \rho_w \cdot \ddot{\mathbf{u}}) + \frac{\dot{p}_w}{Q} = 0 \quad (4.2)$$

where \mathbf{K} is the permeability tensor defined by $\mathbf{K} = \frac{\kappa}{\rho_w \cdot \mathbf{g}}$, κ being the kinematic permeability tensor, and Q is the compressibility parameter ($Q^{-1} = \frac{n}{K_w} + \frac{1-n}{K_s}$), K_w and K_s being the fluid and solid compressibility, respectively.

Note that the pore water pressure generation and dissipation will depend on the permeability tensor and the compressibility parameter. Hence, the DPD model can be simplified by either reducing the compressibility to nearly zero as was done by [Hartvigsen \(2007\)](#), or by increasing the permeability to infinity. In this study another approach was chosen. It consists in keeping the same inertial effects, while no excess pore pressure is generated.

For the inertial effects, the DPD model has a total average unit mass equal to the coupled model, so the weight of the water contributes to the dynamic soil response (equation 4.1). With respect to the pore water pressure (p_w), for the dynamic analysis fixed conditions are used in the DPD model hence no excess pore pressure generation is allowed. Both models are performed with the effective-stress analysis and with the same constitutive model, but for the DPD there is no excess pore pressure generation. The DPD has the same initial state but reproduces a fully drained condition therefore the soil stiffness degradation depends only on the shear strain. In contrast, for the analysis of the effect of the groundwater level (e.g. on the dry versus saturated case) there is a difference in the initial state as the density and the predominant frequency are lower for the dry case. This kind of analysis has been presented by among others [Brennan et al. \(2005\)](#); [Saez et al. \(2013\)](#); [Carrilho Gomes and Lopes \(2014\)](#) and will not be presented in this work.

4.3 Free field response

This section studies the effect of coupling excess pore pressure (Δp_w) generation and soil deformation on the one dimensional signal propagation through nonlinear liquefiable soils. Three aspects of the motion response are evaluated: i) the maximum acceleration and shear strain profile, ii) the maximum surface acceleration and iii) the corresponding response spectra. A discretization of the response spectra for different time steps of the motion and for different levels of liquefaction are analyzed.

4.3.1 Soil behavior

The buildup of excess pore pressure depends on many factors concerning the soil as well as the input motion. Laboratory studies on clean homogeneous soil indicate that the rate of pore pressure generation depends on the soil relative density, the initial effective confining pressure with respect to the overconsolidation ratio (OCR) and the prior strain history, among others ([Ladd et al., 1989](#)). According to the concept of critical-state soil mechanics, the behavior of cohesionless soils is related to the proximity of its initial state to the critical state or steady-state line rather than to the absolute measurements of density ([Roscoe and Pooroshab, 1963](#); [Been and Jefferies, 1985](#); [Ishihara, 1993](#)). For the ECP model, [Aubry et al. \(1982\)](#) defined this distance as the stress ratio p_0/p_{c0} , in which p_0 is the initial mean stress and p_{c0} , the stress

corresponding to the critical state of the initial density. When this ratio is higher than 1, the soil behavior will be contractant; otherwise, it will be contractant/dilatant.

In order to study the effects of coupling pore pressure generation two sand deposits with different initial behavior are used. They correspond to two relative densities: loose-to-medium (LMS) and medium-to-dense (MDS). The model parameters were calibrated and validated with laboratory tests by Saez (2009) and Costa D'Aguiar et al. (2011). They were determined with the procedure defined by Lopez-Caballero et al. (2007) and are presented in the appendix A. Some results of the numerical simulations of two laboratory tests are shown to better understand the behavior of the soils used: a drained monotonic triaxial and an undrained cyclic shear tests.

The volumetric strains (ε_v) as a function of the axial strains (ε_1) from the simulations of the triaxial drained test are shown in Figure 4.4a for three confining pressures (p_0): 50, 80 and 100kPa. The volumetric strains are below zero for the LMS even for low pressures, which means that the soil deposit is contracting. The tendency of densification causes the increase in pore pressure generation, which ultimately triggers the liquefaction phenomena. On the contrary, the MDS presents a contractant/dilatant behavior for the confinement pressures tested.

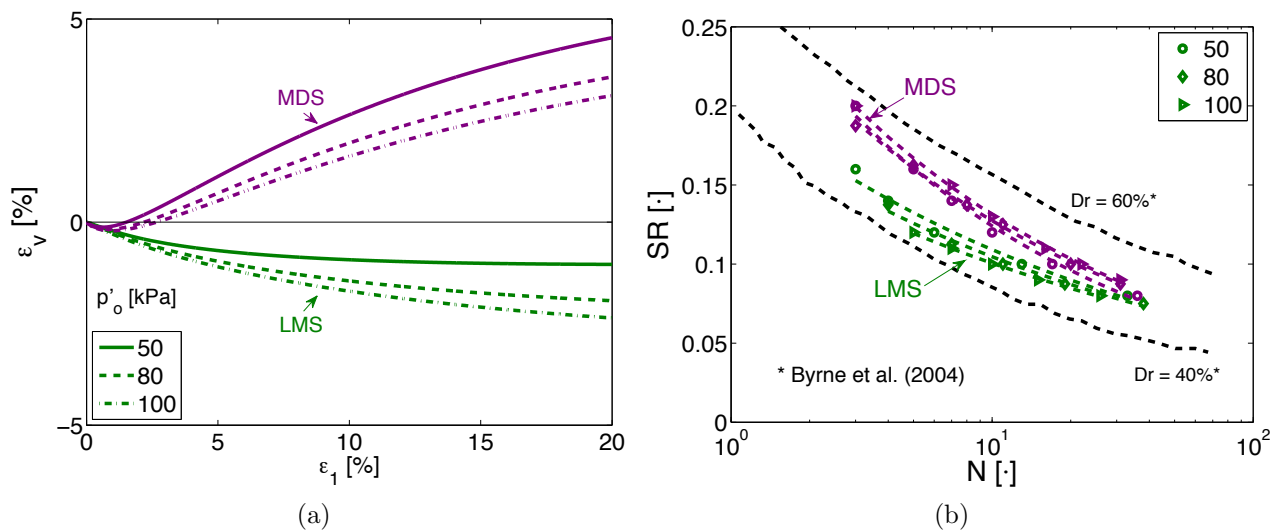


Figure 4.4 – Results of the simulated laboratory tests: a) Volumetric strain (ε_v) as a function of the axial strain (ε_1) from the monotonic triaxial drained test, and b) liquefaction curves from the undrained cyclic shear test

Figure 4.4b shows the cyclic stress ratio ($SR = \tau_{cyc}/p_0$) as a function of the number of loading cycles to produce liquefaction (N) issued from the undrained cyclic shear test. As qualitative comparison, the modeled test results are compared with the curves given by Byrne et al. (2004) for Nevada sand at different relative densities (i.e. $Dr = 40$ and 60%). It is noted

that the obtained curves for the LMS are closer to the reference for $D_r = 40\%$; while, the MDS curves are closer to those of $D_r = 60\%$.

4.3.2 Input earthquake motions

A wide-range selection of recorded accelerograms were used to define an appropriate nonlinear dynamic analysis. The earthquake signals were proposed by [Bradley et al. \(2010\)](#), [Iervolino and Cornell \(2005\)](#), [Sorrentino et al. \(2008\)](#), [Jafarian et al. \(2011\)](#) and [Raghunandan and Liel \(2013\)](#). The earthquake signals used are near-to-source strong motions recorded in dense soil conditions. These signals are supposed to have minimal noise and are appropriate for an outcropping bedrock condition. Thus, 273 unscaled records were chosen from the Pacific Earthquake Engineering Research Center (PEER) database.

The statistics of some intensity measures (IM), defined in appendix C, are calculated at outcropping conditions and are shown in Table 4.1. The coefficient of variation (CV) is high for all parameters and it is about 150% for I_A . A high variation in I_A is of great importance given that after the sensitivity analysis performed by [Lopez-Caballero and Modaressi-Farahmand-Razavi \(2010\)](#), it was proved to be the most influential input variable on the liquefaction index ($Q_{H=10}$). Figure 4.5 shows the response spectra of all the input earthquake motions previously filtered to 20Hz. The spectral amplitude has a 5% structural damping. Similarly, a great variation is presented on the response spectra.

Table 4.1 – Input motions intensity measures for free field response analysis

Parameter	Range	Mean	CV [%]	Median
PHA [g]	0.01 – 1.68	0.32	85	0.28
PGV [cm/s]	0.2 – 121.22	28.38	90	18.97
T_m [s]	0.10 – 1.73	0.55	60	0.50
T_p [s]	0.03 – 1.60	0.34	71	0.27
$T_{V/A}$ [s]	0.08 – 1.44	0.48	50	0.45
I_A [m/s]	0.01 – 12.38	1.46	146	0.52
$D_{5.95}$ [s]	0.87 – 36.65	12.07	68	9.62
I_{rms} [m/s^2]	0.01 – 2.32	0.47	88	0.36
SI [m]	0.01 – 2.14	0.41	78	0.33
SED [cm^2/s]	0.02 – 34100	1919	211	353

4.3.3 Initial soil response

To verify that the only difference in the CPD and DPD models behavior is due to pore water pressure generation, the spectral ratio and the maximum shear modulus profile are evaluated

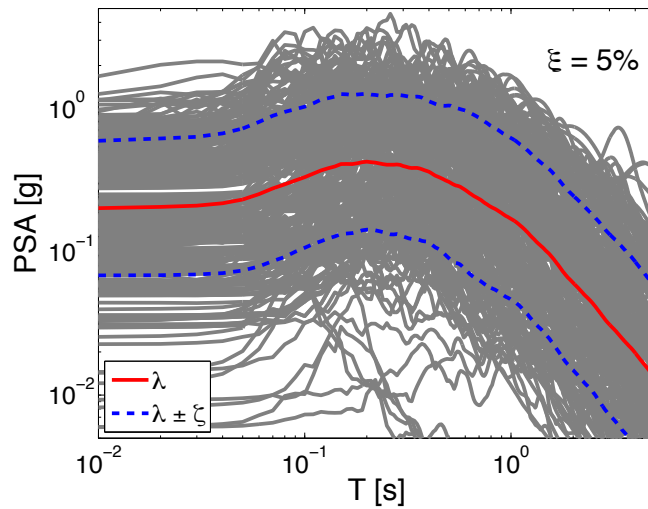


Figure 4.5 – Response spectra of acceleration for the outcropping motions

and shown in Figure 4.6 for LMS. A sample signal at very low amplitudes (i.e. with a PHA $\approx 1 \cdot 10^{-5}g$) is used to ensure elastic soil behavior.

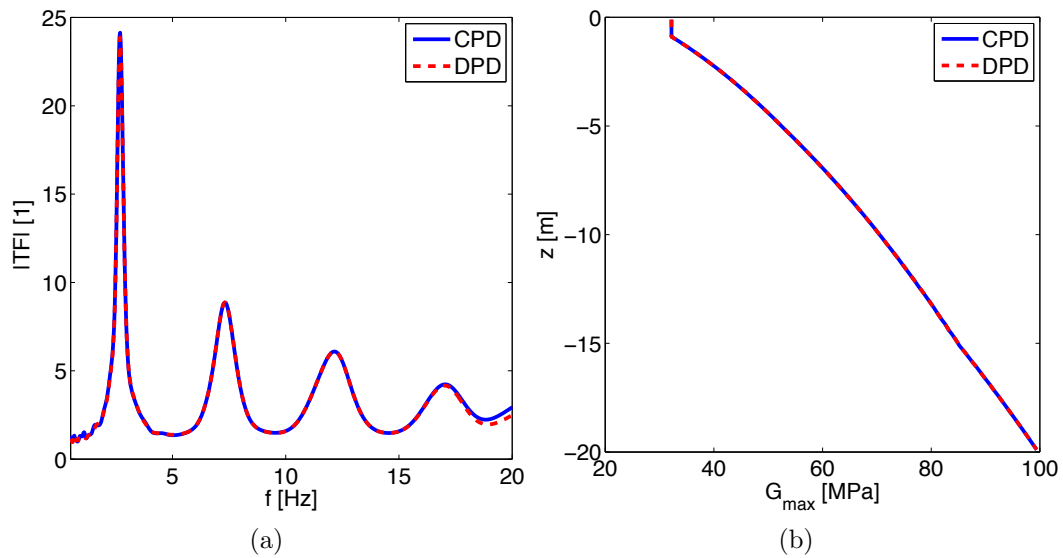


Figure 4.6 – Initial behavior of the coupled (CPD) and the decoupled (DPD) model: a) transfer function and b) the maximum shear modulus profile for the LMS

The transfer function is calculated as the ratio between the Fourier transforms of accelerations in the surface and at the bottom of the soil deposit and it characterizes the amplification produced by the soil deposits. The first amplification peak corresponds to the fundamental elastic period (T_s) of the soil and in this case is equal to 0.27s for both models. As the results are the same; it can be proved that the initial elastic behavior of both soils is identical. Thus, as in the nonlinear model the behavior depends on the initial state, if it is proved to be the same, it should also be the case for the contractant or dilatant tendency. Therefore, differences

in the response will only be due to the effect of Δp_w on the coupled model. Concerning MDS, it was also proved that the initial behavior for both analyzes was identical but it is not shown here for the sake of brevity.

4.3.4 Nonlinear soil response

Nonlinear soil response is usually characterized by a deamplification of the ground motion at high frequencies as well as a shift of the energy towards low frequencies (Beresnev and Wen, 1996). Evidence of such behavior beyond an acceleration threshold dependent on the soil deposit has been observed in seismological observations by among others Field et al. (1997); Assimaki et al. (2008); Bonilla et al. (2011a) and is taken into account by some geotechnical models.

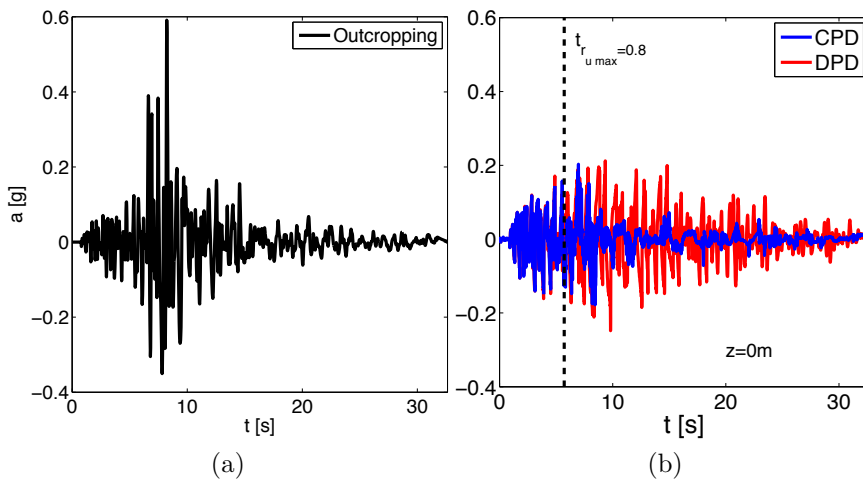


Figure 4.7 – Acceleration time history at a) outcropping and obtained at b) surface with CPD and DPD analyses for the loose-to-medium sand (LMS)

An example of the nonlinear response is presented for one strong ground motion and for the LMS deposit. The motion used corresponds to the Northridge earthquake of 1994, 90 degrees component, recorded in station Castaic - Old Ridge Route with moment magnitude of 6.69 and site-to-source distance of 20 km. The acceleration time history at the outcropping rock is shown in Figure 4.7 together with the corresponding surface acceleration of both models. At the beginning, the two models present similar accelerations, thus for the strongest shaking the responses are very different. In terms of acceleration intensity, there is a strong deamplification at surface for both models of about 3 to 1 with smaller values for the CPD model. Furthermore, after approximately 5s, while the CPD analysis presents a shift towards low frequencies, the DPD column continues to have high amplitudes. At this time, the maximum liquefaction ratio

($r_u(t) = \Delta p_w(t)/\sigma'_{v0}$) through the column is equal to 0.8 (refer to the trace in Figure 4.7b). Liquefaction is described in this analysis as the significant reduction of the effective stress and therefore accounts for both phenomena: *true liquefaction* when $r_u = 1.0$ and *cyclic mobility* when $0.8 < r_u < 1.0$ with development of large strains (Koutsourelakis et al., 2002; Popescu et al., 2006). Thus, liquefaction is said to be triggered when r_u equals 0.8.

As the frequency content is of great interest for nonlinear behavior, the response spectra (PSA) with a 5% structural damping is shown in Figure 4.8 for the three acceleration time histories. PSA were normalized with the peak acceleration value, as recommended by Seed et al. (1976), so that the general forms of the spectra may be examined without reference to the specific variations in acceleration associated with them. With respect to CPD, the DPD model overestimates the amplification for short periods (i.e. $T < 0.2s$) and for the periods between 0.5 and 2s; however it is underestimated for the periods between 0.2 and 0.5s and the long periods (i.e. $T > 2s$). While an overestimation of PSA will lead to higher design costs, the underestimation could be highly prejudicial for the reliability of the seismic structure design.

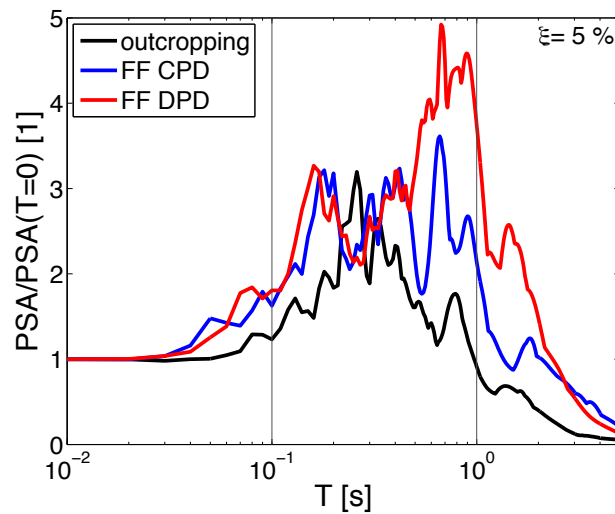


Figure 4.8 – Normalized response spectra for the LMS with a structural damping (ξ) of 5%

In the following sections, to present the results for all the motions tested focus will be given to these two main characteristics of nonlinearity: (1) peak values amplification or deamplification and (2) frequency shift in the response spectra.

4.3.5 Peak surface acceleration

The effect of local geology on the peak acceleration has been studied for many decades. Some researchers as Trifunac and Brady (1975) and Seed et al. (1976), among others, focused on the

correlations between distance from source, earthquake magnitude and site conditions. Concerning soft soil amplification, [Idriss \(1990\)](#) and [Dickenson and Seed \(1996\)](#) studied eight earthquakes of magnitude close to 6.5 recorded at different soil site conditions. The main conclusions were: i) “the peaks of strong motion do not grow linearly with earthquake magnitude”, ii) the accelerations are amplified for weak motions and deamplified for stronger ones and iii) this relationship depends on the local site conditions of the deposit. These studies were based on strong motion recordings and therefore include topographic as well as geological site effects (e.g. basin effect, layering and intrinsic variability).

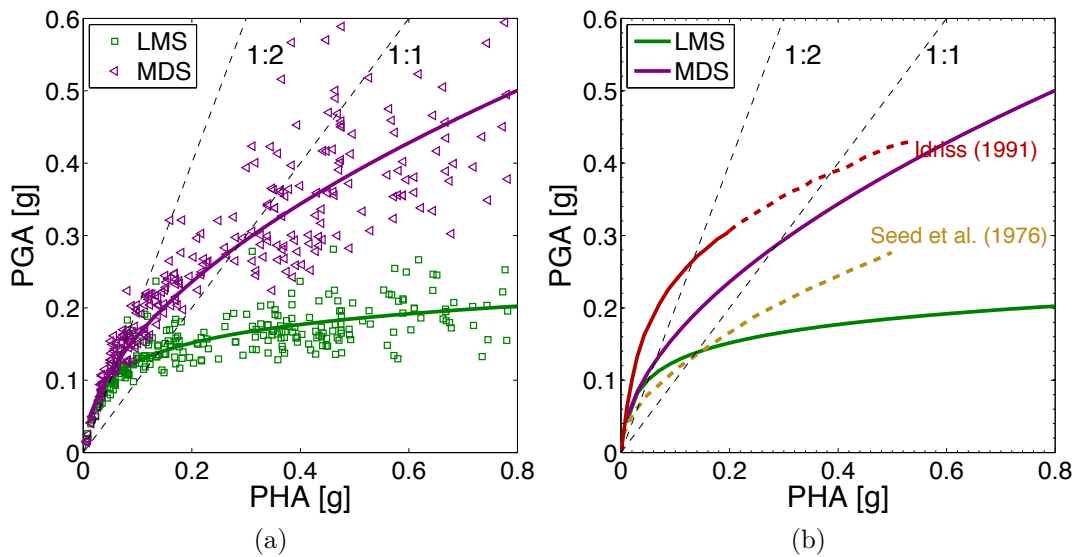


Figure 4.9 – Peak ground acceleration at free field (PGA) as a function of peak horizontal acceleration at outcropping (PHA) for a) both deposits (CPD model) and b) comparison with estimations based on recordings and extrapolations from [Seed et al. \(1976\)](#) and [Idriss \(1991\)](#)

In the studies by [Seed et al. \(1976\)](#) and [Idriss \(1991\)](#), site amplification factors were given as ratios between the peak surface acceleration of a soft deposit (PGA) and the peak horizontal acceleration at outcropping rock (PHA) as was presented in Section 2.3. Similarly, Figure 4.9a shows the relationship between PHA and PGA obtained for the LMS and the MDS deposits. The results shown correspond to the CPD model and a logarithmic curve is fitted to the data. For LMS, an amplification of the signal is presented for PHA less than 0.1g; and PHA < 0.3g for MDS. It appears that this value is a threshold for nonlinearity due to the ground motion as has been shown by [Beresnev and Wen \(1996\)](#) and [Régnier et al. \(2014\)](#) among others; although, it changes for each soil.

The obtained trends for each soil are also shown in Figure 4.9b for comparison with the curves for soft sites given by [Seed et al. \(1976\)](#) and [Idriss \(1991\)](#). It is important to recall

that the amplification/deamplification curve from Seed et al. (1976) were estimated for soft to medium stiff clay and sand based on experience of few peak accelerations recorded at weak and intermediate ground motion. Concerning the factor curve from Idriss (1991), only real data from the 1985 Michoacan earthquake and the 1989 Loma Prieta earthquake were used for PHA below 0.2g while for higher values, site response calculations were used. Compared to the results of Seed et al. (1976), both soils as well as the curve by Idriss (1991) present higher amplifications for small PHA values. However, the latter presents twice the amplification for PHA about 0.1g. Additionally, the threshold for nonlinearity for LMS is similar to that given by Seed et al. (1976), while that of MDS is slightly smaller than that given by Idriss (1991).

The comparison of the results with the coupled (CPD) and the decoupled (DPD) analyses is shown in Figure 4.10 for each soil. For low PHA values, the response is similar for the CPD and the DPD analyses, which is to be expected as there is little or no pore pressure generation. However, above the threshold of nonlinearity, the peak acceleration at surface is bigger for the DPD model as the attenuation given by the liquefaction triggering is not present. Nonetheless, it appears some attenuation caused by the soil resistance degradation given by the induced shear strains, as was shown by Kramer et al. (2011).

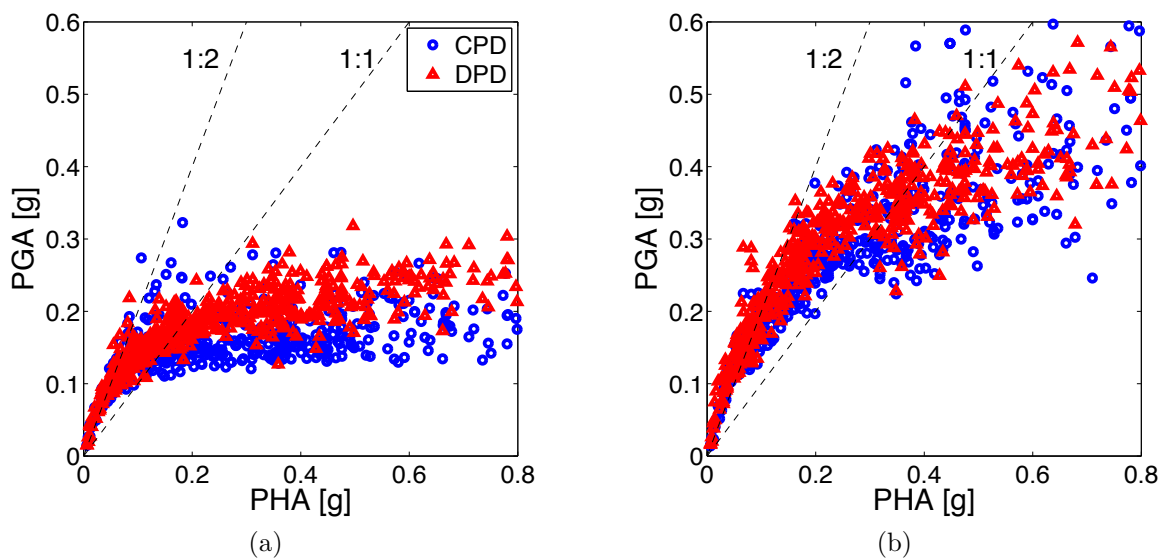


Figure 4.10 – PGA as a function of PHA for the coupled (CPD) and the decoupled (DPD) models for a) LMS and b) MDS

As the MDS has less tendency for densification, less deamplification due to excess pore-pressure is expected hence the differences between both analyses are smaller. In contrast, it can be seen that in the LMS deposit, differences between the two models are bigger and are present from smaller PHA values. Additionally, the MDS presents more dispersion as the PHA

increases, mainly for the CPD analysis, which is probably because of the high frequency spikes in acceleration.

The relationship between the CPD and DPD models for other earthquake's intensity measures is analyzed. First, the Arias intensity (I_A) of the signal at surface for both models is calculated and the ratio I_{ACPD}/I_{ADPD} as a function of PHA is shown in Figure 4.11a. The I_A is a measure of the total energy delivered per unit mass and has been found to be a better measure of earthquake severity and liquefaction triggering (Koutsourelakis et al., 2002; Lopez-Caballero and Modaressi-Farahmand-Razavi, 2010). In general, the DPD model tends to overestimate the energy at the surface compared to the CPD model as the ratio is less than 1 for almost all motions.

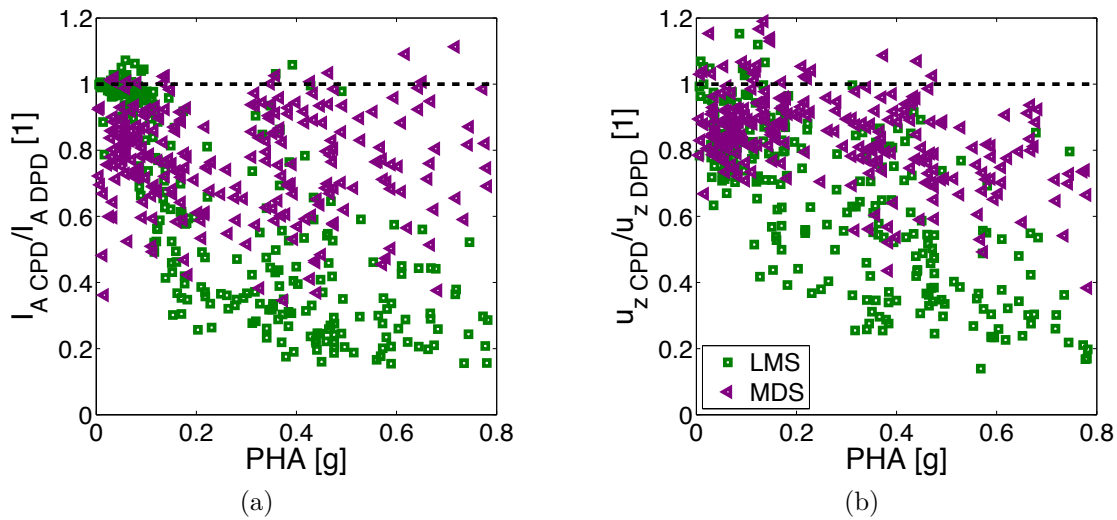


Figure 4.11 – CPD/DPD ratios as a function of PHA: a) Arias Intensity (I_A) and b) Co-seismic settlement (u_z)

However, it seems that the effect of coupling is different for the two sands. In the LMS deposit, the ratio shows almost no dependence on PHA for values below the threshold of 0.2g but for higher PHA, the ratio decreases drastically down to values of 0.2. In other words, when no pore-pressure excess is generated the energy at surface is the same for both models but when the liquefaction ratio is important, more energy is presented in the DPD model. As in general MDS presents smaller values of liquefaction ratio, the ratio between both models does not appear to have a dependence on the PHA value throughout the range tested; although, in average the energy of the DPD is higher than that of the CPD.

Similarly, Figure 4.11b depicts the settlement CPD/DPD ratio. As expected for most cases the settlement is greater for the DPD model as both PGA and I_A are greater. Once more, while

for the LMS the ratio depends on the PHA for values above the threshold; the MDS presents no dependence of the PHA value. It is interesting to note how these two figures are alike, yet more dispersion is present for the co-seismic settlement.

In an effort to integrate liquefaction in the relationship between surface acceleration for both models, the results are ranged by the Liquefaction Index (Q) evaluated at the CPD model for the LMS deposit and shown in Figure 4.12. This value is defined by [Shinozuka and Ohtomo \(1989\)](#) as:

$$Q_H = \frac{1}{H} \int_0^H r_{uend}(z) dz \quad (4.3)$$

where r_{uend} is the liquefaction ratio, previously defined, evaluated at the end of shaking. A value of 1.0 indicates conditions of initial liquefaction throughout the thickness H , thus gives information of the liquefaction ratio as well as the total liquefied depth. The thickness H used in this analysis is 10m however, other values will be tested afterwards.

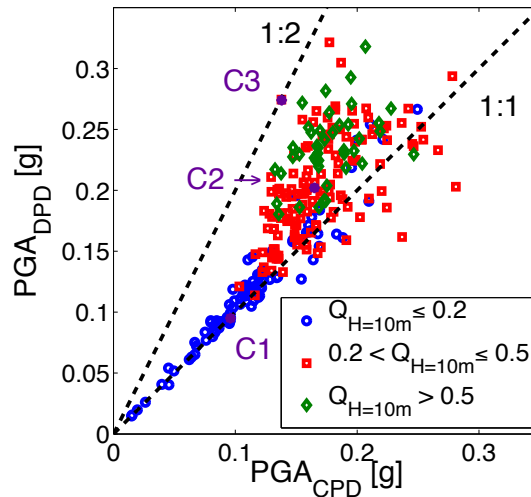


Figure 4.12 – PGA of the DPD and CPD models grouped by the liquefaction index for LMS

In Figure 4.12 it can be seen that PGA values for the DPD model can be twice as big as the ones of the CPD model and that it appears to be a relationship between these differences and the liquefaction index Q . The values were divided in three groups according to the $Q_{H=10m}$ value, namely, $Q_{H=10m} \leq 0.2$, $0.2 < Q_{H=10m} \leq 0.5$ and $Q_{H=10m} > 0.5$, and will be used in section 4.3.7.

4.3.6 Acceleration profile

For the purpose of analyzing the motion variation throughout the soil deposit, three cases were chosen from different stages of the relation between PHA and PGA (shown in Figure 4.12):

for the first case, both columns amplify the maximum acceleration by a factor of 2 ; for the second one, PGA is almost equal to PHA; and for the last case, the peak acceleration is greatly attenuated (i.e. $PGA \simeq 0.25PHA$). Moreover, the difference between DPD and CPD increases with cases. The earthquakes corresponding to each case are identified in Table 4.2.

Table 4.2 – Earthquakes used for detailed analysis. IM values are evaluated at the outcropping motion

#	Event	Year	RSN*	M_w	R^\dagger [km]	V_s [m/s]	PHA [g]	I_A [m/s]	D_{5-95} [s]	PGV [cm/s]	CAV5 [cm/s]
C1	Chi-Chi	1999	1587	7.62	62.11	845.34	0.06	0.06	34.28	5.15	2.41
C2	Landers	1992	882	7.28	26.84	344.67	0.14	0.67	37.04	14.95	10.96
C3	Valparaiso	1985	San Isidro**	7.8	65	814	0.68	20.64	37.32	42.9	66

*Record sequence number at the NGA database [PEER \(2013\)](#); **[COSMOS \(2012\)](#)

\dagger Joyner-Boore source-to-site distance.

The time history profiles of the liquefaction ratio ($r_u(t)$) are shown in Figure 4.13. Case C1 is not shown as r_u is less than 0.05 throughout the profile, while cases C2 and C3 present totally liquefied zones. It is interesting to note that although the same subsoil model is shaken, different motions liquefy different depths. Moreover, the time evolution of the motion's frequency content causes the liquefaction triggering at different time for each depth. For example, the motion in case C3 presents three acceleration peaks (at around 10, 15 and 20s) and with each, liquefaction gradually appears in deeper soil.

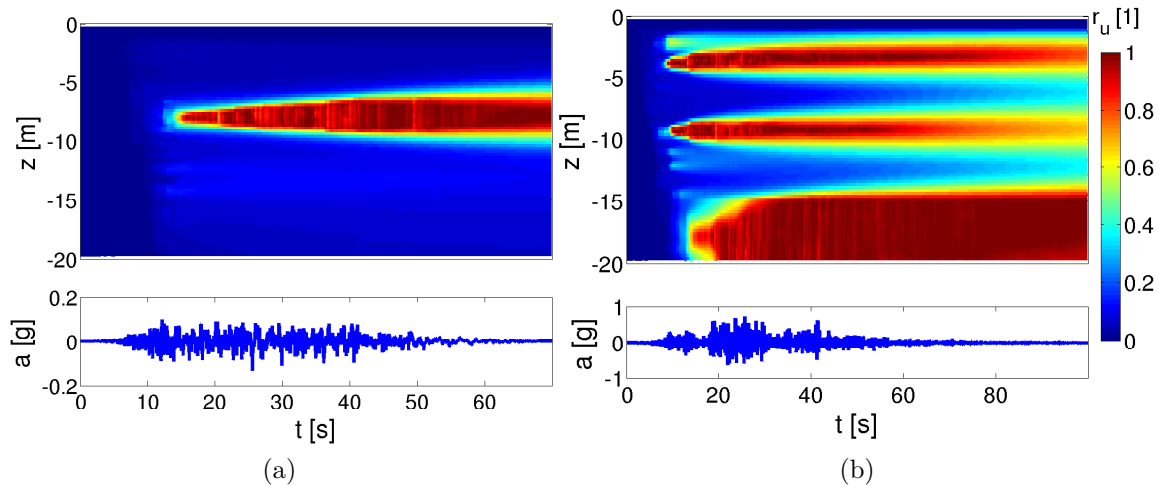


Figure 4.13 – Time history of r_u profile and outcropping input motion for a) C2 and b) C3

To identify the differences between the CPD and the DPD models, a comparison of the evolution with depth of two soil parameters is shown in Figure 4.14 for the three cases. These

parameters are: (i) the maximum horizontal acceleration a_{max} and (ii) the maximum absolute shear strain ($|\gamma_{max}|$). The liquefaction ratio at the end of shaking $r_{u\ end}$ profile from the CPD model is also shown.

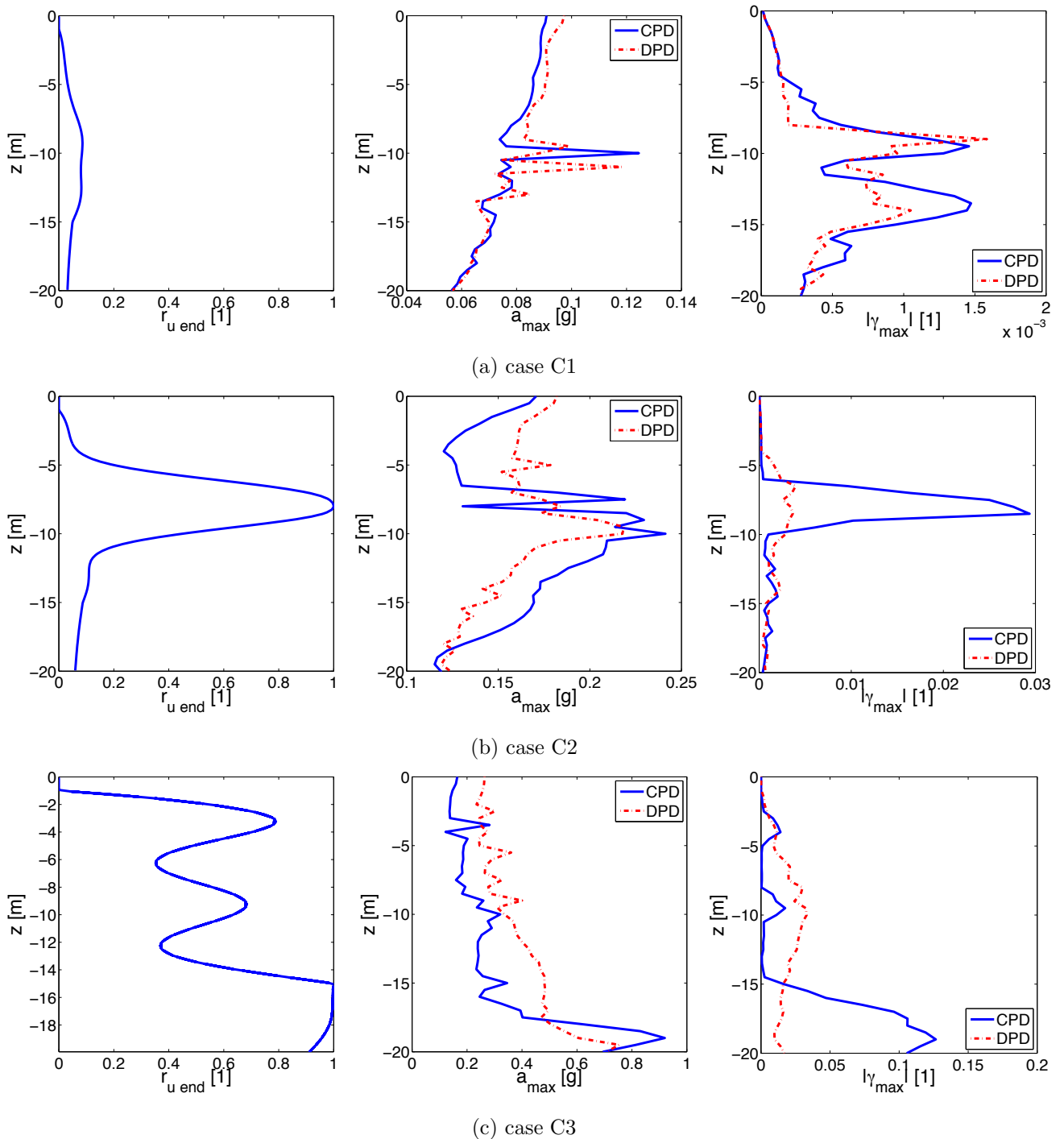


Figure 4.14 – Liquefaction ratio at the end of shaking, maximum acceleration and shear strain profile

For the first case, in Figure 4.14a, the CPD model presents peaks on the acceleration profile that correspond to the peaks on shear strain and the peaks on r_u at about 10m. In the DPD column, however, the peaks on the $|\gamma_{max}|$ and the a_{max} profiles are slightly shifted but follow the

same trend and present the same amplitude. The small differences between the CPD and DPD column can be due to the low pore pressure ratio along the profile ($r_{u\text{end}} < 0.1$). As for the second case, in Figure 4.14b, liquefaction initiated around 8m (i.e. $r_{u\text{end}} > 0.8$) and thus more differences between models are visible. With respect to the a_{max} profile, for the CPD model it can be seen below 8m a maximum twice the PHA value. Immediately above it, the a_{max} drops to values below PHA and once more gradually increases as it reaches the surface. This behavior is important in order to understand the variability in the surface because even if it is a homogeneous deposit, as the motion propagates to the surface a liquefied *layer* attenuates the energy and inhibits liquefaction in shallower soil. Similarly, the $|\gamma_{max}|$ profile has its maximum at the same depth. While for the DPD column, the amplification and deamplification on acceleration are lower, and the peak on the $|\gamma_{max}|$ profile is significantly smaller. Finally, for the third case shown in Figure 4.14c, liquefaction appears in three *layers*, which work as in the previous case. Note how the a_{max} is inversely related to the r_u profile and when the r_u increases, the acceleration is deamplified. The spikes in a_{max} can be distinguished also at the $|\gamma_{max}|$ profile, with strains six times bigger than the average. Regarding the DPD column, and like in the second case, $|\gamma_{max}|$ profile is generally constant and a_{max} has an almost monotonic behavior, although this time it decreases as it approaches the surface.

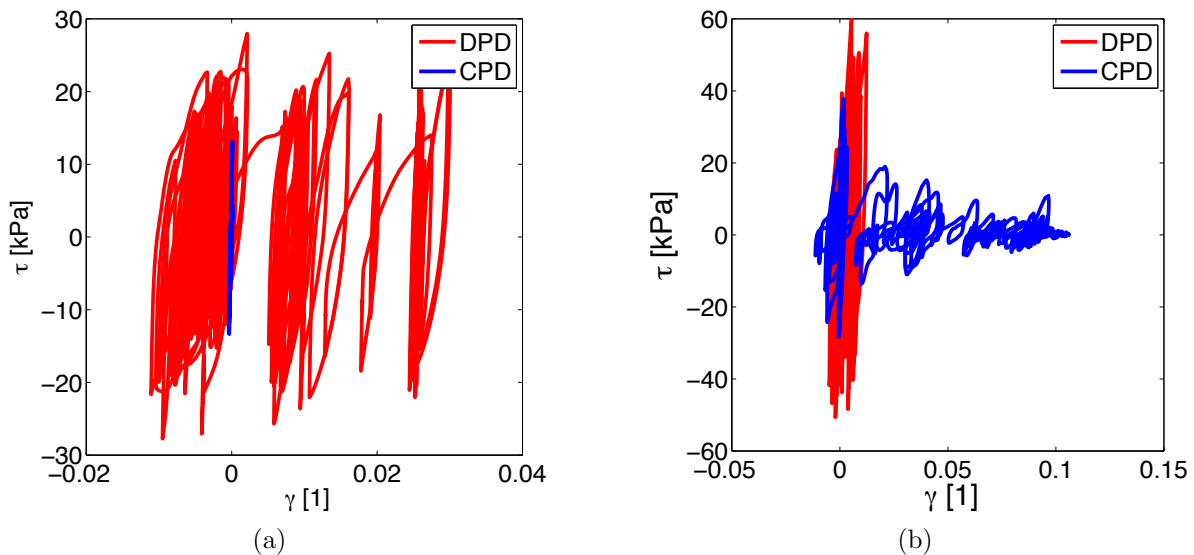


Figure 4.15 – Shear stress and strain plots throughout the shaking with the coupled (CPD) and the decoupled (DPD) model for case C3 at: a) $z=8\text{m}$ and b) $z=18\text{m}$

Figure 4.15 shows the shear stress strain plots throughout the shaking with CPD and DPD analyses for case C3 at two different depths. For Figure 4.15a at $z=8\text{m}$, the DPD analysis presents higher $|\gamma_{max}|$; however, at $z=18\text{m}$, in Figure 4.15b, the soil is completely liquefied and

an important development of permanent deformations is evidenced for the CPD analysis. In contrast, the $|\gamma_{max}|$ of the DPD model is almost constant with depth and there appears to be almost no shear modulus degradation.

4.3.7 Acceleration response spectra

As seen in section 4.3.4, the frequency content of the ground motion is changed because of the nonlinear soil response. This change depends on the evolution of pore water pressure with time and therefore could be better understood if it is separated in different time windows. The influence of coupling excess pore water pressure and deformations will therefore be asset by calculating the response spectra of the surface acceleration from the CPD and DPD models in different time windows. The time instants when the Arias intensity (I_A) of the outcropping acceleration reaches 5 and 95% are used to define these windows because of their relation to the energy of the motion and the evolution of the liquefaction ratio. To exemplify this, the surface accelerogram and the mean and maximum liquefaction ratio in the whole column with the CPD analysis are shown in Figure 4.16 for the 1994 Northridge earthquake presented in Section 4.3.4.

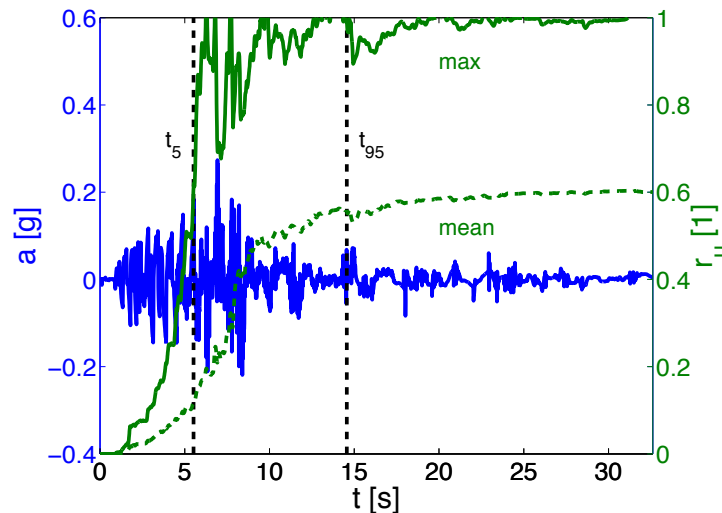


Figure 4.16 – Time histories of the surface acceleration and mean and maximum r_u throughout the profile (CPD model) for Northridge 1994 earthquake

In this case, the spikes on acceleration match the rapid increase of r_u and the two vertical lines, corresponding to t_5 and t_{95} , roughly coincide with the start and end of the maximum and mean r_u increase throughout the profile. To obtain these time series, first the r_u evolution with time is calculated for all depths and the maximum and mean values at each time instant

is taken. It can be seen how the frequency content as well as the amplitude in acceleration changes for the three time windows.

In the surface, the settlement for both analyses is similar at the beginning of the motion (i.e. before t_5), as it is shown in Figure 4.17 for the three cases. During the predominant time window defined by $t_5 < t \leq t_{95}$, important changes are evidenced between the two analyses and as it was seen in Figure 4.11b, the maximum settlement is higher for the DPD model. However, at the last part of the motion (i.e after t_{95}), the settlement is practically constant for the three cases shown.

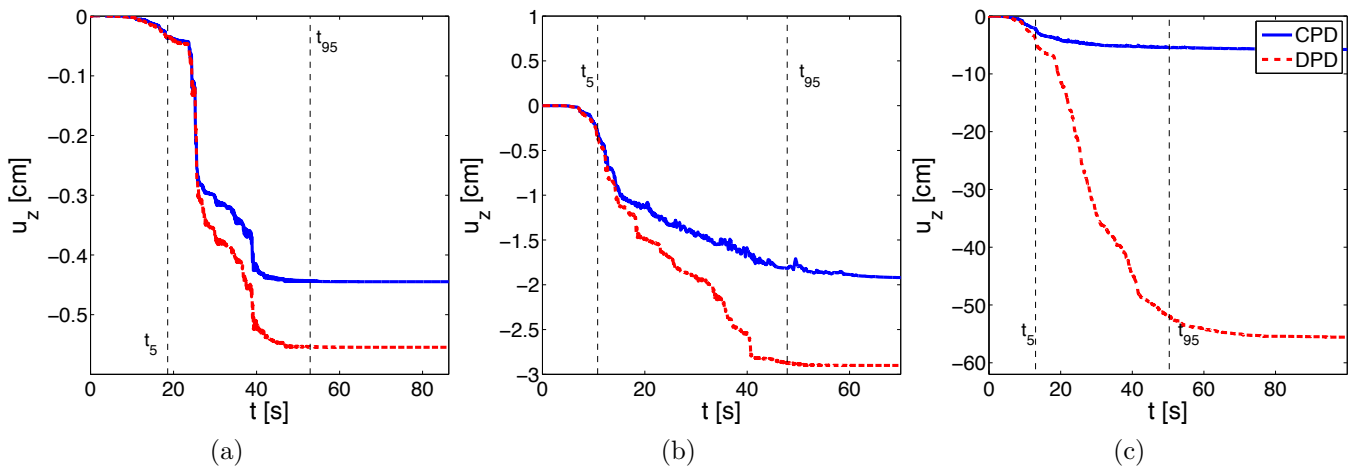


Figure 4.17 – Settlement time evolution at surface for cases: a) C1, b) C2 and c) C3

Similarly, the time evolution of the Arias intensity (I_A) is shown in Figure 4.18 for the three cases. In addition to the surface response, the outcropping Arias intensity is shown in solid black line. In comparison with the settlement time evolution, less differences are evidenced for case C1 while for C2 and C3 the time series differ greatly and earlier. Specially for C3, I_A is still increasing after t_{95} for DPD which is almost ten times the value of CPD. With respect to the outcropping I_A evolution, it can be noted that the energy is first (for C1) amplified by CPD and DPD analyses in the surface by almost seven times. For C2 and C3, the energy rate for CPD decreases when the maximum r_u is above 0.8 hence differences start to be evidenced between the CPD and the DPD analyses. The time instant for this change is close to t_5 , however it can be slightly lower or higher depending on the maximum energy. For this analysis, the latter value is used as it is related to the outcropping motion and is easily obtainable.

The response spectra of the horizontal acceleration at surface are plotted in Figure 4.19 for the three cases and the three time windows. For the first case $r_u \leq 0.03$, thus all time

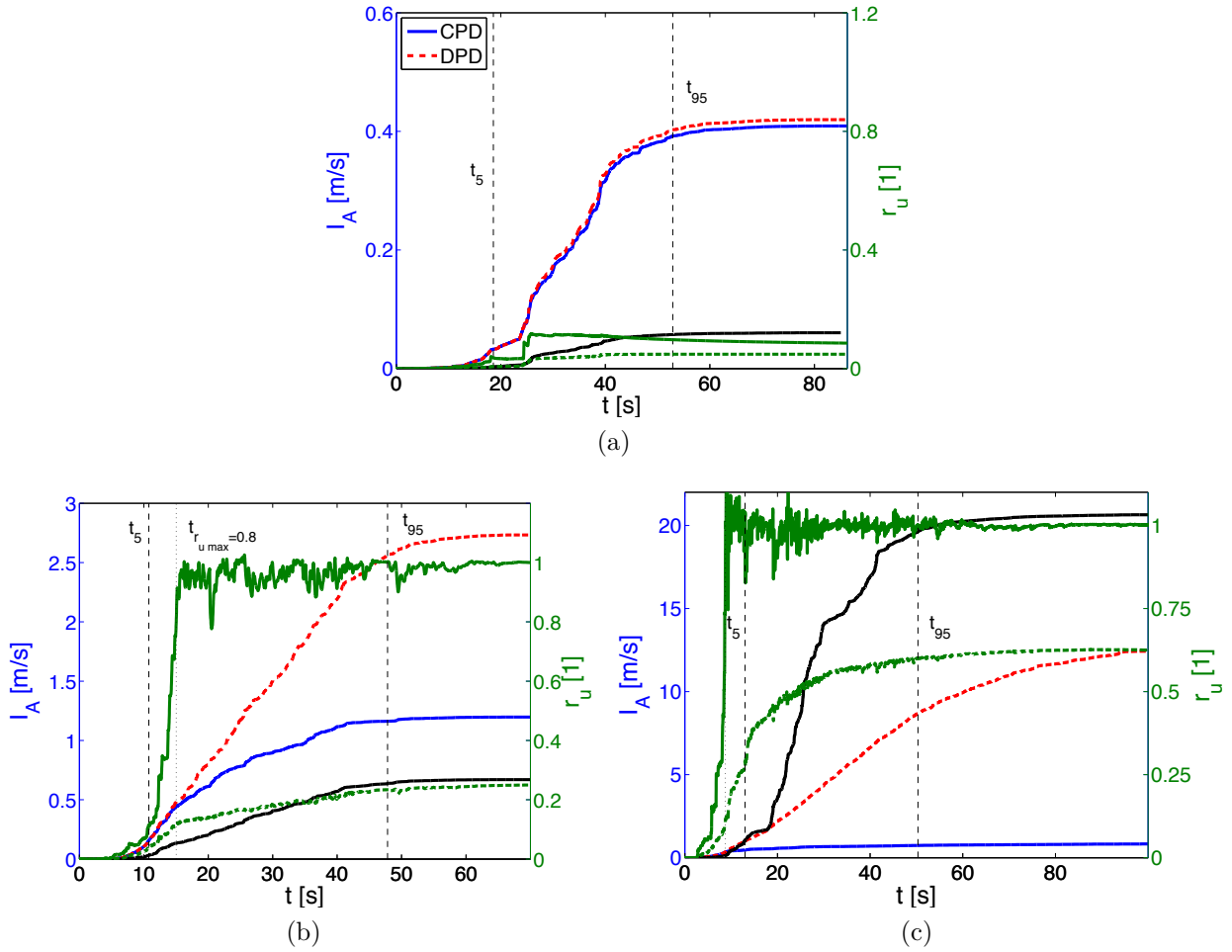


Figure 4.18 – Arias intensity time evolution at surface for cases: a) C1, b) C2 and c) C3. The outcropping I_A is shown in solid black line.

windows have a near match between both models which confirms that significant softening did not occur. While for the second case, only for the first time window (i.e. prior to significant rise of pore pressure), the responses of the CPD and DPD columns are similar. Afterwards, the DPD column produced a much higher peak whereas for the CPD column, the coupling of excess pore pressure and its subsequent soil softening inhibits the transfer of the intense high-frequency peaks to the ground surface. A shift towards the short periods is clearly shown in the second case and after the majority of the energy has passed (i.e. $t > t_{95}$). For periods higher than 1s, the CPD column presents larger spectral values than the DPD column. Lastly, for the third case shown in Figure 4.19c the difference between columns increases, even for the first time window. Thus, as the r_u increases, a great attenuation for the CPD column with respect to the DPD one is seen. As the differences in spectral accelerations between both models are so important, little can be told about the shift in period.

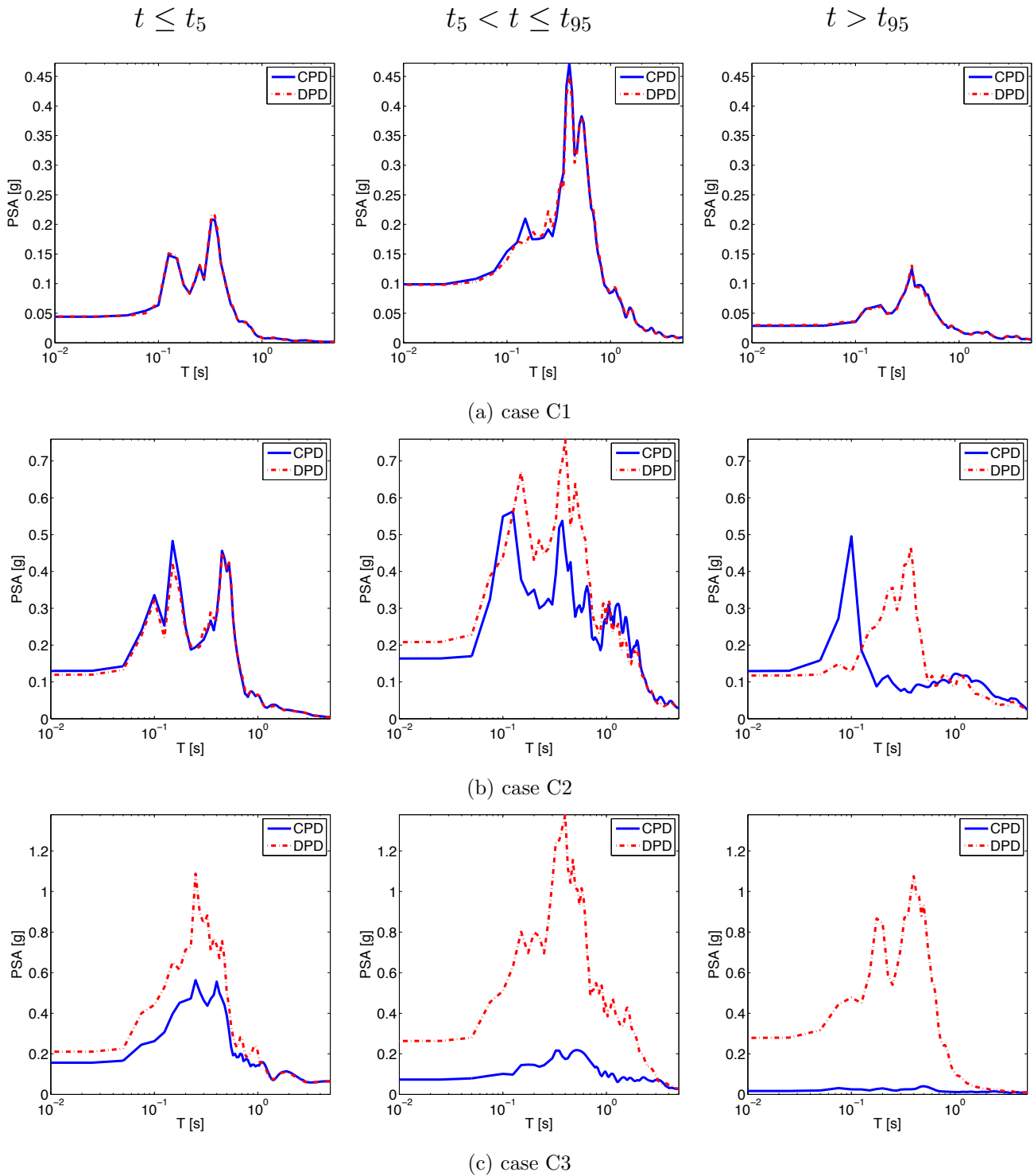


Figure 4.19 – Response spectra of surface acceleration at the different time windows and the different cases

Response spectral ratio

To assess the effect of the soil stiffening on the frequency content of the surface signal, [Hartvigsen \(2007\)](#) proposed to characterize the effects of pore pressure with a response spectral ratio (RSR) defined as:

$$RSR(T) = \frac{PSA_{CPD}(T)}{PSA_{DPD}(T)} \quad (4.4)$$

where $PSA_{CPD}(T)$ corresponds to the horizontal acceleration response spectrum at surface evaluated with the CPD analysis and $PSA_{DPD}(T)$ is the corresponding response spectrum for the DPD analysis. All results are ranged by the $Q_{H=10m}$ value and are shown together with the mean and the standard deviation in Figure 4.20. It can be seen that, although the mean is below unity, some extreme cases presented RSR values above it, i.e. higher PSA values for the CPD analysis. Specially, the CPD amplification at long periods (i.e. $T > 1s$) and also the amplification for periods around 0.05s. Interestingly, this latter is mostly observed for LMS, in Figure 4.20a, while at this period most cases present the minimum RSR values for MDS, in Figure 4.20b. In the previous studies from Hartvigsen (2007) and Gingery et al. (2014), different soils were used and for the analysis they were averaged by the liquefaction resistance (i.e. the inverse of the factor of safety) and the V_{s30} profile, respectively. Thus, probably the particularities of each soil were averaged.

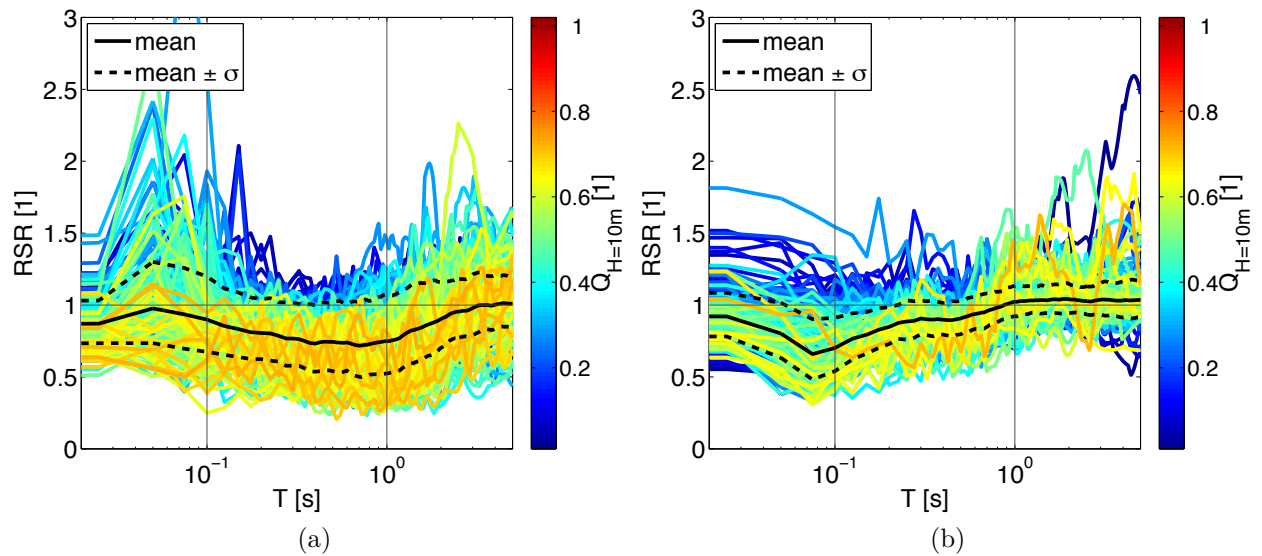


Figure 4.20 – Response Spectral Ratio (RSR) mean and standard deviation for a) LMS and b) MDS. All values are shown ranged by the $Q_{H=10m}$ value

For both LMS and MDS it appears that RSR is related to the liquefaction index ($Q_{H=10m}$). In general, as $Q_{H=10m}$ increases, the RSR decreases for almost all periods. For LMS, at low $Q_{H=10m}$ values the dispersion is higher, but it seems that the average behavior is around unity. However, at the same $Q_{H=10m}$ level, MDS presents a deamplification of the CPD model for periods below 0.1s. For a better comparison with respect to the liquefaction index, the responses

were divided in three groups according to the $Q_{H=10m}$ levels shown in Figure 4.12 and the mean values are shown in Figure 4.21. While for LMS the mean of each group or level are very different from each other, for MDS the three levels presented similar curves.

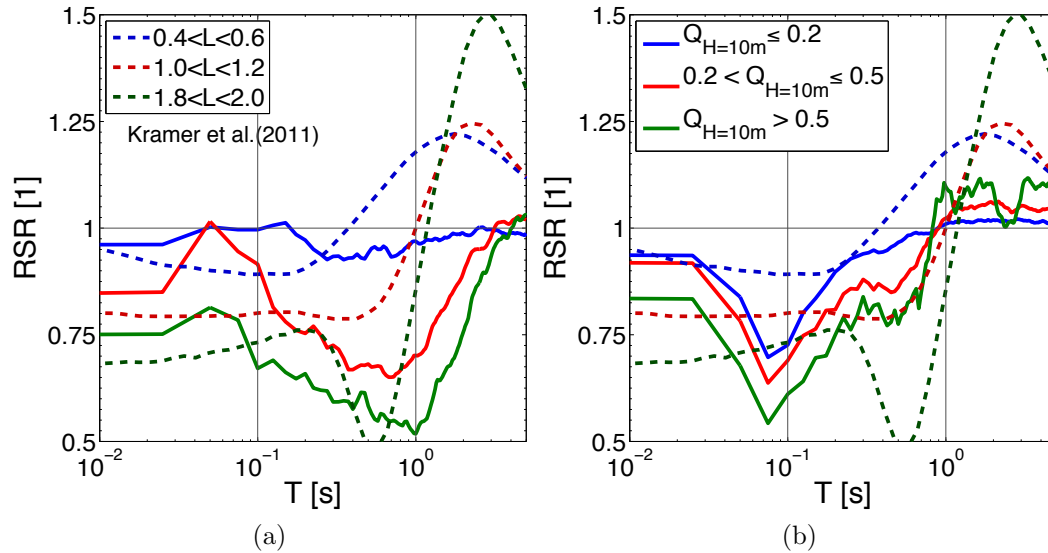


Figure 4.21 – Mean Response Spectral Ratio (RSR) of each $Q_{H=10m}$ level for a) LMS and b) MDS. The mean curves presented by Kramer et al. (2011) are shown in dashed lines.

In Figure 4.21, the mean values presented by Kramer et al. (2011) for different loading parameter (L) ranges are shown for comparison. Recall that L is the inverse of the factor of safety hence, L can be directly related to the liquefaction index. Comparing with the analysis results, the RSR for the smallest period (i.e. the ratio between peak accelerations) are similar to those for LMS. However, the amplifications are higher and shifted to shorter periods. The period between deamplification and amplification presented is about 1s and close to that of MDS. This period appears to be related to the soil type however, as Kramer et al. (2011) used different combinations of very dense gravel with looser sands, the curves present the average shift of all soil types. In addition, the second peak shown for LMS at periods around 0.05s is only visible for the highest L range and is shifted to longer periods (about 0.25s). Once more, the use of very different soil types could explain this difference since for the MDS curves, a trough is presented instead of a peak at about the same periods.

Normalized response spectral ratio

As it can be seen in Figure 4.20, results show a high dispersion, in part because each input motion presents a different peak acceleration. Seed et al. (1976) recommended that to examine a wide range of input motions without reference to the specific variations in acceleration, the

response had to be normalized. Additionally, the deamplification of the PGA due to CPD, has already been discussed in section 4.3.5. Thus, for the normalization, the PGA is used, which corresponds to the value of the response spectra at the shortest period evaluated. Therefore the normalized response spectral ratio (NRSR) is defined as:

$$NRSR(T) = \frac{PSA_{CPD}(T)/PGA_{CPD}}{PSA_{DPD}(T)/PGA_{DPD}} \quad (4.5)$$

where $PSA_{CPD}(T)/PGA_{CPD}$ corresponds to the normalized response spectrum at surface for the CPD model and $PSA_{DPD}(T)/PGA_{DPD}$, for the DPD model. Figure 4.22 shows the mean NRSR for each of the three groups according to the $Q_{H=10m}$ levels shown in Figure 4.12. It can be seen that the CPD amplification of periods around 0.05s for the LMS and the deamplification for the MDS are more visible. Interestingly, at these periods, the highest amplification is for medium levels of liquefaction (i.e. $0.2 < Q_{H=10m} < 0.5$); while at long period, the highest amplification is for the highest liquefaction level (i.e. above 0.5). This aspect agrees with the conclusions of [Gingery et al. \(2014\)](#) concerning the acceleration spikes of cyclic mobility.

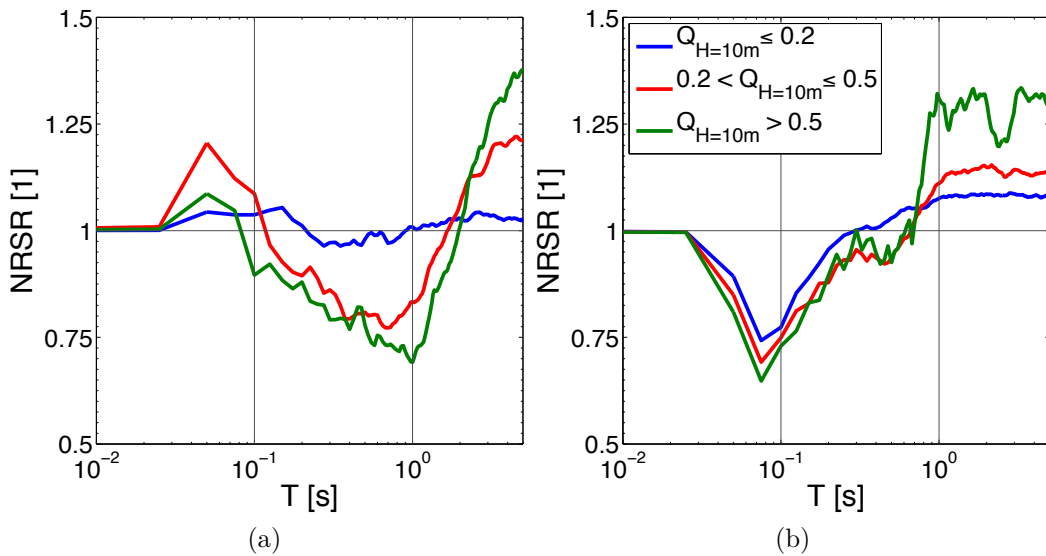


Figure 4.22 – Mean Normalized Response Spectral Ratio (NRSR) of each $Q_{H=10m}$ level for a) LMS and b) MDS

As in the analysis of the individual cases, the NRSR evolution with time is shown in Figure 4.23 for the loose-to-medium sand. In it, the logarithmic mean NRSR curves are obtained for each time window. Once more, for the time window before t_5 (i.e. before the energy of the motion has arrived), the NRSR are almost equal to 1 for all cases. As for the other time windows, 3 parts can be distinguished. For periods between 0.1 and 1s, the DPD model presents higher

values of acceleration. Thus, the analyzes without coupling would be conservative. However, it is interesting to note how as the liquefaction potential and the time increases, the NRSR increases for the low (i.e. $T < 0.1s$) and high ($T > 1.0s$) periods. These values can attain important discrepancies of up to 2.5. As it can be seen, high period amplification in the more liquefied soils is not fully considered in models that lack of coupling pore pressure. Hence, the response of buildings with high predominant periods could be non-conservative. Another important discrepancy between the CPD and DPD models is found for periods around 0.05s and was also shown for the case C2 in Figure 4.19b. The peak in the CPD model could be due to coseismic pore-water migration and consequent soil recovery which could not be present in the DPD model. Once more, structures with periods around this value could be subjected to higher accelerations if a CPD analysis were to be used.

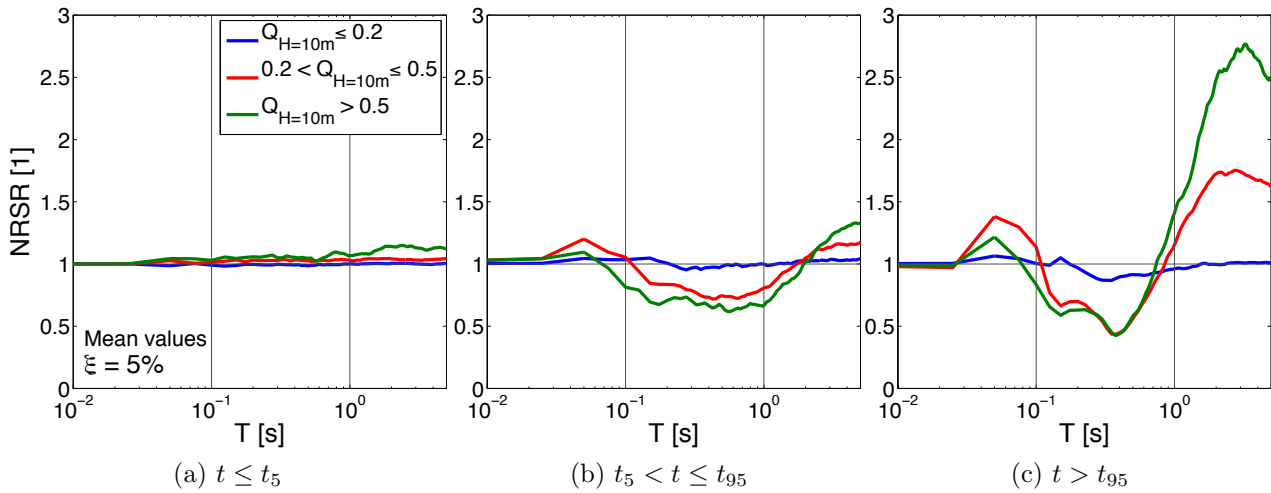


Figure 4.23 – Mean NRSR values ranged by Q levels for LMS

The logarithmic mean NRSR curves obtained for each time window for the medium-to-dense sand are shown in Figure 4.24. Contrarily to LMS, for low levels of liquefaction NRSR is not equal to unity, not even before the ground motion. Instead, for all levels of liquefaction and specially for the first two time windows, a minimum on NRSR is evident at periods around 0.05s. Additionally, the differences between the CPD and the DPD models at long periods is shifted, for $T \approx 0.8s$. Nonetheless, for longer periods the CPD model presents higher values of acceleration. They can attain important discrepancies of twice the value of the DPD model. Even if the soil density is higher and that it appears to have a dilatant tendency; at high acceleration levels, there is still a shift to lower frequencies captured in the CPD models. However, high period amplification for strong ground motions is not present in decoupled pore

pressure and deformation models.

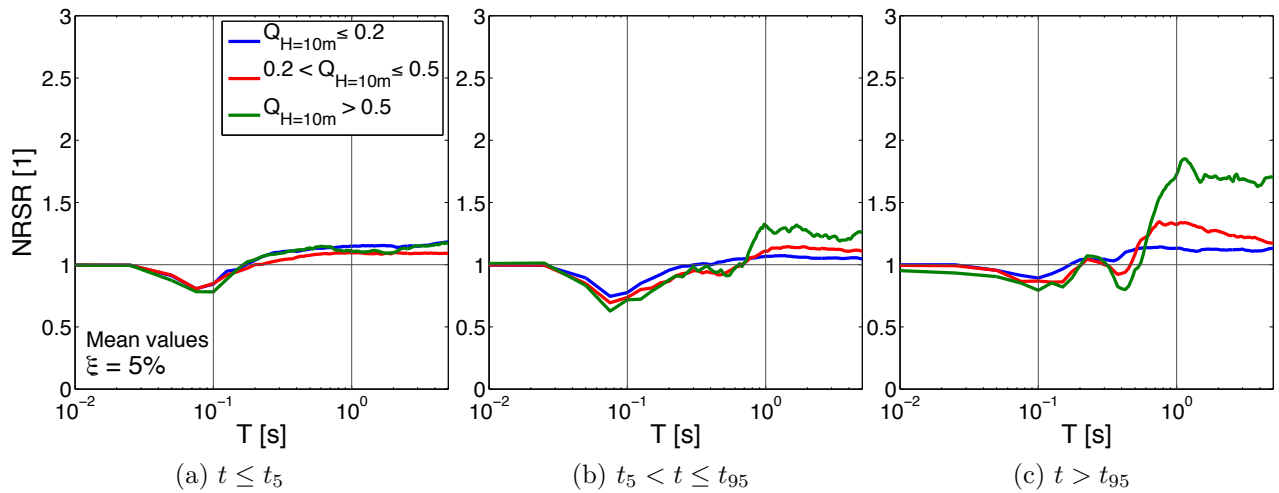


Figure 4.24 – Mean NRSR values ranged by Q levels for MDS

As an attempt to include the effects of pore pressure generation, [Hartvigsen \(2007\)](#) proposed a function relating the amplification of the acceleration with the seismic hazard and the soil properties. However, given the great variability of the spectral ratio with period, input motion and soil properties, as shown in [Figure 4.20](#), it is unlikely to capture the detailed effects of Δp_w coupling on individual response spectra with an overall function. Due to the proper input motion variability, individual cases can be somewhat different of the general case (e.g. peaks for periods around 0.08s). On that account, for a complete analysis of important structures the use of a constitutive model with coupling excess pore pressure and soil deformation would be recommended when Δp_w is significant and strong ground motions are expected.

4.3.8 Partial conclusions

A finite element analysis was used to investigate the effect of coupling excess pore pressure and soil deformation on the nonlinear response. Two soil profiles of 20m have been used: a loose-to-medium (LMS) and a medium-to-dense sand (MDS). Two mechanically equivalent models were subjected to 183 unscaled earthquake motions: one taking into account coupling (CPD) and one without (DPD). The same effective-stress model was used for the calculations and the initial elastic behavior was proved to be the same.

The present study aimed to highlight the importance of accurate modeling of liquefiable soils in order to improve performance-based earthquake engineering. In fact a simple geometry

is used to illustrate the problem, although a 2D SSI model will be presented in the following section to analyze the effect of CPD on the structure performance.

The preliminary conclusions drawn from this study are as follows:

- The acceleration is amplified at surface for small input motions and deamplified for stronger ones in the DPD as well as in the CPD model. Nonetheless, deamplification for strong ground motions is more significant in the CPD column and it increases with PHA as it accounts for softening of liquefied soils in addition to the proper strain-related degradation. As a result, models that do not include coupling of excess pore pressure will predict higher surface accelerations. As the relative density of the soil increases, the effects of coupling decrease thus they are still present.
- The surface Arias intensity as well as the co-seismic settlement are highly overestimated by the DPD model with respect to the CPD one. For strong ground motions, settlements can be even six times greater without coupling.
- It appears that the difference between maximum surface acceleration for the two models is related to the Liquefaction Index ($Q_{H=10}$), hence as the liquefaction zone increases the need for a more complete analysis is required.
- Regarding the soil behavior throughout the profile, it can be concluded that spikes of acceleration are found at the same depth of spikes of shear strain and maximums on liquefaction ratio for the CPD model; however, shear strain spikes on the DPD model do not correspond to spikes in acceleration thus other mechanisms are involved.
- Concerning the response spectra, it appears that the DPD model underestimates the amplification at low and high periods while it overestimates the spectral amplitudes at periods between 0.1 and 1s, for the LMS profile. This variation is more important in the time interval after the 95% of Arias intensity as the soil has softened on the CPD model. Moreover, this variation increases with the liquefaction zone. On the MDS profile, the response spectra is also underestimated by the DPD model for high periods. For cases where the liquefaction index is above 0.5 and after the predominant window of the motion, the DPD model presents twice the value of the CPD model.
- From a probabilistic point of view, the response spectra follows the same trend; although the variation between one event and another is significant. Therefore a generalization would be unlikely to capture the detailed effects of pore pressure coupling.

4.4 Soil structure interaction response

This section concerns the assessment of the effect of excess pore pressure (Δp_w) and deformation for the nonlinear response of liquefiable soils on the structure performance. A 2D soil-structure interaction (SSI) model was analyzed. The ECP elastoplastic multi-mechanism model (Aubry et al., 1982; Hujieux, 1985) is used to represent the soil behavior. Due to computational costs of a 2D model, the models were subjected to 90 unscaled earthquake signals chosen from the previously used set. To account for the effect on the SSI, two structures with different predominant periods were used. As seen in the previous section, the effect of coupling pore water pressure and soil deformation is most important when the soil is loose and significant Δp_w is generated. Hence, in this section only the loose-to-medium sand (LMS) is used. In the interest of quantifying the effect of Δp_w on the SSI, two mechanically-equivalent models -one with coupled pore water pressure and soil deformation (CPD) and one without (DPD) - were performed with the same effective-stress analysis. Three aspects were evaluated: i) the response spectra of acceleration at surface and at the structure, ii) the structure settlement and iii) the structure seismic demand.

4.4.1 Structure model

In order to take into account the interaction effects between the structure and the soil, the modified width plane-strain condition developed by Saez et al. (2013) was assumed in the finite element model. Two soil-structure interaction models are considered in this work. A width of 4m is used for the soil profile in both models. The dynamic performance of the structures tested is different as they have different height, weight and predominant periods. The structures used will be called B01 and T040. They simulate reinforced concrete (RC) buildings with a shallow rigid foundation, standing on saturated cohesionless soil. A schema of the models is shown in Figure 4.25. Three points are marked for future reference: free-field response at 3m from the boundary (FF), structure's base (SB) and structure's top (Top).

B01 is modeled as a RC frame of one span and two stories and T040 is a single-degree-of-freedom (SDOF). Both structures lay on a 6m width and 10cm thick rigid foundation. Concerning the soil model, a 50m wide and 20m thick deposit is overlaying an elastic bedrock. The soil corresponds to the loose-to-medium (LMS) sand of the previous section.

In order to simulate the B01 structure, plastic hinge beam-column elements are used which take into account axial force (F) and bending moment (M) interaction (Prakash et al., 1993).

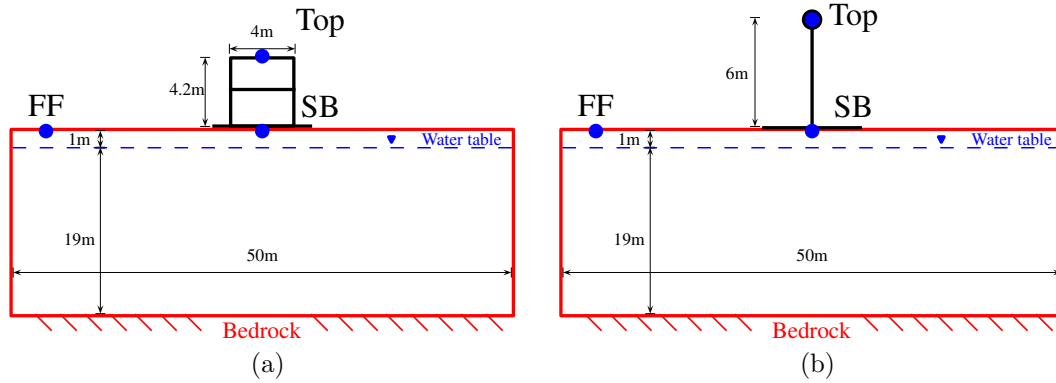


Figure 4.25 – Schema of the numerical model for a) B01 and b) T040

The force and moment diagram for the beam elements in B01 is shown in Figure 4.26. This structure is a large-scale, one-span, two-story frame model proposed by [Vechio and Emará \(1992\)](#). In contrast, the T040 is a single degree of freedom (SDOF) modeled with an elastic perfectly plastic behavior and is equivalent to a one-span, three-story building ([Saez et al., 2013](#)). It is a simplified model of a moment frame mid-rise structure according to the building type classification of [HAZUS-MH MR3 \(2003\)](#). This additional structure is used in this study to highlight the effects of the soil behavior in the structure performance near resonance. The main characteristics of both structures are shown in Table 4.3. Between the structure's foundation and the soil, interface elements are used to allow relative movement of the structure with respect to the soil, in order to avoid the traction effect. These elements follow a Coulomb-type plastic criterion.

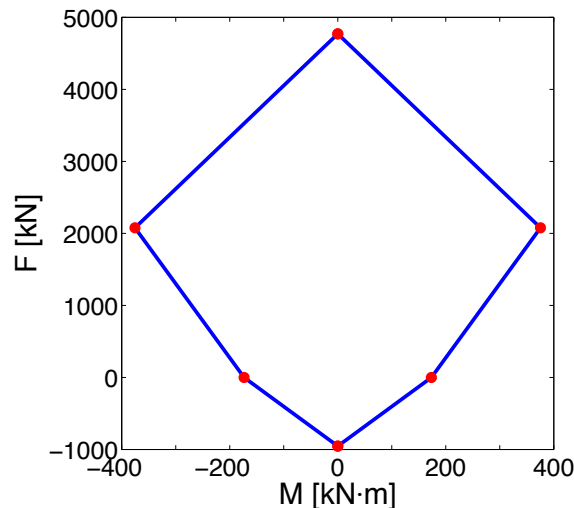


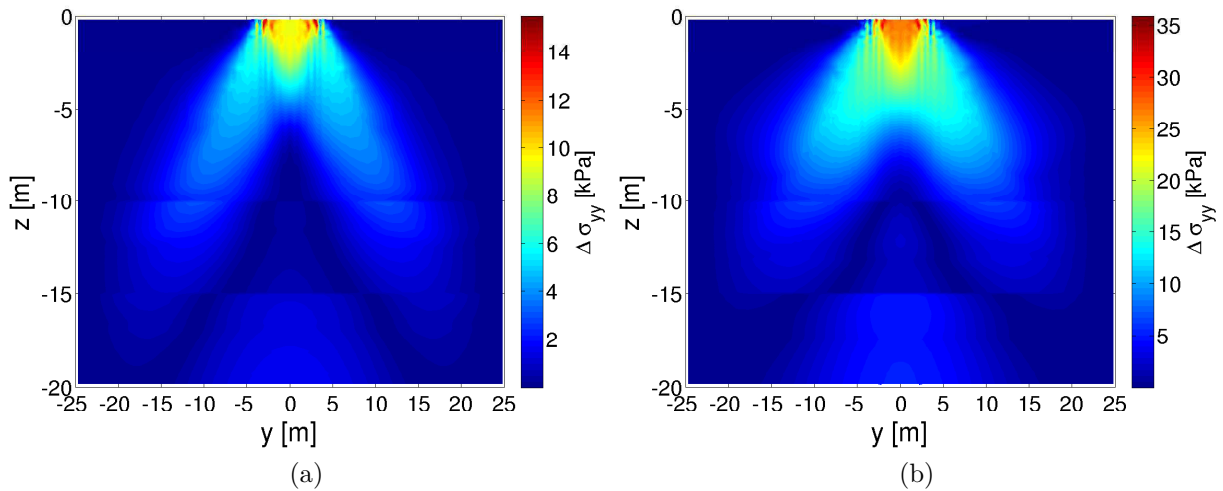
Figure 4.26 – Force and Moment diagram for beam elements in B01

The effect of the building's weight on the increment of the horizontal stress state ($\Delta\sigma_{yy}$) in

Property	B01	T040
Total height [m]	4.2	6
Width [m]	4	N/A
Mass [ton]	45	120
Fundamental fixed-base period T_0 [s]	0.24	0.40

Table 4.3 – Structures properties

the deposit is shown in Figure 4.27. It is noted that as the weight of the structure increases, so does the effect on the soil stress state. The effect on the stress state is greater under the structure's foundation and decreases approximately with the square of depth. The significant depth (D_s) was defined by Terzaghi (1943) as the pressure bulb of 20% of the external loading because approximately 80% of the structure's settlement takes place above this depth. For B01, D_s is about 4m and for T040, it is about 11m.

Figure 4.27 – Increment of the horizontal stress ($\Delta\sigma_{yy}$) before shaking for a) B01 and b) T040

The building's weight affects the stress state (horizontal, vertical and shear) and also the volumetric deformations, hence it affects the “distance to reach the critical state”, defined in the ECP model by the degree of mobilized friction (r_k) explained in section 3.3 as follows:

$$r_k = \frac{q_k}{p'_k \cdot F_k \cdot \sin \phi'_{pp}} \quad (4.6)$$

where p'_k is the mean stress, q_k is the deviatoric stress, ϕ'_{pp} is the friction angle at the critical state and F_k is the isotropic hardening associated with the volumetric plastic strain (ε_v^p). Thus, the effect of the building's weight on the soil behavior is better related to the degree of mobilized friction (r_k) which is shown in Figure 4.28 for both structures. As the r_k value approaches

unity, the soil approaches perfect plasticity. Evidently, the soil under the building presents higher values. Additionally, as T040 is heavier, the effect on r_k is higher. As the coefficient of earth pressure at rest (k_0) also increases with the building load, the surrounding soil is stiffened but without the effect of the shear stress. Thus the soil on this region will present higher liquefaction resistance.

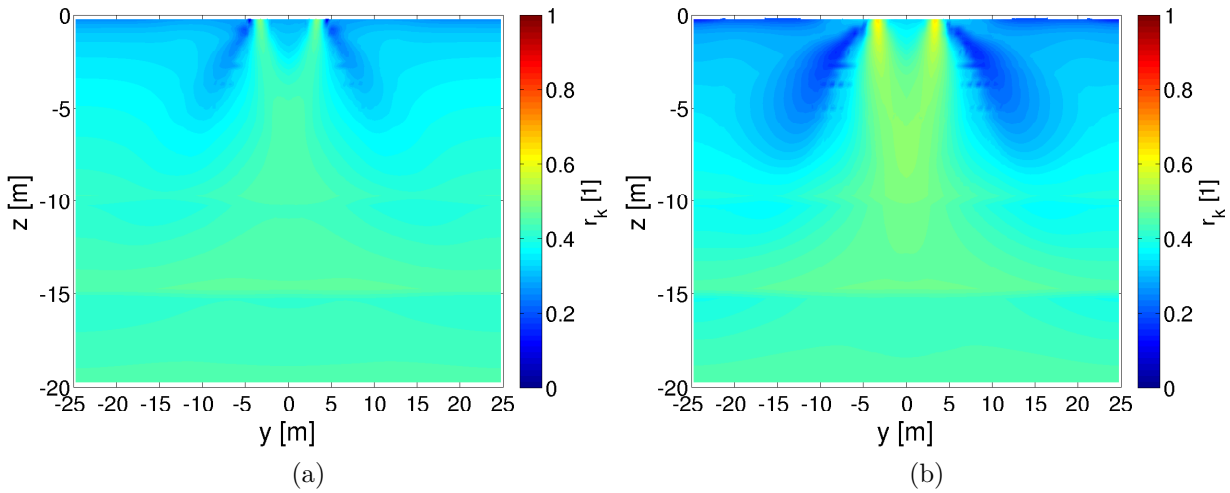


Figure 4.28 – Degree of mobilized friction (r_k) before shaking for a) B01 and b) T040

Concerning the initial seismic behavior, Figure 4.29 shows two transfer functions ($|TF|$) - with fixed base and with soil-structure interaction (SSI) effects (top/FF) for the two structures. In addition, the $|TF|$ of the soil deposit (FF/bedrock) is also shown. A scaled motion with a very low amplitude (i.e. $PHA \approx 1 \cdot 10^{-5}g$) was used to evaluate the pseudo-elastic behavior of both soil and structure. Firstly, it is interesting to note that, even if B01 has two stories, only one resonant frequency (or mode) is observed - as the other one is above 15Hz. Hence both structures behave as SDOFs. The SSI effects consist of a shift to lower frequencies due to the flexibility of the foundation soil and a deamplification due to the material and radiation damping added by the soil (Mylonakis and Gazetas, 2000). As expected, structure B01 being more rigid presents a higher interaction with the soil foundation; hence, the deamplification and the frequency shift are greater. Nevertheless, the relative position of the fundamental frequency of the soil with respect to that of the structure and the frequency content of the input motion is very important for the inelastic dynamic SSI effects (Saez et al., 2013). Thus, as T040 main frequency is lower than that of the soil, higher SSI effects are expected when nonlinear soil degradation causes a shift of the soil frequency to lower values.

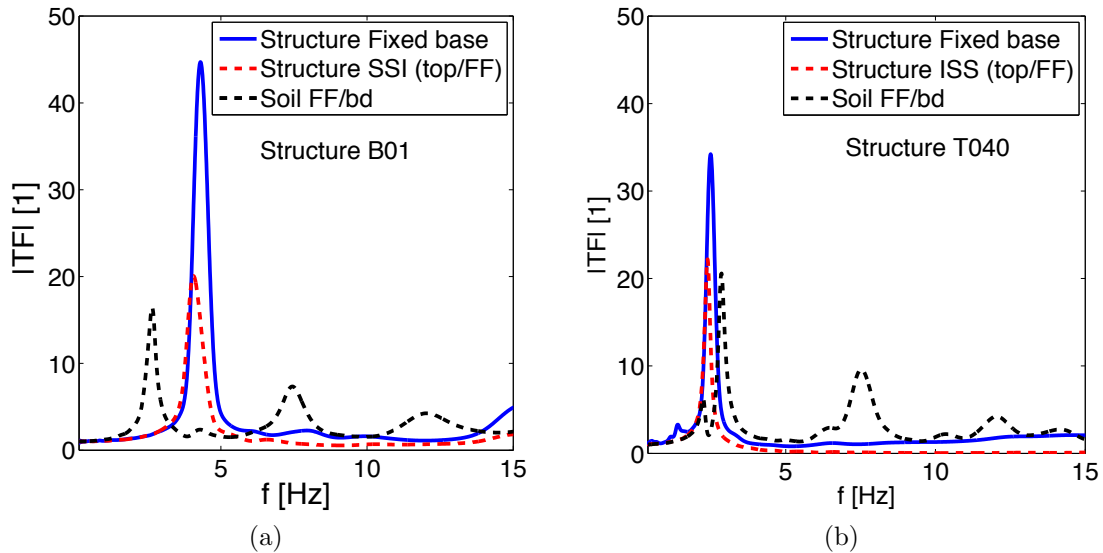


Figure 4.29 – Transfer function of the free-field and the structure for a) B01 and b) T040

4.4.2 Input earthquake motions

Due to the computational cost of the 2D SSI model, not all the input motions used in the analysis of the free field response were used. As was seen in the previous section, the effect of coupling pore-pressure and deformation is mostly important for the nonlinear soil behavior. Therefore, only near-to-source strong motions recorded in dense soil conditions with mostly PGA above $0.3g$ were chosen from the initial selection. In total 90 recordings were used. The events range between 6.2 and 7.7 in magnitude and the recordings have site-to-source distance below 70km and dense-to-firm soil conditions (i.e. 30m averaged shear-wave velocity (V_{s30}) above 600m/s).

The histogram of some intensity measures (IM), defined in appendix C, is shown in Figure 4.30a for the motions used in the 1D FF analysis (in blue) and the motions selected for the 2D SSI model (in red). As it is noted the difference is mostly on the PHA value however, all the other IM distributions are also affected. Figure 4.30b shows the response spectra of all the input earthquake motions. PSA for the motions only used in the 1D FF analysis are shown in light gray while the ones used in both analysis are in dark gray. Concerning the latter, the average PHA is above 0.3 but some weak motions were also tested for comparison.

4.4.3 Initial SSI model response

As in the 1D model, it is important to verify that the only difference in the CPD and DPD models response is due to pore water pressure generation. Thus, the degree of mobilized friction

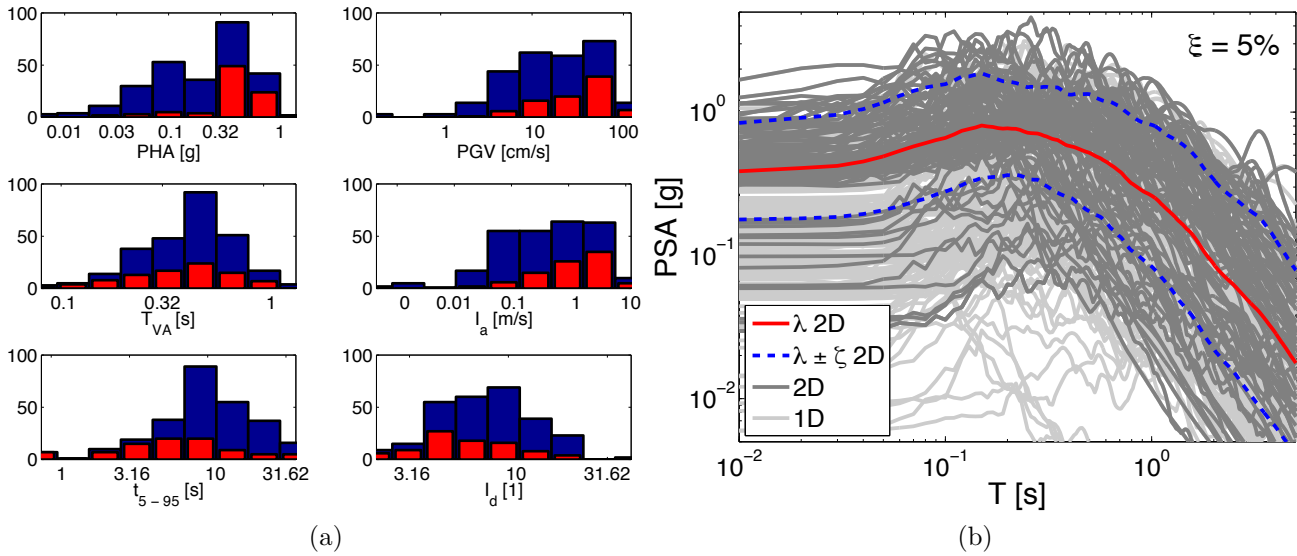


Figure 4.30 – Input motions used for the SSI model: a) IM histogram comparison with 1D FF analysis (in blue) and b) response spectra of acceleration for the outcropping motions

(r_k) before shaking is shown in Figure 4.31 for both analyses in the model with T040. This value accounts for the deviatoric and mean stresses as well as the volumetric strains, thus, if both analyses present similar initial r_k values, it is possible no difference is presented in the other parameters. As no significant difference is noticed; it can be proved that the initial behavior of both deposits is identical. Therefore, differences in the response will only be due to the effect of Δp_w on the coupled model. These parameters were also evaluated for both analysis with B01 but as the results between CPD and DPD were similar, they are not shown here for the sake of brevity.

4.4.4 Seismic soil behavior

The effect of coupling pore pressure and soil deformations on a soil-structure interaction model is highly complex and will affect several aspects of the response. First the analysis for one input motion will be shown and then some results concerning all the motions will be addressed.

As explained in section 4.2, the main difference in the analyses will be given by the induced strains due to pore pressure generation. As the latter increases, the difference in the soil deposit in terms of acceleration, shear strains and settlements increases. Figure 4.32 and Figure 4.33 show the time histories of different parameters observed on the SSI model with T040 structure and for one motion tested. The motion used is the Mw 6.93, January 1994, Northridge earthquake recorded in Pacoima Dam in southern California. The unscaled record was taken from the PEER database under the RSN 788. This station has a site-to-source distance (R_{JB}) of

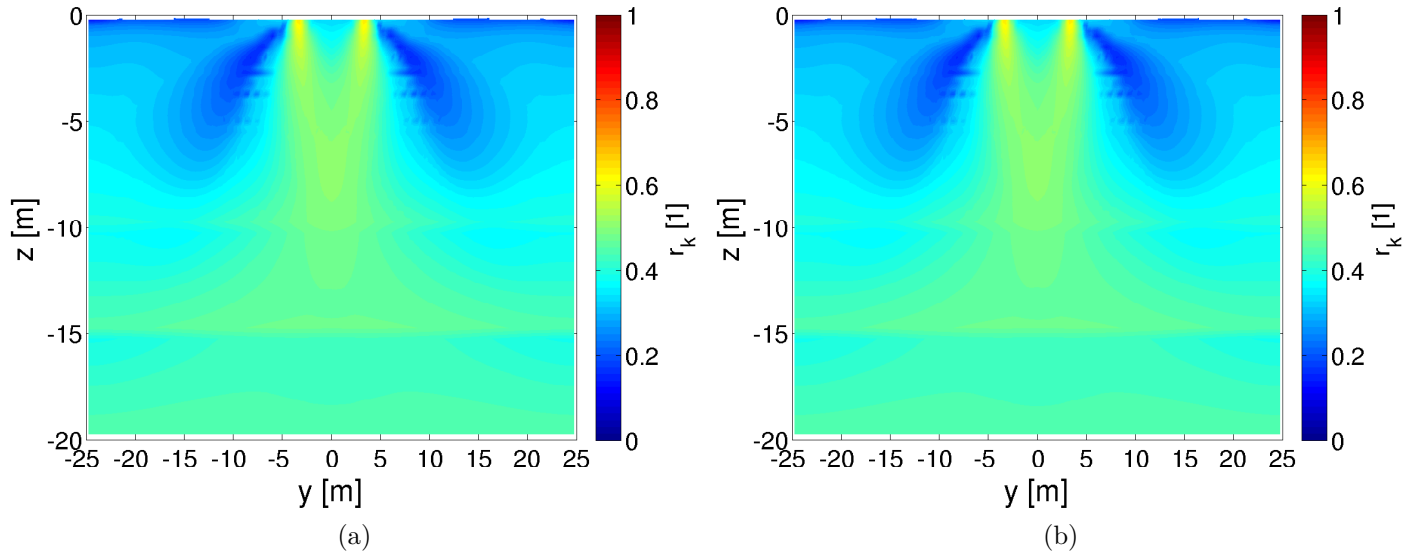


Figure 4.31 – Degree of mobilized friction (r_k) before shaking in the model with T040 for a) CPD and b) DPD analyses.

73km and a 30m-averaged shear-wave velocity (V_{s30}) of 895m/s. First, in Figure 4.32, the time evolution of the liquefaction ratio ($r_u = \Delta p_w / \sigma'_0$) is shown for a profile far from the structure -i.e. in free field, refer to point FF in Figure 4.25. Below the r_u profile, the acceleration time history at the outcropping bedrock is shown. It can be noted that although the same soil properties are used for each layer, due to the increase in mean stress and the stress ratio difference, pore pressure generation appears heterogeneously in the deposit. Additionally, the differences in the frequency content of the motion causes liquefaction at different times. Recalling from the previous section, liquefaction is said to be triggered when r_u equals 0.8. Thus for this motion, liquefaction first appears between 6 and 7m depth at around 8s, then it starts in two other deeper zones. After the predominant duration of the motion, i.e. at around 15s, the pore pressure migrates to other depths. At the end of shaking, r_u is almost evenly distributed and it is above 0.8 for depths between 5 and 15m.

The surface acceleration time history is easily related to the liquefaction evolution with time, as it is shown in Figure 4.33a for the structure's base. With respect to the outcropping motion, the surface peak amplitude is almost one third for the DPD model and is slightly lower for the CPD one. After the first liquefaction triggering at 8s, the responses start to differ. The CPD model presents a shift towards low frequencies after approximately 10s, while the DPD shows higher spikes at higher frequencies. Similarly, the relative settlement of the structure with respect to free field ($|u_z|$), shown in Figure 4.33b, evolves differently starting from 8s. Due

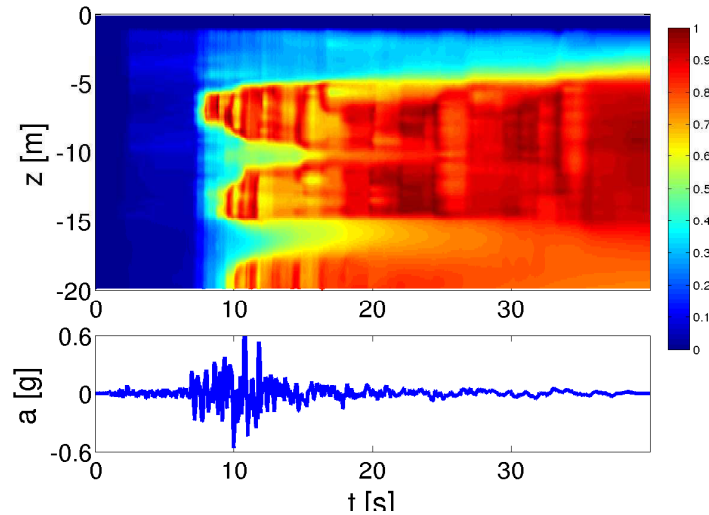


Figure 4.32 – Time history liquefaction ratio at free-field (i.e. near the boundaries of the 2D model with T040 structure) for one motion tested. Below is the acceleration time history at the outcropping bedrock

to the pore pressure migration, evidenced in Figure 4.32, differences in $|u_z|$ are greater after the predominant duration of the motion and by the end of the shaking, the CPD model presents results more than 4 times higher than the DPD. The CPD acceleration time history after liquefaction triggering shows large acceleration peak values riding over a low frequency carrier, which are due to the dilatant tendency of cohesionless soils near the phase transformation line and have been observed in surface earthquake recordings by among others [Bonilla et al. \(2011b\)](#); [Gingery et al. \(2014\)](#); [Kramer et al. \(2015\)](#). Note that the relative settlement rate follows these peaks, for example about 26s and 35s. In contrast, the rate on $|u_z|$ for the DPD model appears to be negligible after the PHA value.

Concerning the entire deposit an important issue is the building load and its effects on the soil behavior. Figure 4.34 shows the liquefaction ratio at the end of shaking for all the deposit with T040. As the soil under the structure is stiffened, liquefaction is not presented there; however, around this area and because of the differences in the stress state, high r_u values appear beyond the structure's influence, with respect to free-field.

Figure 4.35 shows the maximum shear strains for the CPD and the DPD models. For the former, values are often twice the value of those in the DPD model. Furthermore, while for the CPD model, the maximum values appear to be related to the places where maximum r_u values are located; for the DPD, the maximum values are more evenly distributed through the deposit.

In terms of time history and in the entire deposit, the response for each motion varies

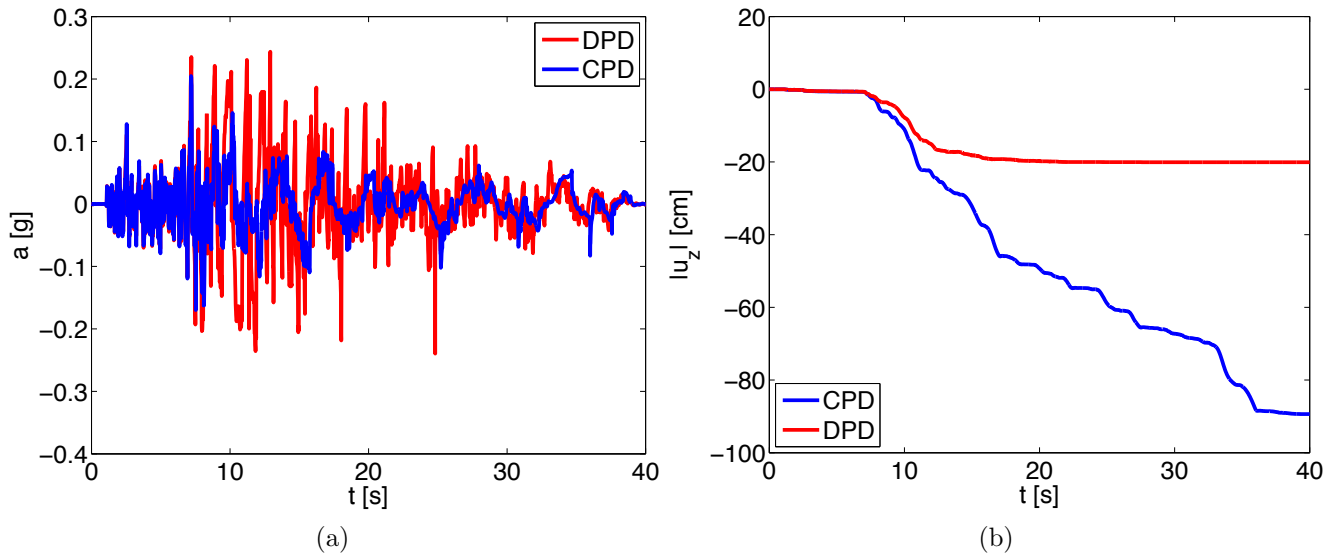


Figure 4.33 – Time history analysis for one motion tested: a) acceleration at T040 structure's base and c) relative settlement of T040 structure with respect to free field

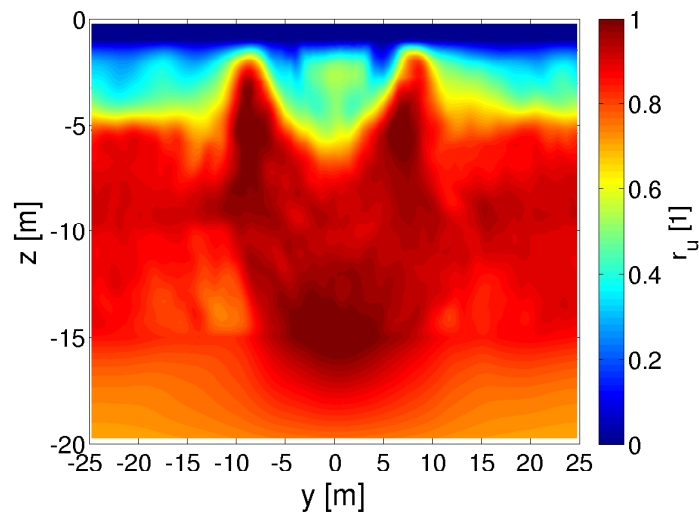


Figure 4.34 – Liquefaction ratio at the end of shaking for one motion tested in the SSI with T040

greatly, due to the differences in frequency, energy and duration content of the motion. Hence to analyze all the motions tested, focus will be given to three engineering demand parameters (EDPs): (1) peak ground acceleration (PGA) at the structure's base, (2) co-seismic relative settlement of the structure with respect to free field ($|u_z|$) and (3) maximum inter-story drift (ISD). These parameters are often used for seismic structure performance when SSI effects are taken into account and are often used for numerical analysis.

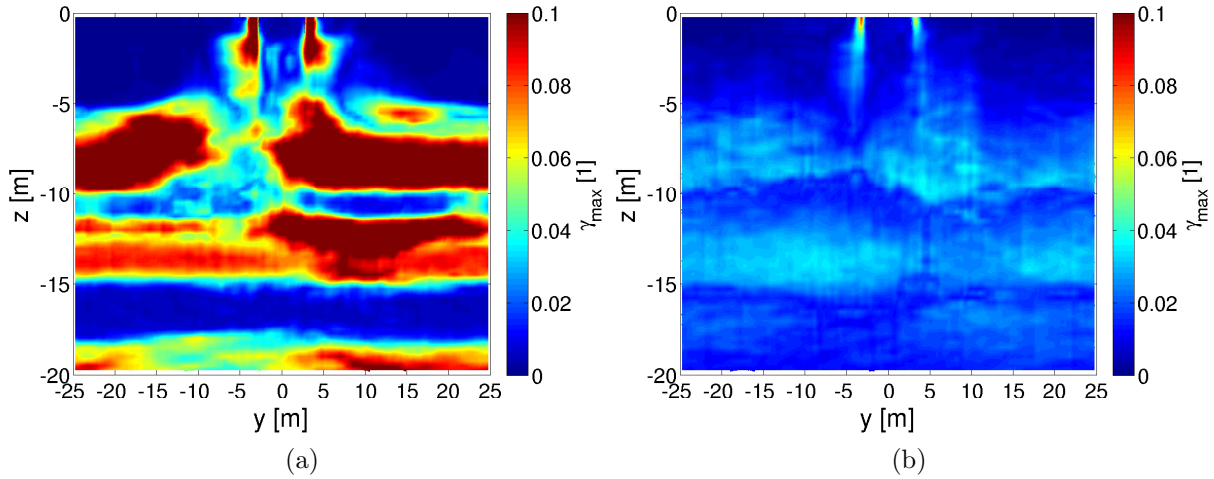


Figure 4.35 – Maximum shear strains for one motion tested in the SSI with T040: a) CPD and b) DPD analyses

4.4.5 SSI effects on a 2D model

Before analyzing the effect of coupling pore pressure and deformations, the SSI effects will be identified. On that account the 2D model without the structure was subjected to the suite of motions. Differences between 1D and 2D models are presented in appendix B and solely the effect of the structure's presence will be presented in this section. Figures 4.36 to 4.38 show the comparison between some EDPs evaluated in the model with the structure (FF SSI) and without (FF 2D). As expected, the results vary for the building used and for the type of analysis.

Regarding the acceleration at surface, the PGA values at 3m from the left lateral boundaries (refer to point FF in schema 4.25) are shown in Figure 4.36. As the PGA level increases, the effect of the SSI is more important. While for B01 the acceleration peak is higher when the SSI is presented, it is the contrary for the T040. Additionally, more differences are presented in the CPD analysis which is expected since it is affected by the liquefaction ratio that evolves differently in the deposit.

The maximum settlement (u_z) at FF 2D is also affected by the inclusion of SSI effect as shown in Figure 4.37. As expected, u_z is reduced when the structure is present. Once more, with the CPD analysis the differences are greater than with DPD analysis and appear to increase with u_z (i.e. increase of PHA). CPD values reached up to 4 times less the value when SSI effect is present. Later on in order to assess the effect of coupling pore pressure and deformations on the SSI response, the settlement of the structure will be given relative to the settlement on FF

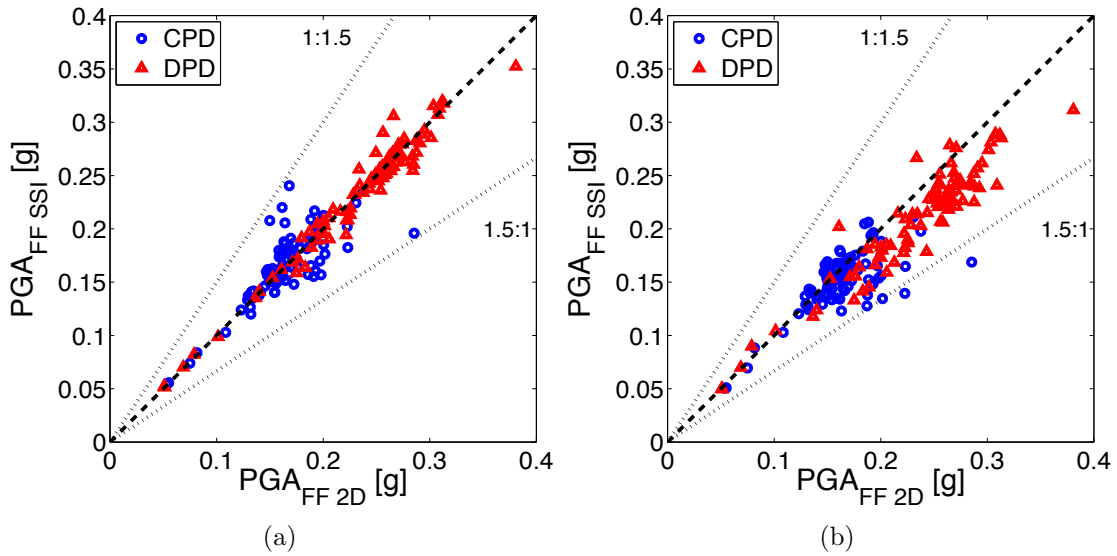


Figure 4.36 – SSI effect on the peak ground acceleration (PGA) at free-field for a) B01 and b) T040.

SSI (i.e., $|u_z| = u_{zSB} - u_{zFF}$).

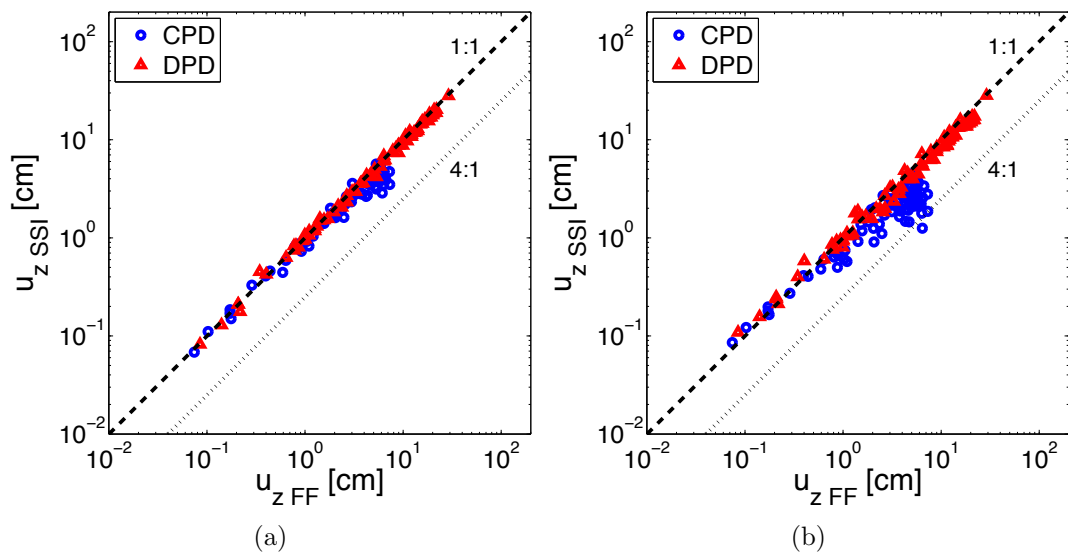


Figure 4.37 – SSI effect on the settlement (u_z) at free-field for a) B01 and b) T040.

Concerning, the liquefaction evaluation in the soil deposit, the liquefaction index (Q) will be used to compare the different models. This index was defined by equation 2.6 in section 4.3.5 for the free-field response analysis in the 1D model, now it is extended to the 2D model as follows:

$$Q_{H.L} = \frac{1}{H \cdot L} \int_0^H \int_0^L r_{u\text{end}}(y, z) dy dz \quad (4.7)$$

where $r_{u\text{end}}$ is the liquefaction ratio evaluated at the end of shaking ($r_{u\text{end}} = \Delta p_{u\text{end}}/\sigma_{z0}$). When $Q_{H.L}$ is equal to unity, it means that liquefaction is present throughout the thickness H and the length L hence it gives information of the liquefaction ratio as well as the total liquefied area. The FF 2D model is compared in Figure 4.38 with the SSI effect of the two structures. Different values of H and L were tested: (1) a box under the structure of $H=4\text{m}$ and $L=10\text{m}$ (in magenta), (2) the entire FEM, $H=20\text{m}$ and $L=50\text{m}$ (in blue), (3) a column of $H=10\text{m}$ in FF and (4) a similar column below the structure.

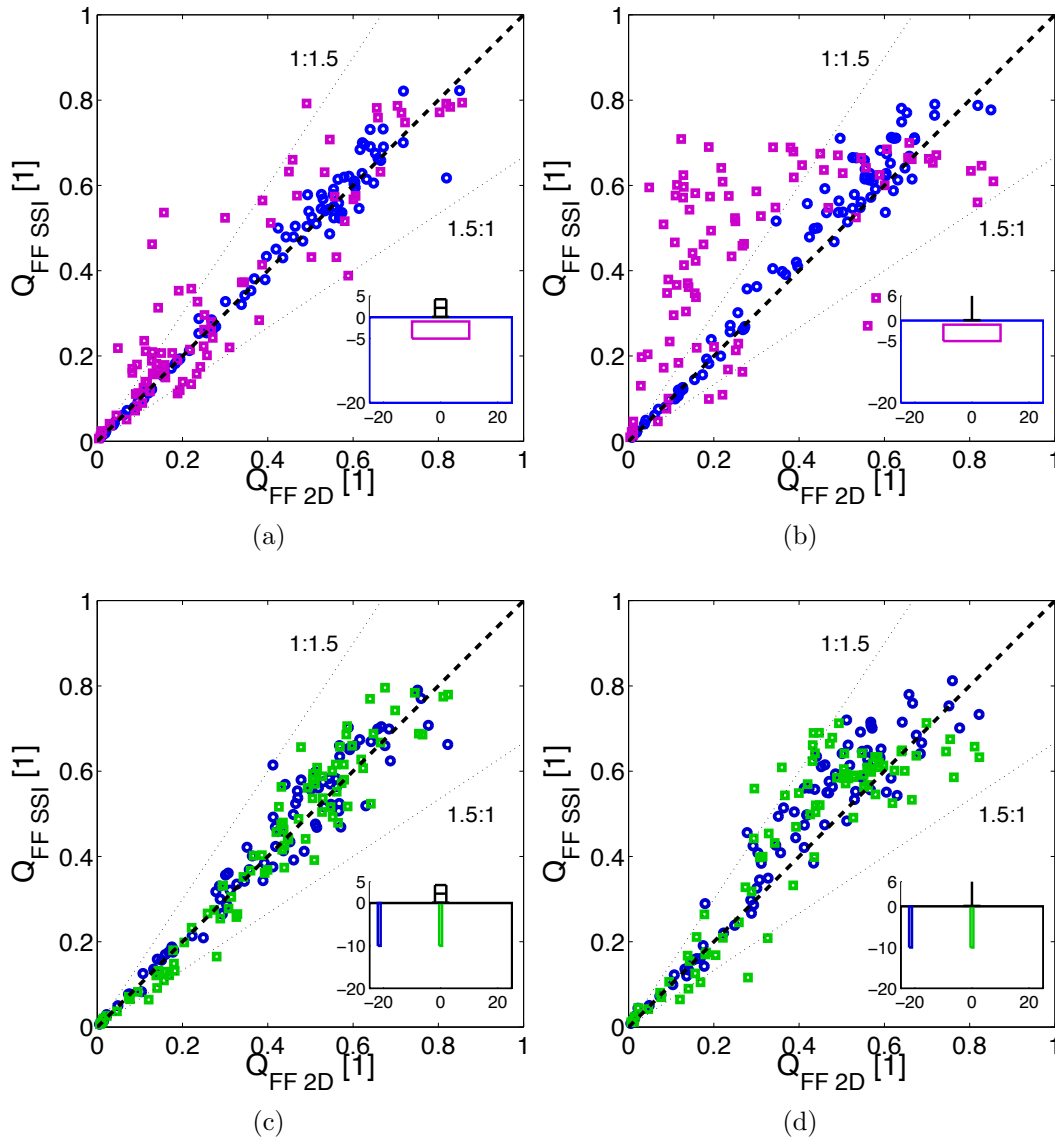


Figure 4.38 – SSI effect on the liquefaction index ($Q_{H.L}$): a) and c) for B01 and b) and d) for T040. The colors correspond to the size of the area depicted on the schema

It can be noted that Q_{FEM} presents only a slight increase when the structure is present, most notably for T040. In contrast, in the 4×10 box under the structure, the effect of SSI on liquefaction varies greatly. First, more dispersion is evidenced and in most cases, more liquefaction will appear when the structure is present. With T040, Q is up to 5 times greater than in the FF 2D model. The results with B01 are somewhat different as it seems that for high liquefaction levels less SSI effect is present. For T040, a plateau at about 0.7 is found for the Q values evaluated with SSI in the box which can be related to the pore pressure migration and the fact that these values are measured at the end of shaking and not at their maximum. With respect to the Q values evaluated at the two columns, once more the SSI effect is more important for Q evaluated for FF 2D model above 0.3 for T040. It is interesting to note that the similarities between both columns might indicate that the SSI effect is similar near the boundaries and in the center of the model. However, this value is an average over height but it does not show the principal depth where liquefaction takes place. In order to better analyze this aspect, two cases will be presented: (1) for a low level of liquefaction where SSI reduces Q under structure and (2) for a high level of liquefaction where SSI increases Q .

Figure 4.39 shows the liquefaction ratio (r_u) at the end of shaking in the whole deposit of the model without structure and with the structures used for a motion that presented a low level of liquefaction. For the case of FF, r_u is not horizontally homogeneous which is probably due to the surface waves as is shown in Appendix B. When a structure is present, the r_u distribution is modified in the whole deposit even near the lateral boundaries (i.e. FF SSI). However with B01, Q evaluation in a FF SSI column is similar than in FF 2D, as the magnitude of r_u is similar even if the depth of maximum r_u has changed. Concerning the SSI effect under both structures, in this case r_u is significantly reduced but it is increased in the surrounding.

For a high level of liquefaction, the response is different as it is shown in Figure 4.40. In this case, more r_u is presented under B01 structure while slightly less is visible in the surrounding. However, for T040, the results are inversed and higher Q values are presented outside the box of 4×10 . It can be seen how the choice of this area will affect the response as if for this case the box would be slightly bigger the results would have been similar as for B01. Liquefaction evolution is shown to be very complex and while only the state at the end of shaking is shown here, the differences within the 2D model can be due to the motion's frequency evolution with time and the consequently difference in r_u . To compare the different motions tested, the liquefaction index evaluated at the whole deposit (Q_{FEM}) will be used as it is an average measure for the entire model.

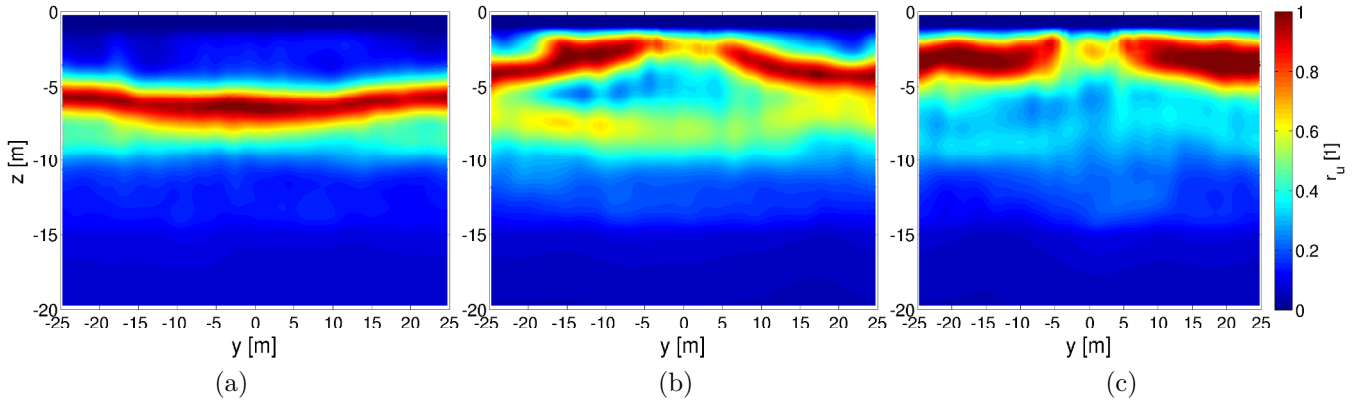


Figure 4.39 – SSI effect on the liquefaction ratio (r_u) at the end of shaking for a) no structure, b) B01 and c) T040

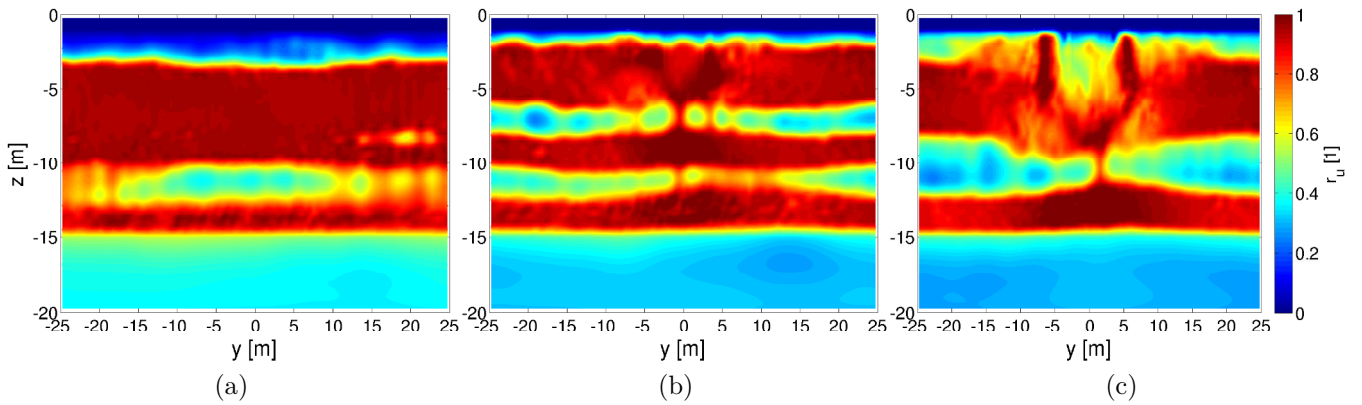


Figure 4.40 – SSI effect on the liquefaction ratio (r_u) at the end of shaking for a) no structure, b) B01 and c) T040

Furthermore, the values obtained for Q_{FEM} appear to be related to the PHA and the equivalent harmonic period ($T_{V/A}$) values as shown in Figure 4.41 for both structures. $T_{V/A}$ is an approximation of the predominant period of the motion taken as the intersection of the constant spectral acceleration and velocity. It is computed by:

$$T_{V/A} = 2\pi \frac{\alpha_V(\xi = 5\%) PHV}{\alpha_A(\xi = 5\%) PHA} \text{ where } \frac{\alpha_V(\xi = 5\%)}{\alpha_A(\xi = 5\%)} = \frac{1.65}{2.12} \quad (4.8)$$

Green and Cameron (2003) found a close relation between this IM and the amplification of soft soil sites. Similarly, Kawase (2011) uses the inverse of $T_{V/A}$ to examine the relationship between observed strong motions and structural damages. In this figure, equi-PGV lines will be a slope from left-down side to right-up side. For the soil tested, the highest liquefaction ratio was found for PGV higher than 50m/s and PGA between 0.2g and 0.8g. It is interesting

to note that even if the peak acceleration is above 0.2g, which has known to be a threshold for nonlinearity, if the PGV is low, Q_{FEM} is also low. With respect to the structures, it can be seen that the same motions present similar results however the liquefaction index is overall higher for T040 as it was already shown.

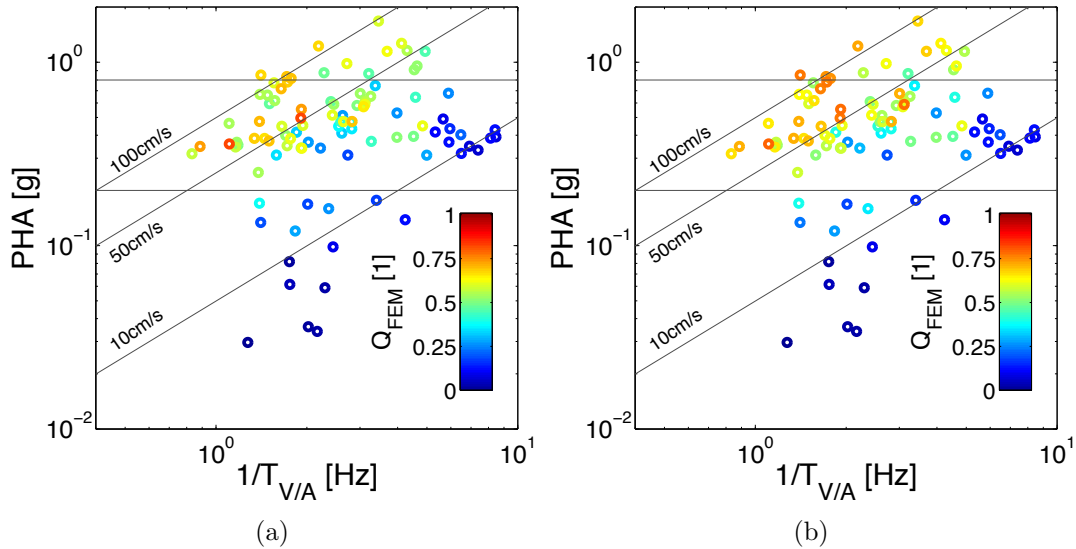


Figure 4.41 – Relation between input IM: PHA and $T_{V/A}$ and liquefaction index (Q_{FEM}) for : a) B01 and b) T040 structures

4.4.6 Surface acceleration

The amplification (or deamplification) of an earthquake motion due to site effects has been studied for many decades. In engineering practice, site amplification factors are often used to take into account these effects. An example of these factors, is the pioneering work of [Idriss \(1990\)](#) and [Dickenson and Seed \(1996\)](#) based on empirical measurements and engineering judgment of ratios between the peak surface acceleration of a soft deposit (PGA) and the peak horizontal acceleration at outcropping rock (PHA) and shown in the previous section. Advanced numerical models of seismic soil behavior are useful to analyze the nonlinear effects on the ground motion; however, when no coupling of pore pressure and soil deformation is present, the model could largely overestimate the peak accelerations at surface.

Concerning the peak ground acceleration (PGA) at the structures base, Figure 4.42 shows the comparison between the CPD and DPD analyses for both buildings. The values are ranged by the liquefaction index evaluated at the entire soil deposit Q_{FEM} , presented previously. For most cases, in Figure 4.42, the coupling produces a deamplification on the acceleration as

it accounts for soil softening due to the pore pressure increase. However, for two motions with T040 structure, the peak acceleration is greater for the CPD analysis. Regarding the liquefaction index, the PGA values appear to be related to the level of liquefaction in the soil. Except for two motions with B01 structure, where the value of Q_{FEM} is low while the deamplification is doubled. In general, PGA is similar for both structures when a CPD analysis is used, while, with a DPD analysis, the PGA appears to decrease for the heaviest structure (i.e. T040). Finally, the differences between the analyses are higher and more dispersive for B01.

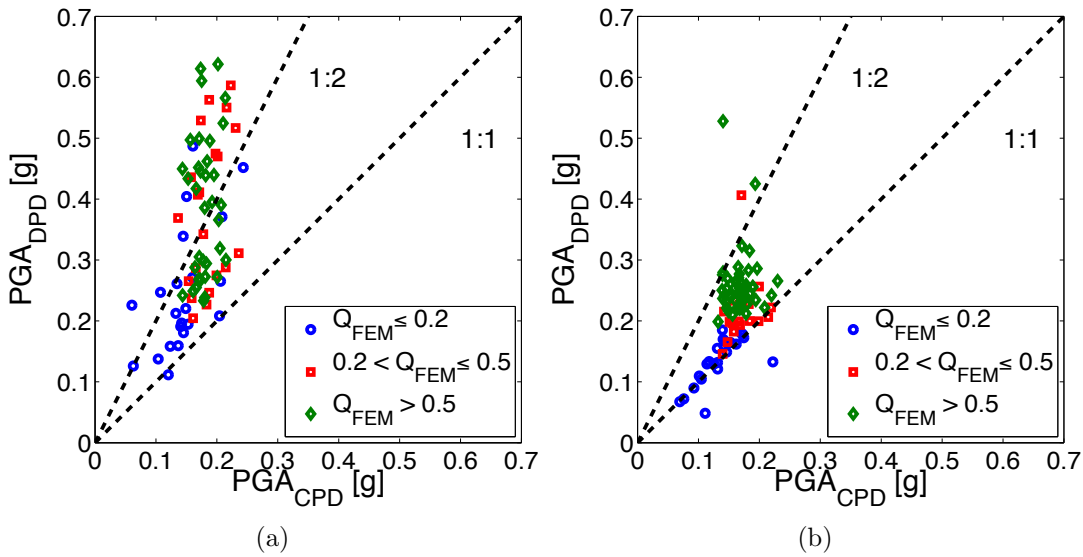


Figure 4.42 – Mean peak ground acceleration (PGA) at structures base for CPD and DPD analyses for : a) B01 and b) T040 structures

Considering that the structures tested have different predominant periods (T_0), the acceleration response spectra (PSA) is evaluated at each T_0 value and the comparison between CPD and DPD is shown in Figure 4.43. For B01, almost 25% of the cases presented higher values when a CPD analysis is performed, mainly those with low levels of liquefaction. In contrast, as the T_0 value of T040 is near the fundamental elastic period of the soil, the behavior presents less dispersion and higher PSA values with the decoupled model for almost all cases. Insofar as surface acceleration is concerned, the lack of coupling will produce a conservative analysis.

Finally, as for the 1D case, the response spectra ratio (RSR) is evaluated for the accelerations at the base of each structure. Recalling that RSR is defined by:

$$RSR(T) = PSA_{CPD}(T)/PSA_{DPD}(T) \quad (4.9)$$

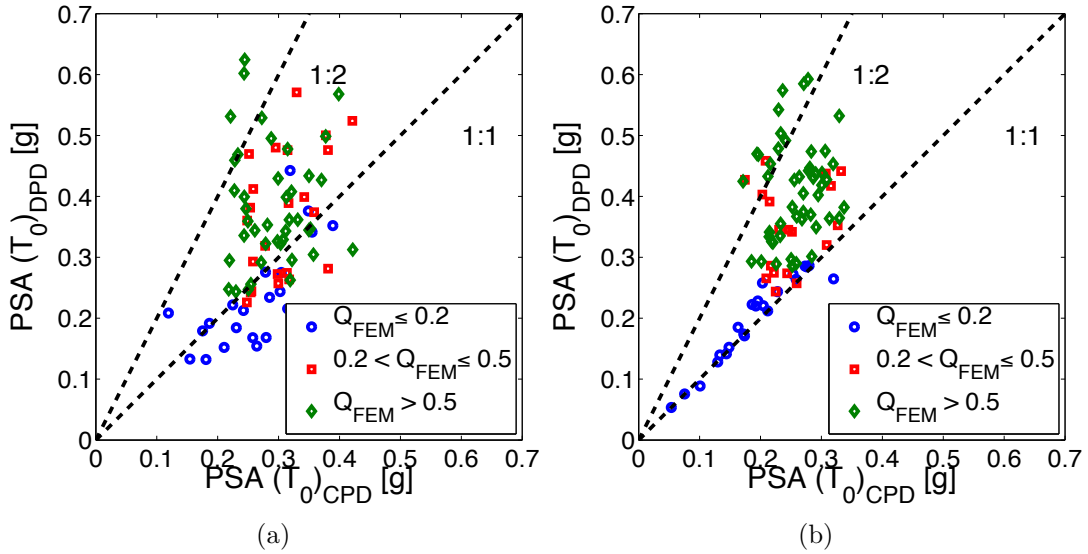


Figure 4.43 – Comparison of CPD and DPD results for the response spectra of acceleration at structures base evaluated at the predominant structure period: a) B01 and b) T040

The mean values for each liquefaction index level are shown in Figure 4.44. In dashed line, the response for the 1D model is also shown. For B01 (Figure 4.44a), the CPD response spectrum is greater for all levels of liquefaction when periods are above approximately 0.1s. In contrast, for T040 (Figure 4.44b), differences between the analyses are smaller and CPD results are only greater for periods above 1s when Q is high. With respect to free-field, it seems that in this case, the relation of RSR with Q is less significant which is probably related to the effect of the soil-structure interaction. For instance, for B01 the mean values for high and intermediate Q levels are similar in all the period range used and it differs from the mean for low Q only above 1s. With respect to the structures predominant period, for B01 ($T_0=0.24s$), the CPD response presents almost twice the DPD values for all levels of liquefaction; while for T040 ($T_0=0.4s$), the CPD is only slightly higher for Q above 0.5. Two aspects are worth highlighting: it seems that the soil-structure interaction (SSI) effect is important for B01 while it is almost negligible for T040 and compared to this effect, the coupling effect is significantly lower and only relevant for periods longer than 1s.

4.4.7 Structure relative settlement

In contrast, regarding the relative settlement of the structure with respect to free-field, shown in Figure 4.45, taking into account the effect of coupling in most cases will result in higher values, except for 25% of motions tested with B01. This could be prejudicial for the structures

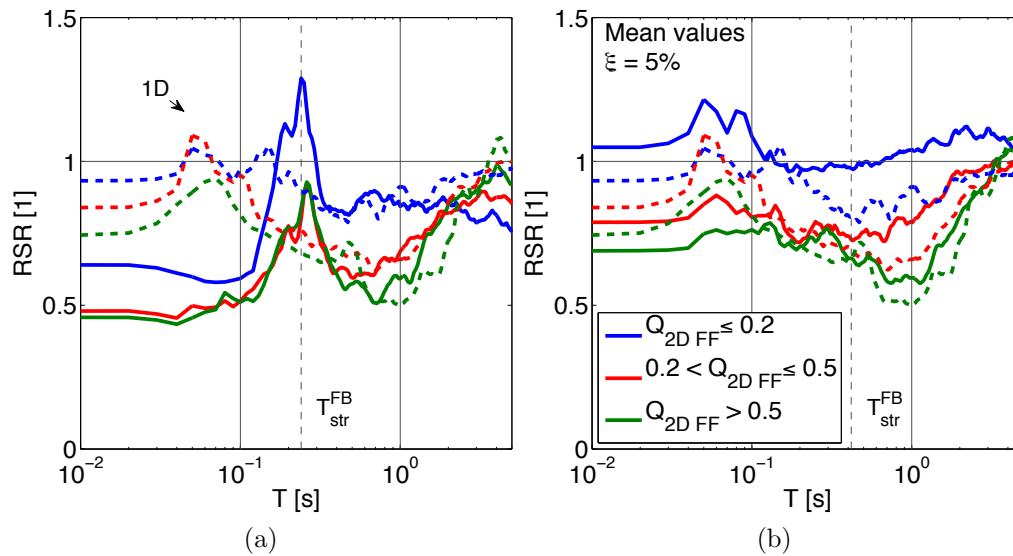


Figure 4.44 – RSR at structure's base for: a) B01 and b) T040

performance. Specially for T040, where the difference between the analyses is bigger and the settlement with CPD is above 10cm for approximately half of the motions tested. This value corresponds to the limit for slight damage state of reinforced concrete frame buildings given by Bird et al. (2006). Above it, cracks in structural elements appear and damage has to be repaired. In some cases, settlement from the DPD analysis is almost ten times smaller than that of the CPD one.

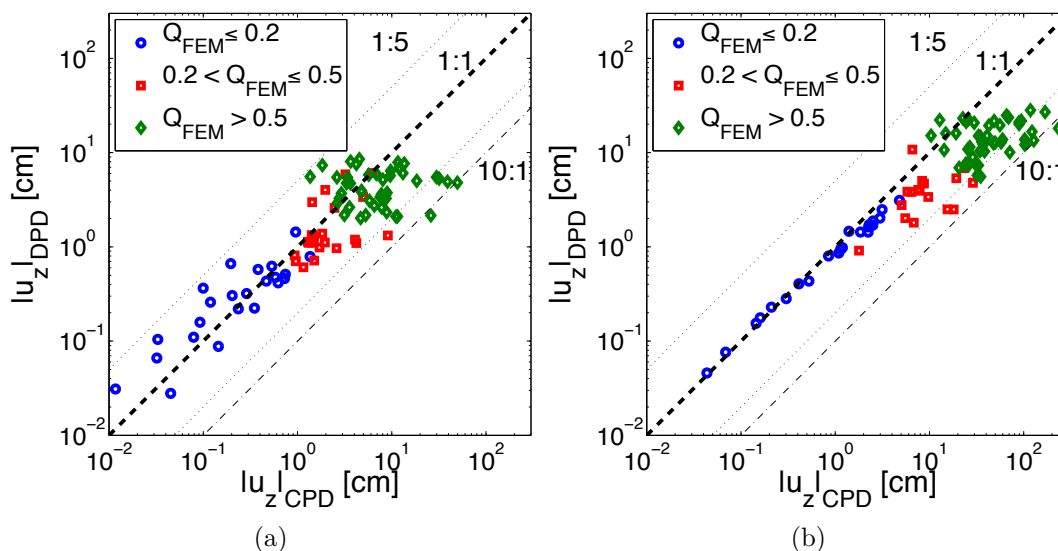


Figure 4.45 – Comparison of CPD and DPD results for the relative settlement with respect to free-field: a) B01 and b) T040

4.4.8 Structure seismic demand

Regarding the seismic demand on the structure, the maximum drift at the top of the building (u_d) and its corresponding base shear, in terms of spectra of acceleration (Sa) are presented in Figure 4.46 for both structures. The capacity curve obtained by modeling the static pushover test is compared to the dynamic SSI and the structure with fixed base with the same outcropping signals. The dynamic response agrees well with the push-over model for all cases except for the high drift values presented by B01 with fixed base, which is due to the nonlinear model used for this structure. However, for the motions used and in the SSI case, results are not affected.

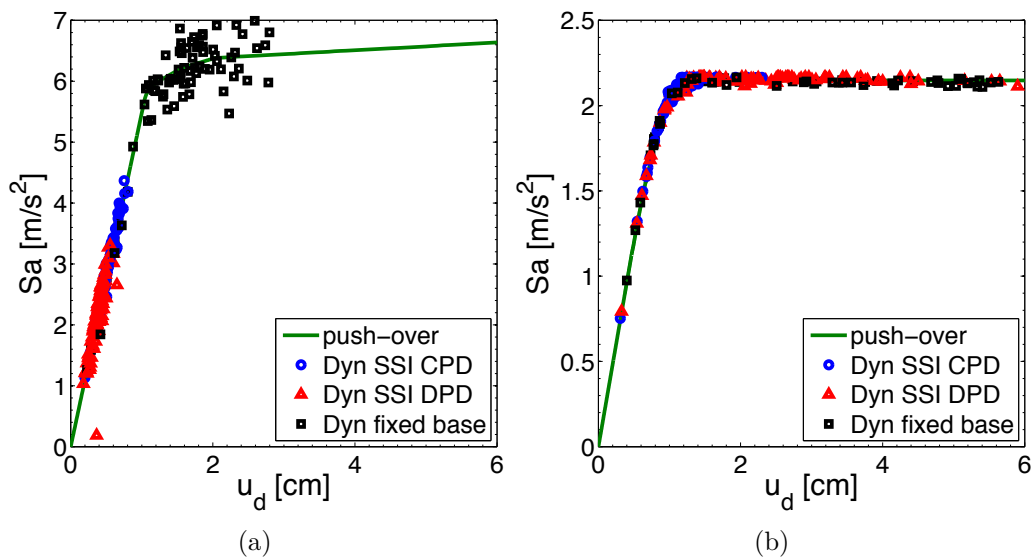


Figure 4.46 – Static and dynamic capacity curves for a) B01 and b) T040

With respect to the SSI effect, it is clearly seen that it is more important for the B01 structure with both CPD and DPD analyses as both the drift and the acceleration are significantly reduced compared to the fixed base. In fact, for this structure, the response is completely linear taking into account the SSI effect; while for T040, the response is still nonlinear - i.e. structural damage appears. The decrease in u_d and Sa for B01, is principally due to the rigidity of the structure and the higher deamplification and frequency shift evidenced for even very weak motions. In contrast, the T040 has a fundamental frequency lower than that of the soil and for weak motions, no important SSI effects are shown.

Figure 4.47 shows the nonlinearity evolution of the soil - B01 structure system by analyzing the transfer function ($|TF|$) between the top floor and the free field (FF). In this case, the whole signal was used to evaluate $|TF|$. As seen in Figure 4.47b, the system without coupling presents a lower amplitude of the predominant frequency even for low PHA values. This deamplification

drops drastically after about 0.7g and the frequency is reduced by more than 1Hz for the highest PHA. In contrast, with CPD analysis the deamplification is smaller and almost no frequency shift is evidenced. The latter can be explained by the liquefaction presented in the deposit that can isolate the SSI effect between the surficial soil and the structure.

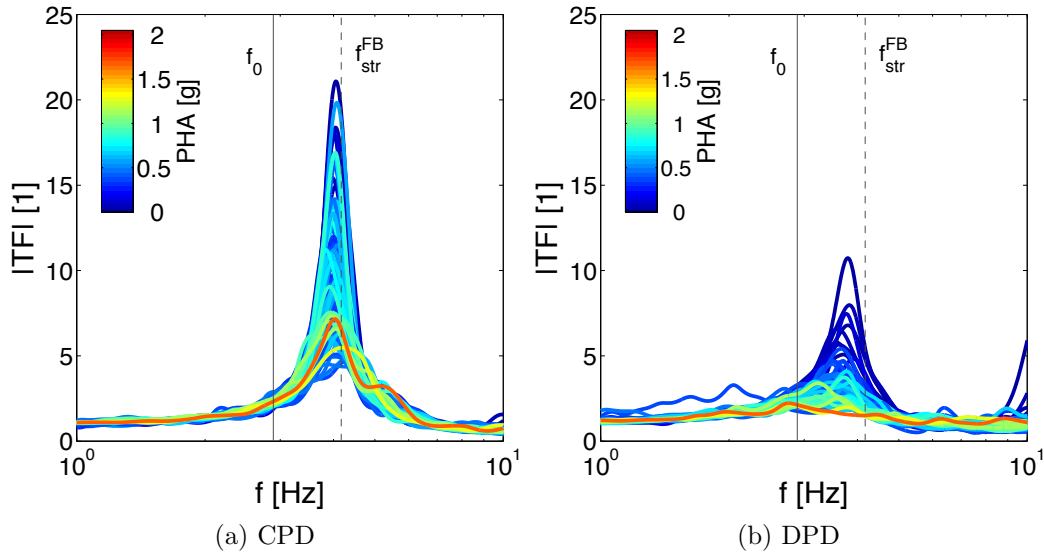


Figure 4.47 – Nonlinearity evolution at the structure's $|TF|$ (Top/FF) for B01

Another way of analyzing structures' nonlinearity evolution is by computing the cross-correlation of the acceleration on the top of the structure with itself (also known as the auto-correlation). According to [Snieder and Safak \(2006\)](#), the amplitude decay gives information of the damping or attenuation while the time delay of the first peak is related to the shear wave degradation and consequent frequency shift. Figure 4.48 shows the cross-correlation of three motions with different levels of PHA for each analysis. With respect to the time delay, only a slight increase is evidenced with CPD analysis. In contrast, with DPD analysis the delay is strongly increased with increasing PHA. For CPD, it is interesting to note that the motion of intermediate level (PHA = 0.8g) presents less attenuation than the low level motion, as the latter presents an acceleration amplification of the soil deposit while the liquefaction that appears with the former attenuates the strain level of the surficial soil layers.

In order to further analyze this, Figure 4.49 shows the maximum shear strain ($|\gamma_{max}|$) in the deposit for the three cases. As the negative of the logarithm is used, the lower the value the higher the shear strain level. For the intermediate PHA level, liquefaction appears around 10m while near the surface, the strain level is low. Hence the soil's behavior is almost elastic and the damping is low. Whereas for the high PHA case, liquefaction appears about 5m and

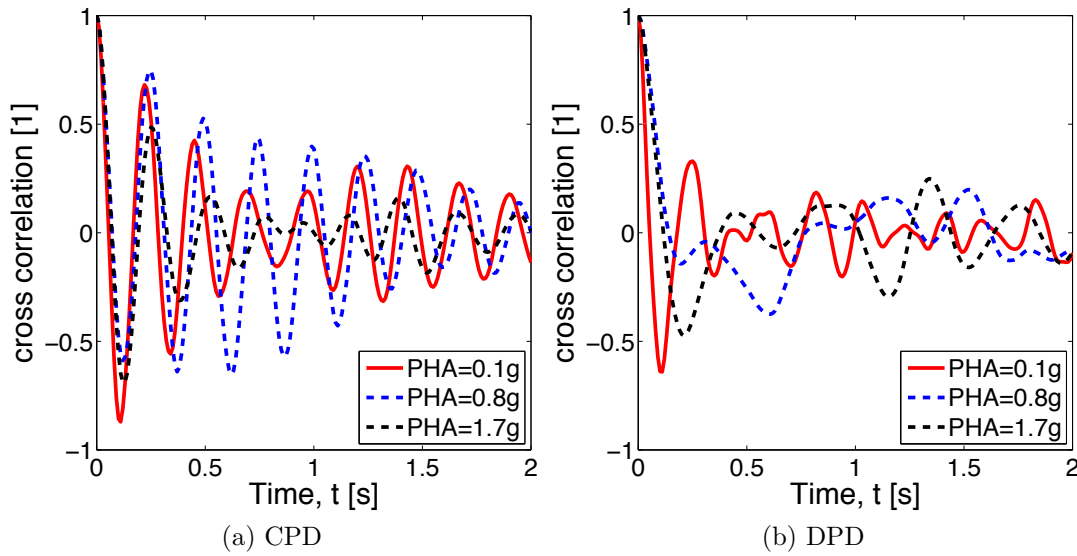


Figure 4.48 – Cross-correlation at the structure’s top of three acceleration levels for B01

the strains are greater at the surface and specially immediately below the structure.

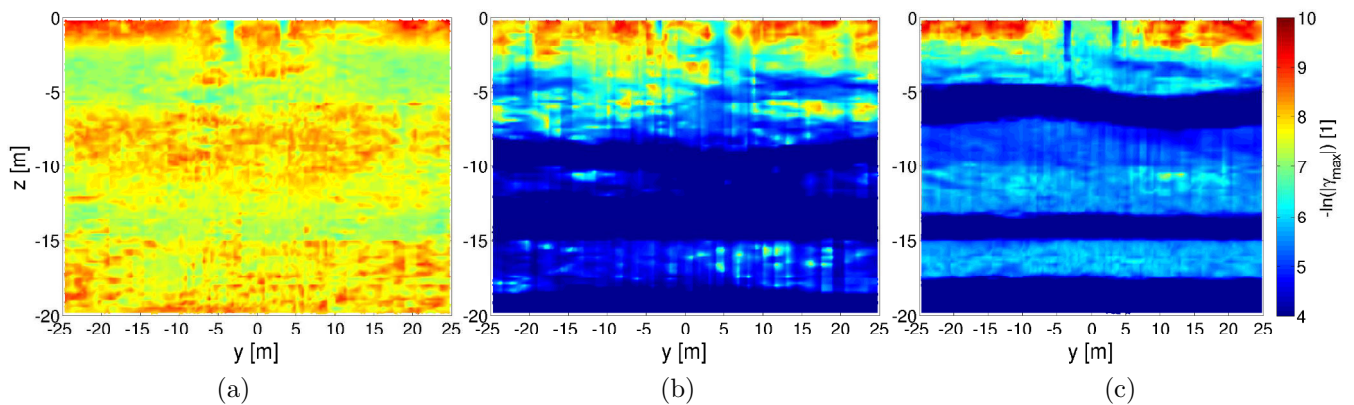


Figure 4.49 – Maximum shear strain level in the CPD analysis with the three acceleration levels for B01

Similarly, Figure 4.50 shows the nonlinearity evolution by $|TF|$ for T040. For this structure, the amplitude of the predominant frequency for the low PHA values is similar for both the CPD and the DPD analyses and it differs only for PHA above 0.7g when DPD presents lower amplitudes and a shift to low frequencies. This can be explained by the position of the soil’s predominant frequency with respect to that of the structure. In this case, for quasi-elastic behavior the latter is lower which means the structure is more flexible than the soil. But as the intensity level of the input motion increases, the soil loses its strength and becomes more flexible than the structure. Hence, the SSI effect is greater and lower amplitudes are evidenced.

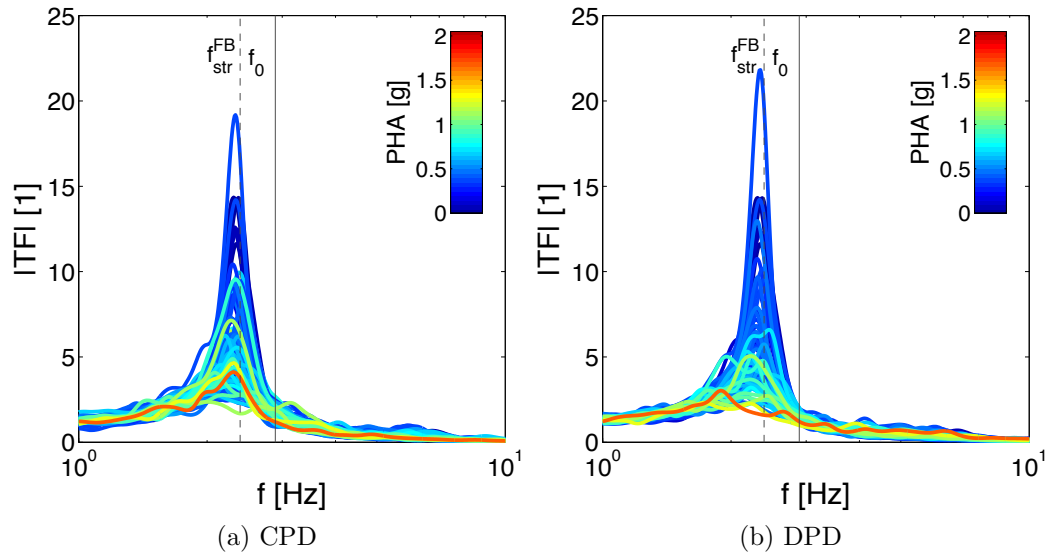


Figure 4.50 – Nonlinearity evolution at the structure's $|TF|$ (Top/FF) for T040

The nonlinearity evolution with the CPD analysis is closely related to the liquefaction level as seen in Figure 4.51 for both structures. In this case, the liquefaction index is measured in a column of 10m at FF SSI (Q_{FF}). For both structures, the amplitude of the predominant frequency is gradually decreasing with Q_{FF} , however for values above 0.3 the amplitude is drastically decreased.

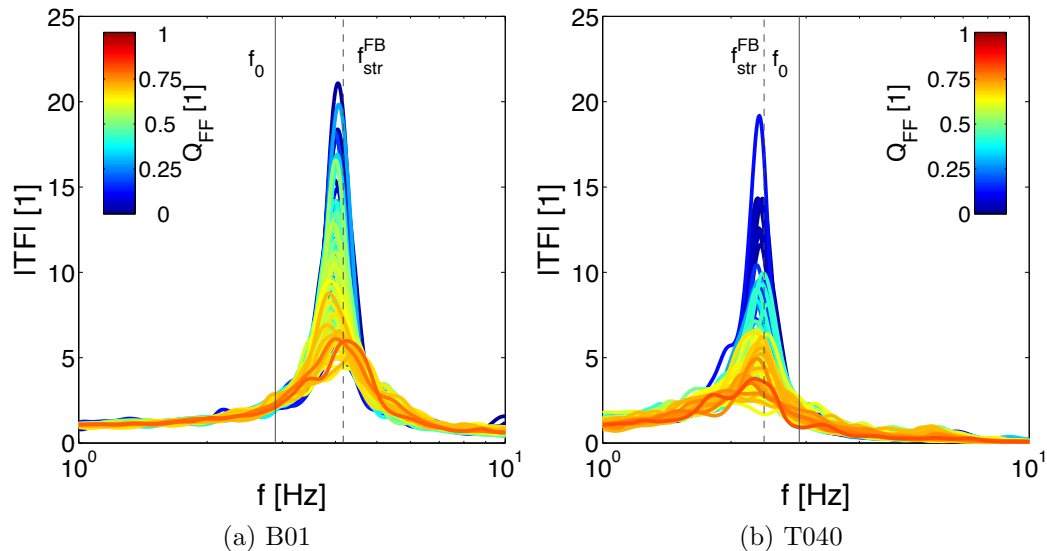


Figure 4.51 – Relation of $|TF|$ (Top/FF) with the liquefaction index (Q_{FF}) for the CPD analysis

Finally to compare the effect on the drift in structures with different height, the maximum horizontal displacement evaluated at each level for B01 and for the top at T040 is normalized

by each corresponding height, which is known as the maximum inter-story rift (ISD). The comparison of CPD and DPD results are shown in Figure 4.52. It is interesting to note how the two structures present very different results. For B01, the CPD values are greater than DPD for almost all cases; while for T040, it is the contrary. Concerning the latter, the values with the DPD analysis are more than doubled when Q_{FEM} is above 0.5. For B01, with CPD analysis the ISD is higher for low levels of liquefaction. In these cases, the SSI effect is higher than the coupling effect, hence the drift is increased. But when the liquefaction increases, the coupling effect is more important as the soil will attenuate the motion and the structure drift will be reduced. With respect to the capacity curve (shown in Figure 4.46), for the same input motions, T040 presents higher seismic demand and for many cases, the structure presents high nonlinearity and possible structure damage evidenced in the higher ISD compared to B01.

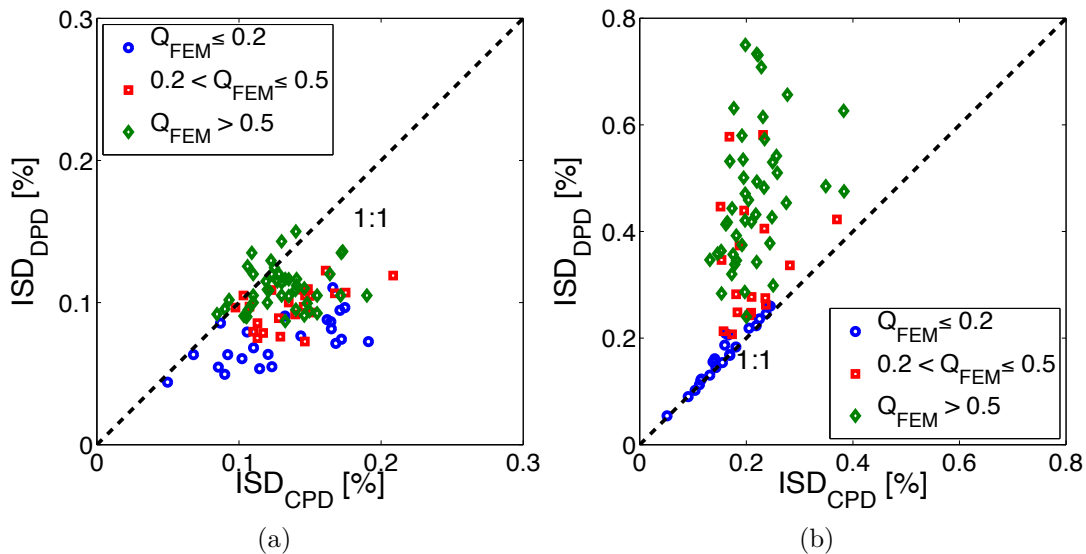


Figure 4.52 – Comparison of CPD and DPD results for the maximum inter story drift (ISD) : a) B01 and b) T040

4.4.9 Partial conclusions

A finite element analysis was used to investigate the effect of coupling excess pore pressure and soil deformation on a soil-structure model. Two mechanically equivalent models were subjected to 90 unscaled earthquake motions: one taking into account coupling (CPD) and one without (DPD). The same effective-stress model was used for the calculations and the initial elastic behavior was proofed to be the same. The present study aimed to highlight the importance of accurate modeling liquefiable soils in order to improve performance-based earthquake engineer-

ing (PBEE). The main finding of this study is the higher differential settlements obtained with CPD model for both structures and most motions tested. Additionally, due to the nonlinear SSI effect of B01, the maximum ISD was consistently underestimated by the DPD analysis. Hence, the use of DPD models will not be recommended for a PBEE design.

Two main effects are involved in this analysis: the coupling of pore pressure and soil deformation and the interactions between the soil deposit and the structure. These can be beneficial or detrimental for different EDPs tested but the analysis should include both as it seems that the complex relation between them will vary for each motion, soil and structure tested.

Chapter 5

Effect of the spatial variability

Soil improvement techniques used to strengthen cohesive soils or to mitigate liquefaction are becoming widely used even though there remains some uncertainties given the spatial variability introduced in the design (Kasama et al., 2012). The success of these techniques is related to the effectiveness of the method - that is, how much of the soil is being changed - but also to its efficiency in improving the soil behavior - that is, how much are the consequences optimized. The effectiveness can be measured by the spatial fraction of the treated soil with respect to the total treatment area, for example the amount of gravel or clay introduced in a sand deposit. However, these techniques present an important uncertainty with respect to the final different spatial configurations on the vertical as well as in the horizontal direction.

To analyze the effects of added spatial variability due to soil improvement techniques a discrete auto-regressive code is coupled to the finite element program presented in the last sections. The former is used to generate the treated ground soil as a binary mixture composed of two materials: the reference soil and the added improved material. Two cases have been analyzed: the effect of a binary mixture of purely cohesive soils on the bearing capacity of a shallow foundation and the effect of a two sand mixture on the seismic liquefaction evolution and the induced structure settlements. The latter, in part, contains material published in *GeoRisk* (Montoya-Noguera and Lopez-Caballero, 2015).

The bearing capacity case is a well known geotechnical problem with an exact solution for the homogeneous case and can be simplified by a linear dependency of one input parameter, i.e. the undrained shear strength (c_u), and one output parameter, the bearing capacity (q_u), thanks to Prandtl's equation : $q_u = N_c \cdot c_u$. Due to its simplicity, this problem was used to test the binary random field given by the auto-regressive code and analyze, among others, the effect of its parameters: the spatial fraction (γ) and the correlation coefficients in each direction (β). First different isotropic and anisotropic correlations were analyzed. Then, for each γ the average effect of spatial variation was used to define an effective c_u for which a uniform model gives the same q_u output, proving that for this problem it is possible to define a homogeneous model that captures the average behavior of spatially varying fields. Afterwards, traditional and more sophisticated homogenization theories were tested to predict the relation between effectiveness given by γ and efficiency measured by the average q_u . Among the former, the Wiener bounds, also known as the arithmetic and harmonic averages, will either underestimate or overestimate the average value, respectively. Instead, the Bruggeman effective medium (BEM) theory is the most suited approximation as it accounts for each material independently and involves a parameter d_{BEM} related to the percolation threshold. These theories were also

used for different contrasts between the two soils' properties and an equation relating the soils c_u ratios and d_{BEM} was found. Lastly, an optimization procedure is given in order to establish the domain of averaging or local average area for which the q_u variation due to the spatial variability is reduced.

Concerning the effect of added spatial variability on soil liquefaction, a finite element soil-structure interaction model is coupled with the auto-regressive code. The reference model is the two-story inelastic structure B01 founded on the loose-to-medium sand (LMS) presented in the previous section. In the treatment zone, a medium-to-dense sand (MDS) is added with the auto-regressive code. First, the interaction between the two soils in the binary random field is analyzed in time. It is shown that more liquefaction can be produced in MDS clusters when they are surrounded by LMS due to the migration of pore-water pressure, which affects both the settlement and the Arias intensity in the deposit. Then, the relation between the technique effectiveness and the average efficiency is evaluated for different input motions. To measure the latter, the relative surface settlement of the structure with respect to free-field ($|u_z|$) at the end of shaking is used. Once more, the traditional theories fail to predict the average behavior, even so, for most motions and γ values, the response is beyond the Wiener bounds. Whereas a good fit was provided by the generalized effective medium (GEM) theory. This theory is an extension of the BEM equation but adds two additional parameters that account for the phase contrast below and above the percolation threshold. These parameters were found by an optimization procedure for each motion tested. Finally, other engineering demand parameters (EDPs) were analyzed but the behavior of the average as well as the variation related to the spatial fraction changed significantly for each motion.

5.1 Introduction

Field and laboratory test results consistently show that soil parameters vary spatially in both the horizontal and the vertical directions. Natural processes and geological formations cause *inherent* spatial variability; in addition, limited observations and measurement errors add an important amount of uncertainty. The quantification and consequences of spatial variability and uncertainty in the soil properties is of great importance for geotechnical earthquake engineering. Commonly, these aleatory and epistemic uncertainties in a soil deposit are addressed with probabilistic analyses. In those analyses, the soil properties change randomly following a specified probabilistic distribution.

Another source of spatial variability is due to the implementation of soil improvement techniques. Methods such as soil-mixing, Bentonite permeations, bio-grouting and densification techniques are becoming widely used to strengthen soft soils and mitigate liquefaction. Significant advances have been made in the equipment and methods used although, the high degree of spatial variability introduced in the design and its effect of the system's performance are less known (Kasama et al., 2012). This *added* spatial variability can differ significantly from the *inherent* or natural soil variability. The former is more likely to be a distribution of different soil deposits with horizontal and vertical correlations than a random continuous change (Jones et al., 2002). In this study, this variability is modeled by a binary random field generated by an auto-regressive code. In it two very different soil types are used and the interaction between these is evaluated. One of the most influential factors on the treated ground is the effectiveness of the mixing process (i.e. spatial fraction of the treated soil) which adds important variations with different spatial configurations on the vertical as well as in the horizontal direction (DeJong et al., 2013).

These spatial configurations will have an important impact in complex phenomena like bearing capacity or liquefaction-induced settlement. Studies on the random heterogeneity of soil properties assert that phenomena governed by highly non-linear constitutive laws are affected the most. Nobahar and Popescu (2000), Griffiths and Fenton (2001) and Popescu et al. (2005a), among others, have studied the effects of inherent random soil heterogeneity on the bearing capacity (q_u) of shallow foundations. All of them have used Monte Carlo (MC) simulations considering a continuous heterogeneous field. The evaluation of the bearing capacity depends on the failure slip surface which preferentially travels through lower strength soil hence depends on the spatial distribution in the mixture. Similarly, the increase of excess pore water pressure (Δp_w) and consequent loss of strength depends on the interaction between the surrounding soil. Laboratory tests in heterogeneous soils have shown that the Δp_w is generated first in loose deposits and when water migrates to neighboring dense sand, it is softened and eventually liquefied. This interaction also affects the liquefaction-induced settlements (Coelho et al., 2004; Dashti et al., 2010; Chakraborty and Popescu, 2012). Extensive research has been performed on the calculation of these settlements but rarely they include the variability of soil properties and modeling of different soil deposits (Koutsourelakis et al., 2002, among others).

The aim of this work is to assess the effect of added spatial variability due to soil improvement techniques. On that account, a 2D finite element model is coupled with a discrete auto-regressive code. The latter is used to generate the treated ground soil as a binary mix-

ture composed of two materials: the original or reference soil and the added material. Two aspects are analyzed: (1) the success of the soil improvement technique, which is related to the effectiveness of the method - i.e. how much of the soil is being changed -, and (2) its efficiency in improving the soil behavior -i.e. how much are the consequences improved. First, an overview of previous studies on inherent and added spatial variability is presented. Then, the auto-regressive code is tested in a simple case concerning the strengthening of purely cohesive soils and its effect on the bearing capacity of a shallow foundation. Afterwards, the effect of a two sand mixture on the seismic liquefaction evolution and the induced structure settlements is evaluated. For this case, the nonlinear behavior of the soil and the complexity of the input motion modify the relationship between the treatment effectiveness and the evaluated efficiency. To assess the efficiency of the mixing process, the co-seismic settlements of the structure founded on a rigid shallow foundation and the liquefaction of the soil deposit are estimated for different levels of effectiveness by ranging the spatial fraction from untreated to fully treated, with different spatial distributions for each case.

5.2 Previous studies on soil heterogeneity

Uncertainty in geotechnical soil properties is often divided into aleatory and epistemic uncertainty as shown in Figure 5.1 (Jones et al., 2002; Helton et al., 2006). The former consists on the spatial variability together with the random testing errors, and the latter, on the systematic errors on measurement procedures, the modeling or conversion errors and the statistical errors due to insufficient data. While the epistemic uncertainty can usually be reduced by acquisition of additional data or improvements in measurement procedures; the aleatory uncertainty is inherent to the variable and cannot be reduced by additional information (Jones et al., 2002).

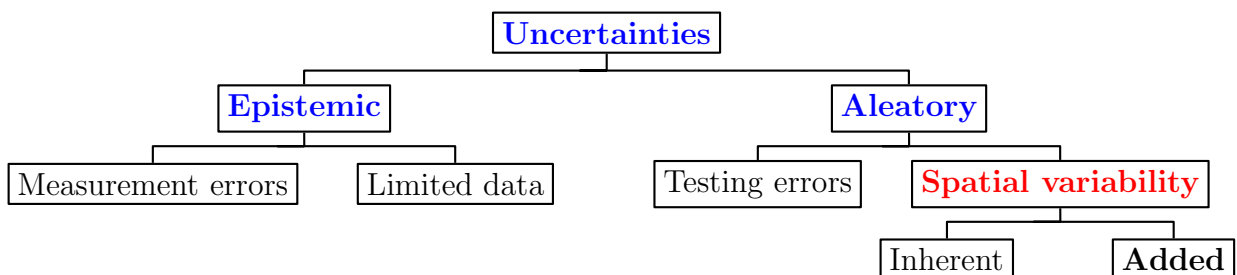


Figure 5.1 – Uncertainty in geotechnical soil properties (adapted from Jones et al., 2002)

Concerning the spatial variability, two types can be distinguished: (1) inherent spatial variability of soil deposits and (2) spatial variability introduced on the soil by means of increasing

its strength and (or) mitigate liquefaction potential. Some studies on soil heterogeneity will be shortly discussed; however, focus was given to those concerning either bearing capacity of shallow foundations or seismic liquefaction.

5.2.1 Inherent spatial variability

Soil variability can be seen in different scales: ranging from the mineral composition at the grain size (micro scale) to the geological size of several kilometers. It is clear that the definition of soil variability can be radically different on each of these scales. However, these are not independent and multiple spatial scales contribute to characterize the soil variability. This study will be focused in the geotechnical scale, between the test specimen scale and the geological scale. [Phoon and Kulhawy \(1999\)](#) decomposed geotechnical variability in three aspects: the inherent variability, the measurement errors, and the transformation uncertainty. Although the separation of these aspects is difficult and will be normally assessed as a whole. The inherent spatial variability originates from the natural geological processes that produced and continually modify the soil mass. Among these processes are the variation in mineral composition, the environmental conditions (temperature, pressure and humidity), past stress and seismic history. The effects of these processes depend on the scale of the study ([Koltermann and Gorelick, 1996](#)). Accounting for spatial variability, a soil property (F) is described by [Phoon and Kulhawy \(1999\)](#) as:

$$F(y, z) = t(y, z) + \epsilon(y, z) \quad (5.1)$$

where $t(y, z)$ is the trend or deterministic function given the mean soil property at horizontal position y and vertical position z ; and $\epsilon(y, z)$ is the residual or fluctuating component that accounts for both inherent spatial variability and uncertainty due to measurement errors or lack of information. This latter is often described as a homogeneous random field ([Vanmarcke, 1983](#)) which is defined by :

- probability density function (PDF) : the statistical function of all the possible values;
- variance: the scatter degree from the mean value which is generally described by the normalized quantity known as the coefficient of variation (CV);
- correlation structure : the coherence degree as a function of distance;

This definition of spatial variability holds by three basic assumptions: stationarity, homogeneity and ergodicity. By which, the mean value (μ) and the standard deviation (σ) are constant over the whole domain. Additionally, the covariance (C) depends only on the separation and not on the absolute position. Furthermore, the field is independent of the size, as each sizable sample is representative of the whole (Webster and Oliver, 2007).

Several studies have been published on the description and estimation of spatial variability in the field of geotechnical engineering. Among the most important contributions are those published by Vanmarcke (1983), Fenton and Griffiths (2008) and Phoon (2008).

5.2.1.1 Probability density function (PDF)

Popescu et al. (1998b) concluded that most soil properties exhibit non-Gaussian distributions that can change for different materials and sites. An evident reason is that most soil properties can not have negative values. For most applications in geotechnical engineering, however, the normal and the lognormal distribution functions are used (Phoon, 2008). Although, for cohesive soil strength, some researchers recommended Beta distributions including Harr (1977) and Failmezger (2001). Additionally, a right skewed PDF was evidenced in shallow layers, indicating a stronger influence of a lower bound; while strength of deeper soils followed a more symmetrical distribution (Popescu et al., 1998b). If experimental data is available, several estimation methods can be used to identify the PDF. For example the method of moments (such as the local average technique), the method of maximum likelihood or the method of Bayesian estimation. Refer to van Gelder (2000) and Huber (2013) among others for more information.

5.2.1.2 Coefficient of variation (CV)

The variance (σ^2) is the second moment of distribution and describes the degree of data fluctuation about the mean value. The coefficient of variation is the ratio between the standard deviation and the mean value (i.e. $CV=\sigma/\mu$) and is more commonly used as it is a normalized quantity. Issued from a variety of *in-situ* measurements and laboratory tests, many researchers have provided recommended CV ranges to account for inherent soil variability. For instance, Cherubini et al. (1993) found that CV decreases as the mean undrained shear strength (c_u) increases: from a range of 30% to 90% for a μ_{c_u} of 20kPa to a range of 12% to 45%, for a μ_{c_u} of 400kPa. These ranges include also the variation due to measurement errors. Without these

Correlation model	Autocorrelation function $\rho(\tau)$ [1]	Correlation length l_c [m]
Exponential	$\exp(-2\frac{ \tau }{\theta})$	θ
Squared exponential	$\exp(-\pi\frac{\tau^2}{\theta^2})$	θ
Triangular	$1 - \frac{ \tau }{\theta}$ if $\tau \leq \theta$, 0 otherwise	2θ
Cubic	$\frac{\theta^3}{(\theta+ \tau)^3}$	$\frac{2\theta}{5}$
Damped sinusoidal	$\frac{\sin(\chi)}{\chi}$ where $\chi = \pi\frac{ \tau }{\theta}$	θ

Table 5.1 – Theoretical autocorrelation functions presented by [Huyse and Walters \(2001\)](#)

errors, [Phoon and Kulhawy \(1996\)](#) recommended CV ranges for the soil strength measured by cone tip resistance measurements at clays between 10% and 40% and at sands between 20% and 60%. A thorough literature review on CV values of inherent spatial variability for various laboratory soil properties is presented by [Jones et al. \(2002\)](#).

5.2.1.3 Correlation structure

The correlation structure describes the similarity or coherence between fluctuations recorded at two points as a function of the distance between those points. This function is called the autocorrelation function ($\rho(\tau)$) which depends on the parameter θ defined as the scale of fluctuation by [Vanmarcke \(1977\)](#) as:

$$\theta = \int_{-\infty}^{\infty} \rho(\tau) d\tau = 2 \int_0^{\infty} \rho(\tau) d\tau \quad (5.2)$$

where τ is the lag separating the pairs of the random field. The scale of fluctuation depends on the sample size, hence, [Journel and Huijbregts \(1978\)](#) recommended a sample distance smaller than 0.2θ . In order to compare the scale of fluctuations of different autocorrelation functions, [Vanmarcke \(1983\)](#) proposed the use of the correlation length (l_c) as shown in Table 5.1 presented by [Huyse and Walters \(2001\)](#).

The amount of information on the correlation length is limited compared to that of CV evaluations of inherent variability. Relatively little quantitative data on the spatial variability of soil properties have been reported and it mostly concerns the variation in the vertical direction ([Jones et al., 2002](#)). [Huber \(2013\)](#) compiled numerous publications on spatial variability in a database to use as guideline for the scales of fluctuation in the vertical (θ_v) and horizontal (θ_h) direction depending on the different properties, soil types and applied theoretical autocorrelation functions. Most of the data came from CPT tests and to calculate the scales of fluctuation a lognormal distribution was used. Additionally, for most cases, an exponential autocorrelation

	frictional soils		cohesive soils		
scale [m]	0 ~ 10	10 ~ 30	0 ~ 15	15 ~ 40	40 ~ 60
θ_v [m]	0.18 ± 0.78	30	0.29 ± 1.14	23.30 ± 1.6	50
scale [m]	0 ~ 50	50 ~ 100	0 ~ 100	100 ~ 500	
θ_h [m]	2.35 ± 0.43	90	2.27 ± 1.72	25.54 ± 0.3	

Table 5.2 – Mean values and standard deviations of the lognormally distributed horizontal and vertical correlation lengths of CPT data for frictional and cohesive soils presented by [Huber \(2013\)](#)

function was used. A summary of the scales of fluctuation for cohesive and frictional soils presented by [Huber \(2013\)](#) is shown in Table 5.2. Note that the values given depend on the sample size, thus, the relation is different for the types of soils and the direction. In general, it seems that θ is slightly shorter for cohesive soils. Concerning the different directions, θ_h is at least thrice the value of θ_v , which is due to the direct relation of the soil properties and the increasing confinement pressure with depth often seen as layering or stratification ([Nobahar, 2003](#)).

5.2.1.4 Effects of inherent spatial variability

It has already been shown, and is generally accepted, that soil properties present a spatial variability; however, its effects on geotechnical systems are still being acknowledged. One common approach to assess the effects of spatial variability on different geotechnical systems is the probabilistic analysis. For over more than 25 years different studies have been presented: for example concerning 2D analysis on settlements ([Phoon et al., 1990](#); [Paice et al., 1994](#); [Fenton and Griffiths, 2002](#)), on liquefaction potential ([Popescu et al., 1997](#); [Fenton and Vanmarcke, 1998](#); [Popescu et al., 2005b](#)), on surface ground motion ([Rahman and Yeh, 1999](#); [Assimaki et al., 2003](#)) and on bearing capacity ([Nobahar and Popescu, 2000](#); [Griffiths and Fenton, 2001](#); [Popescu et al., 2005a](#); [Li et al., 2015](#)), among others. The methodology used in essentially all these studies was Monte Carlo simulation. Studies on the random heterogeneity of soil properties assert that phenomena governed by highly non-linear constitutive laws are affected the most ([Popescu et al., 2005b](#)). In general, they agree that soil heterogeneity affects the system by inducing a certain degree of variability in the response where mainly changes in the mean response are evidenced. In most of these studies, mean values were compared to the response obtained from deterministic analyses (i.e. assuming uniform soil properties). These studies have evolved with the advances on the computer industry; yet, the mayor drawback is

still the high computational cost.

Phoon et al. (1990) analyzed the effect of spatial variability of linear-elastic soils on the settlement of a single pile. The Young modulus was modeled as a homogeneous random field and the first order second moment (FOSM) technique was used to assess the mean and coefficient of variation of the pile head settlement. Design charts were provided for the variation of CV and reliability index for different relative stiffness of soil/pile, slenderness ratio of pile and correlation distances. Paice et al. (1996) modeled elastic soil stiffness with spatially correlated fields and studied its effects on the total settlement of a uniformly loaded flexible-strip footing. A range of coefficients of variation and depths of the spatially variable soil layer were used. The study results indicated significant effects of soil heterogeneity on the response variability. Compared to the deterministic analysis using the mean value, only a modest increase in average settlement was predicted (for instance, a 12% increase with CV equal to 42%). These relatively small changes were explained by the fact that elastic settlement is a linear phenomenon; therefore, the spatial variability effects on the resulting average settlements were modest. Further developments were performed on the model by Griffiths et al. (2002) to investigate the variation of total settlements under a single footing and differential settlements between two footings.

Concerning the effect of soil spatial variability on liquefaction, Popescu et al. (1998a) and Fenton and Vanmarcke (1998), among others, conducted several numerical studies using Monte Carlo (MC) simulations. Their main conclusion on the importance of spatial variability in the liquefaction phenomenon was the presence of pockets that increase the vulnerability of the entire soil deposit and its implications on risk evaluation. Popescu (1995) stated that the pattern and the amount of dynamically induced excess pore water pressure were strongly affected by spatial variability of soil properties. In particular, by the used probability distribution and the description of its left tail, which corresponds to the presence of loose pockets in the soil deposit. Koutsourelakis et al. (2002) and Popescu et al. (2005b) presented their results as fragility curves for different parameters as average liquefaction ratio, maximum horizontal displacement, maximum ground settlement and structure tilting. These curves are strongly dependent on the soil properties and seismic motions; therefore, they are only to be used for a qualitative assessment of similar cases. Comparing the stochastic analysis with “corresponding” uniform soils with the same mean properties, Popescu et al. (2005b) showed an increase of about 20% in the excess pore water pressure when a CV of 40% was used.

Additionally, Nobahar and Popescu (2000); Griffiths and Fenton (2001); Popescu et al. (2005a); Li et al. (2015), among others, have studied the effects of inherent random soil hetero-

geneity on the bearing capacity (q_u) of shallow foundations. Once more, all of them have used Monte Carlo (MC) simulations considering a continuous heterogeneous field. As the evaluation of the bearing capacity is also governed by highly nonlinear constitutive laws, the comparison with uniform soil also showed great differences. For example, [Nobahar and Popescu \(2000\)](#) and [Griffiths et al. \(2002\)](#) found a 20-30% reduction in the mean q_u for heterogeneous soils with CV = 50%, compared to the corresponding value of a uniform soil with the same mean properties.

Instead of focusing on these comparisons, several studies including [Asaoka and Matsuo \(1983\)](#); [Kasama et al. \(2012\)](#); [Ching et al. \(2015\)](#); [Otake and Honjo \(2015\)](#), have concentrated in simplified ways to evaluate the effects of the soil spatial variability on structure performance by defining a Local Average (LA) of soil property for an appropriate volume. The notion of LA was, probably, introduced by [Vanmarcke \(1977\)](#) in the study of geotechnical structures, he stated that the system is controlled by the average over a certain size of line, area or volume, referred as LA, rather than by the soil parameter value at a single point. In fact, LA is recommended in practical design codes, such as Eurocode 7 ([CEN, 2004](#)), to determine characteristic values of geotechnical parameters. To account for the performance of systems with spatially variable soil deposits, a successful assessment on LA could reproduce the same statistical response of random field analysis. On the basis of these arguments, [Honjo and Otake \(2013\)](#) proposed appropriate sizes of LA regions for various geotechnical structures. These regions were supposedly related to the mechanism controlling the limit state; thus they were independent of the random field characteristics and of the absolute soil properties.

Another approach to analyze the effect of spatial variability on geotechnical applications is through laboratory tests. For instance, undrained cyclic triaxial tests on sand-gravel ([Budiman et al., 1995](#)) and sand-silt ([Konrad and Dubeau, 2002](#)) mixtures and centrifuge tests on mixtures of sand with different densities ([Ghosh and Madabhushi, 2003](#); [Chakraborty et al., 2010](#)) and with different permeabilities ([Maharjan and Takahashi, 2012](#)) evidence the decrease of liquefaction resistance of the mixture compared to that of uniform samples. A schema of the centrifuge test performed by [Chakraborty et al. \(2010\)](#) is shown in Figure 5.2d. In general, it was found that the effect of the loose sand zone was to induce increased excess pore water pressure (Δp_w) in the surrounding dense sand or create drainage paths, through which the Δp_w can be drained out causing differential settlements. While the effect on liquefaction is well evidenced, the effect on the induced-settlements is yet to be clarify. Concerning the centrifuge tests, [Garzón et al. \(2014\)](#) presented a new technique to evaluate the spatial variability on the soil properties by coupling a discrete random field generation method of nine cohesive soils

with a centrifuge consolidation test. The resulting effective normal stress, calculated for each cell by measurements of the unit weight and water content, not only depended on the intrinsic behavior but also on the neighboring soil. With respect to the centrifuge tests on liquefaction resistance (e.g. [Ghosh and Madabhushi, 2003](#); [Chakraborty et al., 2010](#)), it is possible that the initial state of the loose and dense sand was greatly affected however, no reference was given on this aspect. This technique could be useful to validate numerical models with controlled spatial variability; however, it is not easily applicable in a probabilistic analysis and thus its application for geotechnical systems is limited.

5.2.2 Added spatial variability

Concerning ground improvement methods, also experimental and numerical analyses can be found. For the former, [Hausler and Sitar \(2002\)](#), [Coelho et al. \(2004\)](#) and [Dashti et al. \(2010\)](#) performed various centrifuge tests to study the densification of liquefiable soils. Important conclusions were drawn with respect to the soil-structure interaction (SSI) effect on the pore-pressure induced softening. Even if a decrease on settlement was evidenced, there appeared to be an increase of energy transmitted to the structure. Furthermore, the presence of the structure reduced vertical flow and caused long-term horizontal pore pressure migration from underneath which induced important relative settlements.

Numerically, [Bradley et al. \(2013\)](#) studied soil improvement by jet grouting on the seismic response of a liquefiable deposit. The improved soil was a cementitious material thus no water migration was allowed. Again, all cases were effective at mitigating liquefaction; yet, some presented negative consequences on surface (e.g. large lateral displacements and vertical settlements). Additionally, soil improvement caused an increase in surface acceleration, specially at moderate-to-long periods. For example, the analysis of a structure vulnerability after a liquefaction countermeasure was performed by [Lopez-Caballero and Modaressi-Farahmand-Razavi \(2013\)](#). The mitigation method modeled was preloading, and the structural behavior was analyzed by two parameters: relative settlement and the inter-story drift. While the former was reduced after preloading, the latter was increased due to the higher surface amplification. These cases highlight the need for an optimization through which liquefaction resistance could be increased without the decrease in the structure vulnerability.

These examples are important; although, densification by compaction, grouting or mixing produces rarely a homogeneous soil. On the contrary, it results in a heterogeneous mixture of

the original soil and the added one (DeJong et al., 2013). Even if in reality, grouted columns are designed to have specific diameters and spacings, the material is in most cases an heterogeneous mixture of the added soil (or cement) and the original one. Generally, it is difficult to measure the mechanical properties of these columns in the field. Lambert et al. (2012) performed laboratory tests in samples from soil-cement mixed columns and found heterogeneities in the sides as well as in the core of the columns, as shown in Figure 5.2a, that consequently affected the mechanical properties. Different studies have assessed the fraction of soil remaining in the columns, for example Boulanger et al. (1998) estimated it at about 20%.

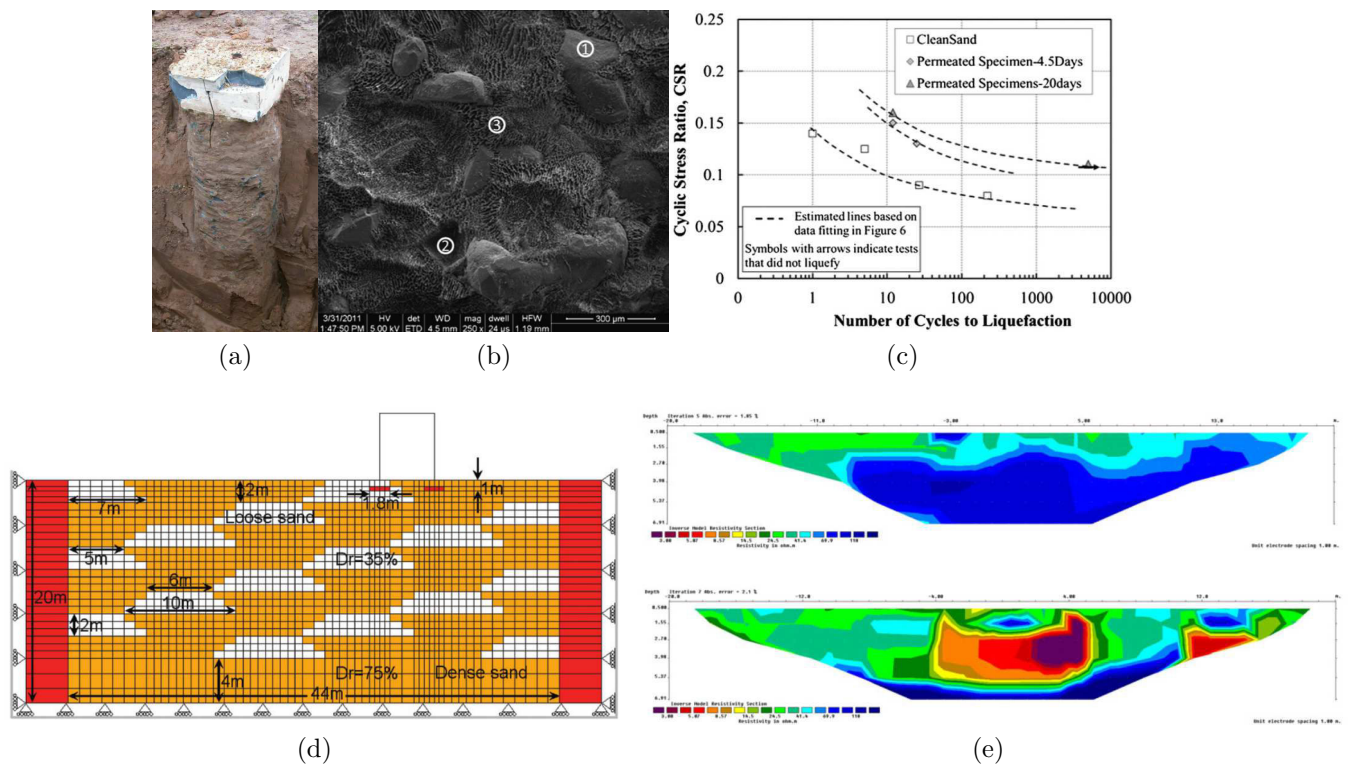


Figure 5.2 – Examples of added heterogeneity after soil treatment: a) *In-situ* soil-cement column (after Lambert et al., 2012), b) laboratory tests of sand specimens with bentonite suspension and c) comparison of liquefaction curves (after El Mohtar et al., 2013), d) centrifuge test modeling of heterogeneous soil model (after Chakraborty and Popescu, 2012) and e) *In-situ* sample of bio-stabilized gravel resistivity mapping before and during treatment (after Van Paassen, 2011)

Other improvement processes such as bentonite suspensions can be used to increase liquefaction resistance in sands. Figures 5.2b and 5.2c show a Cryo-SEM image of a sand-bentonite specimen and the liquefaction curves for a clean sand and the permeated specimens presented by El Mohtar et al. (2013). In the field scale, this technique and others such as vibro-compaction or bio-grouting have additionally an uncertainty of up to which depth or size the soil is affected, e.g. some areas can be more compacted than others or can have more bacteria-induced cemen-

tation. Examples on the latter are shown in Figure 5.2e of resistivity *in-situ* measurements presented by Van Paassen (2011).

To the best knowledge of authors, there is no numerical or experimental studies related to two-soil random mixtures of a liquefiable deposit accounting for both soil and seismic motion variability. These heterogeneous deposits exhibit large, sudden variations from one location to another, unlike natural soil deposits where those variations could be gradual. Therefore, the results of this study may overemphasize the effects of soil heterogeneity on water migration in spatially variable soils. However, as most laboratory soil testing procedures use uniform soil samples for assessing the liquefaction potential, their results in terms of cyclic induced Δp_w may well be on the under-conservative side when applied to natural soil deposits exhibiting inherent or added spatial variability (Chakraborty and Popescu, 2012).

5.3 Discrete random field model

The models to generate binary random fields can be divided in two main approaches according to their definition of spatial dependence: the logistic spatial generalized linear mixed models (SGLMM) that treat dependence indirectly by applying a latent Gaussian Markov random field over the lattice (Banerjee et al., 2003) and the autologistic models that do it directly through the *autocovariate*, i.e. a function of the observations themselves (Hughes et al., 2011). The homogeneous autologistic model was derived by Bartlett and Besag (1969) and is a nearest-neighbor model defined as a conditional probability. On the contrary, the SGLMM, firstly introduced by Whittle (1963), are defined as a joint probability distribution and are computationally costly (Besag, 1972). The spatial discretization for this work follows the autologistic model.

The one-sided approximation of the conditional autoregressive binary model in two dimensions under the assumption of homogeneity was derived from the Ising model to a 1st order Markov serie by Honjo (1985). The main properties of the model will be briefly discussed; even though, more information can be found in Bartlett and Besag (1969); Besag (1972); Honjo (1985). The model is discretized into a rectangular grid $m \times n$, where each element is assigned one of the possible values: 0 (material 1) or 1 (material 2). The binary mixture is defined with the spatial fractions $\gamma_1 = N_1/(N_1 + N_2)$ and $\gamma_2 = 1 - \gamma_1$, where N_{mat} is the number of elements of material *mat*. Since only one of the two definitions is needed, in this work the equations will be given for γ_2 and the subindice will be dropped. This value gives the probability of failure ($P(x_{ij} = 1)$). Thus, the expectation of x_{ij} , a value of the binary random variable X_{ij} , is given

by:

$$E[x_{ij}|x_{i-1,j}, x_{i,j-1}] = \alpha + \frac{1}{2} (\beta_1 \cdot x_{i-1,j} + \beta_2 \cdot x_{i,j-1}) \quad (5.3)$$

where α , β_1 and β_2 are the auto-regressive coefficients and are bounded between 0 and 1.

Evaluating the expectation, gives:

$$E[x_{ij}] = \alpha + \frac{1}{2} (\beta_1 \cdot E[x_{i-1,j}] + \beta_2 \cdot E[x_{i,j-1}]) \quad (5.4)$$

that under the condition of homogeneity, it can be expressed by:

$$\gamma = \alpha + \frac{1}{2} (\beta_1 + \beta_2) \cdot \gamma \quad (5.5)$$

therefore,

$$\alpha = \left[1 - \frac{1}{2} (\beta_1 + \beta_2) \right] \cdot \gamma \quad (5.6)$$

By replacing α in equation 5.3, the model gives:

$$E[x_{ij}|x_{i-1,j}, x_{i,j-1}] = \left[1 - \frac{1}{2} (\beta_1 + \beta_2) \right] \cdot \gamma + \frac{1}{2} (\beta_1 \cdot x_{i-1,j} + \beta_2 \cdot x_{i,j-1}) \quad (5.7)$$

Finally, the binarization is performed by comparing $E[x_{ij}]$ to a random number (u_{ij}) that follows a uniform distribution function between 0 and 1, where each element is independent. This process makes use of MC simulations to converge to a given γ value. The procedure to generate the field of size $m \times n$ is schematized in Figure 5.3 and has the following steps:

1. Assign the value of the corner element ($x_{i=1,j=1}$): As it is assumed that the model tends to homogeneity, $E[x_{1,1}]$ equals γ , thus the binarization process turns to:

$$x_{1,1} = \begin{cases} 0, & \text{if } \gamma \leq u_{1,1}[0, 1] \\ 1, & \text{otherwise} \end{cases} \quad (5.8)$$

2. Assign the values for the lower horizontal boundary $x_{i=2,\dots,m,1,j=1}$: Based on the 1D model where $\beta_1 = \beta_2$, so:

$$E[x_{i,1}|x_{i-1,1}] = (1 - \beta_1) \cdot \gamma + \beta_1 \cdot x_{i-1,1} \quad (5.9)$$

Again if $E(x_{i,1}) \leq u_{i,1}$, then $x(i, 1) = 0$; otherwise, $x(i, 1) = 1$.

3. Repeat previous step but for the left vertical boundary $x_{i=1,j=2,\dots,n}$:

$$E[x_{1,j}|x_{1,j-1}] = (1 - \beta_2) \cdot \gamma + \beta_2 \cdot x_{1,j-1} \quad (5.10)$$

4. Fill up the interior of the rectangle $x_{i=2,\dots,m,j=2,\dots,n}$: 2D model with equation 5.7.

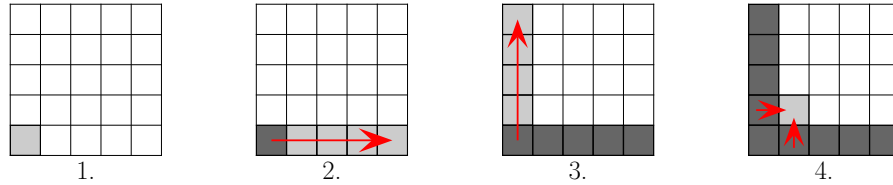


Figure 5.3 – Procedure scheme for the auto-regressive discretization model

Some simulations of a binary random field of size $m=40$ and $n=16$, with element size ($1\text{m} \times 0.5\text{m}$), are shown in Figure 5.4. Different cases are shown: Figure 5.4a shows one case without correlation (i.e. $\beta_1 = \beta_2 = 0$) and $\gamma = 0.4$. For the same spatial fraction, Figure 5.4b shows the effect of the (nearly) isotropic correlation; thus patches or clusters are formed. As β increases, so does the average area of the patches. This area is related approximately to the exponential of β^2 ; however, when β approaches unity, an anisotropy is introduced by the one-sided approximation. Honjo (1985) measured this anisotropy for different cases and concluded that it is not significant for low β values (i.e. approximately less than 0.7). Further developments, for example, the centered autologistic model proposed by Caragea and Kaiser (2009) remedies the bias due to non-negative autocovariate by applying a parametrization similar to the auto-Gaussian models. However, according to the comparison of this new model with the traditional one performed by Hughes et al. (2011), the regression parameters in the centered model are only reliable for very large lattices ($m, n > 900$) and no more than moderate spatial dependence.

Two extremes cases are also shown for perfect correlation in one direction and not at all in the other: when $\beta_1 = 1$ and $\beta_2 = 0$, horizontal layers are formed (shown in Figure 5.4c); and when $\beta_1 = 0$ and $\beta_2 = 1$, vertical columns can be simulated (in Figure 5.4d). In these cases, the anisotropy is seen as the patches are elongated in the direction with larger β .

5.3.1 Correlation structure

Honjo (1985) stated that the one-sided approximation is preferred to the general case, because of the simple derivation of the autocovariance function ($Cc(r, s)$) which is evaluated by

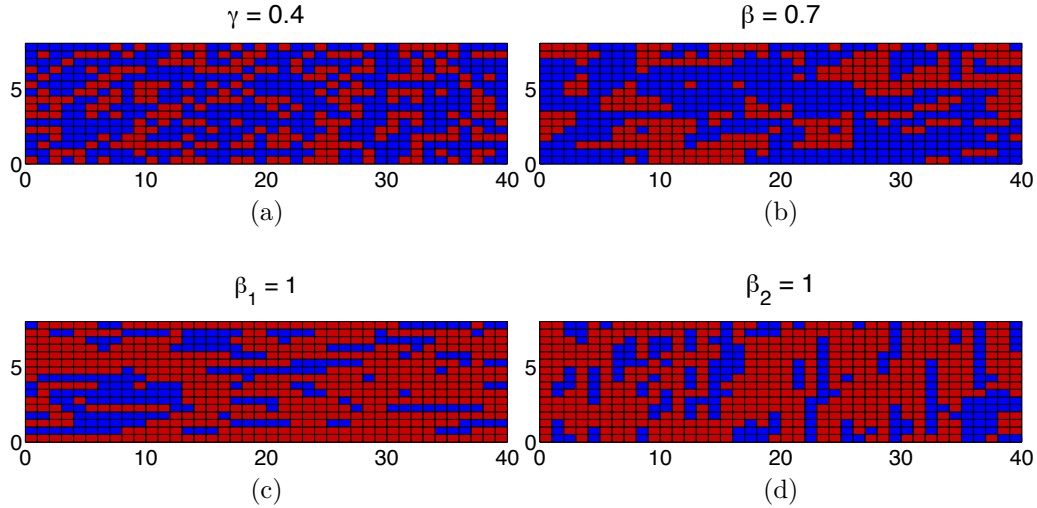


Figure 5.4 – Simulations of a binary random field for : $\gamma = 0.4$ with a) no correlation ($\beta_1 = \beta_2 = 0$) and b) high isotropic correlation ($\beta_1 = \beta_2 = 0.7$); and for $\gamma = 0.7$ with high anisotropic correlation : c) horizontal layers ($\beta_1 = 1$ and $\beta_2 = 0$) and d) vertical columns ($\beta_1 = 1$ and $\beta_2 = 0$)

cross-correlation at two points separated by r and s in the horizontal and vertical directions, respectively, as :

$$Cc(r, s) = \gamma \cdot (1 - \gamma) \cdot \beta_1^r \cdot \beta_2^s \quad (5.11)$$

According to equation 5.11, β_1 and β_2 have a direct physical interpretation as they give the one step correlation of the process in the horizontal and vertical direction, respectively. Note that the element expectation ($E[x_{ij}]$) is influenced only by its *nearest-neighbors* $x_{i-1,j}$ and $x_{i,j-1}$, which is a Markov property (Honjo, 1985). The correlation structure shows an exponential decay, which is expected as it was assumed the Markov definition of order 1. Recall that the autocorrelation (ρ) is the autocovariance normalized by the variance (σ^2) in this case equal to $\gamma \cdot (1 - \gamma)$. Figure 5.5a shows ρ values for different β values with β_1 equal to β_2 and r equal to s , which is equivalent to the lag (τ) defined for the random fields in section 5.2.1.3. Note that when τ is equal to 1, ρ is equal to the product of the correlations (i.e. $\beta_1 \cdot \beta_2$).

The failure probability for the system of $m \times n$ lattice points was also found by Honjo (1985) as follows:

$$p_f = 1 - \left[\beta_1^{m\gamma} \cdot \beta_2^{n\gamma} \cdot \exp \left(-m \cdot n \left(\frac{\gamma}{2} \right)^2 \cdot \ln \beta_1 \cdot \ln \beta_2 \right) \right] \cdot (1 - \gamma) \quad (5.12)$$

where $\beta_1^{m\gamma}$ and $\beta_2^{n\gamma}$ come from the boundaries, $\exp(\cdot)$ term results from the inside 2D lattice and $(1 - \gamma)$ is the marginal non failure probability of the initial point. Figure 5.5b shows the

calculated p_f for an increasing square area of size $N = m = n$ with two different γ values. It can be seen that when β is equal to unity, the whole area acts as one element, thus $p_f = \gamma$. On the other hand, when $\beta = 0$, the system has a p_f equal to 1. It is interesting to note that p_f is highly sensitive to β , even for very low values (e.g. 0.1 or 0.2) and specially for low γ values.

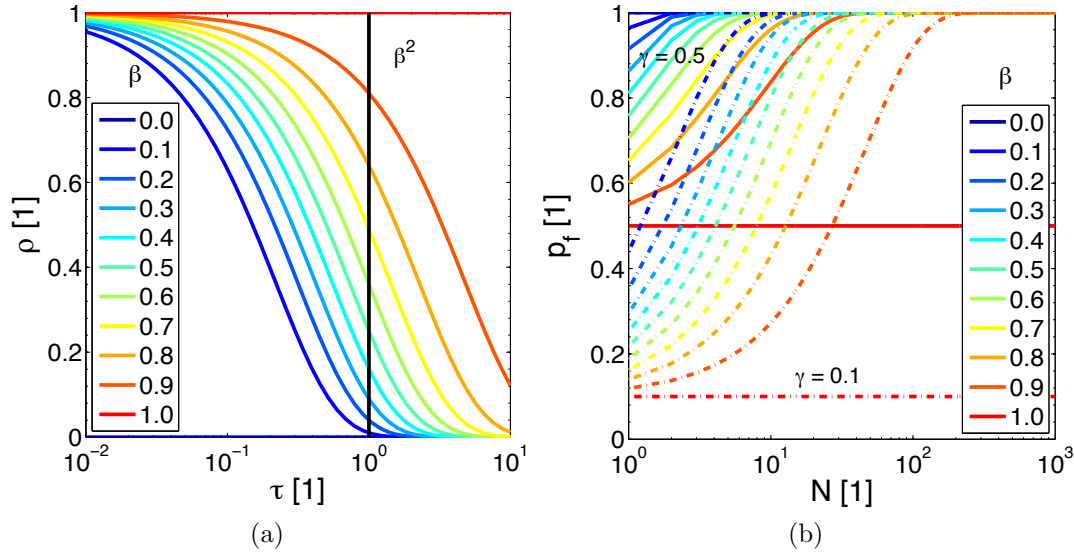


Figure 5.5 – Correlation structure of the binary random field for $\beta_1 = \beta_2$: a) autocorrelation function with $\tau = r = s$ and b) failure probability for γ equal to 0.1 and 0.5

5.3.2 Homogenization theories

The process of homogenization consists of deriving the effective properties for an heterogeneous system so that it can be viewed as homogeneous on a particular macroscopic scale depending on the property of interest (Koplik, 1991). Most of the advancements in this field come from the analytic and experimental work in a variety of transport processes, such as the electric current, heat flux, mass flux or magnetic induction, among others. The effective medium depends on the *geometry* (e.g. shape and size of particles) and the *topology* or connectivity among particles. Traditional theories are based on certain geometric arrangements, such as vertical or horizontal layers, for which the effective properties have an exact solution. These arrangements are only extreme cases and are often regarded as bounds of the solution. In contrast, while the effective medium theories (EMTs) are also based on one exact solution, they combine the effect of each material on the system. The other theories presented have only studied the geometry of the particles hence, they have neglected all possible interactions. On this purpose, EMTs have been combined with the percolation theory, which is a statistical tool to study the probabilistic and

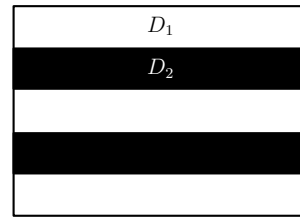
geometric properties of connected clusters of one material in a heterogeneous system (Frary and Schuh, 2005).

5.3.2.1 Traditional theories

Traditional homogenization theories are often used to describe geotechnical properties. For example, the work on spatial variability effect on bearing capacity of Popescu et al. (2005a) often compares the average results of the heterogeneous soil models with the “corresponding homogeneous soil”. According to the authors, the homogenization is the mean value of the Monte Carlo simulations; although this is only true for vertically layered materials (i.e. parallel to the bearing capacity) described by classical homogenization theories. If, on the contrary, the layers are horizontal (i.e perpendicular or serial) the effective properties of the homogeneous model would be a harmonic average. It is clear that for random fields, these are only extreme cases which are known as Wiener (1912) bounds. For a mixture of properties D_1 and D_2 where γ is the spatial fraction of D_2 , the Wiener (1912) bounds are defined as:

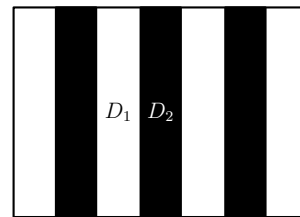
- Parallel :

$$D_{\parallel} = (1 - \gamma) \cdot D_1 + \gamma \cdot D_2 \quad (5.13)$$



- Serial :

$$D_{\perp} = \frac{1}{\frac{(1-\gamma)}{D_1} + \frac{\gamma}{D_2}} \quad (5.14)$$



As previously stated, the Wiener (1912) bounds correspond to two averages: the arithmetic and harmonic averages. However, an additional average called the geometric average is often used to compare values with different ranges, which is the case in study. The geometric average normalizes the ranges by applying the sum on a logarithmic scale, as follows:

$$D_G = \exp[(1 - \gamma) \ln D_1 + \gamma \ln D_2] \quad (5.15)$$

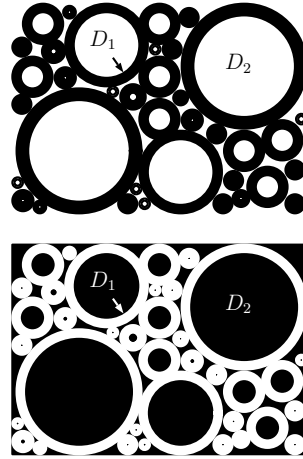
Another case that can be exactly modeled as homogeneous consists of concentric-shell structures, i.e. one material coating the other at spheres of different size. When $D_2 > D_1$, the properties can be described by the HS equation expressed by Hashin and Shtrikman (1962) as:

- Material 1 coating material 2:

$$D_{HS^+} = D_2 + \frac{1 - \gamma}{\frac{1}{D_1 - D_2} + \frac{\gamma}{d \cdot D_2}} \quad (5.16)$$

- Material 2 coating material 1:

$$D_{HS^-} = D_1 + \frac{\gamma}{\frac{1}{D_2 - D_1} + \frac{1 - \gamma}{d \cdot D_1}} \quad (5.17)$$



where d is the dimensionality. This parameter binds the model to fluctuate between the Wiener bounds; hence, when d is equal to unity, they become the parallel bound and as it tends to infinity it approaches the perpendicular one. Actually, HS bounds are narrower than the Wiener bounds and are often used as they are simple and intuitive. However, they still give wide predictions, specially if the ratio between the material properties is big.

5.3.2.2 Bruggeman symmetric effective medium (BEM)

Besides these traditional homogenization theories, another approach consists in identifying an effective property for which the average behavior of the heterogeneous model remains unchanged. This approach is known as the effective medium theory (EMT) and is based on the exact solution for one single spherical inclusion embedded in an infinite medium. There are two types of EMTs: the asymmetric which deals with dilute particles of very small size in a matrix, and the symmetric, which treats each phase independently and equally. The former is also known as the Maxwell-Garnett equation:

$$\frac{D_{eff} - D_1}{D_{eff} + (d_{BEM} - 1) \cdot D_1} = \gamma \frac{D_2 - D_1}{D_2 + (d_{BEM} - 1) \cdot D_1} \quad (5.18)$$

Note that this equation coincides with the lower HS bound when $D_2 > D_1$ and the upper HS bound otherwise. In the other hand, the symmetric EMT is the classical theory of conduction in mixtures presented by [Bruggeman \(1935\)](#) and known as the BEM approximation. When the properties of both materials are of similar magnitude, the BEM equation is:

$$(1 - \gamma) \frac{D_1 - D_{eff}}{D_1 + (d_{BEM} - 1) \cdot D_{eff}} + \gamma \frac{D_2 - D_{eff}}{D_2 + (d_{BEM} - 1) \cdot D_{eff}} = 0 \quad (5.19)$$

where d_{BEM} is equal to half the mean number of bonds presented at any site of the network (Kirkpatrick, 1973). The BEM equation gives a more precise solution as it accounts for each material independently. An additional advantage is the possibility to include multi-soil mixtures as follows:

$$\sum_i \gamma_i \frac{D_i - D_{eff}}{D_i + (d_{BEM} - 1) \cdot D_{eff}} = 0 \quad (5.20)$$

Although the EMTs are based on spherical inclusions, they have been widely used in the literature for various particle geometries and microstructural arrangements.

5.3.2.3 Generalized Effective Medium (GEM)

Traditional homogenization theories are based on the geometric arrangements among the phases, e.g. parallel and series (Wiener, 1912) or concentric (Hashin and Shtrikman, 1962). Effective medium theories (EMT) are derived on the exact solution for a single spherical inclusion in an infinite medium therefore also neglect interactions among particles. However, percolation theories as statistical tools have been developed to describe the topology of heterogeneous materials.

The percolation theory is focused on the existence of a percolating cluster that connects opposite sides of a system. Two types of percolation processes can be identified in lattices as shown in Figure 5.6 given by Bunde and Kantelhardt (2005): the bond, related to the junctions or paths (marked with bold lines), and the site percolation, related to the nearest-neighbors or elements (marked with dashed lines). The first emergence of the percolation cluster corresponds to the critical fraction (γ_c , often noted by p_c but to keep consistency in the case study, γ will be used instead). The specific value of the threshold depends on: (1) the lattice type which includes dimensionality and symmetry, (2) the percolation type, (3) the system size (being finite or infinite), and (4) the correlations among the materials (Brunini et al., 2011).

Some systems have exact solutions though they correspond to infinitely large non correlated occupations. For example, for a square lattice the exact bond percolation is 0.5 and for site percolation it is slightly higher (about 0.59); as for a triangular one, the bond percolation is about 0.35 while the site percolation is 0.5. When the system is not sufficiently large, there is a range of fractions, spanning over a width Δ , in which the percolation transition can possibly occur. As the system size increases, Δ decreases and γ_c approaches the infinite value. When positive correlations exist, more clusters will be formed and γ_c tends to decrease. When in a

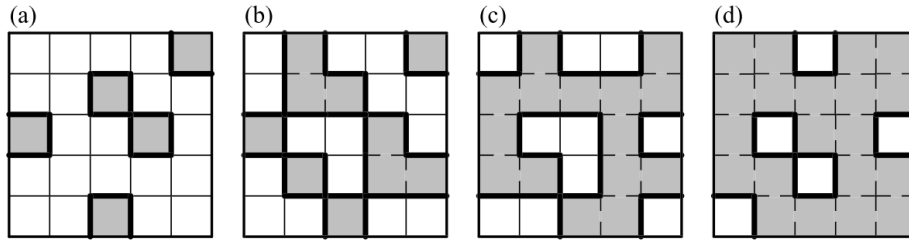


Figure 5.6 – Example of the percolation types on a discrete random field: a) $\gamma < \gamma_c^{bond}$, b) $\gamma = \gamma_c^{bond}$, c) $\gamma = \gamma_c^{site}$ and d) $\gamma > \gamma_c^{site}$ (after [Bunde and Kantelhardt, 2005](#))

square lattice, the next-nearest-neighbor is considered in site percolation, γ_c decreases to about 0.41 ([Roman et al., 1986](#)).

When a perfect phase contrast is present, that is, the property of interest of one of the two materials is either zero or infinite, the percolation theory describes the effective properties as:

$$D_{eff} \propto (\gamma - \gamma_c)^t \quad \text{for } \gamma > \gamma_c, \quad 0 \quad \text{otherwise} \quad (5.21)$$

$$D_{eff} \propto (\gamma_c - \gamma)^{-s} \quad \text{for } \gamma < \gamma_c, \quad \infty \quad \text{otherwise} \quad (5.22)$$

As in most cases, no perfect phase contrast is present, an approximation defined for all γ values is required. [McLachlan et al. \(1990\)](#) derived a semi-empirical correlation that includes the effective diffusivity in the BEM equation. They replaced the dimensionality by the inverse of the percolation threshold (i.e. $1/\gamma_c$) and introduced the exponents s and t . The resulting equation is known as the generalized effective medium (GEM) equation:

$$(1 - \gamma) \frac{D_1^{1/s} - D_{eff}^{1/s}}{D_1^{1/s} + (\gamma_c^{-1} - 1)D_{eff}^{1/s}} + \gamma \frac{D_2^{1/t} - D_{eff}^{1/t}}{D_2^{1/t} + (\gamma_c^{-1} - 1)D_{eff}^{1/t}} = 0 \quad (5.23)$$

where s and t are the scaling exponents for $\gamma < \gamma_c$ and $\gamma > \gamma_c$, respectively. They are universal percolation quantities and are supposedly independent on the discrete or percolation type, the size nor the correlation of the system. Their values can be found via numerical simulations and if certain physical processes can be described by the same set of scaling exponents, then the physical laws governing these phenomena must be fundamentally the same ([Sahimi, 2003](#)). Although equation 5.23 is semi-empirical, it has been shown both experimentally and numerically to yield good predictions for many transport properties when dealing with binary heterogeneous materials ([Chen, 2008](#)).

5.4 Bearing capacity model

A finite element model is used to evaluate the bearing capacity of a shallow foundation situated on the middle of the model. Two-dimensional, plane-strain analyzes are performed with the general purpose finite element code GEFDyn (Aubry and Modaressi, 1996). The numerical model uses quadrilateral isoparametric elements with eight nodes. A rigid perfectly plastic model is implemented to simulate the behavior of purely cohesive soils. While the Young modulus (E) and the Poisson's ratio (ν) influence the computed settlement, the bearing capacity of a footing depends primarily on the undrained shear strength (c_u) (Griffiths et al., 2002). Thus in the present study, to simplify the analyses, E and ν are kept constant and equal to 100MPa and 0.3, respectively; while, each simulation of the binary random field is used as input for c_u at each element on the model. Hence, for binary value (x_{ij}) equal to 0, the soil 1 is used with c_{u1} equal to 20kPa; and for $x_{ij}=1$, soil 2 is used with $c_{u2} = 100$ kPa. A schema of the model is shown in Figure 5.7. The dimensions are given by the width of the base (B), in this case 4m, and are taken from the recommendations of Griffiths and Fenton (2001): a depth of 2B (8m) and a width of 5B (20m). The size of the elements is 0.25 m in both directions which corresponds to B/16, which was also used by Chen et al. (2012). A rigid bedrock underlies the soil and as only vertical loads are applied, horizontal displacements are inhibited on the lateral boundaries. Additionally, no friction is assumed between the footing and the soil thus a perfectly smooth footing is simulated, i.e. free horizontal displacements.

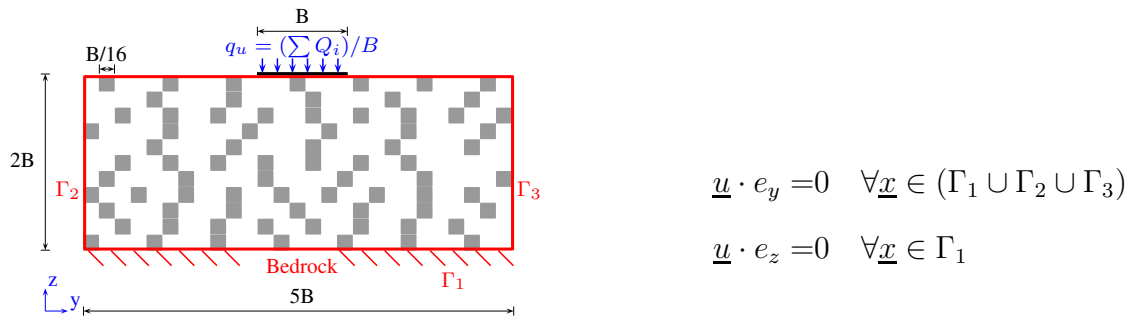


Figure 5.7 – Schema of the numerical model

The test consists of applying an increasing vertical displacement (u_{zmax}) at the center of the foundation (i.e. at one node) with free rotations allowed for the foundation. As the latter is rigid, a uniform displacement is considered in this interface. The ultimate bearing capacity is taken when $u_{zmax}/B = 2.5\%$ (10 cm) and is equal to the sum of the nodal forces (Q_i) in the interface between the soil and the structure's foundation divided by the width of the base

(i.e. $q_u = (\sum Q_i)/B$). For a homogeneous weightless soil, this value is given by the Prandtl's solution as $q_u = N_c \cdot c_u$, where N_c is the dimensionless bearing capacity factor and equals $2 + \pi$ or 5.14 (Prandtl, 1921). The finite element analysis for the homogeneous cases of soils 1 and 2 presented a relative difference with respect to Prandtl's solution of 14.7 and 6.85%, respectively. The latter is one percentual point below to the results of Chen et al. (2012) with the same properties and mesh size and similar to those of Popescu et al. (2005b). These differences are due to some of the assumptions in the model, for example, the use of a rigid foundation, including shear stresses at the soil-structure interface, gradual development of plastic zones, as well as inherent approximations induced by the numerical methods which are further explained by Nobahar (2003).

Furthermore, because of the inherent approximation of the numerical method, the results depend on the mesh size. By refining the mesh, these differences could be reduced (thus not eliminated) but the computational cost would increase for the ensuing random-field simulations. The effect in the increase of the mesh discretization, i.e. number of elements in each direction, has been evaluated by other authors, for example the results presented by Chen et al. (2012) show about 50% decrease in the numerical error when the mesh discretization is increased by 4. Due to the rigid footing, the vertical stress distribution is not uniform; instead, a stress concentration is presented at the vicinity of the footing edge which will cause higher plastic strains. If a finer mesh is used in this region, the capability to reproduce plastic strain concentration in narrower zones is enhanced hence the accuracy in q_u will improve; however, it will add more complexity to the generation of the random field and it will not be considered in this study. Given the large amount of random field simulations, the present mesh size was judged to be sufficiently accurate and efficient. Figure 5.8 shows the relative difference of the finite element model with respect to the Prandtl's solution (δ_{FE}) as a function of the undrained shear strength (c_u) for the homogeneous cases. It is noted that the rate decreases with increasing c_u almost exponentially. As in the study of Griffiths et al. (2002) and in order to take into account this discretization error, most of the results will be normalized by the deterministic value of the uniform case for soil 2, hence the effect of this marginally higher numerical estimation will be relatively insignificant.

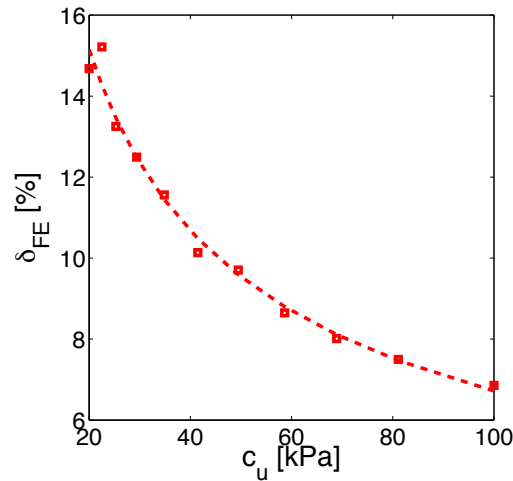


Figure 5.8 – Relative difference of the Finite Element model with respect to the Prandtl solution (δ_{FE}) as a function of the undrained shear strength (c_u) of a homogeneous soil deposit

5.4.1 Coupling binary random field with FEM

The spatial discretization is used to analyze the heterogeneous deposit. The spatial fraction (γ) is varied from 0.1 to 0.9 (9 values) and several spatial distributions per value were done. Different auto-regressive coefficients on both directions were tested to analyze the effect of the correlation length. As an example, two spatial distributions for the same spatial fraction ($\gamma = 0.5$) and the same auto-regressive coefficients ($\beta_1 = \beta_2 = 0.9$) are shown in Figure 5.9. They correspond to the extreme values of bearing capacity found for this set of values: the minimum shown in Figure 5.9a ($q_u=148$ kPa) and the maximum, in Figure 5.9b ($q_u=287$ kPa). Soil 1 that has a smaller c_u is in red and soil 2 is in blue. It is clear that for the mesh that presented the minimum q_u the weaker soil is mostly concentrated near the foundation; while for the other one, the stronger soil under the foundation interconnects from the surface to the deeper zone. The spatial variability is not simply affecting the value of the bearing capacity but it modifies the basic form of the failure mechanism. These two distributions presented very different q_u values, thus a convergence analysis was performed to choose the sufficient number of simulations per γ value.

The convergence of both the mean and the standard deviation obtained for the bearing capacity is shown for one case ($\gamma = 0.1$ and $\beta_1 = \beta_2 = 0.4$) in Figure 5.10. The average values are shown in red and the confidence intervals, in dotted blue lines. The latter are obtained with the t-student and χ^2 statistical models with 5% confidence level for the mean and standard deviation, respectively. 200 spatial distributions were tested; although, after approximately 50 the statistical convergence appears to be stable hence is sufficient for the application considered

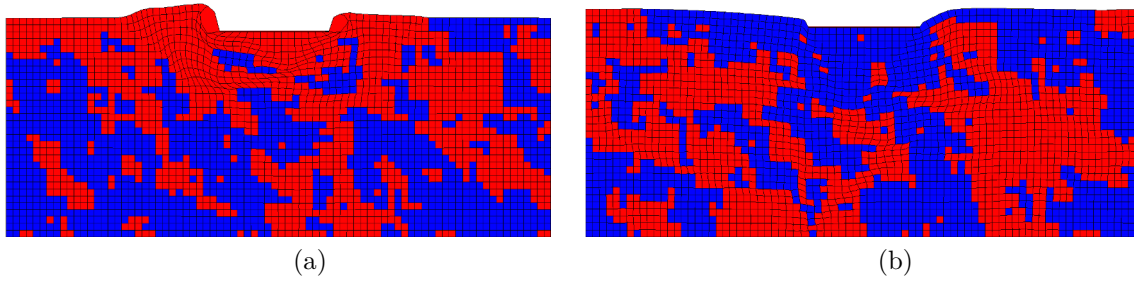


Figure 5.9 – Binary mixture for 2 distributions with $\gamma = 0.5$ and $\beta_1 = \beta_2 = 0.9$: a) minimum q_u (148 kPa) and b) maximum q_u (287 kPa). In red ($c_{u1}=20\text{kPa}$) and in blue ($c_{u2}=100\text{kPa}$).

in this work. As expected the mean value converges more quickly and presents less variation. In contrast, the standard deviation has more variation and wider confidence intervals. Here on, a maximum of 50 simulations are performed for each case.

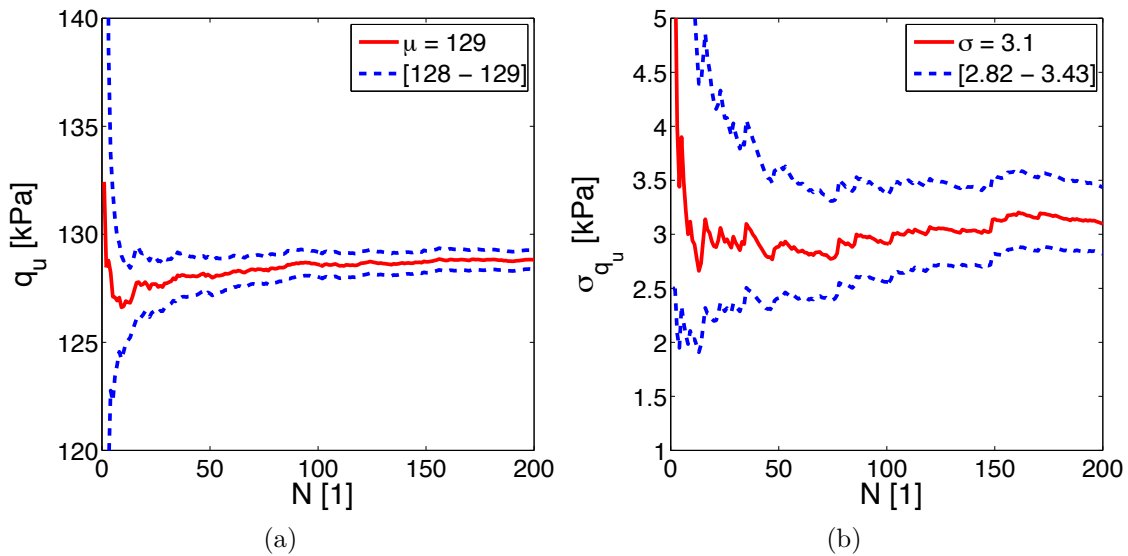


Figure 5.10 – Convergence of the a) mean and b) standard deviation of the bearing capacity (q_u) for $\gamma = 0.1$ and $\beta_1 = \beta_2 = 0.4$. The average values are shown in red and the confidence intervals, in dotted blue lines.

5.4.1.1 Effect of the mixture fraction

The uniform vertical displacement ($u_{z\max}$) at the rigid foundation is normalized by the width of the foundation and shown in Figure 5.11 for all γ values used as a function of the q_u value which is also normalized by q_u evaluated for $\gamma = 1$. It is noted that even if the ultimate bearing

capacity is taken for 2.5% of the normalized settlement, the value is already stable at 2% for the highest q_u , while for lower q_u values $u_{z\max}/B$ is constant at about 1%. Additionally, it seems that the variation increases with γ .

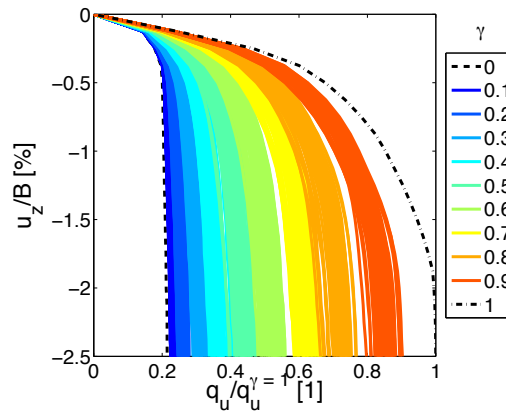


Figure 5.11 – Normalized settlement as a function of the normalized bearing capacity for different spatial fractions. An isotropic correlation of $\beta_1 = \beta_2 = 0.3$ is used

The evolution of q_u as a function of γ is shown in Figure 5.12 for different correlation values. For the sake of brevity only four cases are presented: the uncorrelated model (i.e. $\beta_1 = \beta_2 = 0$) and 3 other values of isotropic correlation. The box-and-whiskers plot is useful to show scalar-value statistics because of the large amount of uncertainty information compared to mean and standard deviations. Additionally, due to its flattened shape, box plots are better when it is desired to compare the uncertainties in a number of related variables (Helton et al., 2006). The box is composed of three quartiles, corresponding to 25%, 50% and 75% of data and the whiskers are the lowest and highest values within 1.5IQR (Inter-quartile range). Values outside the whiskers are outliers and are drawn as blue dots. The mean values are in red and joined by the curve. The relative position of the mean value with respect to the median (i.e. the second quartile) is an indicator of the symmetry, and with respect to the other quartiles, of the skewness. Moreover, the size of the box and length of the whiskers gives information about the spread or dispersion of the data.

It can be seen in Figure 5.12a that when no correlation is used less dispersion is presented. Whereas, when a high correlation is used, like shown in Figure 5.12d, the dispersion increases. Additionally, the dispersion is higher for the middle spatial fractions; though, it seems that the spatial configuration is of key importance when a similar fraction of both materials is used. This could be explained by the higher interaction between the soils and the resulting failure surfaces. When the isotropic correlation increases, the soils are “packed” in clusters and therefore each distribution will have a different behavior.

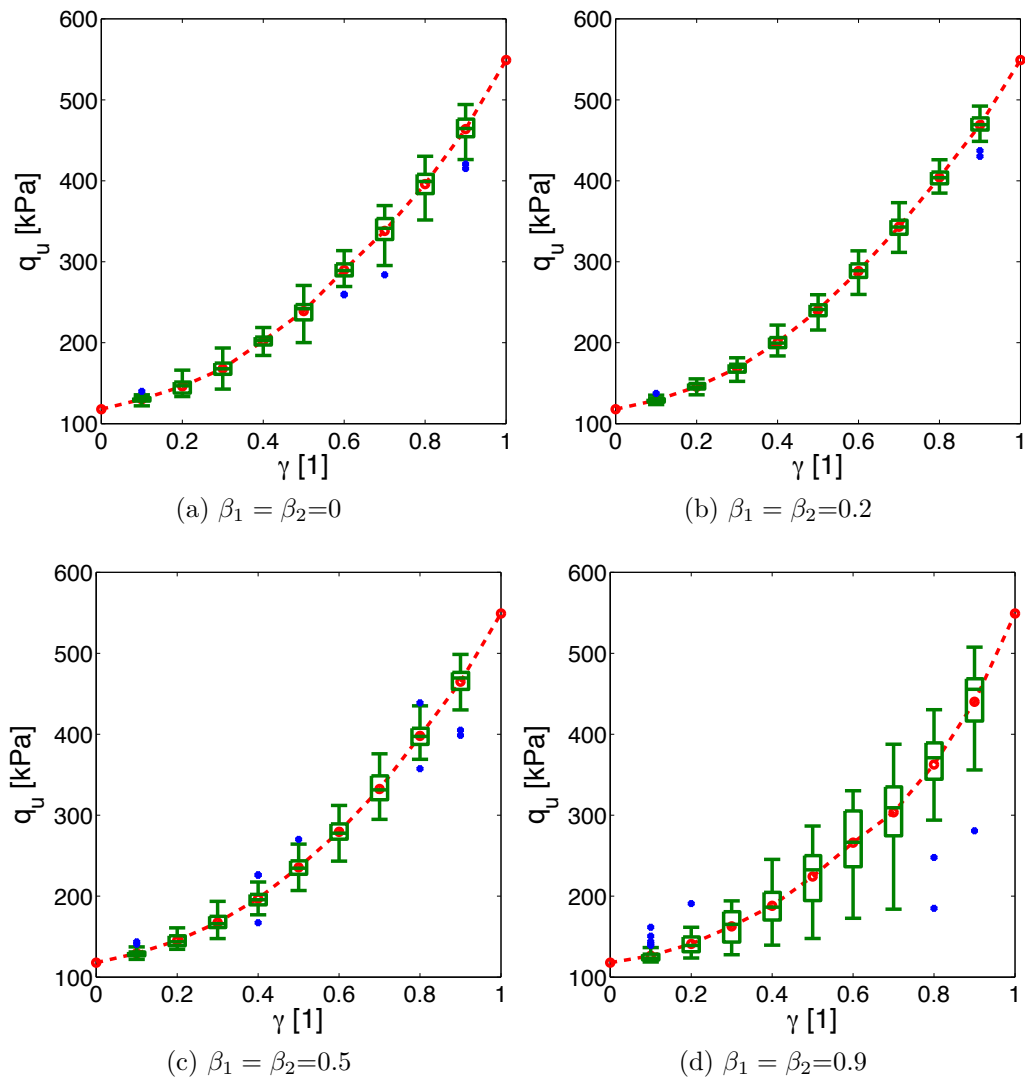


Figure 5.12 – Models with different heterogeneity surface fraction γ and different auto-regressive coefficients

On the other hand, the uncertainty fluctuation (or dispersion) in soil properties is commonly quantified by the coefficient of variation (CV). It is defined as the ratio between the standard deviation and the mean value; thus it is a normalized quantity and it is of great use in probabilistic analysis. Representative values of CV can be found in the literature based on laboratory data, *in-situ* tests or engineering judgment and they range from 10 to 50% for the undrained shear strength (Phoon and Kulhawy, 1999). In this analysis, the CV of the bearing capacity (q_u) due to discrete spatial variability was calculated for the different spatial fractions and isotropic correlations.

Figure 5.13 shows the CV value as a function of the spatial fraction for each correlation and for all the distributions tested. It is interesting to note how the CV increases with the degree of correlation and it is more important for spatial fractions near 0.5. In general, compared to the ranges given by Phoon and Kulhawy (1999), the values are very low (i.e. never above 20%). This is due to the fact that the variability measured is only induced by the spatial variability, referred by other authors as inherent random heterogeneity, and it does not take into account the measurement errors and uncertainty in physical parameters, present in experimental data. According to these values, thus, it seems that uncertainties due to spatial variability are lower to those related to the strength values (induced by measurement, statistical and transformation errors).

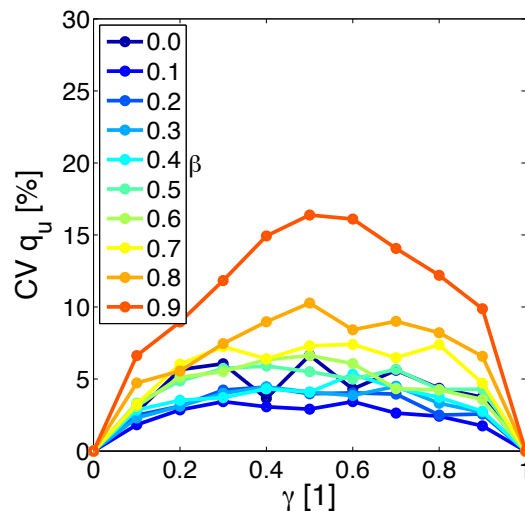


Figure 5.13 – Coefficient of variation (CV) of the bearing capacity (q_u) as a function of the spatial fraction (γ)

5.4.1.2 Effect of anisotropic correlation

An important effort is evidenced in geotechnical engineering in order to quantify the correlation length in the spatial variability. Jones et al. (2002) present a literature review of some laboratory and *in-situ* tested properties scale of fluctuation in horizontal and vertical direction, however the amount of information concerning these values is limited in comparison to the CV of inherent variability. In general, the correlation length in the horizontal direction is more than one order of magnitude larger than in the vertical one. However, if the spatial variability due to improvement technique is modeled, the vertical correlation will be increased. At the moment, very little information can be found hence a parametric analysis was performed for different correlations. For two spatial fractions (0.4 and 0.6), only one correlation was changed from 0.1 to 0.9 while the other one was fixed and equal to 0.1. The mean and CV of the bearing capacity are shown in Figure 5.14. As the correlation increases, the mean decreases and the CV increases. However, the effect of the correlation is more important for the CV value (e.g. for $\beta = 1$ the CV is twice the one without correlation; while the decrease in the mean value is only 2%). For $\gamma = 0.4$, the vertical correlation presents in general higher values for both mean and CV values; although it is the contrary for $\gamma = 0.6$.

5.4.2 Homogeneous equivalent models

In theory, homogeneous equivalent models are uniform fields described by an effective property that takes into account the effect of spatial variability. They are interesting from an engineering point of view because instead of analyzing N simulations of heterogeneous or random fields, it is easier to carry out simulations of spatially uniform fields with a random variable. In the same manner, the variability drawn from the spatial variability could also be used to generate marginal probability density functions (PDF) or cumulative density functions (CDF). Figure 5.15 shows the normalized CDF of the bearing capacity for a γ of 0.1, 0.5 and 0.9 and all different correlations. As it is seen, again, the isotropic correlation plays an important role in the CV (refer to the inclination in the CDF in Figures 5.15b and 5.15c). Additionally, for γ of 0.9, the type of the distribution changes; though, for instance, the results for a β of 0.9 have a lognormal distribution -as it presents a positive skewness- while for a β of 0.1, a normal distribution is adequate. Jones et al. (2002) summarized the inherent variability on strength characteristics given by *in-situ* and laboratory measurements and suggest a lognormal PDF for undrained shear strength (c_u) in clays and a normal one for c_u in silty-clays. Hence, as the c_u

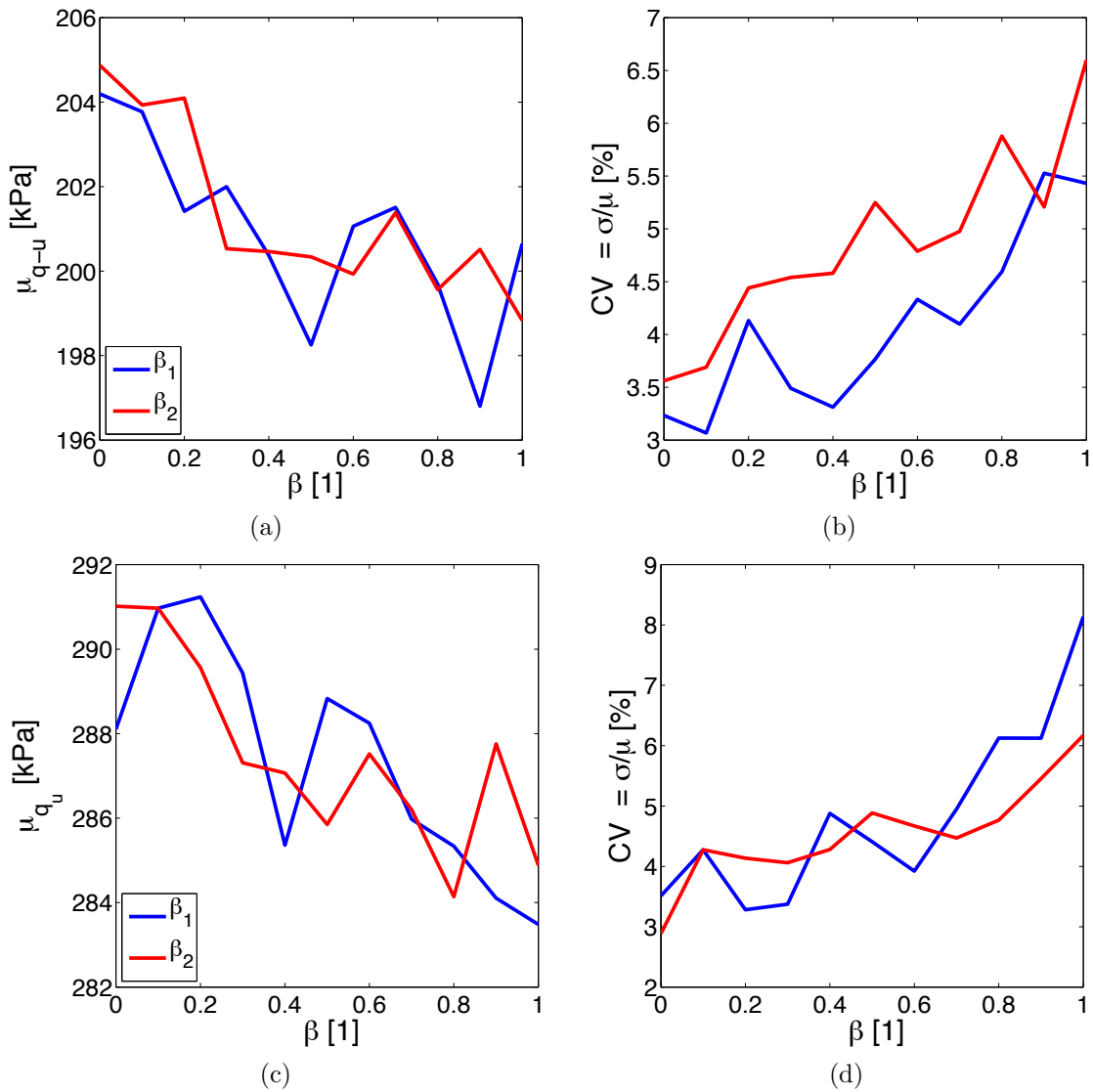


Figure 5.14 – Anisotropic correlation effect on the a) and c) mean and b) and d) CV of the bearing capacity for a spatial fraction of 0.4 and 0.6, respectively. The coefficient in the horizontal (β_1) and vertical (β_2) correlation is varied while in the other direction it is fixed to 0.1.

decreases, the distribution shifts from lognormal to normal, as it does with the results for γ of 0.9. An accurate function of probability could be very useful to construct fragility curves that take into account the spatial variability uncertainty due to a soil improvement technique. However the success of this kind of analysis requires an accurate safety limit or threshold related to the deterministic properties.

The evaluation of the bearing capacity (q_u) is linearly dependent to the undrained shear strength (c_u). Though, the effective property ($c_u^{eff}(\gamma)$) is equal to $\mu_{q_u}(\gamma)/5.14$, where μ , indicates the mean value of all the q_u values resulting from the heterogeneous models for a specified γ . It is reasonable to believe that the same numerical error - i.e. 10% in average - with respect

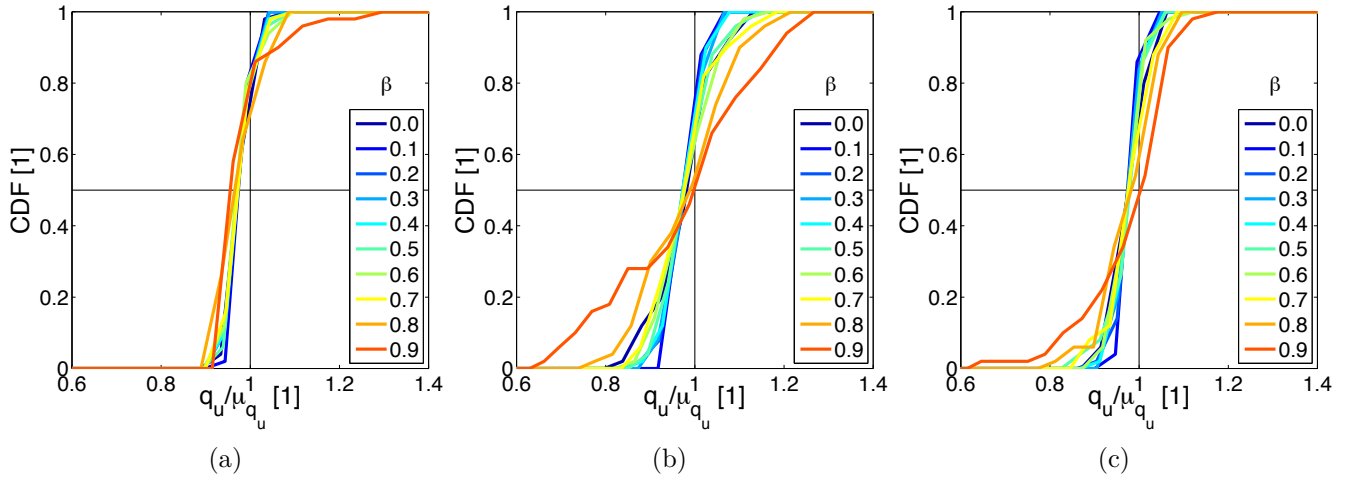


Figure 5.15 – Experimental cumulative density function of the bearing capacity for : a) $\gamma=0.1$, b) $\gamma=0.5$ and c) $\gamma=0.9$

to the Prandtl's solution is present in all cases; therefore, for the homogeneous model the error is deducted from the effective property (otherwise it would be counted twice). Figure 5.16a shows the mean of c_u^{eff} as a function of γ for the different correlations tested. The average corrected effective property (c_u^{eff*}), shown in the figure in black, was used for the homogeneous equivalent model. In Figure 5.16b, the results are compared with the q_u mean values for all correlations. As expected, the homogeneous models have the same behavior and could be described by an equation. It is important to note that these models take into account all the correlations tested and their respective dispersion; however the general behavior with respect to the spatial fraction (i.e. the shape of the function) is the same for all cases hence the equation should be similar.

Now, the traditional homogenization theories are compared to the numerical results. Figure 5.17a shows the mean q_u values normalized by the q_{u2} as a function of γ and the Wiener and HS bounds. As it is shown, if the homogeneous models take the arithmetic mean as the effective property, the heterogeneous model will always present lower resistance (i.e. lower q_u values). Additionally, for lower spatial fractions ($\gamma < 0.4$) the mean values are lower than the HS^- bound.

When comparing to the geometric average, shown in Figure 5.17b, results for $\gamma > 0.6$ and low correlation ($\beta < 0.4$) are well fitted, on the contrary, they will present lower values. Because the log-transformed variable is symmetric and quantiles are preserved under monotonic transformations, the geometric mean of a lognormal distribution is equal to its median. In the study performed by Griffiths et al. (2002), the random field had a lognormal distribution, hence,

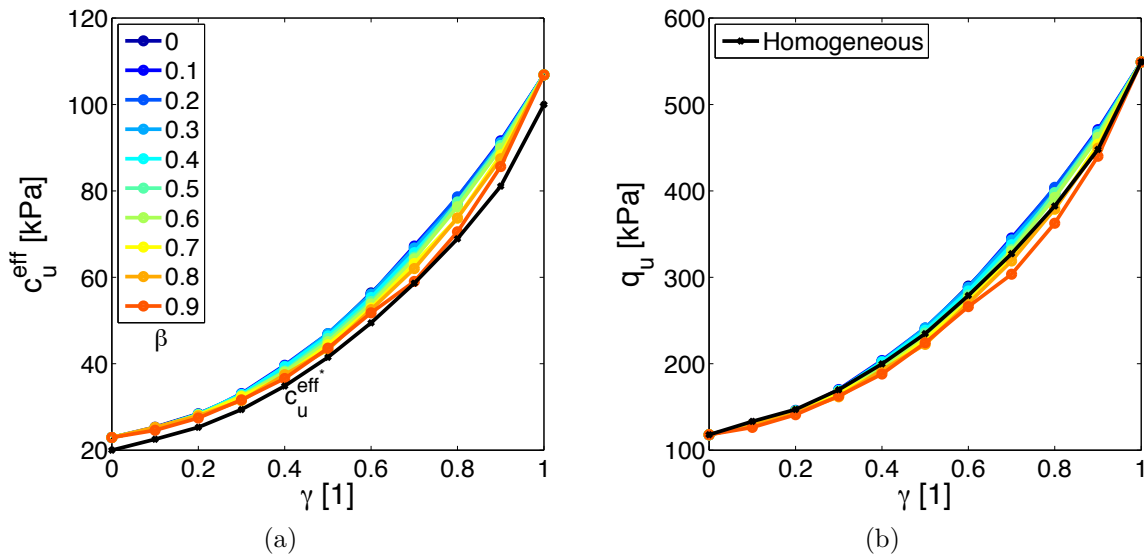


Figure 5.16 – Input and Output of the homogeneous equivalent model : a) Effective property ($c_u^{eff} = \mu_{q_u}(\gamma)/5.14$) for all isotropic correlations and average corrected value (c_u^{eff*}), in black, used as input and resulting b) Bearing capacity q_u as a function of the spatial fraction (γ) in black compared to the average of the heterogeneous models

as expected the mean bearing capacity was closely related to the geometric average (or median) of the shear strength. In similar studies but with other probability distribution (e.g. [Popescu et al. \(2005a\)](#) used gamma and beta distributions), the median is different from the geometric average and random field results were almost always below the deterministic case.

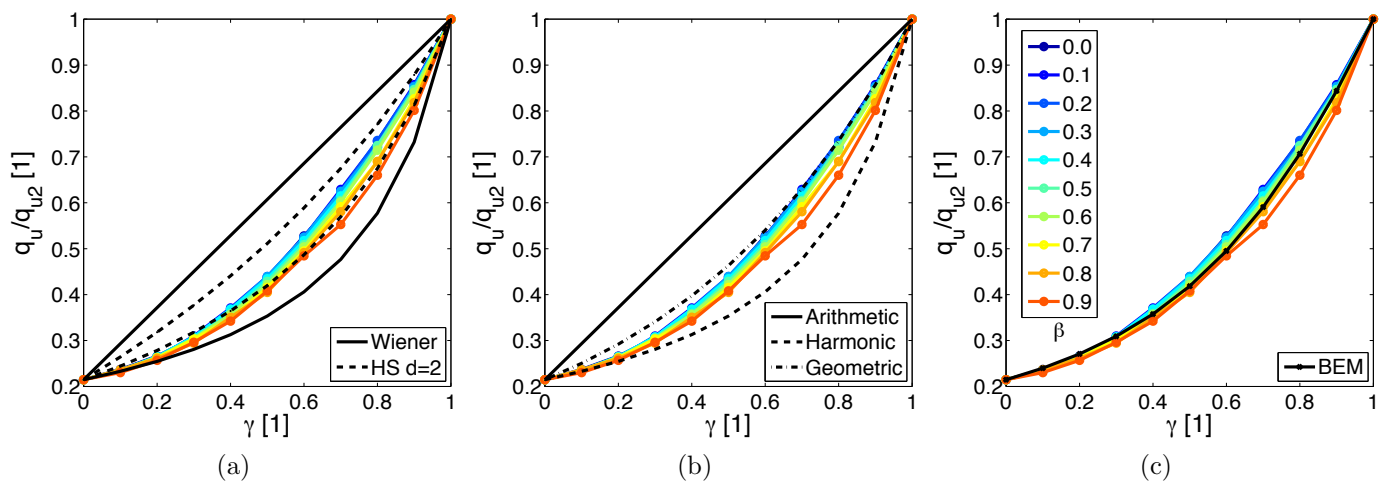


Figure 5.17 – Heterogeneous mean normalized q_u values compared to a) traditional homogenization, b) different averages and c) Bruggeman symmetric effective medium theories ($d_{BEM} = 1.5$)

Finally as it can be seen in Figure 5.17c, the mean values are well fitted by the BEM equation in which, for the case tested, d_{BEM} was found by a root-mean-square fit to a value

of 1.5. Though if an homogeneous equivalent model should be compared with discrete spatial heterogeneous models, the BEM could be used.

5.4.2.1 Effect of the contrast ratio of the soil properties

The spatial variability effect depends on the soils tested; hence, seven more soil property ratios (c_{u2}/c_{u1}) were used and the normalized mean and CV values are shown in Figure 5.18. In this case no correlation was introduced, which was found to increase the variability, and its effects have been formerly addressed. The undrained shear strength (c_u) of each set and the respective ratios are shown in Table 5.3. In Figure 5.18a, the lower and upper quartiles (i.e. 25 and 75%) are also shown however the dispersion is very low compared to the mean value. Note that as the ratio increases, the shape of the model changes thus it could only be represented by an equation with an additional parameter, such as the d_{BEM} of equation 5.19. Figure 5.18b shows the CV values of all the c_u ratios tested, in general, as the difference between the materials increases, the dispersion increases, like with higher isotropic correlation. Which is to be expected as the failure surface changes more drastically. Additionally, the CV values tend to be higher for spatial fractions near 0.5, except for the ratio of 20. However, for all cases the CV is lower than 7%, which is less than half the maximum value due to isotropic correlation.

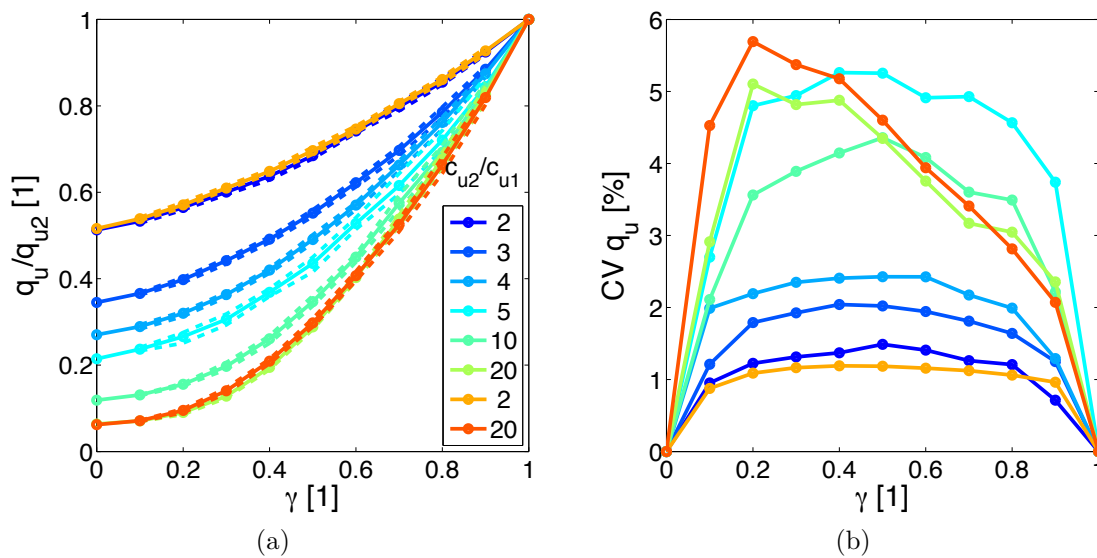


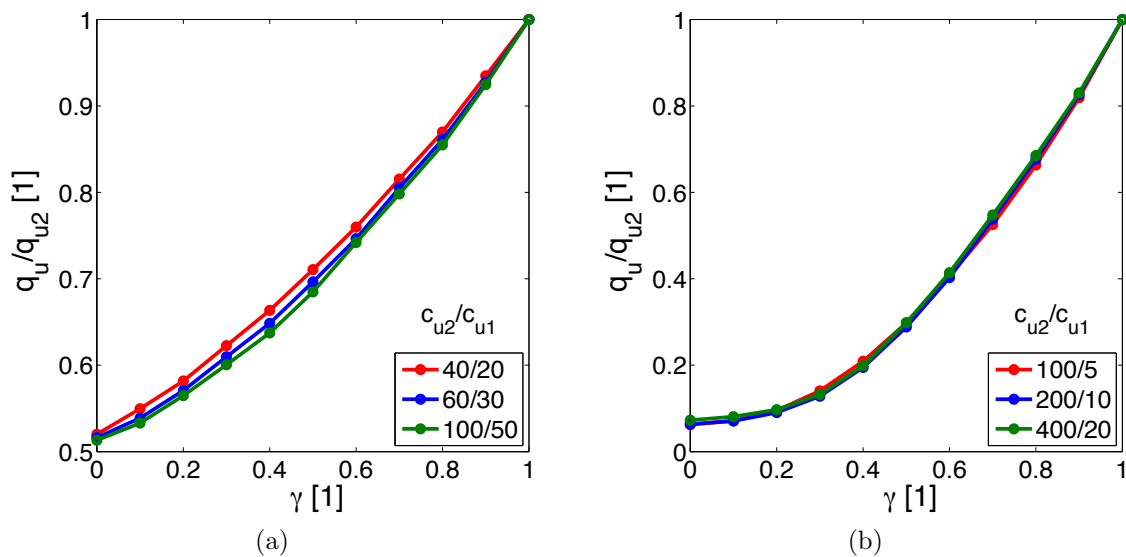
Figure 5.18 – Different soils c_u ratios tested: a) mean and percentiles 25 and 75% and b) CV values

Concerning the cases of equal ratio and different c_u , the results are similar and hence it depends more on the contrast between the materials and not so on the values used. Figure 5.19 shows the mean values of the normalized q_u for different soils with the same c_u ratio. Results

c_{u2}/c_{u1} ratio	c_{u1} [kPa]	c_{u2} [kPa]
2	20	40
3	20	60
4	20	80
5	20	100
10	10	100
20	10	200
2	30	60
20	5	100

Table 5.3 – Sets of soil model parameters tested

are only slightly different when both shear strengths are low; which is probably due to the slightly higher numerical error. Yet, the general relationship of q_u with γ is the same and is mostly dependent on the ratio.

Figure 5.19 – Mean normalized q_u for different soils with the same c_u ratio of : a) 2 and b) 20

Finally, with regard to the homogenization theories, the BEM equation was used to fit the bearing capacity of the different sets of soils tested. The parameter d_{BEM} was found by the minimization of the root-mean-square error. The results are shown in Figure 5.20. It is interesting to note that the changes in the shape of the curves from the bearing capacity ratio as function of the spatial fraction, shown in Figure 5.20a, for the different c_u ratios, agree very well with the d_{BEM} proposed. Figure 5.20b shows the relationship between the proposed values for d_{BEM} and the c_u ratio. A logarithmic equation appears to fit the data with a coefficient of determination (R^2) equal to 0.99, as following:

$$d_{BEM} = (c_{u2}/c_{u1})^{0.28} \quad (5.24)$$

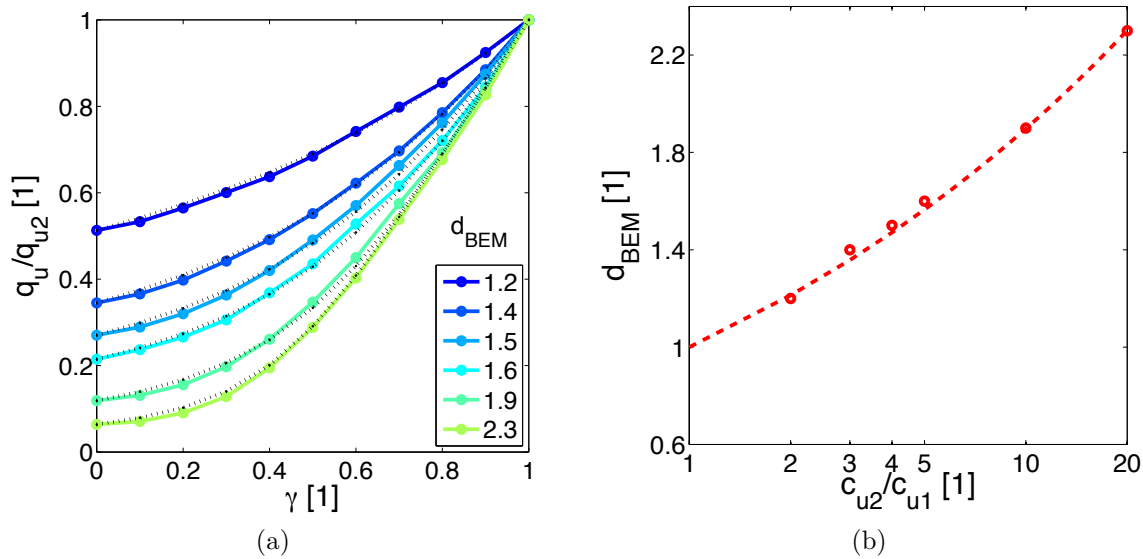


Figure 5.20 – BEM equation for the different c_u ratios tested: a) bearing capacity ratio as function of the spatial fraction and b) d_{BEM} values as a function of the c_u ratio

5.4.2.2 Effect of the effective loaded zone

As was seen in Figure 5.9, it seems that for evaluating the bearing capacity (q_u) of the foundation, not all the soil deposit strength is mobilized. Instead, there appears to be a defined region for which the average shear strength is related the most with the q_u value. The existence of an equivalent homogeneous soil deposit that could reproduce (statistically) the same response as a spatially variable deposit is encouraging for practical purposes. The Local Average (LA), introduced by Vanmarcke (1977), determines the characteristic value of the homogeneous deposit. LA applications in the assessment of the bearing capacity have been studied by Asaoka and Matsuo (1983), Griffiths and Fenton (2001), Kasama et al. (2012) and Honjo and Otake (2013), among others. The former proposed appropriate sizes of local averages to evaluate the effects of spatial variability for various geotechnical structures. Concerning the bearing capacity of shallow foundation in cohesive soils, a size of $L_y \times L_z = 2B \times 0.7B$ was suggested. It corresponds to the rectangle where is located the majority of the plastic zone obtained by the Prandtl-type ultimate bearing capacity equation. This size was said to be independent of the random field characteristics and of the absolute strength of the cohesive soils. Thus, the size of the averaging area purely depends on the mechanism controlling the limit state, but not on

the spatial variability properties of the soil parameters.

For the discrete random field presented in this analysis, an optimization procedure was established to find the LA area. For the sake of brevity, only the case of maximum variation is presented, i.e. $\beta_1 = \beta_2 = 0.9$; however, the other cases were also analyzed and the results were similar. The optimization consisted in maximizing the coefficient of determination (R^2) that is a measure of how well the BEM model fits the numerical response. In the fit, the bearing capacity values are related to the effective spatial fraction (γ^{eff}), calculated at the area below the foundation of size $L_y \times L_z$. The distances $L_y/2$ and L_z were varied every element size ($B/16$). As an example, three cases are shown in Figure 5.21 : a) evaluated in all the deposit ($5B \times 2B$), b) at the suggested area from Honjo and Otake (2013) ($2B \times 0.7B$) and c) the optimized area found ($2.4B \times 1.1B$). The optimized area is shown in dark shade in Figure 5.9. Globally, the dispersion is reduced when using an appropriate γ^{eff} , although some dispersion is still present for the optimized area. Concerning the mean values evaluated at different bins, the BEM equation is in general appropriate for the three cases, except for higher γ^{eff} as shown in Figure 5.21b.

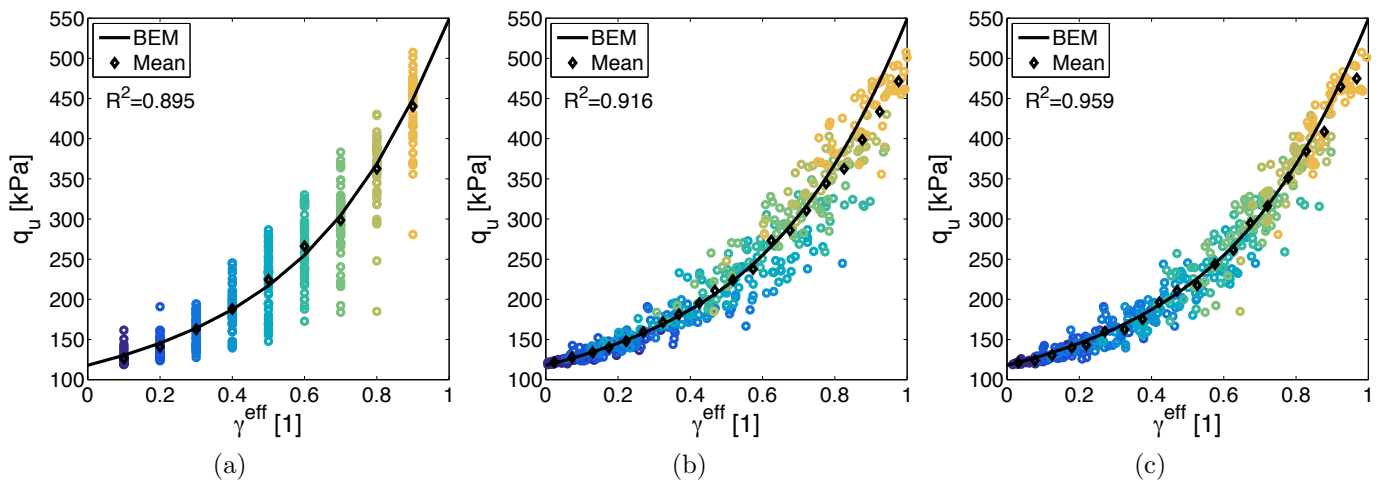


Figure 5.21 – Bearing capacity as a function of γ^{eff} for $\beta = 0.9$: a) evaluated in all the deposit ($5B \times 2B$), b) at the suggested area by Honjo and Otake (2013) ($2B \times 0.7B$) and c) the optimized area ($2.4B \times B$).

Recalling the two random fields simulations presented in Figure 5.9 of maximum and minimum q_u values, the results for $\gamma = 0.5$ are isolated from the previous figure and shown in Figure 5.22. Once the effective γ is evaluated, in the optimized area, the extreme cases are closer to the BEM equation hence, less dispersion is presented. Note that the difference between the γ for all the model and for the optimized area is almost 50% for the extreme cases. However,

there is still some dispersion around the trend.

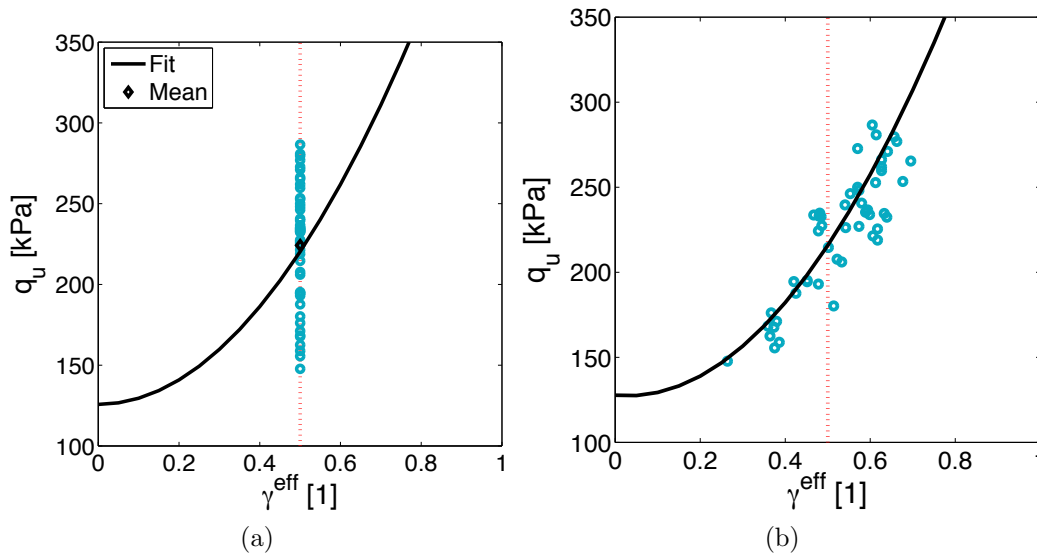


Figure 5.22 – Bearing capacity as a function of γ^{eff} for $\gamma = 0.5$ and $\beta = 0.9$: a) evaluated in all the deposit ($5B \times 2B$) and b) at the optimized area ($2.4B \times B$).

A summary of the optimization is shown in Figure 5.23 for two correlations. The R^2 value for each area tested is mapped into the mesh. As the results are horizontally symmetric, only half of the mesh is shown. For $\beta = 0.9$, even if R^2 for the area of $2B \times 0.7B$ (shown in dashed box in Figure 5.23a) is above 0.9, it is improved for the optimized area (shown in the solid box). The remaining box, in dash-dot, corresponds to the entire plastic zone of the Prandtl-type ultimate bearing capacity equation, equal to $1.5B \times 0.7B$, which presented a slightly smaller R^2 value. When the correlation is low, for instance $\beta = 0.3$ shown in Figure 5.23b, in general R^2 values are closer to 1 and more evenly distributed compared to the results for $\beta = 0.9$ that drop faster.

Additionally, the resulting coefficient of variation (CV) is shown in Figure 5.24 for the same correlations. CV is reduced when the optimized area is used, yet there is still a remaining dispersion due to the different failure mechanisms induced by the spatial variability. The reduction is more important for $\beta = 0.9$ and compared to the initial CV values, from Figure 5.13, the corresponding maximum value is still higher for this isotropic correlation. In other words, the variation due to the spatial correlation is more important than that of the local average.

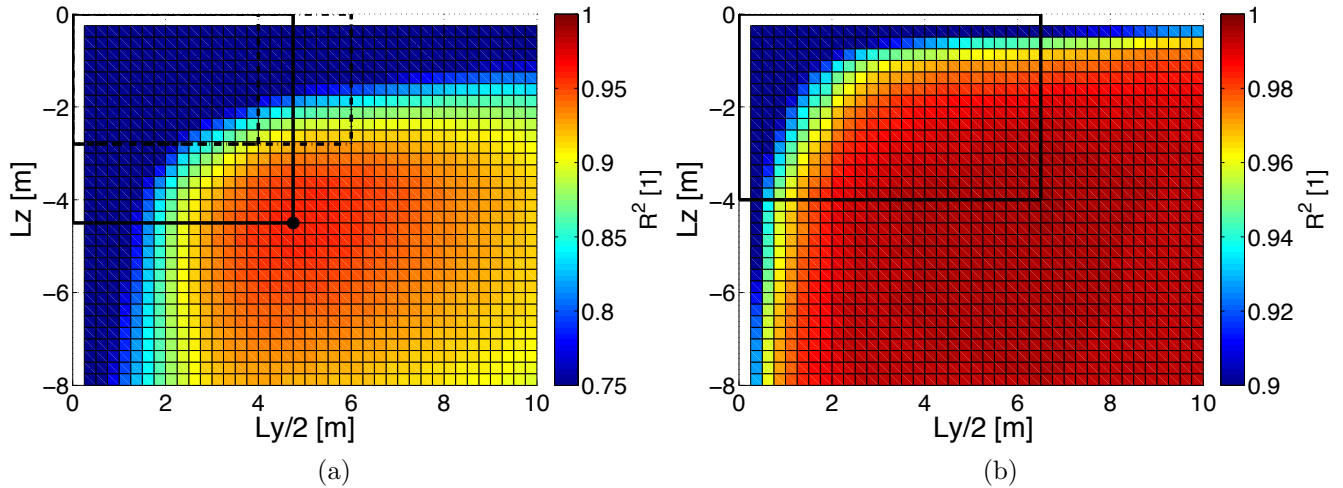


Figure 5.23 – Optimization summary results for the coefficient of determination R^2 values of varying LA area in the mesh with different correlations: a) $\beta=0.9$ and b) $\beta=0.3$

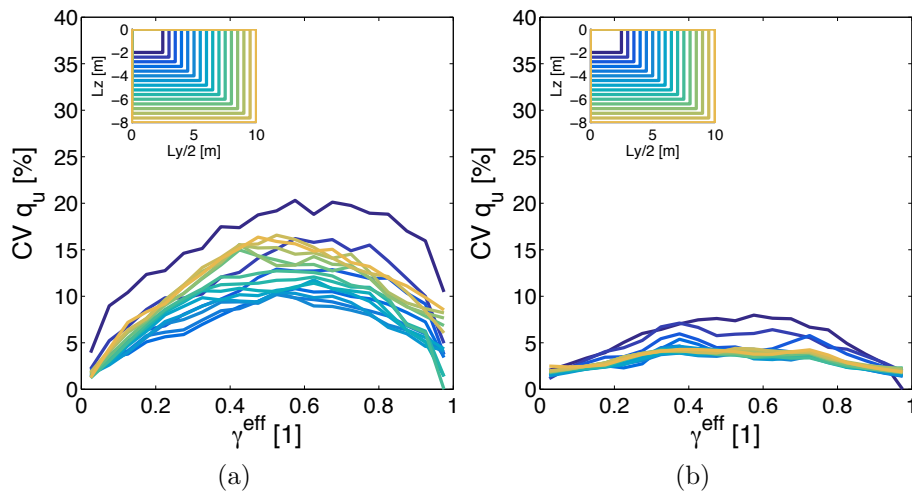


Figure 5.24 – CV decrease due to the optimization for a) $\beta=0.9$ and b) $\beta=0.3$

5.4.3 Partial conclusions

Homogeneous equivalent models can present the same q_u values when the accurate mean shear strength (c_u) of the binary random field is taken as input, due to the linear dependency between q_u and c_u . Because of its capability to account for the different mixture properties, the Bruggeman effective medium (BEM) equation appears to accurately predict the mean bearing capacity for varying spatial fractions (γ); while, traditional homogenization techniques will, in general, overestimate the resistance of the two-soil mixtures. However, for a given γ and a given correlation, the spatial distribution affects the q_u with coefficient of variation (CV) of approximately 20%. CV can be reduced if the optimized LA area is taken into account, although it

can not be avoided as it is due to the radically different failure mechanisms (surfaces) that are developed.

The results shown in this analysis have taken into account the FEM model error. First, it has been measured as the ability of the finite element method to reflect the actual behavior of an homogeneous (ideal) soil and it has been subtracted before applying the Prandtl's formula. It has been assumed that both the finite element method and the Prandtl's formula are sufficiently reasonable approximations to the behavior of soils to allow the investigation of the major features of stochastic soil behavior under loading from a rigid foundation. Note that the effects of the spatial variability in the CV of q_u have been evaluated independently of these assumptions and are associated with traditional usage of this engineering problem.

The numerical model of discrete spatial variation applied in a probabilistic framework appears to properly include heterogeneity on the soil. Other cases of added spatial variability by soil improvement techniques, such as soil-mixing for liquefaction mitigation, will be analyzed with this random discrete model in the next section.

5.5 Settlement induced by seismic liquefaction

For the purpose of studying the effect of soil heterogeneity induced by a mitigation method on the seismic response of a structure, the model presented in section 4.4 will be used. It consists of a reinforced concrete building with a shallow rigid foundation standing on saturated cohesionless soil. A schema of the model is shown in Figure 5.25. The reference soil deposit is composed of 20m of loose-to-medium (LMS) sand overlaying an elastic bedrock. The soil deposit used is the same as the one used in the previous chapter. Additionally, the same elastoplastic multi-mechanism model is used to represent the soil behavior and the model parameters are shown in section 4.3. As for the structure, only the nonlinear model of the previous chapter is used, called B01. Its parameters and additional information are shown in section 4.4.

Concerning the treated ground soil the recommendations of Mitchell et al. (1998) were used. By which height (H) should be given by the extension of the liquefiable layer, in this case $H = 4\text{m}$ below the water table, and length (L) should extend from the edge of the foundation of size B a distance bigger to the depth of treatment (i.e. $L > B + 2H$). The soil heterogeneity is simulated with the discrete autoregressive-model defined in section 5.3.

For this application the treated zone is composed of two materials: a treated medium-to-dense sand (MDS) and the original LMS. These materials were also used in chapter 4.2. Their

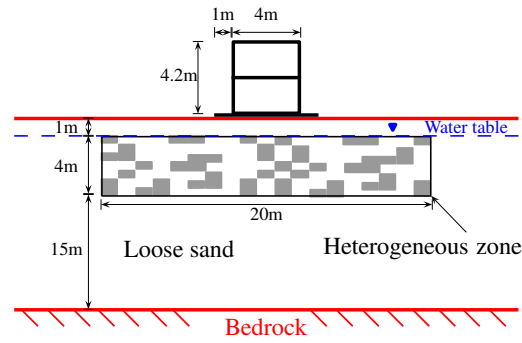


Figure 5.25 – Schema of the numerical model

model parameters and some laboratory test simulations are shown in Appendix A. The soil behavior differs in a number of aspects, for instance, concerning the liquefaction resistance an undrained stress controlled cyclic shear test was simulated. The cyclic stress ratio ($SR = \tau/\sigma'_{v0}$) as a function of the number of loading cycles to produce liquefaction (N) is shown in Figure 5.26 for both soils. As a qualitative comparison, the modeled test results are compared with the curves given by El Mohtar et al. (2013) for a clean sand and a sand with 3% of bentonite permeations. It is noted that the obtained curves are closer to the reference for a clean sand corresponding to the LMS; while, the MDS curves are closer to those of a treated soil. It is also worth noting that, the hydraulic conductivity (κ) is different for the two soils: $1 \cdot 10^{-4}$ for LMS and $1 \cdot 10^{-5}$ for MDS. These values were taken from the literature of the soil model calibration and their influence in the response will be evaluated in section 5.5.5.

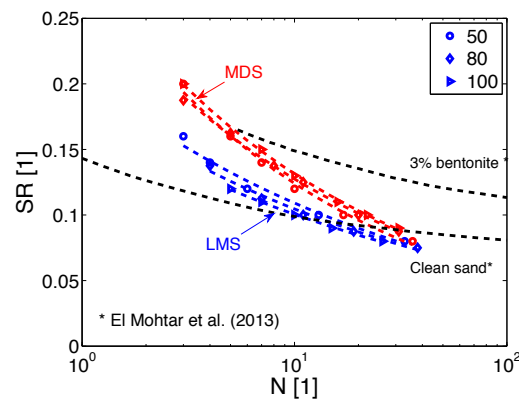


Figure 5.26 – Simulated liquefaction curves for both soils and comparison with results from El Mohtar et al. (2013)

As an example, a zoom on the heterogeneous zone of two spatial distributions are shown in Figure 5.27 and correspond to a spatial fraction (γ) of 0.5 and auto-regressive coefficients (β_1 and β_2) equal to 0.4. As it can be seen, β does not give a constant correlation length in each row or column, but it is an average on the model. Similarly, γ is the average over the

entire area; even though, there are regions with different composition as in the top left corner in Figure 5.27a.

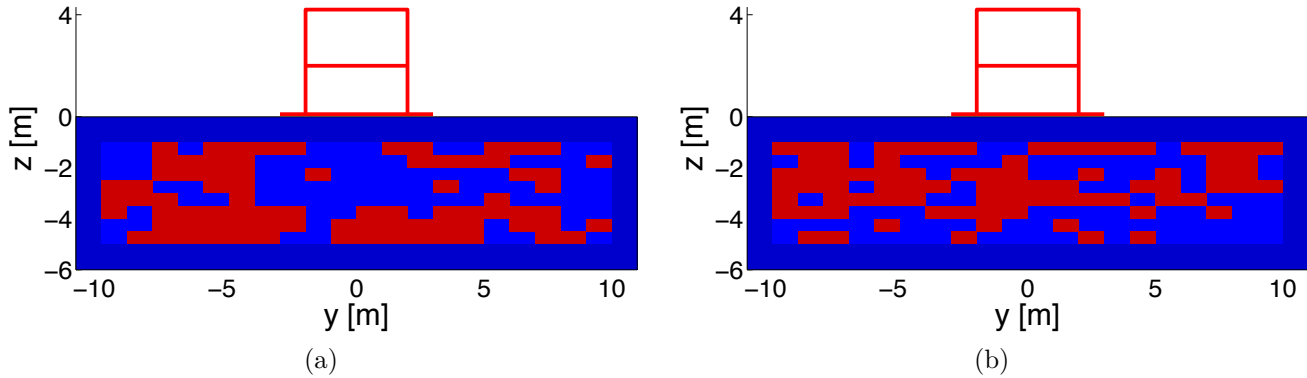


Figure 5.27 – Zoom on the heterogeneous zone for 2 distributions with $\gamma = 0.5$ and $\beta_1 = \beta_2 = 0.4$

5.5.1 Input earthquake motion

As the computational cost of many random field simulations is important, a careful selection was performed to have strong input motions appropriate for the numerical model. As a deformable bedrock is used and the hypothesis of outcropping rock recordings is made, the earthquake signals should be near-to-source strong motions from dense soil stations. These signals are supposed to have minimal noise at high frequencies. The selected earthquake motions and some intensity measures (IM) are shown in Table 5.4. The definition of these IM can be found in the appendix C.2. Figure 5.28 shows the acceleration time histories, the normalized response spectra of the signals with a structural damping (ξ) of 5% and the smoothed Fourier spectra. During this study, the PEER center launched a new database called NGA-West2 with several changes and updated information (Wair et al., 2012). Among the changes, EQ4 was originally reported with a V_{s30} of 1000m/s and in the new database, a value of 382m/s was given. However, since the calculations were already performed, the results will be presented. The last motion, EQ 9, is only used in section 5.5.7 as an additional test case.

5.5.2 Non-treated soil deposit response

First, the response of the model without treatment is analyzed. This is the reference case when $\gamma = 1$. In this section, focus will be given to the spatial distribution effect on the liquefaction evolution; though, for the sake of brevity, only results for EQ1 will be presented. Figure 5.29a

Table 5.4 – Input motions' identification and some intensity measures

#	Event	Year	RSN*	M_w	R_{JB} † [km]	V_{s30} [m/s]	PHA [g]	I_A [m/s]	D_{5-95} [s]	PHV [cm/s]
EQ1	Northridge_01	1994	1050	6.69	4.9	2016	0.43	1.79	9.84	51.23
EQ2	Kocaeli, Turkey	1999	1165	7.51	3.6	811	0.21	0.80	13.3	34.64
EQ3	Friuli, Italy_02	1976	133	5.91	14.4	660	0.23	0.22	2.83	12.5
EQ4	Irpinia, Italy	1980	292	6.9	6.78	382	0.25	1.19	15.07	36.40
EQ5	Loma Prieta	1989	765	6.93	9.64	1428	0.41	1.05	6.53	31.57
EQ6	Northridge_01	1994	1012	6.69	9.87	706	0.25	0.93	8.07	27.39
EQ7	Loma Prieta	1989	810	6.93	18.41	714	0.40	2.04	9.66	17.53
EQ8	San Fernando	1971	77	6.61	1.81	2016.1	1.18	8.59	6.68	103.23
EQ9	Loma Prieta	1989	763	6.93	9.96	729.7	0.32	0.68	4.64	20.66

*Record sequence number at the NGA database (<http://ngawest2.berkeley.edu/>)

† Joyner-Boore source-to-site distance.

shows the pore pressure ratio ($r_u = \Delta p_w / \sigma'_{v0}$) at the end of the shaking (i.e. co-seismic analysis). When r_u is equal to unity, the soil has loosened all its strength and it is totally liquefied. As it can be observed, most part of the deposit is liquefied, with the highest ratio above 5m.

The relative settlement of the structure with respect to free-field at the end of shaking ($|u_z|$) is 26cm. According to the limits given by Bird et al. (2006) for rigid body settlement, it corresponds to a moderate damage state, between 10 and 30cm, where some structural damage in load-bearing elements are visible and serviceability is affected. Figure 5.30 shows the co-seismic and post-seismic relative settlement and liquefaction ratio under the right column and at 3.5m depth. Although, all Δp_w is not dissipated, there is almost no contribution of post-seismic consolidation to the total settlement (i.e. less than 0.2%). By comparing the time histories with the acceleration at outcropping, also shown in Figure 5.30, it is interesting to note that while the high acceleration peak produces the biggest increase in the liquefaction ratio, the relative settlement is gradually increased and its rate is higher after 10s. At this time a second peak in acceleration is evidenced at higher frequencies which is probably also affecting the LMS Δp_w evolution.

5.5.3 Liquefaction mitigation analysis

Deep mixing techniques such as jet-grouting, bio-grouting, bentonite suspensions or wet-soil mixing use stiffer materials to form foundation elements to stabilize soft soils and mitigate liquefaction. These techniques are widely used even though there remain some uncertainties

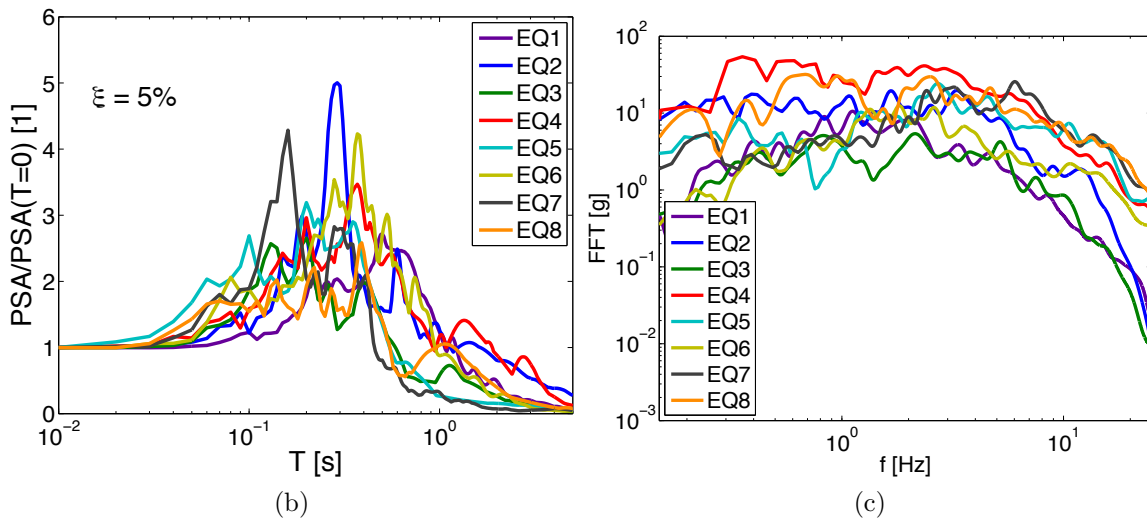
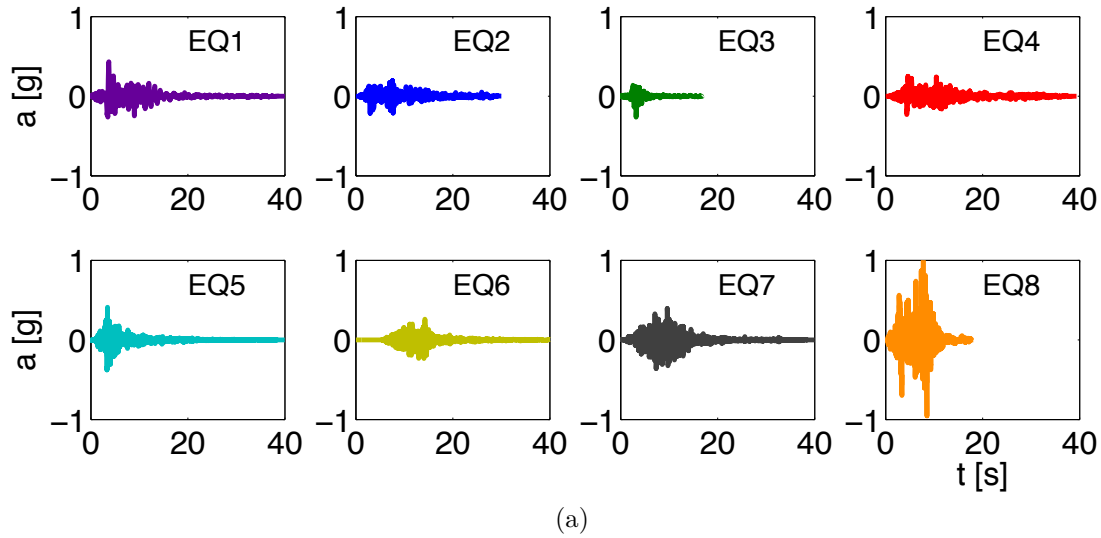


Figure 5.28 – Input earthquake motions: a) acceleration time histories, b) Normalized response spectra of acceleration and c) Fourier spectra

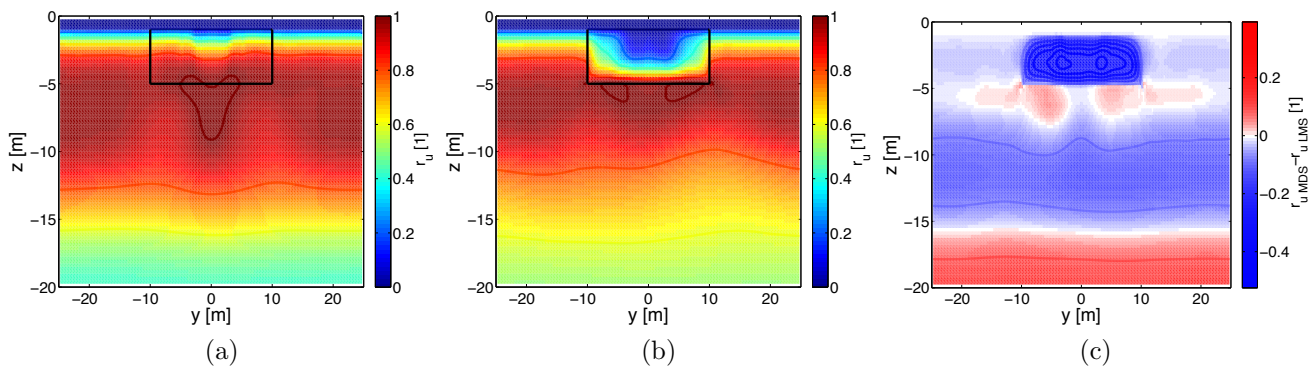


Figure 5.29 – Liquefaction ratio (r_u) at the end of shaking for EQ1: a) before and b) after soil treatment and c) difference between them

given the spatial variability introduced in the design (Kasama et al., 2012). Sometimes, given the poor soil conditions and the high seismic demand, soil mixing is used to replace an entire

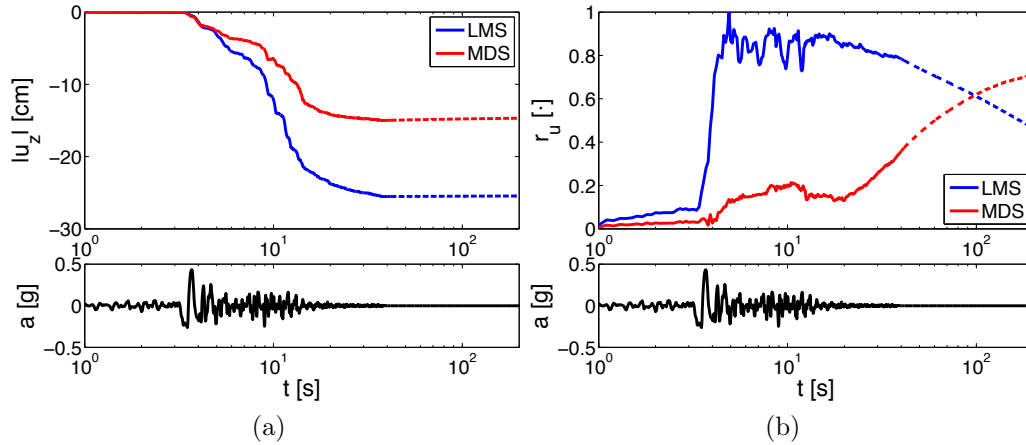


Figure 5.30 – Time histories of the (a) relative settlement ($|u_z|$) and the (b) liquefaction ratio (r_u) under the right column and at 3.5m depth before and after mitigation for EQ1. Post-seismic behavior is depicted with dotted lines. The acceleration time history at outcropping is shown below

portion of the deposit. This last case is analyzed and is also used as reference ($\gamma=0$). The liquefaction ratio at the end of shaking is shown in Figure 5.29b. It is interesting to note that while r_u decreases directly under the structure, it increases on the surrounding soil. Figure 5.29c shows the difference between the two cases. Negative values, in blue, denote the places where the liquefaction is greater before treatment (LMS case) and the places where liquefaction increases after treatment (MDS case) are the positive values, shown in red. Two zones presented higher r_u values after treatment: (1) a layer of a couple of meters immediately below the treatment zone and (2) the soil below 15m.

Recalling the definition of the liquefaction index (Q) given by Shinozuka and Ohtomo (1989) to quantify the excess pore-pressure generation as:

$$Q_{H \cdot L} = \frac{1}{H \cdot L} \int_0^H \int_0^L r_u(y, z) dy dz \quad (5.25)$$

where r_u is the liquefaction ratio evaluated at the end of shaking and H and L are the height and length of the soil deposit. A value of 1.0 indicates conditions of initial liquefaction throughout the $H \cdot L$ area and thus gives information of the liquefaction ratio as well as the total liquefied zone. After the entire portion of the soil is replaced, and if $Q_{H \cdot L}$ is evaluated in the mitigation zone (i.e. $H=4\text{m}$ and $L=20\text{m}$), it decreases 44%. However, for the entire soil deposit (i.e. $H=20\text{m}$ and $L=50\text{m}$) the use of soil mixing only decreases 6% the $Q_{H \cdot L}$ value, which means that liquefaction in the model is reduced under the structure, but is present in other locations. These results are in accordance with those of Coelho et al. (2004) and Lopez-Caballero and

Modaressi-Farahmand-Razavi (2013) and can be explained by the energy of the motion that must be dissipated. As it is constant for both cases, the reduction in one zone will necessarily affect other parts of the deposit. Additionally, the pore-pressure migration can be seen from the loose untreated sand to the mitigation zone in the boundaries between both soils. An interaction is therefore present in the mixture which will be of great importance in the heterogeneous deposit case.

Concerning the relative settlement ($|u_z|$), shown in Figure 5.30a, the damage state is still moderate according to the limits given by Bird et al. (2006) however it corresponds to a reduction of more than 40% compared to the case before treatment (i.e. LMS). As the pore-pressure migration continues after shaking, the liquefaction ratio under the right column and at 2.5m depth increases (shown in Figure 5.30b); although, there is almost no contribution of post-seismic consolidation to the total settlement.

5.5.4 Heterogeneous models

One of the most influential factors on the treated ground is the effectiveness of the mixing process, which adds important variations in the soil. This heterogeneity depends on the mitigation technique, but will in general have a spatial correlation on the vertical and horizontal direction. Studies on this topic usually apply homogeneous random field techniques to account for the spatial variation (Jones et al., 2002). In them, properties are described by a probabilistic function where a mean value and a coefficient of variation is provided. In the present analysis, it was assumed that the heterogeneous deposit is composed of two materials: a treated-soil and the remaining soft soil. This could be the case of mixing techniques such as soil-mixing or bio-treatment. The interaction of these soils is important as the loose sand induces an increase in excess pore-water pressure in the surrounding treated sand.

As recalled before, Chakraborty and Popescu (2012) analyzed centrifuge experiments of heterogeneous sand deposits. Results show an increase in excess pore water pressure for the heterogeneous case compared with an average-density homogeneous sand. However, the analysis was deterministic and the use of a traditional homogeneous equivalent model could be inappropriate due to the fully nonlinear behavior. The spatial discretization described in Section 5.3 is used here to generate the heterogeneous deposits. The spatial fraction (γ) is varied between not treated to fully treated (i.e. from 1 to 0) and 20 independent spatial distributions per γ value were realized.

As already shown, the auto-regressive coefficients β_1 and β_2 control the correlation length in the horizontal and vertical direction. These parameters, which are normalized by the size of the heterogeneous zone, describe the degree of correlation of the spatially random values. Thus, a value close to 1 will imply a smoothly varying field, while a small value will imply a ragged field. Concerning added spatial variability due to soil improvement, little is known of the possible correlation lengths thus for this analysis, both coefficients were fixed to 0.4 (i.e. a correlation length close to 8m in the horizontal direction and of 1.6m in the vertical one). This values are slightly higher than those found in the literature for inherent or natural variability in CPT data shown in section 5.2.1, specially for the vertical direction, which is probably the case given the soil improvement techniques that can be possibly used. The effect in the liquefaction-induced settlement of different spatial correlations (e.g. magnitude of the correlation lengths and differences between the horizontal and the vertical correlations) could be interesting but it is out of the scope of this study.

5.5.4.1 Relative settlement of the structure

In order to better understand the interaction between the two soils in the heterogeneous deposit, the results for different treatment efficiencies (i.e. γ values) will be analyzed. Figure 5.31 shows the box-and-whisker plots for the relative settlement of the structure with respect to free-field ($|u_z|$). These plots were already used and explained in Section 5.4. They provide a clear representation of various statistic parameters and help indicate the distribution of the data. For instance, if the mean value (shown in red) is equal to the median or 50% quartile (i.e. shown in the middle of the box), the distribution is symmetric, as is the case of most of the γ values in Figure 5.31 except for $\gamma=0.4$ and 0.9 . Additionally, the size of the box is an indicator of the spread or dispersion of the data. Moreover, when the quartiles are not equidistant as for some of the γ values in Figure 5.31, the distribution is skewed: e.g. data at $\gamma=0.3$ shows a positive skew while data at $\gamma=0.4$ has a negative skew. However, the length of the whiskers provide more information on the skewness to identify if it is due to a few extreme values, as is the case of $\gamma=0.3$. In order to analyze the effect of the treated soil in the relative settlement, concerning Figure 5.31, two aspects will be discussed : the variation of the average value and the dispersion for each γ value.

At first, the efficiency of the soil improvement can be analyzed from the evolution of the average relative settlement with the spatial fraction, shown in Figure 5.31 in red. For this case, it seems that a small amount of treated soil (e.g. $\gamma= 0.9$) will not reduce, in average, the

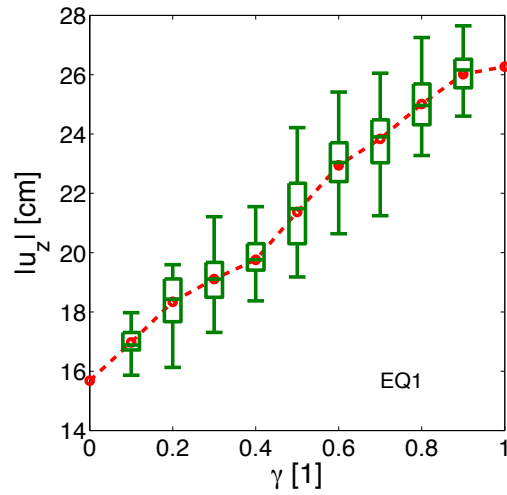


Figure 5.31 – Box-and-whiskers plot for the relative settlement ($|u_z|$) of the structure with respect to free-field for EQ1

relative settlement. In contrast, it appears that below a certain spatial fraction, the average settlement will be greatly affected if a greater amount of denser soil is used. In other words, it seems that the relation between the relative settlement and the spatial fraction is nonlinear and divided into two concave curves: one that is mostly related to the natural soil (higher γ values) and another highly sensitive to the introduced soil (lower γ values).

Furthermore, regarding all values it can be observed that higher variation is present for γ equal to 0.3 and 0.5 while for 0.4, it is very small. This value could be the percolation threshold dividing the two curves, from which the interactions between the two soils change. It can be noted that this relation differs from the arithmetic or geometric average value of both soils, hence, traditional homogenization theories should not be used as reference. Otherwise, while for some spatial fractions the average value will be overestimated; for others, it will be underestimated. This aspect will be treated in detail in section 5.5.7.

In order to verify that the number of simulations (N) used is sufficient, the statistical convergence of the mean and the standard deviation of the relative structure settlement is shown in Figure 5.32 for γ equal to 0.3 and 0.4. The blue dashed lines correspond to the 5% and 95% confidence intervals obtained with the t-student and χ^2 statistical model, respectively. Although there is still some variation in the results, for $N=20$ the statistical convergence is satisfactory for this analysis.

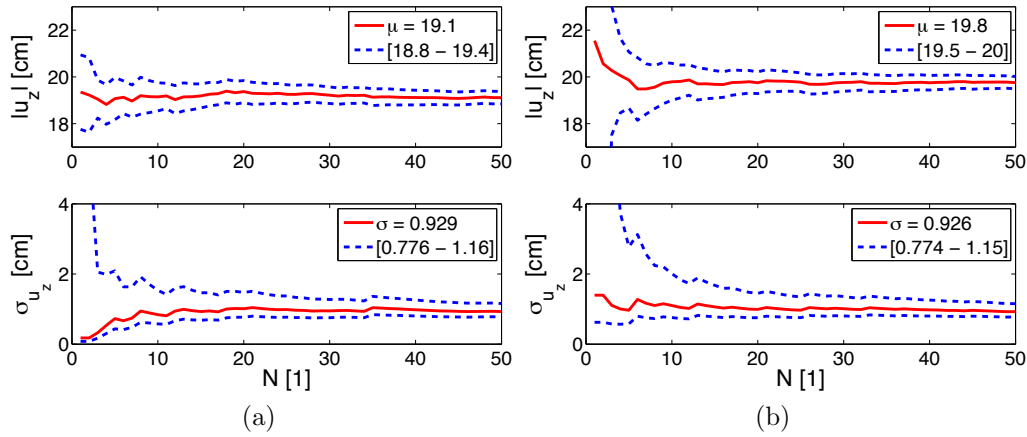


Figure 5.32 – Convergence of the mean and standard deviation of $|u_z|$ with EQ1 and $\beta_1 = \beta_2 = 0.4$. Two spatial fractions are shown: a) $\gamma = 0.3$ and b) $\gamma = 0.4$.

5.5.4.2 Water migration and soil-interaction in a heterogeneous deposit

For the same spatial fraction, the relative settlement can vary greatly only due to the distribution of the two soils in the deposit. As an example, a zoom on the heterogeneous zone of the spatial distributions for $\gamma = 0.5$ that present the minimum and maximum $|u_z|$ was shown in Figure 5.27 and correspond to 19.4 and 24.2 cm, respectively (i.e. a relative difference above 20%). It is noted that for the minimum $|u_z|$ in Figure 5.27a, the MDS elements (colored in red) are mostly near the bottom of the intervened zone while most LMS are in the center and surrounded by MDS. Even so a site percolation is present near the left column, that is a vertical path of MDS nearest-neighbor elements. On the contrary, for the maximum $|u_z|$, in Figure 5.27b, the soils are in smaller clusters and only a bond percolation is present on the middle. Additionally, the LMS elements are mostly at the bottom. The different interactions between the LMS and MDS elements could be the cause of the difference in $|u_z|$. Thus, as more clusters develop (i.e. for very low or very high spatial fractions), more interactions develop between the two soils; therefore, more variation on the $|u_z|$ value is shown.

Before analyzing the seismic behavior, it is important to see the effects of spatial variability in the stress state on the deposit prior to shaking. The structure's weight imposes in the deposit an increment in the vertical, horizontal and shear stresses. Concerning the shear stress (τ), interface elements between the structure foundation and the soil are used to allow relative movement of the structure with respect to the soil, in order to avoid the traction effect and the concentration of τ in the center line below the foundation. Hence, as shown in Figure 5.33a for the homogeneous case before the mitigation method, τ is primarily concentrated in the foundation's edges due to its rigidity and is distributed in depth. After replacement of all

the soil in the intervened zone, shown in Figure 5.33b, the weight of the treated soil induces an additional τ for greater depths. When spatial variability is included, the previous effect is replicated in each interface between the two soils. Figures 5.33c and 5.33d show the initial τ at the extreme cases, i.e. with minimum and maximum $|u_z|$, respectively. The LMS elements are drawn as boxes with a diagonal and show in general, less τ . Comparing the two cases, it can be noted that τ is greater below the intervened zone for the case of maximum $|u_z|$, specially at the left side below the foundation's edge where a column of LMS elements is almost completed through the deposit.

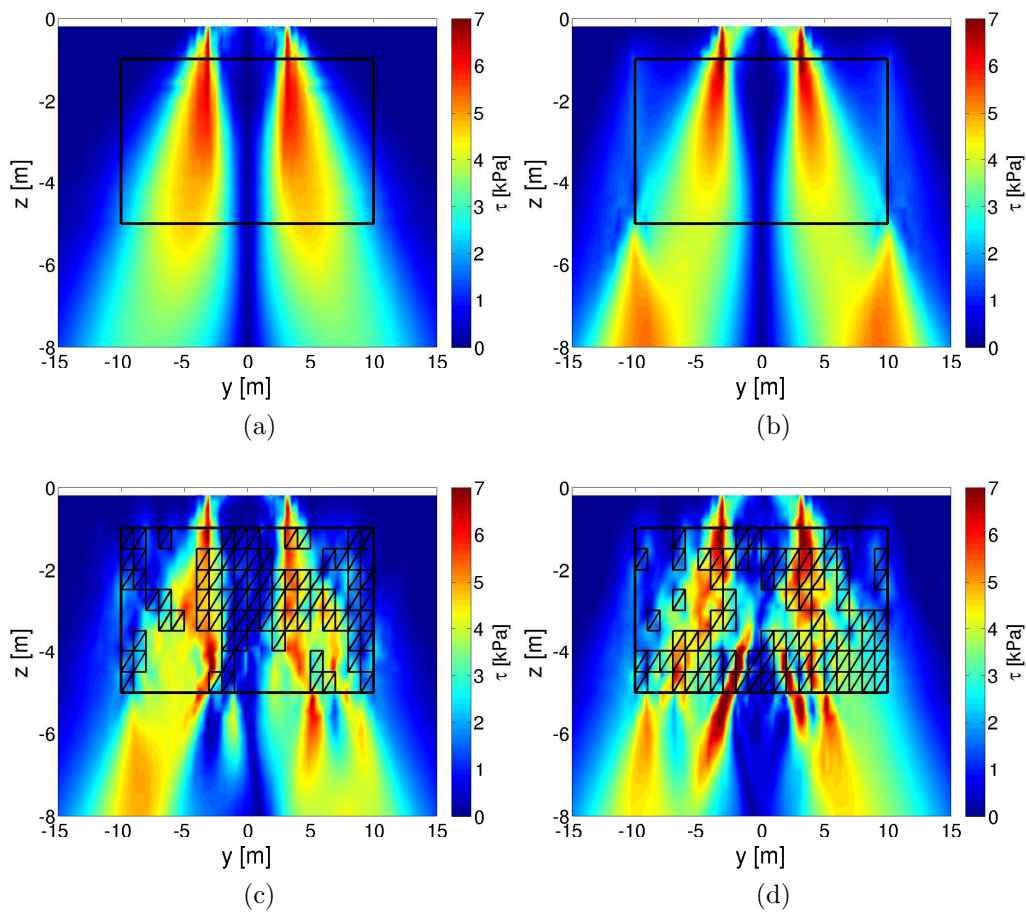


Figure 5.33 – Shear stress (τ) distribution for the homogeneous cases before shaking: a) LMS and b) MDS, and the extreme cases with $\gamma=0.5$ and $\beta=0.4$: c) minimum and d) maximum $|u_z|$. Diagonal marked boxes represent the LMS elements.

As shown in chapter 3.3, the behavior of the soil depends on the mean stress (p'_k) and the deviatoric stress (q_k) in the deviatoric plane, as well as in the isotropic hardening (F_k) associated with the evolution of volumetric plastic strains (ε_v^p) and the friction angle at the critical state (ϕ'_{pp}). These variables are all related by the degree of mobilized friction (r_k), as follows :

$$r_k = \frac{q_k}{p'_k \cdot F_k \cdot \sin \phi'_{pp}} \quad (5.26)$$

Thus as r_k approaches unity, the soil approaches perfect plasticity. r_k before shaking is shown in Figure 5.34 for the same cases shown above: the homogeneous models and the extreme $|u_z|$ cases for γ and β equal to 0.4. The effect of the building's weight, shown in Figure 5.34a before treatment, is mostly perceived above 5m and 20m width, which coincides with the treatment zone. Specially, the soil under the structure's base presents higher values of up to 0.6 which will tend to an increase of pore pressure generation; while near the foundation's edge r_k is near zero, hence low liquefaction susceptibility. When all the soil is replaced in the treatment zone by more dense sand, shown in Figure 5.34b, r_k is reduced in all this area and specially around the building. It is interesting to note that although the zone is below 1m, it affects the soil above as r_k is also decreased. However, just under the foundation's edge r_k still presents values of about 0.6, yet recall that the water table is also at 1m thus no liquefaction is possible. Concerning the extreme heterogeneous cases with γ and β equal to 0.4, a zoom on the treatment zone is shown in Figures 5.34c and 5.34d, as it is mostly in this area where changes are visible. It is clear that for the distribution that gave the maximum $|u_z|$, the LMS elements are in places where the building's weight had greater effect: under the structure's base and above 5m.

In order to analyze the different interactions between the two soils, three aspects will be presented: (i) the time history at one element that is at the same depth, (ii) the profile below the left column and (iii) the entire model. First, the comparison of the time evolution of the liquefaction ratio (r_u) between the homogeneous cases (i.e. before treatment - LMS - and fully treated - MDS) and the 20 simulations of heterogeneous cases are shown in Figure 5.35 for one element. It is situated below the right column and at 2m depth. Other positions were analyzed, but the response varies greatly with the confinement pressure and the effect of the structure and are not shown here for the sake of brevity. The comparison in the same element position of the different spatial distributions is interesting as it permits to analyze the numerous soil interactions (e.g. when the element is embedded in a cluster or in contact with the other soil) while leaving the majority of other factors unchanged, such as the depth, the stress state and the initial shear modulus. Nonetheless if different positions in the same model are compared, these will have different confinement pressures with distinct liquefaction evolution. For the sake of brevity, only one element is shown in the present analysis. The responses are divided into two figures: the behavior of the models where the element in the chosen position is composed

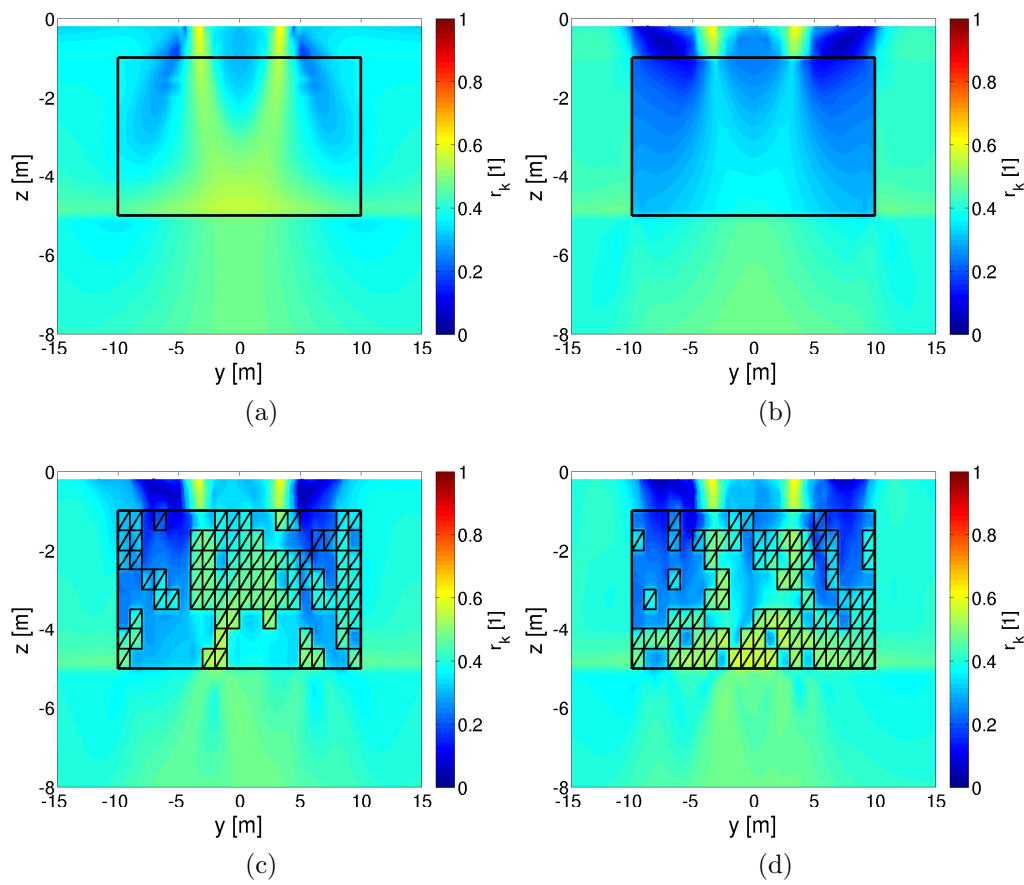


Figure 5.34 – Degree of mobilized friction (r_k) before shaking in the model for the homogeneous cases: a) LMS and b) MDS, and the extreme cases with $\gamma=0.5$ and $\beta=0.4$: c) minimum and d) maximum $|u_z|$. Diagonal marked boxes represent the LMS elements.

of LMS is shown in green in Figure 5.35a and those composed of MDS are shown in magenta in Figure 5.35b.

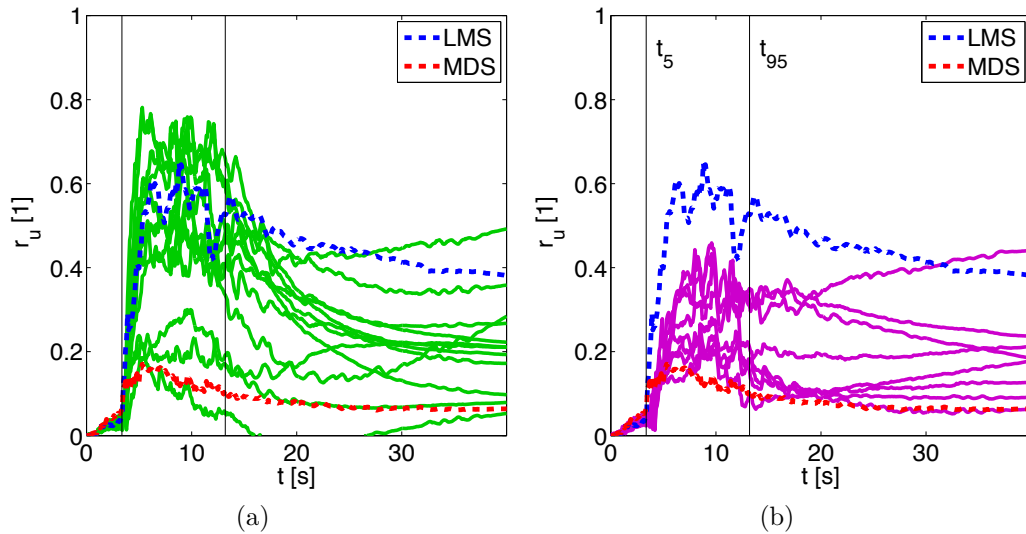


Figure 5.35 – Liquefaction ratio evolution with time for (a) LMS and (b) MDS elements at 2m depth and under the right column for $\gamma = 0.4$ and $\beta_1 = \beta_2 = 0.4$. The homogeneous cases before (LMS) and after (MDS) treatment are also shown.

Concerning Figure 5.35a, it is interesting to note that some LMS elements in the heterogeneous model present more pore pressure generation than those of the homogeneous LMS model. In contrast, some cases resemble the MDS model behavior. For these cases, the LMS element is principally surrounded by more denser sand, hence less pore-pressure migration can occur. In general, the behavior is affected by its neighbors although it depends on the position and the clusters formed. A clear example is shown in Figure 5.36 for a LMS element completely surrounded by MDS. The LMS has less liquefaction resistance; however, MDS elements act as a barrier for excess pore pressure generation.

Similarly in Figure 5.35b, almost all MDS elements have higher r_u than the corresponding homogeneous model. Additionally, for some MDS elements in the heterogeneous model the r_u starts increasing after the predominant time of the motion (i.e. for $t > t_{95}=13s$), while it mostly decreases or stays constant for those composed of LMS, which emphasizes the interaction between the different soils. This interaction was also shown in the centrifuge analyses of Chakrabortty et al. (2010); although the comparison was made with a density-average homogeneous deposit and the elements compared were not at the same depth. While, in general, in the homogeneous deposits the pore-water pressure starts to dissipate at the end of shaking, the LMS elements in the heterogeneous model keep feeding water to neighboring MDS elements. This water migration has been analyzed by Chakrabortty et al. (2004), Ghosh and Madabhushi

(2003), Popescu et al. (2005b), among others.

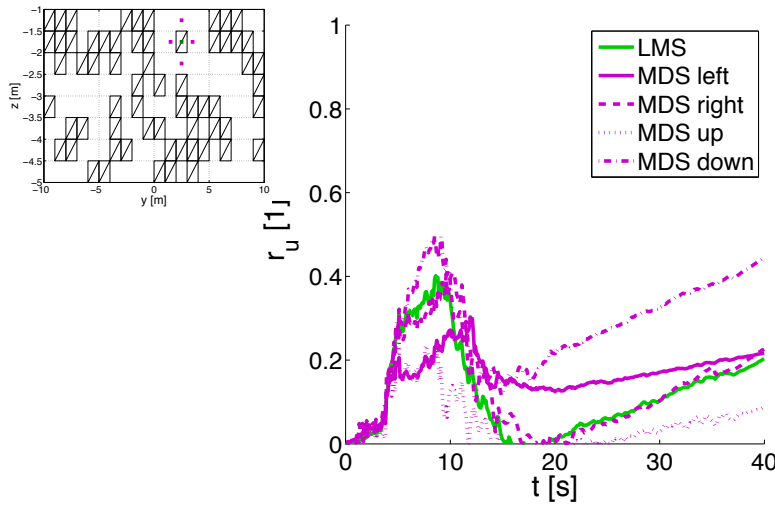


Figure 5.36 – Liquefaction ratio evolution with time for a LMS element surrounded by MDS elements for $\gamma = 0.4$ and $\beta_1 = \beta_2 = 0.4$.

Two profiles below the left column of the structure are shown in Figure 5.37 for all the spatial distributions used with $\gamma = 0.4$ and $\beta_1 = \beta_2 = 0.4$. The homogeneous models before (LMS) and after (MDS) treatment are also shown as reference. The γ chosen presented the highest variation of the liquefaction index evaluated at the soil deposit (Q_{FEM}) shown in Figure 5.45a. The profiles correspond to: a) the settlement and b) the Arias intensity (I_A). Regarding the settlement profile in Figure 5.37a, it can be seen the important fluctuations in the heterogeneous zone and down to almost 10m. For the LMS model, the settlement is concentrated in the treated zone but for the MDS and most of the heterogeneous models, the settlement is greater for lower depths. This is reasonable because the MDS inclusions will stiffen the soil above, creating a higher impedance with the deeper zones where the profile will become more vulnerable.

In addition, Figure 5.37b shows the I_A profile. This value is a measure of the total energy per unit mass defined by Arias (1970) as:

$$I_A = \frac{\pi}{2} \int_0^{t_{end}} a(t)^2 dt \quad (5.27)$$

Its evolution expresses the amplification (or deamplification) of the energy through the soil profile. As r_u increases and the soil softens, the seismic energy is deamplified by the soil. In contrast, as the heterogeneous models present less r_u below 7m, the energy is amplified for deeper soil. However, as γ is small, the behavior of the heterogeneous model is closer to that of the MDS model. For all heterogeneous models, I_A at surface is higher than that of the

untreated LMS model which will cause an amplification of the structure motion.

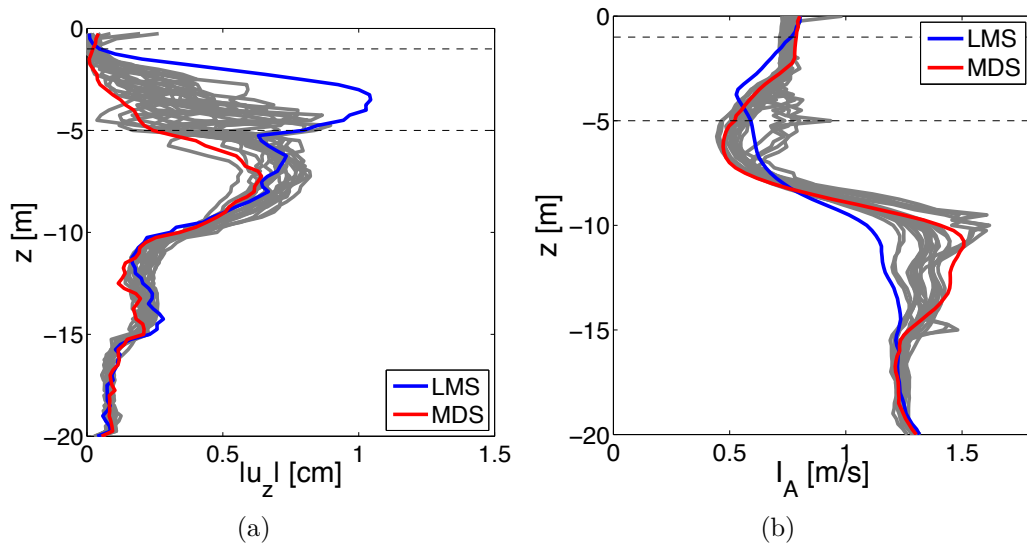


Figure 5.37 – Profile below the structure of (a) settlement and (b) Arias intensity at the end of shaking for $\gamma = 0.4$ and $\beta_1 = \beta_2 = 0.4$.

To compare the results of the entire deposit, Figure 5.38 shows the differences between the heterogeneous model with the maximum $|u_z|$ and the homogeneous LMS model. Again, results are shown for $\gamma = 0.4$ and $\beta_1 = \beta_2 = 0.4$, as an example. Figure 5.38a shows the r_u differences (i.e. $r_{uHET} - r_{uHOM}$) and it clearly depicts the interactions between the two soils. As in the time histories (Figure 5.35a), the results vary greatly from one position to another. For this case, the heterogeneous model presents, in general, lower r_u values, specially in the treated zone (except for some regions). Although, immediately below the treated zone and at the bottom of the model, r_u increased after the inclusion of the denser sand. The explanation is that the interface around this zone acts as a barrier for the water migration and as the layered cases studied in the laboratory, a water film is formed around the liquefied sand (Fiegel and Kutter, 1994; Kokusho and Kojima, 2002; Konrad and Dubeau, 2002, among others).

Similarly, the settlement at the end of shaking difference ($sett_{HET} - sett_{HOM}$) between the heterogeneous and the homogeneous model before treatment is shown in Figure 5.38b. As in the profile under the building column, before treatment the most part of the settlement is located below the structure, but after the heterogeneity is added, the highest settlement is found under the treated area. These two comparisons are evidence of the complexity added with the spatial variation by which neither the liquefaction apparition nor the settlement is homogeneous even for the untreated remaining soil, that is, below and beside the intervened zone.

However, the comparison of the Arias intensity ratio (i.e. I_{AHET}/I_{AHOM}), in Figure 5.38c,

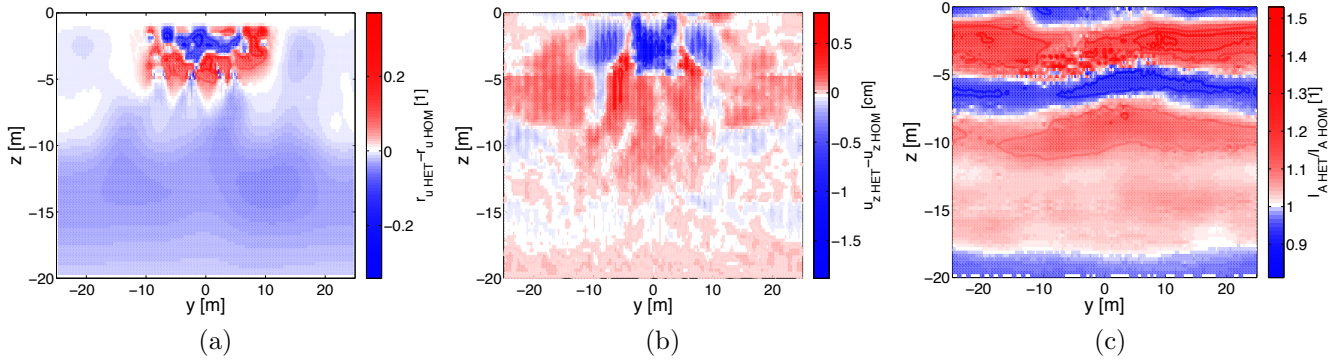


Figure 5.38 – Difference between the heterogeneous with maximum $|u_z|$ and the homogeneous LMS model for (a) the liquefaction ratio (r_u), (b) the settlement and (c) the Arias intensity (I_A) at the end of shaking

is mostly regular in the horizontal direction. The seismic motion is more amplified by the heterogeneous model for the soil near the surface and at the lower half of the soil deposit. The ratio is the lowest immediately below the treatment zone which corresponds to the highest values of liquefaction ratio in the heterogeneous model.

5.5.5 Permeability and soil type effect

In order to further understand the effect of the spatial variability, some changes in the soils were tested. Principally, the effect of the permeability was analyzed. As was noted, the two soils have different soil parameters, among them, different hydraulic conductivity (κ). As has been shown, the pore pressure migration plays an important role in the effect of the spatial variability on $|u_z|$. The excess pore pressure (Δp_w) generation is related to the state of the soil with respect to the critical state, i.e. the dilatant or contractant tendency. Additionally, Δp_w dissipation and redistribution is related to κ . Hence, different scenarios were tested and are summarized in Table 5.5 as three types: (1) two soils with the same soil parameters except for κ , in other words, spatial variability is only affecting κ ; (2) all soil parameters are different except for κ ; and (3) the same as the previous case but with different sets of κ values. In general, all the soil parameters are related, though when the permeability decreases, the other soil parameters decrease too. However, when a cementitious process is used the permeability can be varied, while leaving the other soil parameters practically unchanged.

In Figure 5.39a, the previously used soil mixture with different soil parameters (LMS and MDS) is compared to the first scenario where only LMS soil parameters are used and γ denotes the spatial fraction of κ equal to 10^{-4} (corresponding to that of the LMS). The first case corre-

Table 5.5 – Cases tested for permeability and soil type

ID	Soil 1	Soil 2	κ_1	κ_2
	LMS	MDS	$1 \cdot 10^{-4}$	$1 \cdot 10^{-5}$
	LMS	LMS	$1 \cdot 10^{-4}$	$1 \cdot 10^{-5}$
	LMS	LMS	$1 \cdot 10^{-4}$	$1 \cdot 10^{-3}$
	LMS	MDS	$1 \cdot 10^{-4}$	$1 \cdot 10^{-4}$
	LMS	MDS	$1 \cdot 10^{-4}$	$1 \cdot 10^{-3}$
	LMS	LMS	$1 \cdot 10^{-4}$	$1 \cdot 10^{-6}$

sponds to a 5% Bentonite permeation on sand, which as measured by [Gueddouda et al. \(2010\)](#) produces a decrease in κ of one order of magnitude (i.e. for this case, $\kappa=10^{-5}$). Results show that if the whole treated area is changed, the settlement is increased by less than 10%. Additionally, a 10% Bentonite inclusion was modeled, that is a decrease of two orders of magnitude yet, the average effect on the spatial variability was the same. If however, κ is increased in one order of magnitude due to inclusions of a more coarser material, the settlement decreases 20%. In contrast, when both κ and the dilatant tendency is increased, which is the previously used soil, the reduction is about 40%.

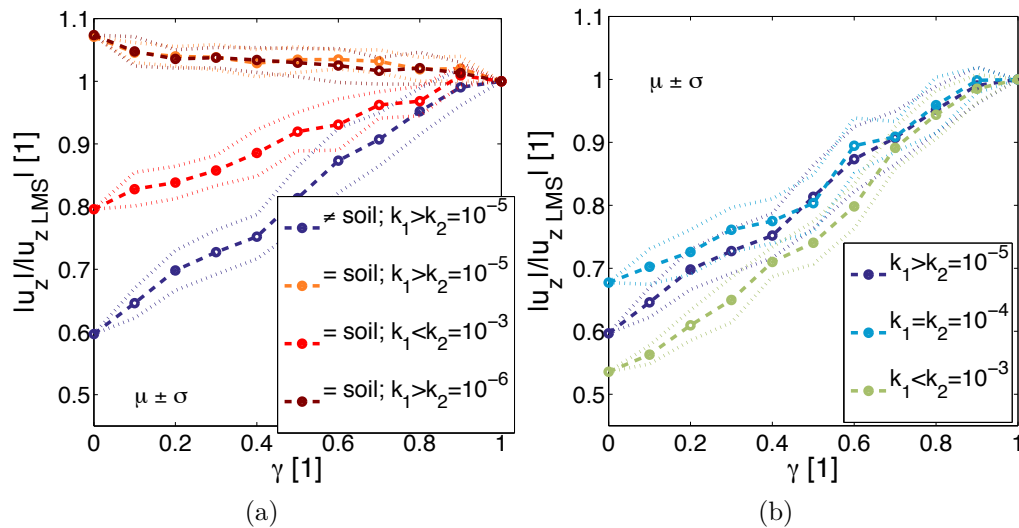


Figure 5.39 – Effect of the spatial variability of different soil parameters on $|u_z|$: a) when only the permeability varies and b) when various soil parameters vary. Mean and the envelope of one standard deviation.

Furthermore, in Figure 5.39b, two additional scenarios are shown: the opposite case is shown in light blue, which is increasing the dilatant tendency while κ is kept constant; and in olive green, the soil parameters change and for this case MDS κ is higher than that of LMS. For the former, the results are similar to those of the original mixture. Once more, κ shows little effect

on the settlement of spatial variable soil. However, when MDS κ equals to 10^{-3} , Δp_w is easily dissipated and the soil improvement is slightly more efficient, as the settlement reduction is more than 45% for $\gamma=0$. Concerning the different spatial fractions tested, it can be noted that significant changes in the average value are only seen for γ below 0.7 for a lower κ and below 0.5 for a higher one. In other words, it seems that for high γ values the response is mainly controlled by the original soil. However, as shown in Figure 5.39a, if only κ is changed the system response is affected even when a small amount of treated soil is added (i.e. for γ about 0.8).

As the difference in κ is mainly observed in the pore pressure generation and dissipation, Figure 5.40a shows the time evolution of r_u under the structure right column and at 3m depth for the MDS case, that is where all the treated area has been replaced. Once more, the interaction between the soils is evidenced as r_u starts increasing after the predominant duration, i.e. above t_{95} , for almost all soils as consequence of the pore pressure migration from LMS at the surroundings. Concerning the highest κ , r_u does not increase at this depth because of the high rate of pore pressure dissipation. Hence the absolute relative settlement at the end of shaking is smaller than for other permeability values tested as shown in Figure 5.40b. Once more, for κ equal to 10^{-5} and 10^{-6} , the response is very similar. Moreover, the different jumps on the settlement roughly coincide for all the soils with the peaks in the input displacement time history, shown also with a scaling factor of 50.

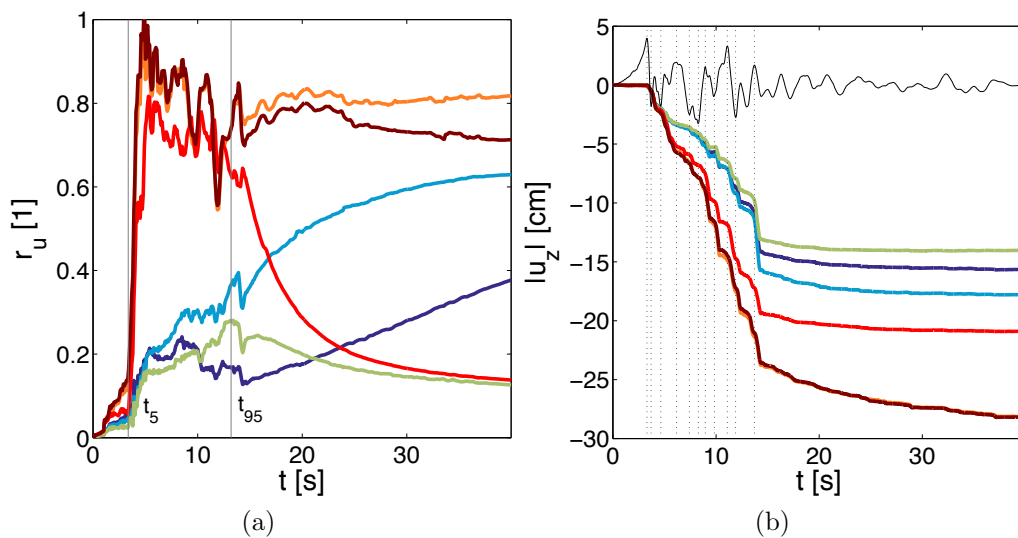


Figure 5.40 – Time evolution of a) liquefaction ratio and b) $|u_z|$: for different soil parameters. The input displacement time history, shown also with a scaling factor of 50.

5.5.6 Random field discretization

The effect of the random field discretization was analyzed by reducing the element size in the horizontal direction by half for the entire FEM. The $|u_z|$ results for the original coarse mesh are compared with the fine one for two motions in Figure 5.41. As expected, the average $|u_z|$ is slightly higher with the fine mesh for almost all γ values tested. However, the difference in the mesh discretization appears to affect all the spatial fractions similarly. Concerning the variation, it is only slightly reduced with the fine mesh and is mostly noted for EQ4.

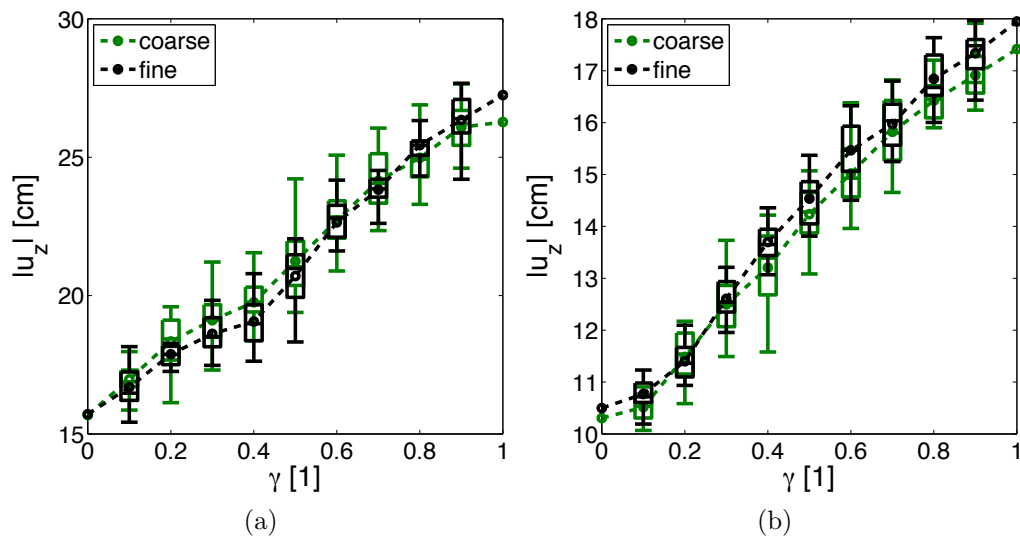


Figure 5.41 – Effect of the mesh size of the binary random field on $|u_z|$ for : a) EQ1 and b) EQ4

5.5.7 Homogenization theories and other input motions

In the previous chapter, concerning the bearing capacity of shallow foundations over cohesive soils, some homogenization theories were compared with the average behavior as a function of γ . Similarly, Figure 5.42a shows the mean $|u_z|$ values normalized by the value for the homogeneous LMS and the Wiener and HS bounds. Contrarily to the results obtained for the bearing capacity, the heterogeneous model presents higher $|u_z|$ than all bounds tested, which could be prejudicial for engineering design. As seen with the effect of other soil parameters, the relation of the settlement with γ appears to be related to either the response of one material or the other; in other words, it is mainly controlled by the interaction between the materials. Compared to the bearing capacity assessment, the emergence of a percolation-like behavior is caused by the properties contrast and its effect in the behavior. For a highly heterogeneous

system in the vicinity of the percolation threshold (γ_c), there are several local clusters that are mainly composed of the more stiffer material (MDS), and which are the principal components of what becomes the percolating cluster.

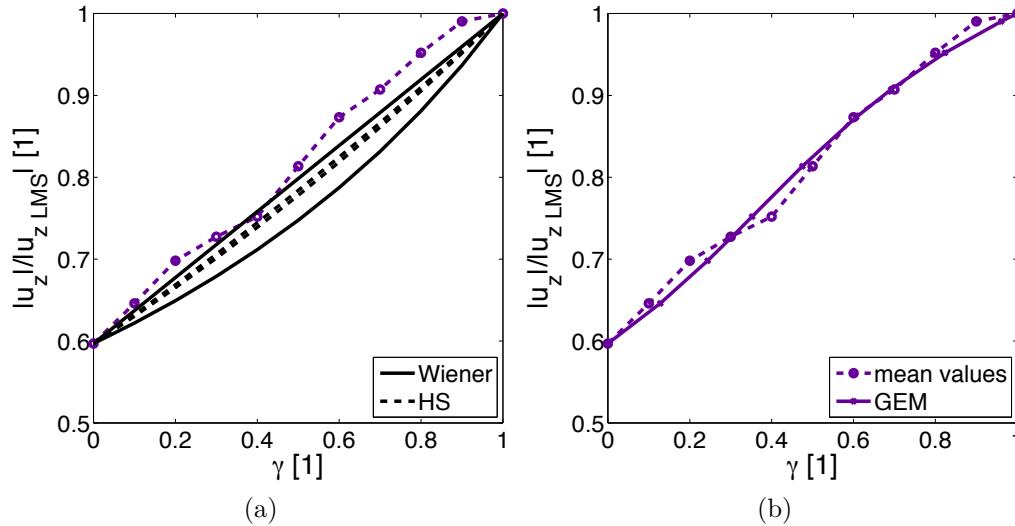


Figure 5.42 – Homogenization theories for the original LMS -MDS soil mixture: a) traditional theories and b) generalized effective medium (GEM) equation for EQ1

Figure 5.42b shows the GEM equation for EQ1. The percolation threshold and the scaling exponents were found by an optimization of the average $|u_z|$ of all γ values. The least-squares method was used and the variables were bounded between 0 and 1. The γ_c found is equal to 0.35, which is slightly below the values found in the literature for transport properties which is expected given the correlation in both directions and the important interactions between the soils shown previously. The scaling exponents s and t are equal to 0.24 and 0.21, respectively. As these are similar, the effect of having very high or very low γ is relatively similar. In other words, the system is affected for even a small amount of spatial variability. The GEM equation gives a well suited fit for the effective settlement of the structure, which is related to the theory of the percolation threshold, i.e. that after a certain value, there is a well-connected cluster that connects opposite sides of the system.

Figure 5.43a shows the mean $|u_z|$ as a function of γ for the eight motions tested. It is noted that the effect of the spatial variability is very different for each input motion but as the initial $|u_z|$ is also different, the relative difference values ($\Delta|u_z|$) are shown in Figure 5.43b. Note that the shape of the function, i.e. positive or negative concavity or s shape, appears to be related to other factors than only the initial $|u_z|$ value. For instance, EQ2 and EQ7 have a similar $|u_z|$ for the non-treated case however the former presents a positive concavity and the latter

a negative one. This shape is related to the interactions between the two soils, though when the addition of a small fraction of treated soil affects only slightly the response and then for low γ values it drops, the relation has a positive concavity as for EQ2 and EQ5. In the other hand, when by only adding a small fraction, the settlement is drastically reduced while it is not greatly affected by low γ values, the shape is described as a negative concavity as for EQ3 and EQ7. Concerning the other motions, a combination of both phenomena is identified.

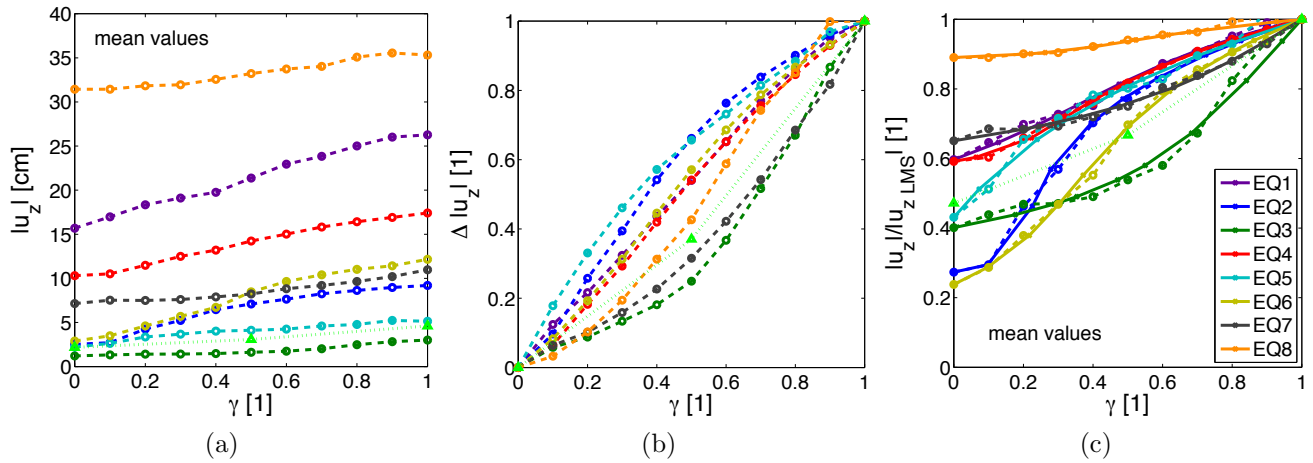


Figure 5.43 – $|u_z|$ relation with γ for all motions tested: a) mean values, b) relative difference and c) normalized mean values compared to GEM equation

Furthermore, Figure 5.43c shows the normalized $|u_z|$ with respect to the case before treatment (i.e. LMS). The average values are shown in dashed lines. Additionally, the GEM equation was calibrated for all motions and results are shown in Figure 5.43c as solid lines. The percolation threshold γ_c and the scaling exponents found also by least squares optimization are shown in Table 5.6.

Table 5.6 – Calibration of GEM parameters

	s	t	γ_c
EQ1	0.24	0.21	0.35
EQ2	0.1	0.26	0.18
EQ3	0.54	0.99	0.53
EQ4	0.14	0.19	0.3
EQ5	0.31	0.29	0.1
EQ6	0.73	0.3	0.44
EQ7	0.59	0.94	0.76
EQ8	0.02	0.08	0.1

The GEM equation gives a well suited fit for the effective settlement of the structure under

the earthquake motions tested. Note that EQ1 and EQ4 have a similar normalized response and thus similar coefficients. Contrary to the results of the previous section concerning the bearing capacity for different clay mixtures, it appears that in this case the response is not only depending on the values of the extreme cases. For instance, even if EQ3 and EQ5 have similar $|u_z|$ ratio between the extreme cases (i.e. $|u_{zMDS}|/|u_{zLMS}|$), the effect of different γ values is very different. Additionally, the percolation threshold does not seem to depend on the $|u_{zMDS}|/|u_{zLMS}|$, as seen for EQ2 and EQ6.

In an effort to understand the relation between the input motion and the effect of the different spatial fractions, the value $\Delta|u_z|$ for $\gamma = 0.5$ was compared to 15 intensity measures (IM), defined in the appendix C.2. Figure 5.44 shows the relation with the three IM that presented the best relation: the Arias intensity (I_A), the peak horizontal velocity (PHV) and the period of equivalent harmonic wave ($T_{V/A}$). As it can be seen, the values appear to be closely related to the input PHV values except for three motions (EQ1, EQ4 and EQ8). The black line corresponds to a logarithmic fit without the outliers motions and the coefficient of determination (R^2) is calculated without the latter. Besides the fact that these motions present the highest PHA and highest $|u_{zLMS}|$, EQ1 and EQ8 were the only ones to be identified as pulse-like according to the procedure defined by Baker (2007). Additionally, as was noted above, EQ4 was recorded in soft soil, with a V_{s30} below 400m/s, though it could have high frequency content. This motion was not identified as pulse-like by Baker (2007) procedure but it could be according to another definition of pulse-like developed by Dickinson and Gavin (2011). The PHV is more likely to characterize ground-motion accurately at intermediate frequencies because it is less sensitive to the higher frequency components Kramer (1996). Finally, Figure 5.44c shows $\Delta|u_z|$ for $\gamma = 0.5$ as a function of $T_{V/A}$, which gave the highest efficiency from all IM tested taken into account all motions. $T_{V/A}$ is the equivalent period corresponding to the intersection of the constant spectral acceleration and spectral velocity and is computed by:

$$T_{V/A} = 2\pi \frac{\alpha_V(\xi = 5\%) PHV}{\alpha_A(\xi = 5\%) PHA} \quad \text{where} \quad \frac{\alpha_V(\xi = 5\%)}{\alpha_A(\xi = 5\%)} = \frac{1.65}{2.12} \quad (5.28)$$

where α_V and α_A are the Newmark-Hall median spectrum amplification factors for the constant velocity and the constant acceleration regions with 5% damping. Green and Cameron (2003) found a close relation between this IM and the amplification of soft soil sites. In this case, $T_{V/A}$ appears to better describe $\Delta|u_z|$ for $\gamma = 0.5$ as it takes into account the PHV as well as the inverse of the PHA. According to Kawase (2011), $T_{V/A}$ is a simplified indicator of the dominant

period of the motion which appears to be related to the potential damage of structures. While for PHV, R^2 is closer to unity it does not take into account all motions. In Figure 5.44c, the predominant period of the soil (T_0) and the structure (T_{str}^{FB}) is shown in solid and dashed lines, respectively. The differences of EQ3 and EQ5 with respect to the general trend, once more evaluated by logarithmic fit, can be due to the resonance with the soil for these motions.

Lastly, an additional motion was used to test only the relation of $\Delta|u_z|$ for $\gamma = 0.5$ with the different IM. It corresponds to the Loma Prieta earthquake of 1989 and identified as EQ9. This motion is also classified as non-pulse like according to Baker (2007). Fifty simulations were performed and the mean value is shown as a green triangle in Figures 5.43 and 5.44. As it can be seen, this additional motion agrees well with the trend found by logarithmic fit for PHV and $T_{V/A}$.

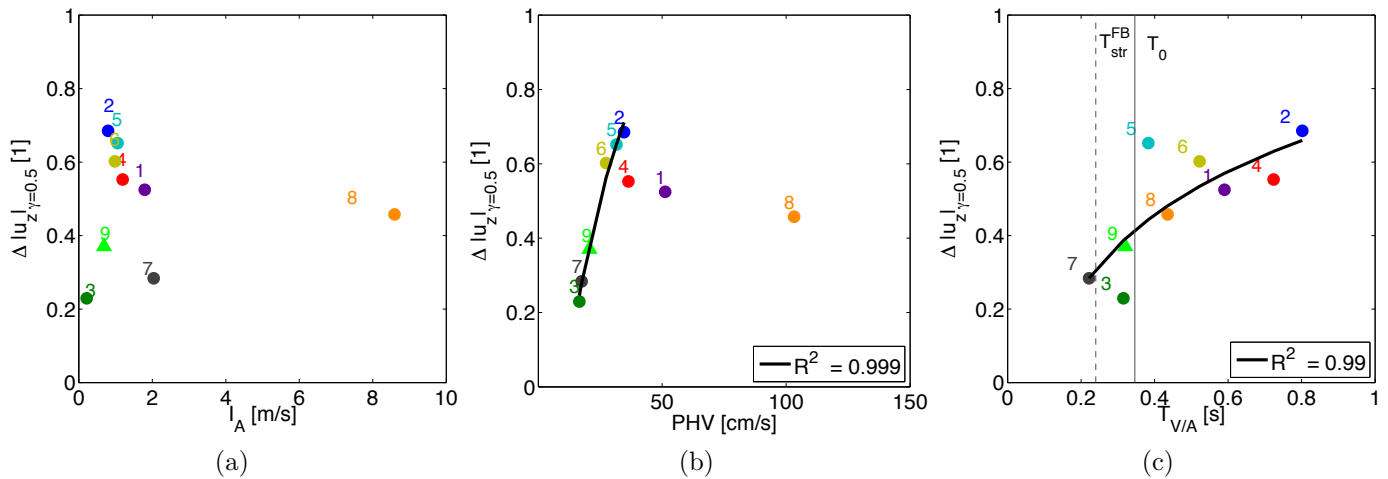


Figure 5.44 – Relation of the relative difference for $\gamma=0.5$ and different IM: a) I_A , b) PHV and b) $T_{V/A}$

5.5.8 Other EDPs

The effect of spatial variability in the seismic response on a soil structure interaction model can be analyzed by different engineering demand parameters (EDPs). In this study, focus was given to the assessment of this effect on the relative settlement of the structure with respect to free field. However, as the soil behavior is nonlinear and the seismic excitation is highly complex, the effect on other EDPs is different.

Regarding the liquefaction index (Q) evaluated at the end of shaking for the whole deposit shown in Figure 5.45a, there is a clear relationship with $|u_z|$ (seen in Figure 5.31), which explains the importance of pore water pressure generation and migration through the soil deposit. How-

ever, Q presents higher variation specially for lower spatial fractions. A possible explanation is that liquefaction triggering depends on the spatial distribution and the presence of clusters while the relative settlement depends on the response of the entire deposit. Similarly, the Arias intensity (I_A) evaluated at the structure's base at the end of shaking is shown in Figure 5.45b and presents a close relationship with the inverse of Q and of $|u_z|$, though the variation is generally higher.

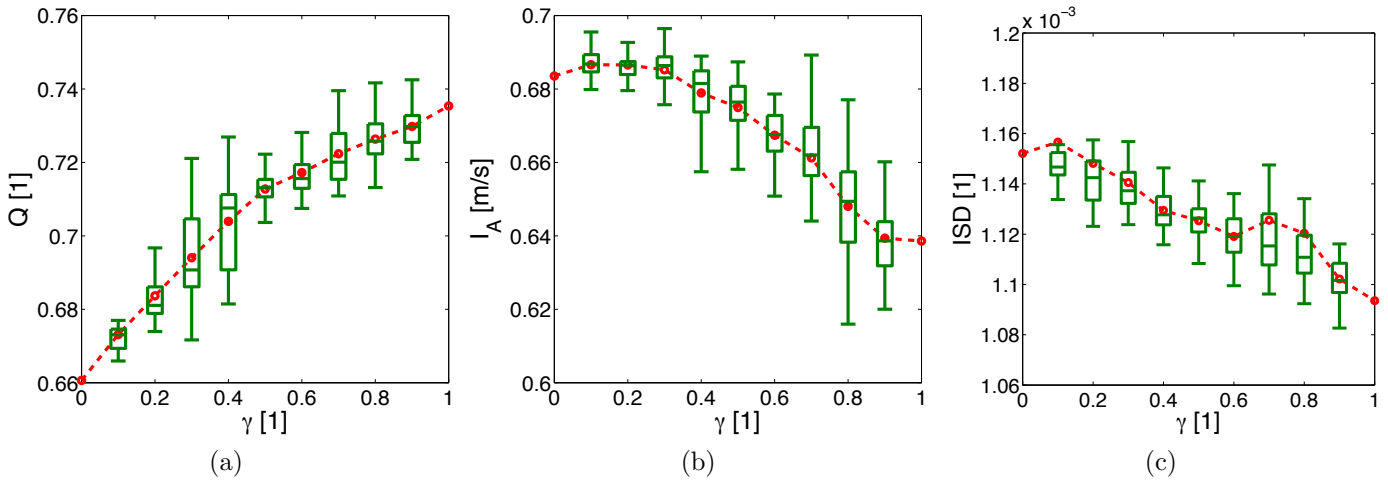


Figure 5.45 – Box-and-whiskers plot for: a) the Liquefaction Index (Q), b) Arias intensity (I_A) and c) maximum inter-story-drift (ISD)

In contrast, the maximum inter-story drift (ISD) of the structure, shown in Figure 5.45c, presents a very different relation with the spatial fraction. The mean values change drastically and the dispersion is significantly high. Probably, more simulations are required to have a convergence of the mean and standard deviation on this parameter, as it depends on the non-linearity of the structure behavior as well as on the soil variability. However, it is important to highlight that in spite of the average increase in ISD as more MDS is included, the drift is not very high and the structure has not suffer significant damage.

Finally, Figure 5.46 shows the same EDPs relation with γ for all input motions tested. In this case, the input motions that presented some similarities in the $|u_z|$ response have a different behavior for other EDPs. For instance, while EQ1 and EQ4 presented similar overall response for $|u_z|$, they present substantial differences regarding the EDPs shown in Figure 5.46. For instance, with EQ4 and for γ equal to 0, ISD is decreased more than 20% compared to γ equal to unity, while with EQ1, the corresponding value is slightly increased. In general, the EDP normalized values are higher than those for $|u_z|$. For some motions, values can be greater than unity which means that after the soil improvement these EDPs have increased thus it will be

prejudicial for the system. In particular, the increase in I_A is above twice the initial value for EQ7 and for EQ5, all EDPs shown present a considerable increase.

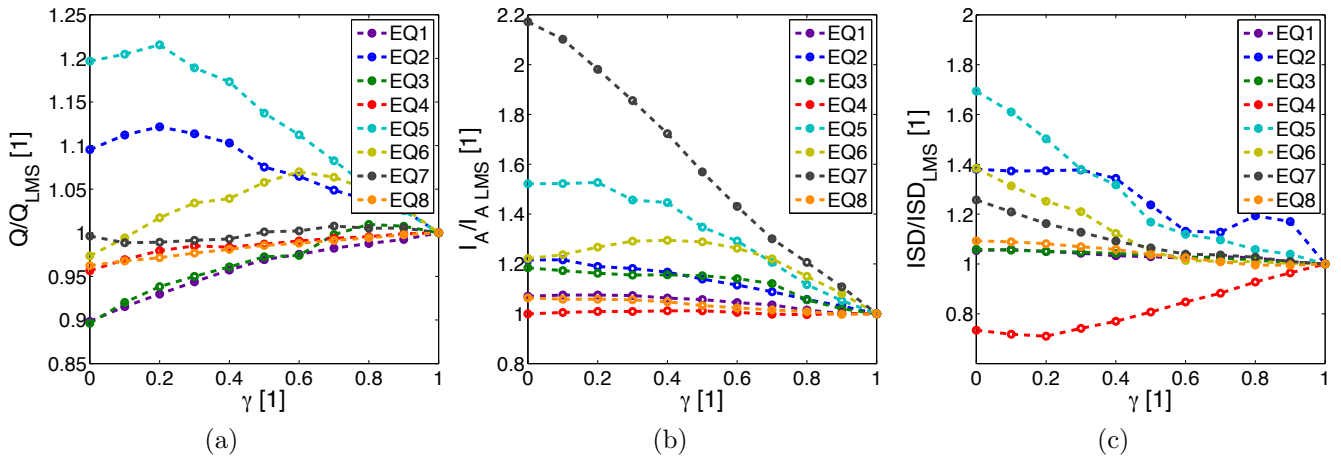


Figure 5.46 – Mean values relation with γ for all motions tested for: a) the Liquefaction Index (Q), b) Arias intensity (I_A) and c) maximum inter-story-drift (ISD)

5.5.9 Partial conclusions

A numerical model of discrete spatial heterogeneity was used to assess the liquefaction induced settlement of an inelastic soil-structure system. Correlation in both directions was introduced by the *nearest-neighbor* model. The effect of the spatial fraction (γ) of the treated-untreated soil mixture was analyzed. At least twenty simulations were used for each γ . The main conclusions of the present study are:

- For all motions tested, the case of the fully-treated soil reduces the relative settlement of the structure with respect to free-field but increases the liquefaction ratio under and around the treated area.
- Owing to excess pore-pressure migration, treated soil surrounded by loose sand can present liquefaction and therefore low fractions of soil treatment have very low efficiency. Similarly, once the loose sand is well surrounded by treated soil, improvement in the relative settlement is small.
- While the relative settlement ($|u_z|$) appears to be related to the liquefaction index (Q), the latter presents more variation due to the pore-pressure migration. Even so, with some motions, Q could be increased at adding denser soil to the deposit.

- The generalized-effective-medium (GEM) equation is well fitted for the average $|u_z|$ as a function of γ with all the earthquakes tested; while, the traditional homogenization techniques will overestimate the efficiency of the inclusions for most motions.

The coupling of the discrete spatial variation code and the finite element model applied in a probabilistic framework appears to properly include heterogeneity on the soil. However, the effect of multivariate discrete models should be further analyzed. Furthermore, the effect of the soil properties correlation (in the horizontal and vertical direction) on the liquefaction-induced settlements should be investigated and, if possible, related to real *in-situ* measurements of added spatial variability due to mitigation techniques.

Chapter 6

Conclusions

The current seismic design philosophy is based on nonlinear behavior of structures where the foundation soil is often simplified by a modification of the input acceleration depending on the expected site effects. The latter are generally limited to depend on the shear-wave velocity profile or a classification of the site. Findings presented in this work have illustrated the importance of accounting for both soil nonlinearity due to seismic liquefaction and for soil-structure interaction. The first part of this work was devoted to show the need to take into account in the numerical modeling the coupling of excess pore pressure (Δp_w) and soil deformation (CPD). In this regard, the differences between this approach and the decoupled one were quantified via the simulation of nonlinear 1D wave propagation and SSI. The effect of coupling was evaluated in both the structure's settlement and its seismic performance. The second part was focused on the efficiency of soil improvement techniques (e.g. soil-mixing, bentonite permeations or biogrouting) on mitigating excessive seismic ground settlements of a structure on liquefiable sandy profiles. In this case, the effect of the added spatial variability due to improvement techniques was assessed by coupling FEM with a binary random field generated by an auto-regressive code.

General Conclusions

Even if partial conclusions were already given throughout the dissertation, the main obtained results are highlighted in this chapter and discussed in the light of their contribution to the main objective:

- With respect to the nonlinear modeling, the ECP model was validated with a real site for the 1D response analysis in a blind test. The model parameters were calibrated with

few laboratory and *in-situ* data and enriched with empirical correlations found in the literature. According to the Anderson criteria, the model provides good similarities for different motion intensity levels, specially for frequencies above 1Hz. In this case, the similarity is less for the weak motions as the model overpredicts the first peak amplification; however it is able to capture the shift to lower frequencies as well as the deamplification due to the nonlinear behavior for strong motions.

- With respect to the effects of CPD on the free-field (FF) response it was found that even though the maxima on acceleration, Arias intensity and settlement are overestimated with the DPD analysis, the acceleration response spectra (PSA) is underestimated for periods below 0.1s and above 1s. Moreover, if PSA is evaluated after the predominant period of the motion differences between the analyses increase as the CPD causes a deamplification due to soil softening. The effects of CPD on PSA were found to depend on the Δp_w generation thus on the soil's contractant tendency and the liquefaction index (Q) measured in the deposit hence a period-dependent correction function described by the ratio between the PSA for CPD and for DPD, called the Response Spectra Ratio (RSR), is presented for different Q and different time windows. The general tendency of this function was found to be similar to others found in the literature, even though only two soil profiles were studied.
- Concerning the effects of CPD on the structural response it is important to analyze also the soil-structure interaction (SSI). Even if in FF, the DPD presented higher settlement, the structure's weight affects the soil behavior and hence the structure's settlement with respect to FF is in general underestimated with DPD models. Additionally, if the SSI effects are significant, the differences in the PSA found in the FF are amplified by the structure's predominant period. Moreover, the combination of these effects causes an underestimation of the maximum ISD by the DPD analysis. However these results are dependent on both the soil's and structure's behavior as well as in the input motion.
- In the last chapter, an important aspect of the numerical modeling of liquefaction mitigation techniques was addressed: the uncertainty in the technique's efficiency due to the spatial variability introduced in the deposit. The water migration from natural to treated soil causes the latter to liquefy thus for low levels of treatment, the structure's settlement could be even increased depending on the spatial distribution of the two soils. Furthermore, it was shown that the relation between the levels of treatment and the resulting

settlement can not be described by traditional homogenization theories such as arithmetic or harmonic averages, as it is usually done. In addition, this relation is dependent on the input motion used because of the different interactions within the deposit.

Further research

- The ECP model validation of nonlinear 1D site response analysis has been presented however additional cases of borehole arrays dealing with liquefaction evolution should be tested, for example the liquefaction array sites of Port Island (Japan), Wildlife (USA) and Belleplaine (France). Additionally, it is desirable to improve the database of validation cases of liquefiable soil and structure interaction models with instrumented sites or physical experiments performed in shaking tables or in centrifuge tests.
- The relation of both SSI and CPD effects was shown to be highly complex. Thus, the effects of CPD could be further evaluated for other soil deposits and other structures in order to increase the reliability of the results. In addition to the nonlinearity of the soil, the structure's nonlinearity could be further analyzed comprehending the evaluation of damage and failure.
- Furthermore, in order to take into account the three components of the input motion and its effects on the CPD analysis a 3D modeling is desirable but this will cause an important increase in computational resources. In this case, it is necessary to include a model able to reduce the added computational cost to a more rational size with reliable and accurate results. For example, the Domain Reduction Method briefly described in section 3.4 could be used. In addition, this method could allow to introduce the whole incident wave in the model.
- Concerning the numerical modeling of the added spatial variability for the evaluation of the bearing capacity of a cohesive deposit, the model could account for multi-soil variability thus incorporating the Bruggeman effective medium theory for discrete random fields. Furthermore, the validation of this model could be possible via centrifuge tests with controlled spatial variability.
- With regard to the induced spatial variability by liquefaction mitigation techniques, two approaches could be envisaged for further research. On one hand, a total coupling of FEM

with a model of the transport, permeation or injection process of the treated material to a saturated soil deposit could provide an insight of the different spatial distributions. Thus, the interactions within the deposit will be taken from the initial static case and the evolution of the mechanical properties would be modeled. However, this approach will need to take into account the inherent spatial variability and other uncertainties that will cause the eventual heterogeneity in the process. On the other hand, the latter could be addressed in a probabilistic framework from which a probability distribution function and random field properties could be assessed by only modeling the application of the soil improvement process. Afterwards, this model would be used as input for the binary or multi-soil discrete random field coupled to FEM. Doubtlessly, validation of the model with *in-situ* measurements or laboratory tests could contribute to this work.

Appendix A

Soil model parameters

According to the concept of critical-state soil mechanics, the behavior of cohesionless soils is related to the proximity of its initial state to the critical state or steady-state line rather than to the absolute measurements of density (Roscoe and Pooroshasb, 1963; Been and Jefferies, 1985; Ishihara, 1993). For the ECP model, Aubry et al. (1982) defined this distance as the stress ratio p_0/p_{c0} , in which p_0 is the initial mean stress and p_{c0} , the stress corresponding to the critical state of the initial density. When this ratio is higher than 1 and under drained conditions, the soil behavior will be contractant; otherwise, it will be contractant/dilatant.

Several soil mechanics tests are modeled in order to show the general response of the ECP elastoplastic model with the different soils tested. The tests concern both monotonic and cyclic paths at drained and undrained conditions with varying effective consolidation pressures (p'). In order to ease the comparison between the soils tested, all simulations were performed with the same p' values: 10kPa, 40kPa and 60kPa, which correspond to depths of 1m, 5m and 10m, approximately.

Two soil deposits were used in this study. They present different initial behaviors and correspond to two relative densities: (LMS) loose-to-medium and (MDS) medium-to-dense. The model parameters were determined with the procedure defined by Lopez-Caballero et al. (2007) and their calibration and validation is presented in Lopez-Caballero and Modaressi-Farahmand-Razavi (2013).

A.1 LMS

The parameters are divided into five groups corresponding to the different mechanisms and are shown in Table A.1.

A.1.1 Drained triaxial test

Figures A.1 and A.2 show the results obtained by the model for a simulated triaxial drained test. The response is showed in four planes: the $q - \varepsilon_1$, $\varepsilon_v - \varepsilon_1$, $\varepsilon_v - p$ and $\eta - \varepsilon_1$. For the LMS, the volumetric strains are below zero for all confinement pressures tested, which means that the soil deposit is contracting. This densification is presented even for low pressures, for example in the case of the soil near the surface. The tendency of densification causes the increase in pore pressure generation, which ultimately triggers the liquefaction phenomena.

Parameter	[0-1]m	[1-10]m	[10-15]m	[15-20]m
ρ_s [kg/m ³]	2700	2700	2700	2700
n_0	0.35	0.59	0.59	0.47
k_0	0.6	0.6	0.6	0.6
κ [m/s]	$1 \cdot 10^{-5}$	$1 \cdot 10^{-5}$	$1 \cdot 10^{-5}$	$1 \cdot 10^{-4}$
Elasticity				
K_{ref} [MPa]	69.74	628.0	628.0	628.0
G_{ref} [MPa]	32.19	290.0	290.0	290.0
n_e	0.0	0.5	0.5	0.5
p_{ref} [MPa]	1.0	1.0	1.0	1.0
Critical State and Plasticity				
ϕ'_{pp} [°]	30	30	30	30
β	33	33	33	33
d	2.00	2.00	2.00	2.00
b	0.20	0.20	0.20	0.20
p_{c0} [kPa]	39.8	39.8	50.0	80.0
Flow Rule and Isotropic Hardening				
ψ [°]	30	30	30	30
α_ψ	1.0	1.0	1.0	1.0
a_1	$1 \cdot 10^{-4}$	$1 \cdot 10^{-4}$	$1 \cdot 10^{-4}$	$1 \cdot 10^{-4}$
a_2	$2 \cdot 10^{-3}$	$2 \cdot 10^{-3}$	$2 \cdot 10^{-3}$	$2 \cdot 10^{-3}$
c_1	$1 \cdot 10^{-3}$	$1 \cdot 10^{-3}$	$1 \cdot 10^{-3}$	$1 \cdot 10^{-3}$
c_2	$2 \cdot 10^{-3}$	$2 \cdot 10^{-3}$	$2 \cdot 10^{-3}$	$2 \cdot 10^{-3}$
m	1.5	1.5	1.5	1.5
Threshold Domains				
r^{ela}	$3 \cdot 10^{-2}$	$3 \cdot 10^{-2}$	$3 \cdot 10^{-2}$	$3 \cdot 10^{-2}$
r^{hys}	$4 \cdot 10^{-2}$	$4 \cdot 10^{-2}$	$4 \cdot 10^{-2}$	$4 \cdot 10^{-2}$
r^{mob}	$8 \cdot 10^{-1}$	$8 \cdot 10^{-1}$	$8 \cdot 10^{-1}$	$8 \cdot 10^{-1}$
r^{iso}	$1 \cdot 10^{-3}$	$1 \cdot 10^{-3}$	$1 \cdot 10^{-3}$	$1 \cdot 10^{-3}$

Table A.1 – ECP model parameters for loose-to-medium sand (LMS)

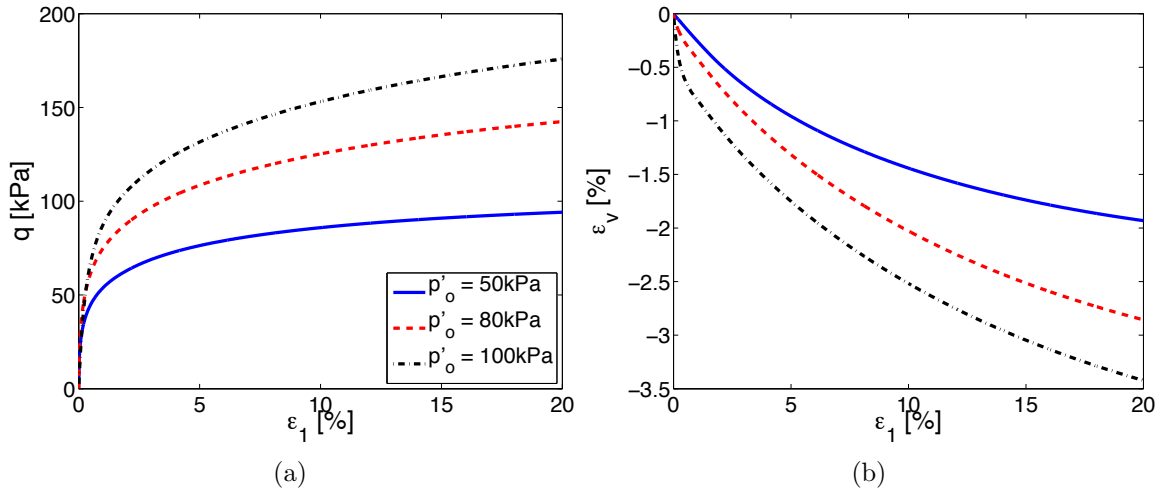


Figure A.1 – Simulated drained triaxial tests for LMS: a) $q - \varepsilon_1$ and b) $\varepsilon_v - \varepsilon_1$

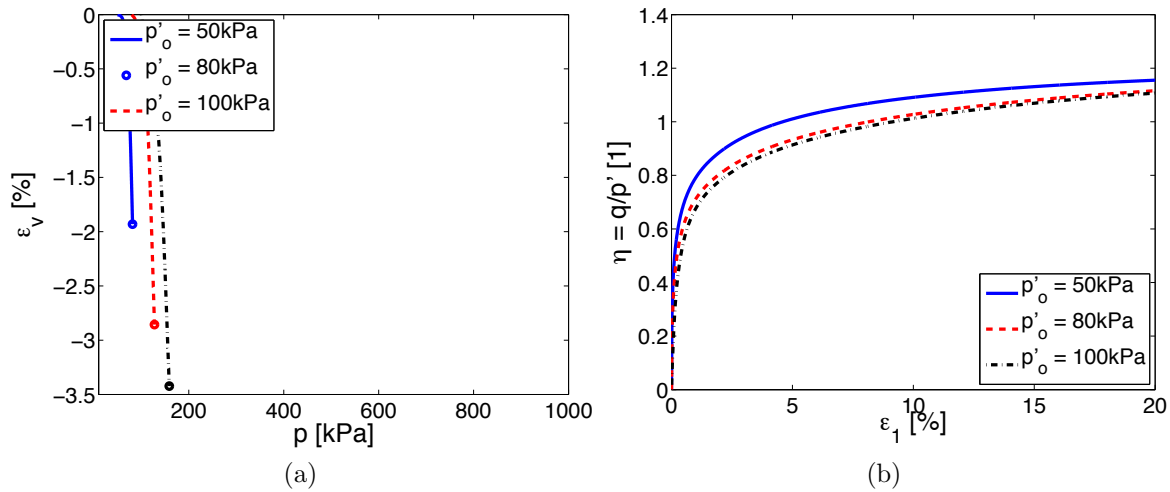


Figure A.2 – Simulated drained triaxial tests for LMS: a) $\varepsilon_v - p$ and b) $\eta - \varepsilon_1$

A.1.2 Consolidation test

Figure A.3 shows the simulated response of cyclic isotropic and oedometric consolidation tests.

A.1.3 Drained cyclic strain-controlled shear test

To define the cyclic behavior, drained cyclic shear tests with strain control are simulated for different confinement pressures. The shear modulus degradation and damping evolution with shear strain is shown in Figure A.4. As a reference, the mean of the empirical equation of Darendeli (2001) for the same effective stresses, $IP = 0\%$, $OCR = 1$, $f = 1\text{Hz}$ and $N = 10$ cycles are also shown in the figure. The obtained shear modulus degradation curves ($G/G_{max} - \gamma$) match

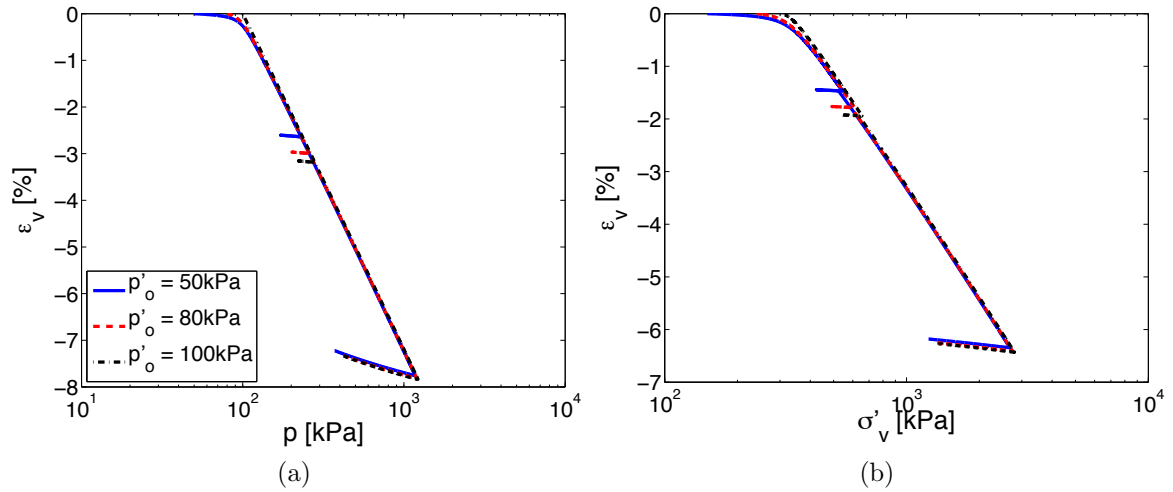


Figure A.3 – Simulated consolidation tests for LMS: a) isotropic and b) oedometric

relatively good; whereas for the damping (D) it can be seen an underestimation for strains less than 0.001% and an overestimation for large strains.

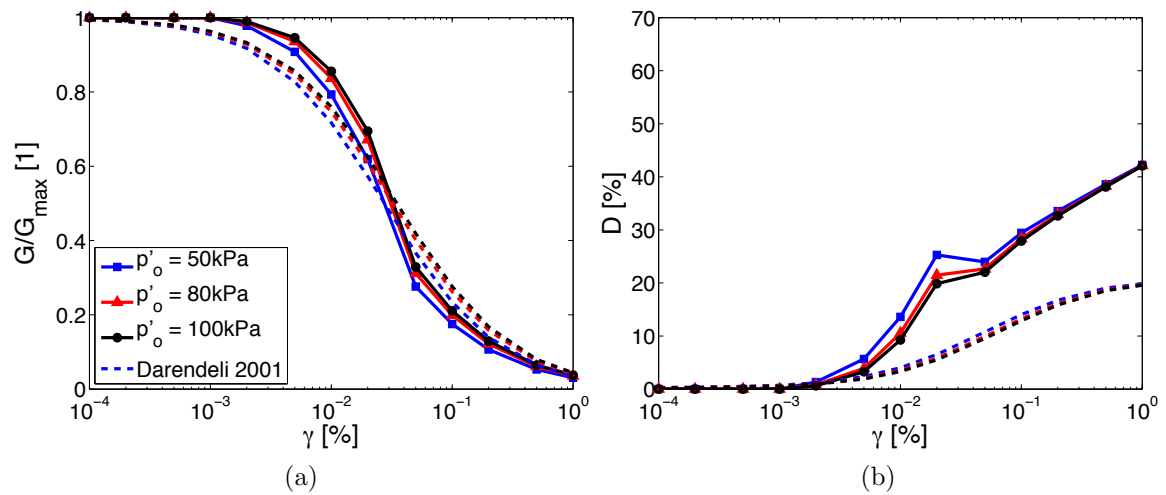


Figure A.4 – Simulated drained cyclic shear test for LMS: a) normalized shear modulus degradation (G/G_{max}) and b) damping (D) curves as a function of γ

A.1.4 Undrained cyclic stress-controlled shear test

Regarding the characterization of the liquefaction resistance, an undrained cyclic shear test was modeled for varying confinement pressures. Figure. A.6 shows the cyclic stress ratio ($SR = \tau_{cyc}/p_0$) as a function of the number of loading cycles to produce liquefaction (N). As qualitative comparison, the curves given by Byrne et al. (2004) for Nevada sand at different

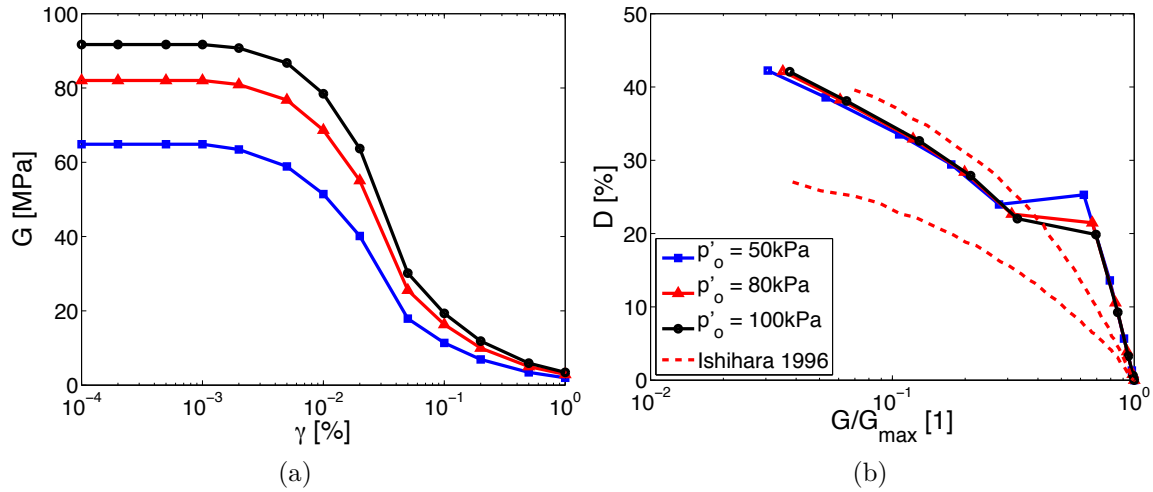


Figure A.5 – Simulated drained cyclic shear test for LMS: a) $G - \gamma$ and b) $D - G/G_{max}$

densities (i.e. $D_r = 40$ and 60%) are also shown. It is noted that the obtained curves are closer to the reference for a $D_r = 40\%$ and that the resistance is similar for the levels of stress tested.

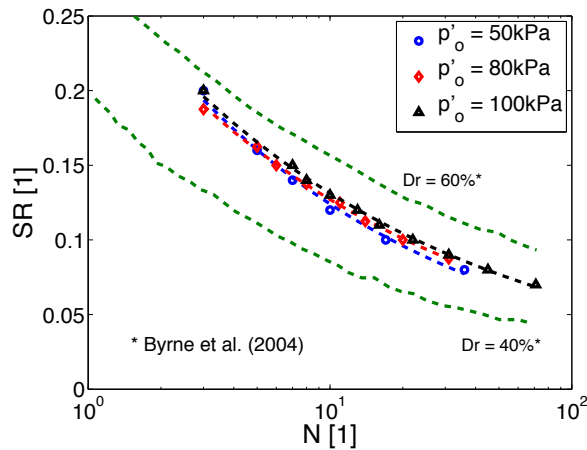


Figure A.6 – Simulated undrained cyclic shear test for LMS: $SR - N$

A.2 MDS

Table A.2 shows the parameters for the MDS deposit.

A.2.1 Drained triaxial test

Figures A.7 and A.8 show the results obtained by the model for a simulated triaxial drained test for MDS. The response is showed in four planes: the $q - \varepsilon_1$, $\varepsilon_v - \varepsilon_1$, $\varepsilon_v - p$ and $\eta -$

Parameter	[0-5]m	[5-10]m	[10-15]m	[15-20]m
ρ_s [kg/m ³]	2700	2700	2700	2700
n_0	0.35	0.59	0.59	0.47
k_0	0.5	0.5	0.5	0.5
κ [m/s]	$1 \cdot 10^{-4}$	$1 \cdot 10^{-4}$	$1 \cdot 10^{-4}$	$1 \cdot 10^{-4}$
Elasticity				
K_{ref} [MPa]	79.47	444.0	444.0	444.0
G_{ref} [MPa]	36.68	222.36	222.36	222.36
n_e	0.0	0.4	0.4	0.4
p_{ref} [MPa]	1.0	1.0	1.0	1.0
Critical State and Plasticity				
ϕ'_{pp} [°]	31	31	31	31
β	43	43	43	43
d	3.50	3.50	3.50	3.50
b	0.20	0.20	0.20	0.20
p_{c0} [MPa]	1.80	1.80	1.80	1.80
Flow Rule and Isotropic Hardening				
ψ [°]	31	31	31	31
α_ψ	1.0	1.0	1.0	1.0
a_1	$1 \cdot 10^{-4}$	$1 \cdot 10^{-4}$	$1 \cdot 10^{-4}$	$1 \cdot 10^{-4}$
a_2	$4 \cdot 10^{-3}$	$4 \cdot 10^{-3}$	$4 \cdot 10^{-3}$	$4 \cdot 10^{-3}$
c_1	$6 \cdot 10^{-2}$	$6 \cdot 10^{-2}$	$6 \cdot 10^{-2}$	$6 \cdot 10^{-2}$
c_2	$3 \cdot 10^{-2}$	$3 \cdot 10^{-2}$	$3 \cdot 10^{-2}$	$3 \cdot 10^{-2}$
m	1.5	1.5	1.5	1.5
Threshold Domains				
r^{ela}	$5 \cdot 10^{-3}$	$5 \cdot 10^{-3}$	$5 \cdot 10^{-3}$	$5 \cdot 10^{-3}$
r^{hys}	$3 \cdot 10^{-2}$	$3 \cdot 10^{-2}$	$3 \cdot 10^{-2}$	$3 \cdot 10^{-2}$
r^{mob}	$8 \cdot 10^{-1}$	$8 \cdot 10^{-1}$	$8 \cdot 10^{-1}$	$8 \cdot 10^{-1}$
r^{iso}	$1 \cdot 10^{-3}$	$1 \cdot 10^{-3}$	$1 \cdot 10^{-3}$	$1 \cdot 10^{-3}$

Table A.2 – ECP model parameters for medium-to-dense sand (MDS)

ε_1 . In contrast with the previous soil, for the MDS the volumetric strains are above zero for strains larger than 1%, for all confinement pressures tested, which means that the soil deposit is contractant/dilatant.

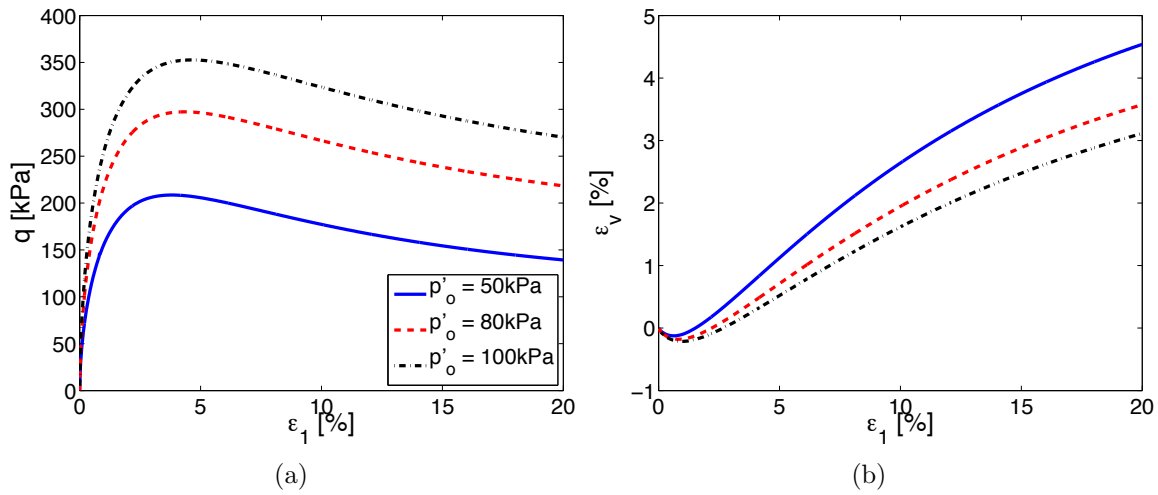


Figure A.7 – Simulated drained triaxial tests for MDS: a) $q - \varepsilon_1$ and b) $\varepsilon_v - \varepsilon_1$

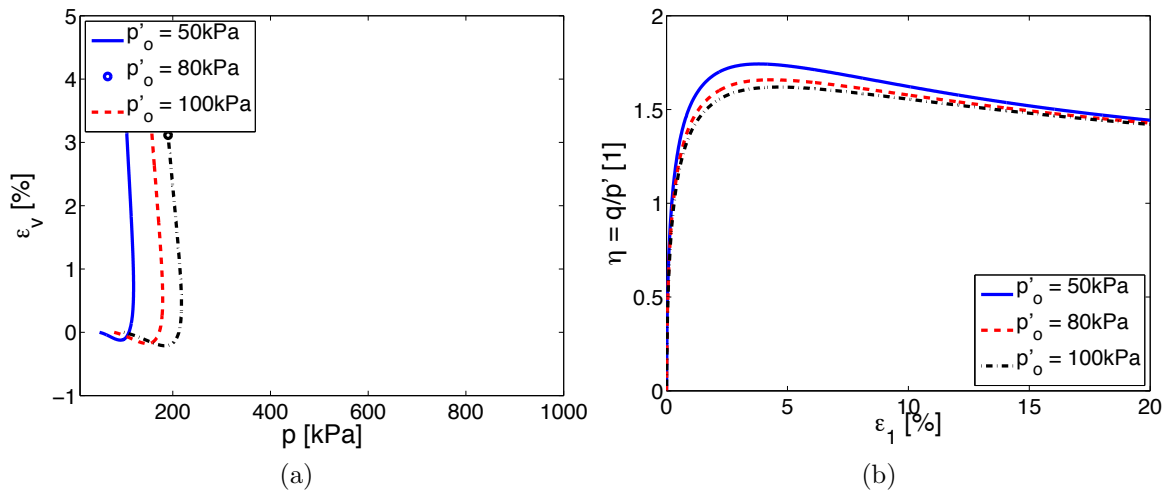


Figure A.8 – Simulated drained triaxial tests for MDS: a) $\varepsilon_v - p$ and b) $\eta - \varepsilon_1$

A.2.2 Consolidation test

Figure A.9 shows the simulated response of cyclic isotropic and oedometric consolidation tests.

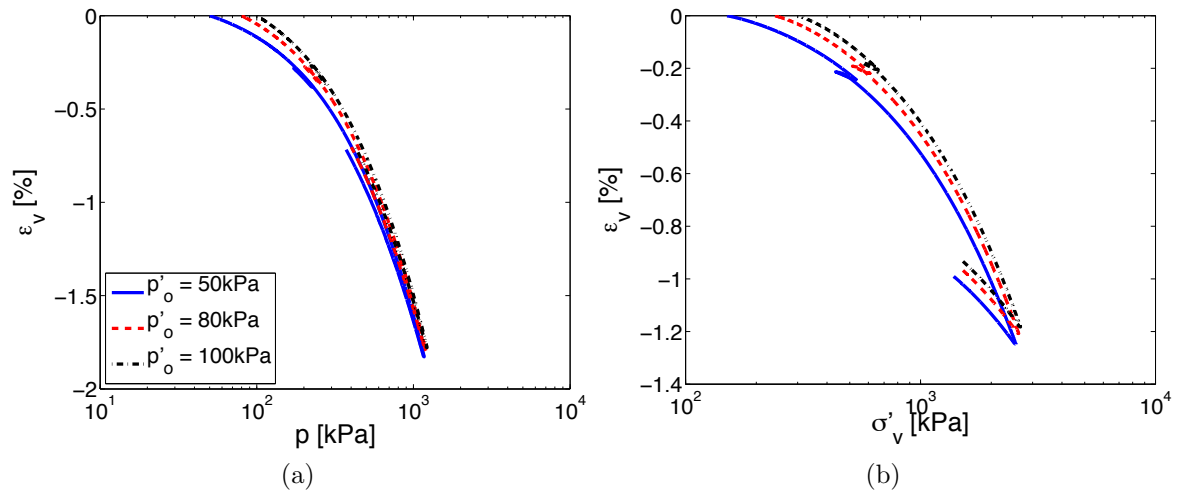


Figure A.9 – Simulated consolidation tests for MDS: a) isotropic and b) oedometric

A.2.3 Drained cyclic strain-controlled shear test

To define the cyclic behavior, drained cyclic shear tests with strain control are simulated for different confinement pressures. The shear modulus degradation and damping evolution with shear strain is shown in Figure A.10. As a reference, the mean of the empirical equation of Darendeli (2001) for the same effective stresses, IP= 0%, OCR=1, f=1Hz and N=10 cycles are also shown in the figure. The obtained shear modulus degradation curves ($G/G_{max} - \gamma$) match relatively good; whereas for the damping (D) it can be seen an underestimation for strains less than 0.001% and an overestimation for large strains.

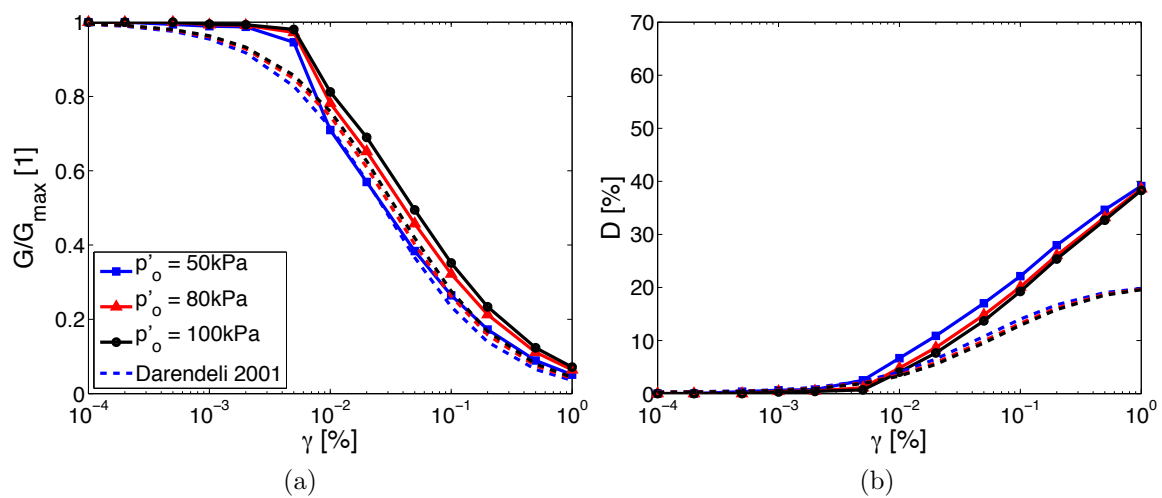


Figure A.10 – Simulated drained cyclic shear test for MDS: a) normalized shear modulus degradation (G/G_{max}) and b) damping (D) curves as a function of γ

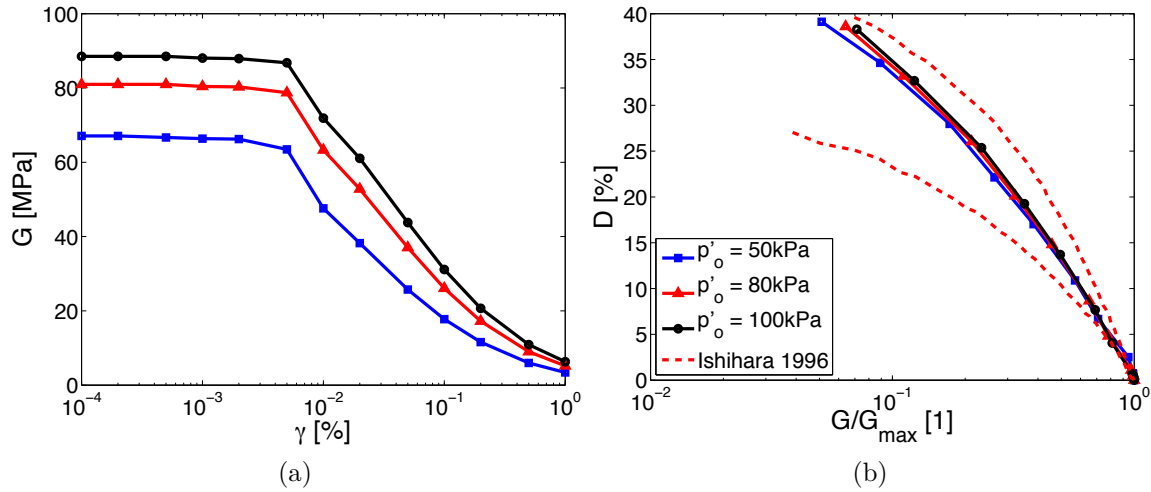


Figure A.11 – Simulated drained cyclic shear test for MDS: a) $G - \gamma$ and b) $D - G/G_{max}$

A.2.4 Undrained cyclic stress-controlled shear test

Regarding the characterization of the liquefaction resistance, an undrained cyclic shear test was modeled for varying confinement pressures. Figure. A.12 shows the cyclic stress ratio ($SR = \tau_{cyc}/p_0$) as a function of the number of loading cycles to produce liquefaction (N). As qualitative comparison, the curves given by Byrne et al. (2004) for Nevada sand at different densities (i.e. $D_r = 40$ and 60%) are also shown. It is noted that the obtained curves are closer to the reference for a $D_r = 40\%$ and that the resistance is similar for the levels of stress tested.

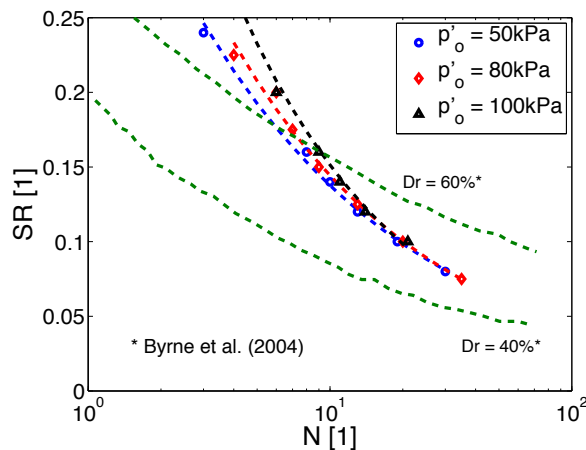


Figure A.12 – Simulated undrained cyclic shear test for MDS: $SR - N$

A.3 Soils used in chapter 2

In chapter 3, three additional soil profiles were used. They consist of the cases for the verification and validation of the nonlinear model presented for the international benchmark PRENOLIN. The first two are called P1 and P2 and are canonical soil profiles used in this study to analyze the model's sensibility with respect to the numerical parameters. The model parameters for each layer are shown in Tables A.3 and A.4 for the two soil profiles, correspondingly. As only limited information was available, most parameters do not vary between layers. So as to maintain a constant mean stress ratio, p_{c0} varies and therefore β changes. Additionally, the geometric parameters for the calibration of the shear modulus degradation were varied: i.e. r^{ela} , r^{hys} and a_1 and a_2 .

Layer z [m]	1 1	2 5	3 10	4 15	5 20
Elasticity					
K_{ref} [MPa]	840.0	840.0	840.0	840.0	840.0
G_{ref} [MPa]	180.0	180.0	180.0	180.0	180.0
n_e	0.00	0.00	0.00	0.00	0.00
p_{ref} [MPa]	1.0	1.0	1.0	1.0	1.0
Critical State and Plasticity					
ϕ'_{pp} [°]	30	30	30	30	30
β	55	54	53	52	52
d	2.00	2.00	2.00	2.00	2.00
b	0.80	0.80	0.80	0.80	0.80
p_{co} [MPa]	0.01	0.06	0.11	0.17	0.23
Flow Rule and Isotropic Hardening					
ψ [°]	30	30	30	30	30
α_ψ	1.00	1.00	1.00	1.00	1.00
a_1	8.0e-07	1.0e-05	2.0e-05	2.0e-05	7.0e-05
a_2	2.0e-06	5.0e-05	6.0e-04	1.5e-03	5.5e-03
c_1	1.7e-01	1.7e-01	1.7e-01	1.7e-01	1.7e-01
c_2	3.5e-01	3.5e-01	3.5e-01	3.5e-01	3.5e-01
m	1.00	1.00	1.00	1.00	1.00
Threshold Domains					
r^{ela}	0.100	0.026	0.013	0.005	0.007
r^{hys}	0.600	0.080	0.040	0.030	0.060
r^{mob}	0.800	0.800	0.800	0.800	0.800
r^{ela}_{iso}	0.0010	0.0010	0.0010	0.0010	0.0010

Table A.3 – ECP model parameters for P1 - Verification phase

Additionally, in section 3.5, some results for the validation of the model with the surface recordings of a japanese borehole site are presented. The site is the PARI station Sendai. The

Layer	1	2	3	4	5	6	7	8	9
z [m]	1	5	10	15	20	40	60	80	100
Critical State and Plasticity									
ϕ'_{pp} [°]	30	30	30	30	30	30	30	30	30
β	55	54	53	52	52	52	51	51	51
d	2.00	2.00	2.00	2.00	2.00	2.00	2.00	2.00	2.00
b	0.80	0.80	0.80	0.80	0.80	0.80	0.80	0.80	0.80
p_{co} [MPa]	0.01	0.06	0.11	0.17	0.23	0.45	0.68	0.91	1.13
Flow Rule and Isotropic Hardening									
ψ [°]	30	30	30	30	30	30	30	30	30
α_ψ	1.00	1.00	1.00	1.00	1.00	1.00	1.00	1.00	1.00
a_1	5.0e-6	1.0e-5	1.7e-5	2.0e-5	2.5e-5	4.0e-5	2.0e-5	4.0e-5	5.0e-5
a_2	5.0e-5	1.0e-4	5.0e-4	1.0e-3	1.5e-3	9.0e-4	1.0e-3	9.0e-4	2.0e-3
c_1	1.7e-1								
c_2	3.5e-1								
m	1.00	1.00	1.00	1.00	1.00	1.00	1.00	1.00	1.00
Threshold Domains									
r^{ela}	0.020	0.012	0.007	0.006	0.006	0.009	0.005	0.004	0.005
r^{hys}	0.050	0.090	0.070	0.050	0.050	0.060	0.010	0.010	0.030
r^{mob}	0.800	0.800	0.800	0.800	0.800	0.800	0.800	0.800	0.800
r_{iso}^{ela}	0.0010	0.0010	0.0010	0.0010	0.0010	0.0010	0.0010	0.0010	0.0010

Table A.4 – ECP model parameters for P2 - Verification phase

Table A.5 shows the ECP model parameters for the two layers. However the parameters for both layers are very similar as the difference between the mean pressures is not significant

As the shear wave velocity changes each meter, the shear and bulk moduli were set to be pressure independent hence $n_{el} = 0$. Note that only four parameters differ for the two layers. They correspond to the hardening parameters (a_1 and a_2) and the threshold domains (r_{ela} and r_{hys}) that control the hardening evolution and are calibrated with the nonlinearity curves of shear degradation modulus with strain, as explained in section 3.3.

A.4 General conclusions

Concerning the simulated damping (D) evolution with strain, generally an underestimation for strains less than 0.001% and an overestimation for large strains is present. For purely elastic behavior, no hysteretic dissipation of energy should take place; however, even if the mechanism is not well understood, there is experimental evidence of such dissipation [Kramer](#)

Layer	1	2
z [m]	3	7
Critical State and Plasticity		
ϕ'_{pp} [°]	32	30
β	30	30
d	2.00	2.00
b	0.20	0.20
p_{co} [MPa]	0.20	0.55
Flow Rule and Isotropic Hardening		
ψ [°]	32	30
α_ψ	1.00	1.00
a_1	6.96e-5	1.12e-4
a_2	1.39e-4	2.23e-4
c_1	2.00e-3	2.00e-3
c_2	1.00e-3	1.00e-3
m	1.00	1.00
Threshold Domains		
r^{ela}	6.00e-2	2.96e-2
r^{hys}	4.20e-1	5.00e-1
r^{mob}	8.00e-1	8.00e-1
r^{iso}	1.00e-3	1.00e-3

Table A.5 – ECP model parameters for P1 - Validation

(1996). Some advanced constitutive models, as the one used in this analysis, require the addition of a small amount of damping to avoid spurious response at very low strain levels. This damping is introduced by the numerical algorithm of the dynamic equilibrium solution in the time domain known as the predictor-corrector Newmark scheme [Katona MG \(1985\)](#). In this case, the numerical damping “added” into the model is 0.1% and is applicable for strains less than 0.01% [Montoya-Noguera and Lopez-Caballero \(2016\)](#). Concerning the large strains, the damping overestimation is due to the fact that in the ECP model the Massing rules are verified. This overestimation is supposed to cause an underestimation of displacements and some ground motion properties. In this regard, a new version of the model including a degradation factor for the plastic rigidity was implemented by [Carrilho Gomes et al. \(2015\)](#). This factor depended on the shear strain level and controlled the damping at large shear strains. The preliminary results showed that for sands “the reduction achieved in damping curves had no significant influence on the seismic soil response, since the profiles of maximum shear strain, PGA at surface and normalised PSA were similar”.

Appendix B

Nonlinear soil behavior in 2D models

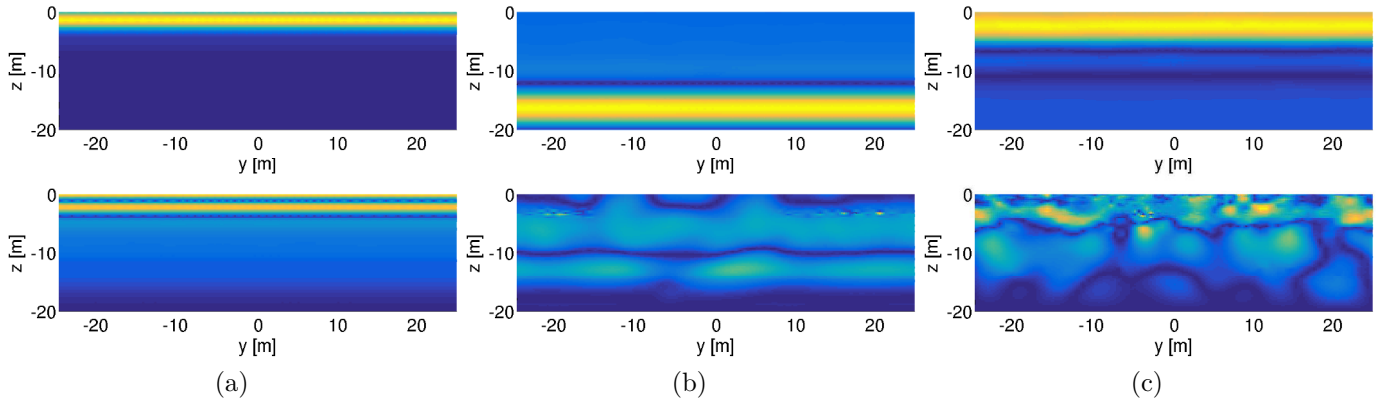


Figure B.1 – Horizontal and vertical acceleration at three time instants for a very weak motion: a) after SH waves are reflected from the surface ($t=0.1s$), b) when it is reflected from the bottom ($t=0.2s$) and c) once more reflected from surface ($t=0.3s$)

As the wave propagates through the model, the soil degrades and soil deformations cause the modification of the wave. In a 2D model, when this phenomena occurs, some heterogeneity is evidenced due to the differences in soil deformation throughout the deposit. Though, when a vertically shear wave propagates through a soft soil, surface waves and vertical accelerations can be evidenced. As the 2D model increases in width, more differences can be evidenced in the wave propagation and in the soil behavior through the deposit. Additionally, differences increase as the intensity of the motion increases; hence, while for quasi-elastic behavior almost no difference appears, as soil nonlinearity evolves, more the models will differ.

In this section, the effects of soil deformation on the signal response will be analyzed. First, differences between a 2D soil column of 1m length, called hereafter the 1D model, and a 50m length soil deposit, called 2D model. The main difference in the models is the length while all the other geometric and numerical parameters were kept constant. The elements in the 2D model are discretized each 0.5m in the horizontal direction in the center of the model and in a zone of 20 length; outside this zone, the discretization is doubled (i.e. each 1m).

When the SH waves are reflected from the surface, vertical waves are generated in a 2D model as can be seen in Figure B.1 for three time instants after a motion of $PHA \approx 0.01m/s^2$ is injected into the base of the model. As V_s is below 200m/s, at $t=0.1s$ the first SH wave is already reflected from the surface and the vertical wave appears. But as soon as the waves are reflected, differences are observed at the horizontal as well as in the vertical acceleration amplitudes in the center of the model.

The models present differences in various aspects, however, for the sake of brevity, results will be shown mainly on three:

- Shear stress and strain;
- Liquefaction ratio ;
- Acceleration

Firstly, the maximum shear modulus (G_{max}) profile and the transfer function (TF) of the soil deposit, evaluated between the surface and the bedrock, are shown in Figure B.2. The soil is modeled with the ECP elasto plastic model but, since a scaled motion with a $PHA = 1 \cdot 10^{-6}g$ was used, the behavior is quasi-elastic. At this stage, the only differences observed between the 1D and the 2D model are in the TF for frequencies higher than 20Hz; although this is a known limitation of the finite element model due to the discretization in time and space. Concerning other aspects of the analysis, no significant difference can be observed.

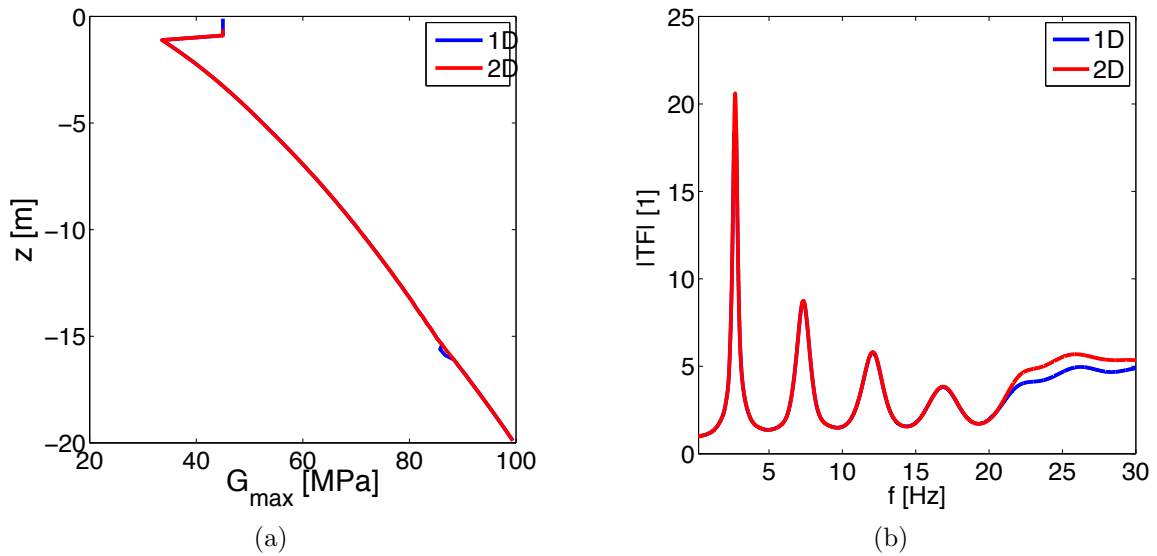


Figure B.2 – a) Shear modulus profile and b) TF - surface/bedrock - quasi-elastic behavior

B.0.1 Shear stress and strain

In contrast, when a strong motion is used differences can be important between the 1D and the 2D models. Figures B.3 to B.7 show the profiles of the maximum values for some parameters for a strong ground motion with a $PHA = 0.2g$. Profiles in the 2D model were taken from the centerline, although, only small differences are perceived for other profiles. In other words,

the 2D model does not differ in the horizontal direction. Figure B.3 shows the profiles of maximum shear stress and strain. Concerning the maximum shear stresses, the 2D model presents slightly higher values. However, the biggest difference is in the shear strains; where the 2D model presents the maximum value at 8.5m while for the 1D model, it is 0.5m below.

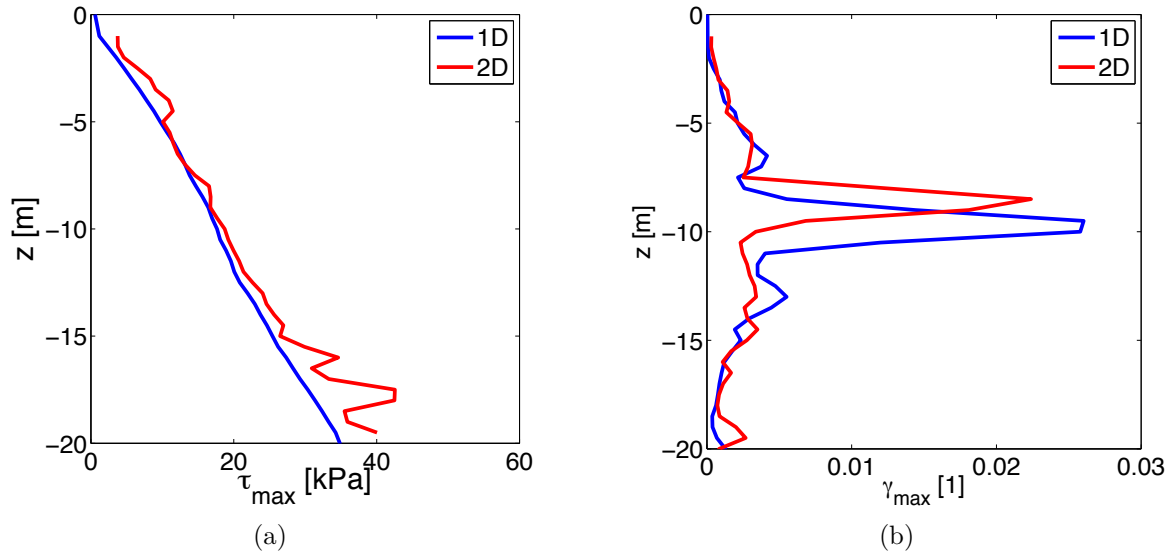


Figure B.3 – a) Maximum shear stress and b) strain for a strong motion - Nonlinear behavior

To better understand the shear stress and strain differences, Figure B.6 shows the time history for the depth of maximum values for 2D, i.e. $z=8.5\text{m}$ and 1D, $z=9\text{m}$. Note that the difference between the models does not start at the same time. Yet, the shape of the stress-strain loops are similar.

B.0.2 Liquefaction ratio

The profile of liquefaction ratio (r_u) at the end of shaking is shown in Figure B.5 for both models. The models present similar values above 5m, then differences start to increase and are larger at the bottom of the deposit. Again, the location of the maximum values differ for about 0.5m; thus, the liquefaction ratio is intimately related to the shear strains in the soil.

Finally, regarding the same depths of maximum values, the time evolution of the liquefaction ratio is shown for 8.5 and 9m. For the former, the models start to differ after 12s when the 2D model presents a rapid increase of pore pressure. For the latter, the difference is greater after 32s, when pore pressure dissipation is evidenced in the 2D model.

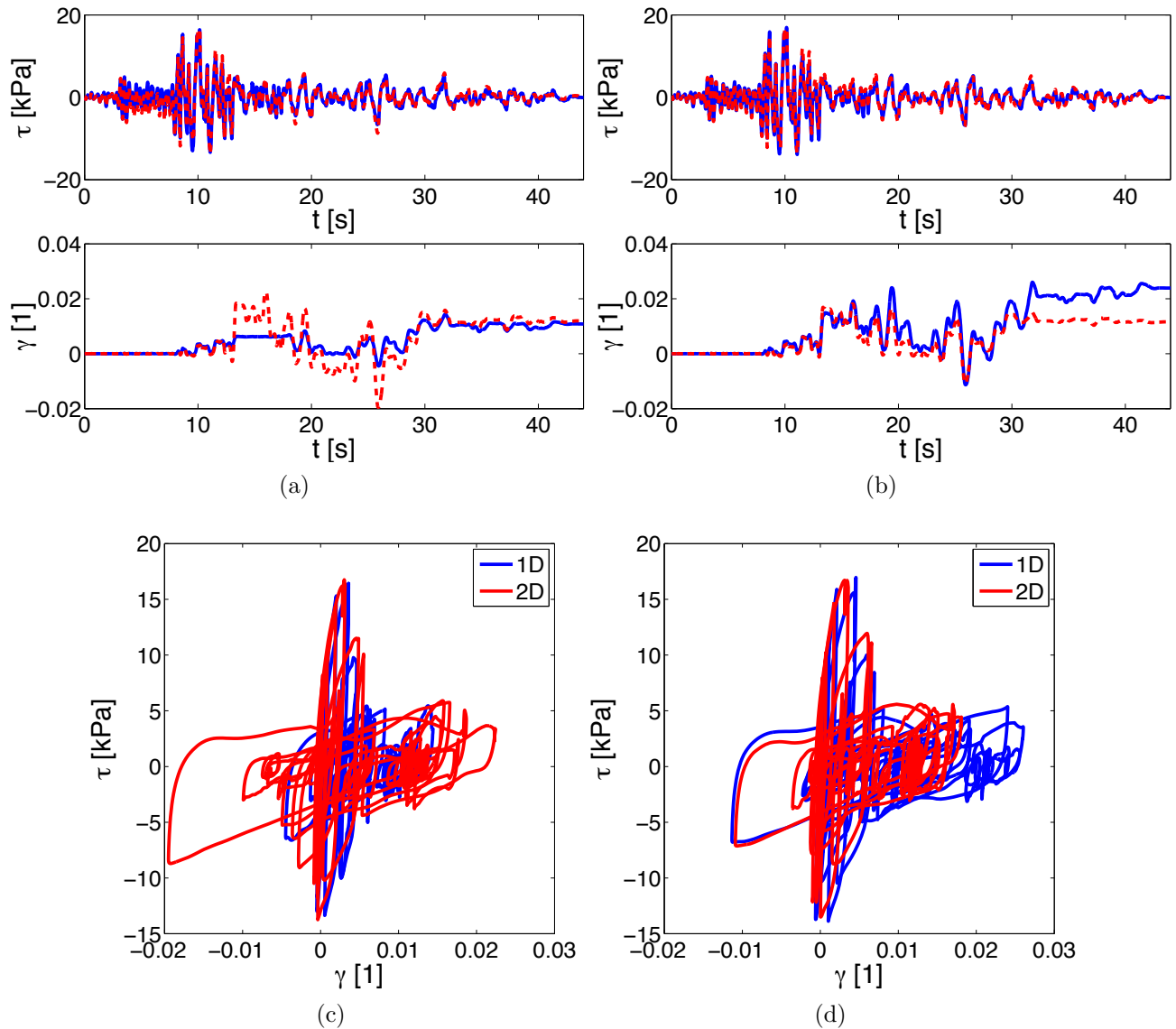


Figure B.4 – Time history of shear stress and strain: a) and c) at 8.5m and b) and d) at 9m

B.0.3 Acceleration

The difference in peak values is also observed in the profile of maximum horizontal acceleration shown in Figure B.7 where the 2D model presents a maximum value at the same depth. Although the 1D model presents also some peaks about this depth, the maximum value is found at 16m. Concerning the maximum vertical acceleration profile, most of the peaks are at deeper soil.

Although some differences have been evidenced concerning shear stresses and strains, liquefaction ratio and acceleration, the main difference bears on the high frequencies, or low periods, as it can be seen in the response spectra shown in figure B.8 for two depths. At surface, slightly

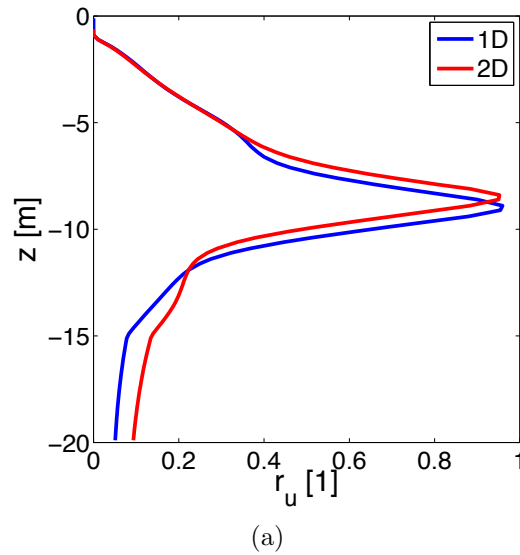


Figure B.5 – Profile of liquefaction ratio r_u at the end of shaking for 1D and 2D centerline

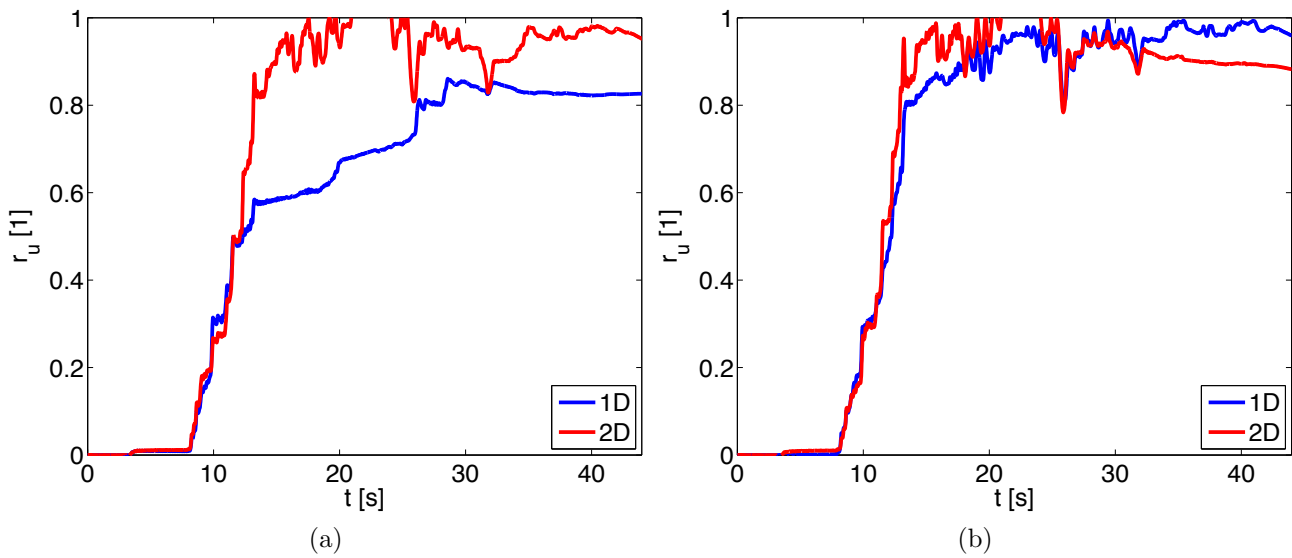


Figure B.6 – Liquefaction ratio time evolution at : a) 8.5m and b) 9m

smaller values are observed for the 2D model response below 0.2s, i.e. frequencies above 10Hz. However, differences are more important at 8m, where the 2D model response has clearly a spurious energy for periods shorter than 0.2s which is probably due to the previously observed high shear strains and liquefaction.

Due to the complexity of the acceleration in terms of frequency, duration and energy, two methods are applied to compare and quantify the differences between signals.

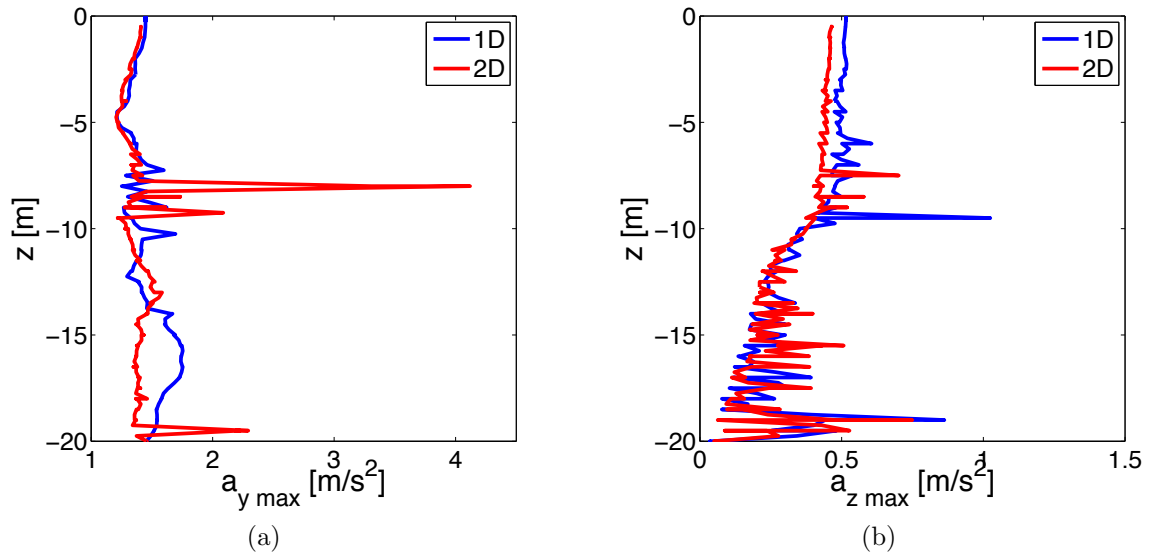


Figure B.7 – Differences in the Peak acceleration profile : a) horizontal and b) vertical

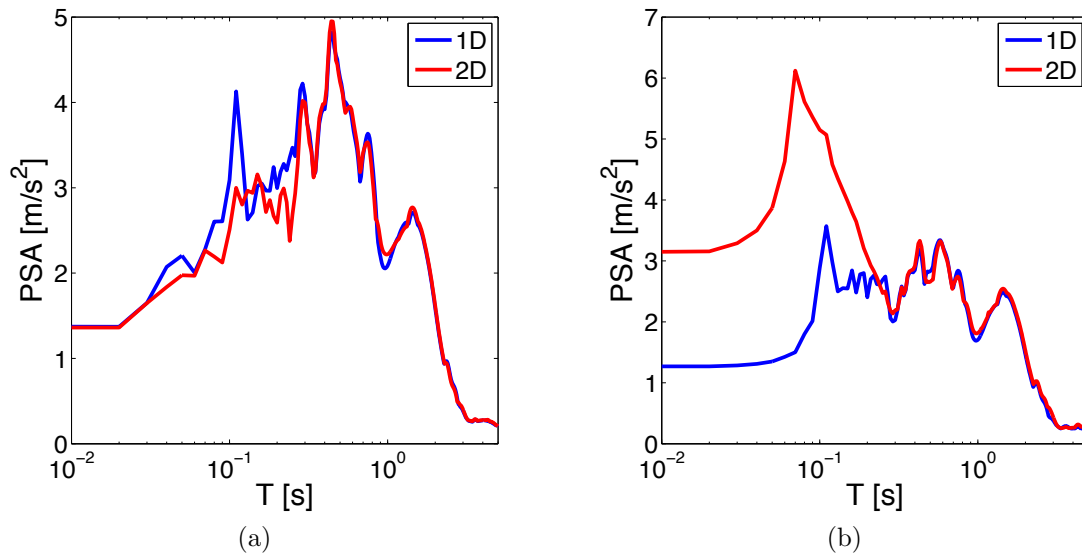


Figure B.8 – Response spectra of the horizontal acceleration : a) at surface and b) at 8m

B.0.3.1 Signal coherency

Figure B.9 shows the evolution with time of the coherency (γ_c) between the two models for two depths. The γ_c is evaluated between the two motions with an incremental time window. For the motions in the surface, above the watertable, γ_c is above 0.8 during all the time for frequencies below 10Hz. Additionally, no loss of coherency is perceived before 8s, not even for very high frequencies (e.g. above 30Hz). In contrast, at the liquefied area at 8m depth, the coherency for small frequencies drops to 0.8 between 12 and 18s. However, it seems that the coherency loss with frequency has a similar trend for both depths tested.

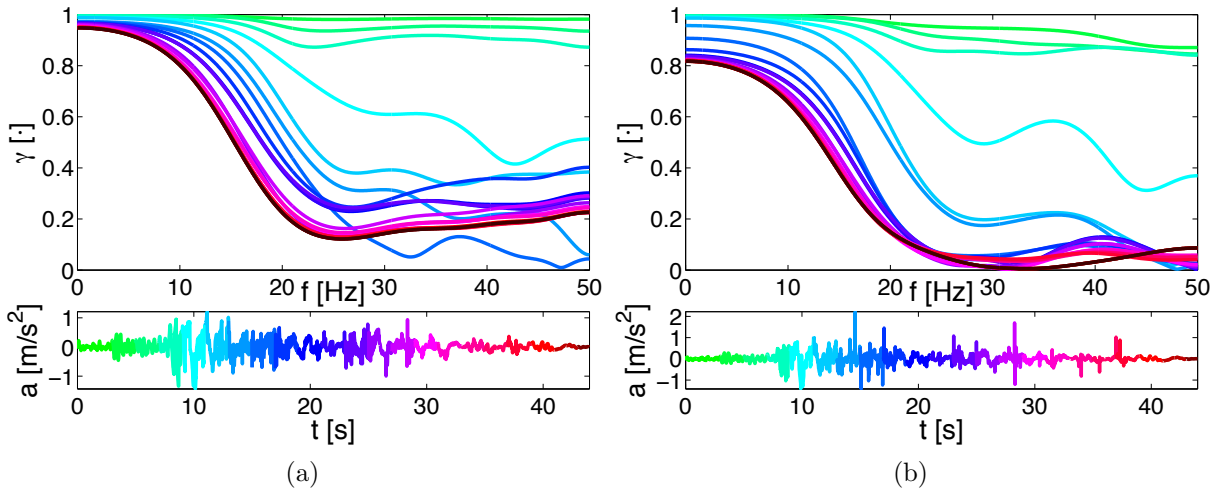


Figure B.9 – Coherency between 1D and 2D models with incremental time windows : a) at surface and b) at $z=9$ m (liquefied area)

It is interesting how the loss of coherence at the liquefied area has little incidence in shallower soil, as shown in Figure B.10. While for the liquefied area, the coherence is lost, γ_c is above 0.9, 1m below and above. As seen previously, it appears that the loss of coherency with frequency is constant through depth; except for a more rapid loss near the surface and near the bottom of the deposit.

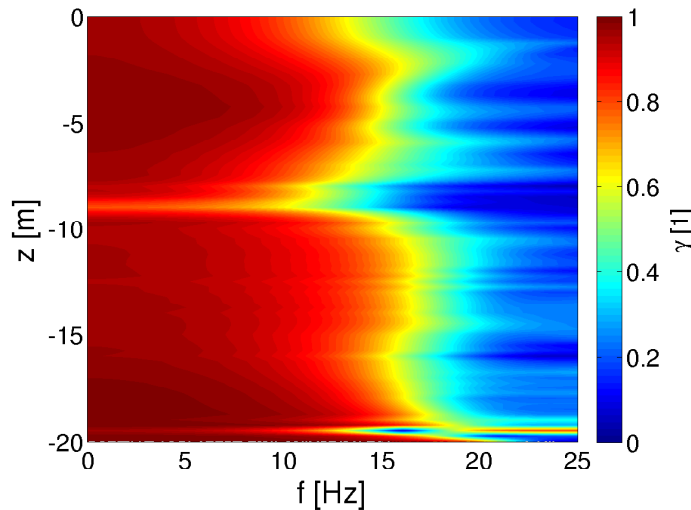


Figure B.10 – Signal coherence between 1D and 2D centerline with depth

B.0.3.2 Signal similarity: Anderson Criteria

Figure B.11 shows the maximum, minimum and mean values of all the frequency bands for the 10 similarity criteria defined by Anderson (2004). Again, the accelerations at the surface

and at 9m depth are used. Most of the criteria show a good fit, with mean values above 9. As expected, the peak ground displacement (PGD) shows the lowest values as only the acceleration was used as input and the velocity and displacement are derived values. Besides PGD, the Fourier spectra (Fs) also presented low values, specially at surface.

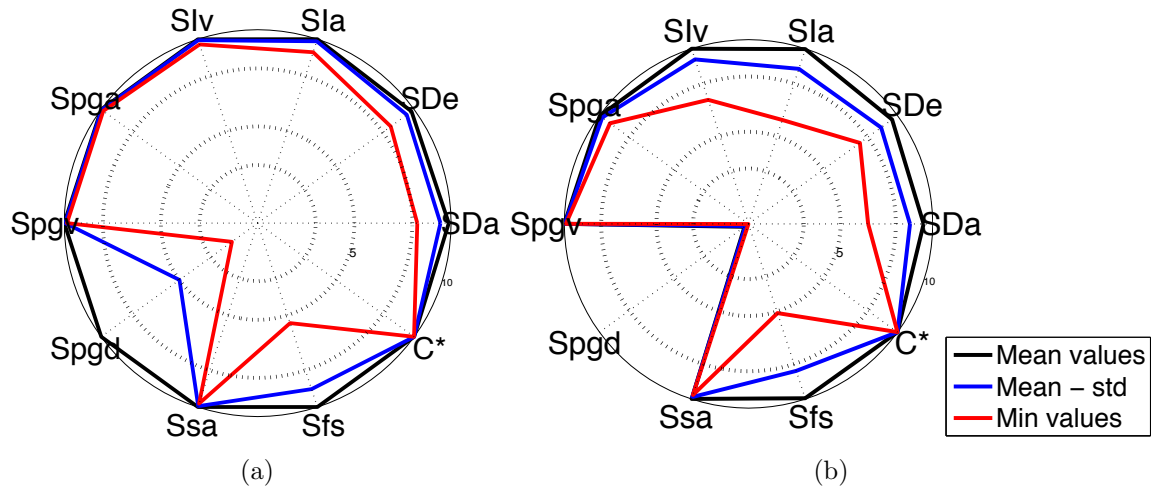


Figure B.11 – Anderson signal similarity between 1D and 2D models : a) at surface and b) at $z=9\text{m}$ (liquefied area)

The mean of all criteria evaluated at different depths is shown in Figure B.12 for all frequency bands used. The last column shows the criteria evaluated at large band (LB), i.e. from 0.05 to 15Hz. As was previously observed, the differences between the models is shown principally at the liquefied area and at the high frequency band. Additionally, two criteria are also shown in Figure B.12 : peak ground displacement (PGD) and Fourier spectra (Fs). The former presents low values practically at all depths and all frequency bands, while the latter, is principally affected for frequencies above 5Hz and for the LB.

B.0.3.3 Interferometry

Finally, the interferometry by cross-correlation with the surface was used in the two models and is shown in Figure B.13. Once more, the effect on liquefaction is clearly visible at 9m for the 1D model and at 8.5m for the 2D model; where the down-going wave (at the positive time delay) is completely attenuated. As liquefaction weakens the soil deposit, the motion is again reflected to the surface. The main difference between the models is in the amplitude of this new upgoing reflection which as it concerns principally high frequencies, is less visible in the 2D model.

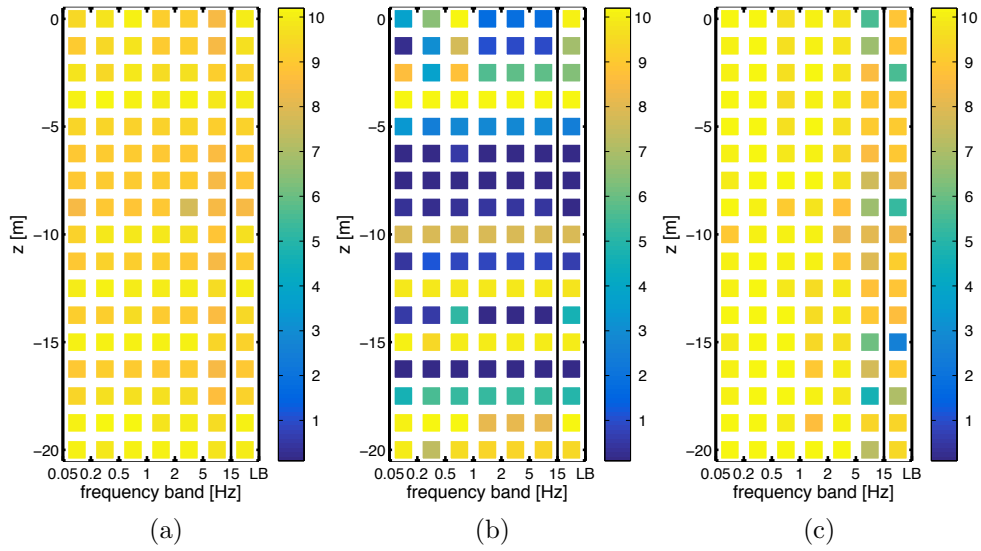


Figure B.12 – Signal similarity between 1D and 2D centerline with depth : a) mean of all criteria, b) PGD and c) F_s

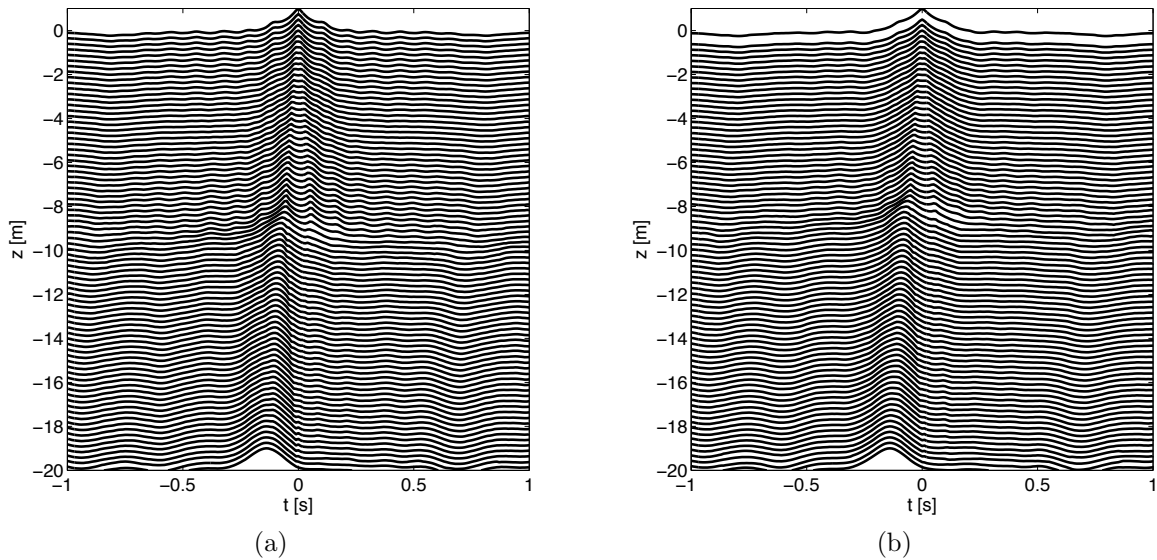


Figure B.13 – Interferometry with strong ground motion - Nonlinear behavior : a) 1D and b) 2D centreline

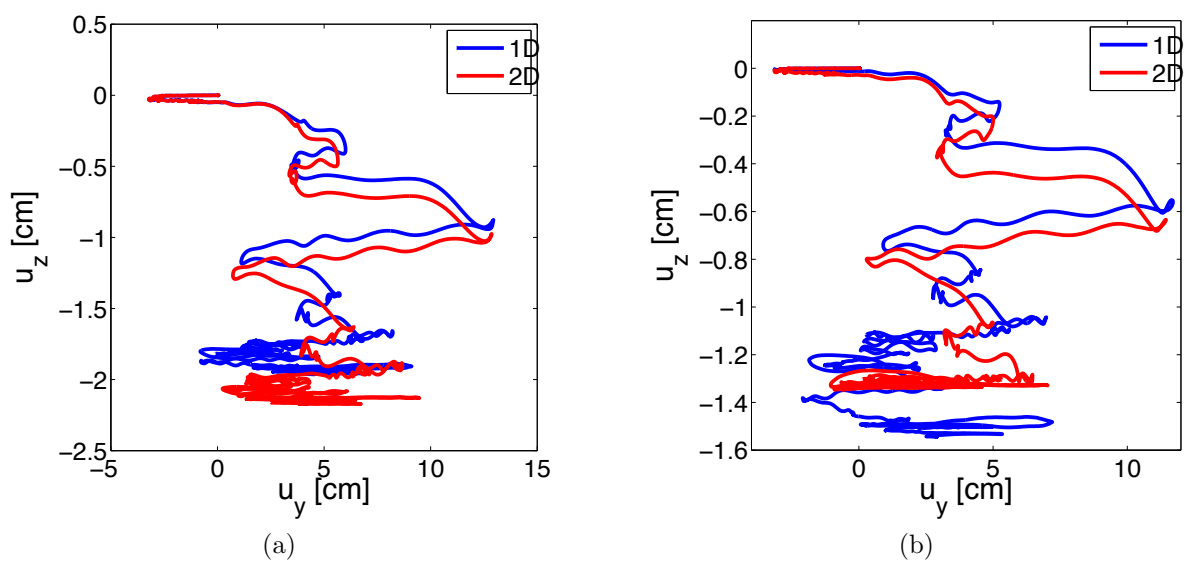


Figure B.14 – Particle trajectory : a) at surface and b) at $z=8$ m (liquefied area)

Appendix C

Signal tools and processing

C.1 Signal processing

Most of the times, recorded ground motions are processed before any engineering and seismological analysis. According to the PEER center, this processing has two major objectives: (1) correction for the response of the strong-motion instrument itself; and (2) reduction of random noise in the recorded time series (Chiou and Youngs, 2008). Different signal processing techniques have been established and several studies on this subject have been published by, among others, Boore et al. (2002); Bazzurro et al. (2004); Boore (2005); Mollova (2007); Graizer (2012).

Three important aspects or steps can be identified : (1) instrument correction, (2) baseline correction and (3) filtering. Most discussions of signal processing are on the latter two. Commonly, velocities and displacements are integrated from the acceleration time vectors which introduces a non-realistic residuals. The aim of baseline correction is to remove this spurious trends by fitting polynomials with different degrees to the velocity or displacement vector and subtracting the derived fit to the acceleration vector. The fits depend on the time points for which different linear, bilinear or quadratic segments are fitted and mostly a qualitative assessment is required based on a constant, or nearly constant, overall level of permanent displacement (Bazzurro et al., 2004).

Concerning filtering, causality in filters alter the phase spectrum in order to preserve the correct arrival time for each frequency component but affects the spectral values at frequencies much higher than the high-pass corner frequency (Boore et al., 2002). Whereas acausal filtering results in fewer phase distortions which leaves the phase spectrum unaltered but results in spurious pre-event low frequency transients in the time history. Additionally, acausal filtering requires significantly larger quiet periods added (i.e., padding) to maintain compatibility with velocity and displacement time histories and spectra. Boore (2005) recommend to keep the padded portion if motions are used in structural or site response calculations to avoid higher amplitudes for long periods in the response spectra or, conversely, for low frequencies in the Fourier spectra. Globally, the question on whether to use causal or acausal filters depends on the intended use of the data, desirability for compatible processed time series and considerations of computer storage space. For analyses of spatial arrays, where relative timing is important, causal filtering is preferred, as is done in seismological observatories for earthquake locations (Chiou and Youngs, 2008).

Bazzurro et al. (2004) presented a statistical evaluation on the causality of filters, of the filter order and high pass cut-off frequency (f_{HP}) and of the residual displacement offset. Only

the Butterworth filter was used. They found that neither causality nor the filter order affect statistically the amplitude of the response spectra even if causal filters result in a slightly larger variability in both elastic and inelastic response. However, when causal filters are used PGV and PGD are on average reduced up to 10% and 15%, respectively. Differences in PGA, I_A and duration were negligible. Similarly, the order of the filter showed no significant effect on the IM tested. Yet, as expected, increasing f_{HP} caused a decrease in PGV of 5% and in PGD of 15-20%. With respect to the residual displacement, when it is preserved, the generated inelastic response spectra are consistently higher than those caused by records with offset removed. Furthermore, PGV and PGD are considerably larger when residual displacements are preserved (5-20% and 50-60%, correspondingly).

Mollova (2007) investigated the effect of different types of causal filters with different orders on six intensity measures (IM): PGA, PGV, PGD, I_A , T_p and $D_{5, 95}$. All parameters except to T_p showed a dependence on the choice of the filter. $D_{5, 95}$ presented small changes whereas the peak values and I_A changed significantly. For instance, a 20% decrease on PGA was observed with increasing the passband ripple used for Chebyshev filter. A rather small suite was used thus more studies should be performed to verify these findings. The sensitivity on the filtering method presented by Pacific Engineering at the NGA COSMOS joint working group meeting showed that for most of the nearly 1000 components studied the elastic response spectra differences associated with the different filtering methods are small and they do not appear to result in systematic high or low bias of response spectra within the common pass band (Chiou and Youngs, 2008).

Most processing schemes are still subjective, non-unique and uncertain (Boore, 2005). For instance, corner frequencies are often selected by visual examination of the Fourier amplitude spectra, time points and polynomial orders for baseline corrections are hand picked and the length of padding is subjected to numerical computational cost. According to Bazzurro et al. (2004), unless there are independent sources of information, such as co-located Global Positioning System (GPS) sensors for the case of recovering static displacements, or estimates of low-frequency noise levels for the case of high-pass filtering, the selection of processing parameters relies on judgment.

In the present study, the following signal data processing was established. It is a collection of techniques used by the PEER center, the California Institute of Technology and the US Geological Survey (USGS), among others (Wang, 1996; Withers et al., 1998; Chiou and Youngs, 2008). The procedure is based on near-field pulse-like time histories associated with a

strong ground motion. The important small frequency components are recovered by the data processing technique developed by [Iwan and Chen \(1995\)](#). All signal motions are processed before being introduced in the numerical model and a visual inspection was performed in the time histories for acceleration, velocity and displacement. The main steps are:

1. Apply a 4th order [Butterworth \(1930\)](#) band pass filter between 0.01 - 25Hz (zero-phase digital filter) to the acceleration time history. This filter is smooth compared to other known transforms such as the Ormsby or cosine taper, as it never goes to zero and does not reject (filter out) completely frequency content of the signal higher than the certain level ([Graizer, 2012](#)).
2. Apply a least-mean-square linear fit in order to eliminate any uncertainty in the instrument centering.
3. Integrate the acceleration time history to obtain a zero initial velocity vector. The trapezoidal integration rule is used.
4. Apply a segmented polynomial baseline fit to the velocity to remove any non-physical trends. Since the ground velocity physically starts and ends at zero, the baseline is fitted to the initial and final portions of the velocity time history. The start and end point are found via an LTA/STA ratio ([Withers et al., 1998](#)). These two polynomials are continuously connected by the lowest order (smoothest) polynomial baseline. The objective of this correction is to diminish the small frequency noise or drift introduced in the signal recording and playback process ([Wang, 1996](#), According to Report No. EERL 96-04 of California Institute of Technology).
5. Integrate the baseline corrected velocity time history to obtain a displacement time history, assuming zero initial displacement. And differentiate the velocity to obtain the corrected acceleration time history. A central difference differentiation scheme is used.
6. Apply a Hanning taper of 2.5% as the signal is theoretically infinite but signal analysis is only defined on finite signals. The taper consist on multiplying the first and last parts by a cosine-type signal in order to obtain an acceleration time history starting and ending in zero.
7. Apply a multiplicative filter that accounts for the diminution of the low-frequency motions. The high pass filter used is the Butterworth filter. Similar to [Boore et al. \(2002\)](#), the order

used is 4. The corner frequency is calculated as:

$$f_c = \frac{1}{D_T [H_0^2 / (1 - H_0^2)]^{1/2n}} \quad (\text{C.1})$$

where D_T is the motion duration in seconds and H_0 is the modulus of the transfer function corresponding to frequency $1/D_T$.

An example of the baseline correction scheme is shown in Figure C.1. It can be seen that the acceleration, velocity and displacement are zero at the end of the corrected signal. Although, there are some motions where the proposed scheme deteriorates the displacement vector like in Figure C.2 due to the high amplitude observed at the end of the signal.

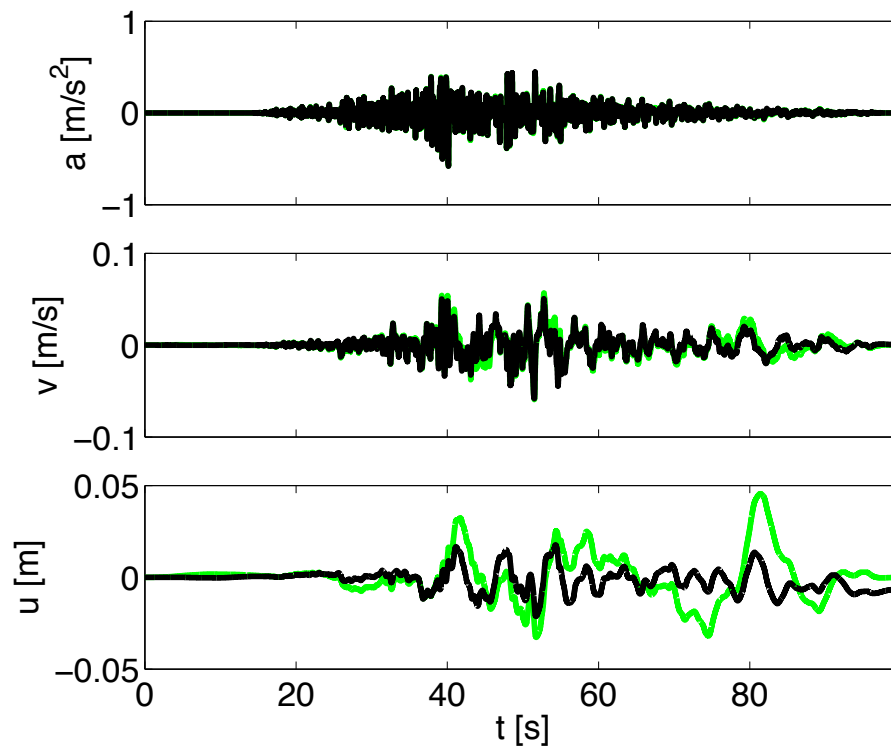


Figure C.1 – Signal processing scheme

C.2 Earthquake parameters

Motions that have sufficient strength to affect people and their environment are described as strong ground motions and are the primary interest of earthquake engineers. However, evaluation of the earthquakes' effect at a particular site requires quantitative descriptions that given the complexity, require a large amount of information. The primary three characteristics of

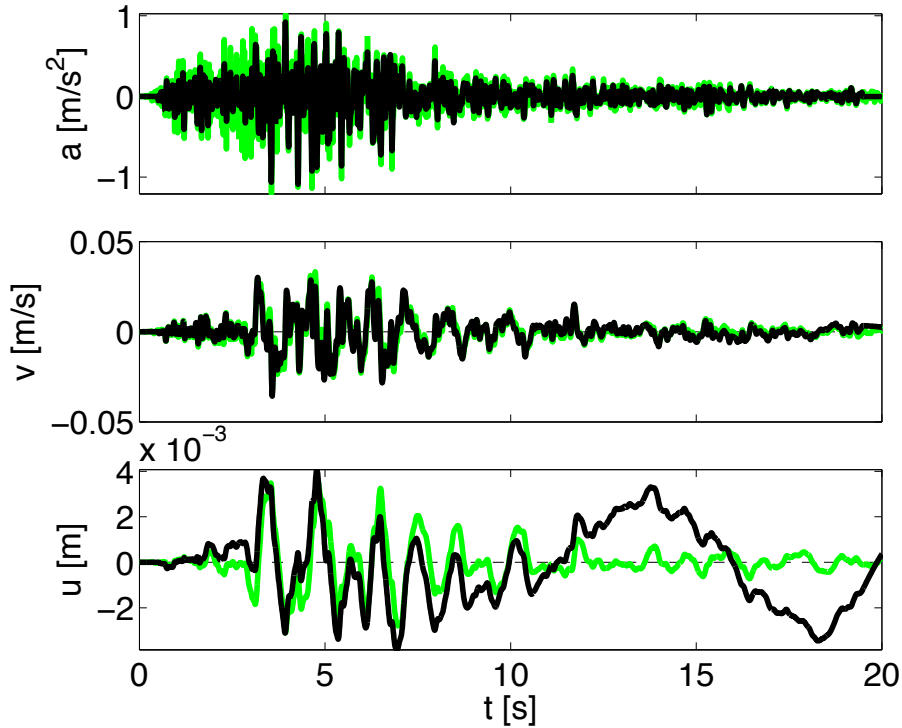


Figure C.2 – Signal processing scheme

strong ground motions are: amplitude, frequency content and duration. The ground-motion parameters often called intensity measures (IM) provide information of one or more characteristics. To involve the liquefaction hazard and assess its effects, it is important to perfectly characterize the ground motion by an IM efficient, sufficient and predictable (Kramer and Mitchell, 2006). In this section, some parameters are defined, taken from Lopez-Caballero and Modaressi (2011b). Where $a(t)$ is the acceleration as a function of time (t), $v(t)$ the velocity, D_T the duration of the strong motion, PSV the pseudo-velocity spectra and f_i and C_i are the i th frequency and Fourier amplitude respectively.

1. Peak Horizontal Acceleration (PHA) [g]

The largest absolute value of horizontal acceleration obtained from the accelerogram. It is often presented in units of gravity acceleration: $g = 9.81 m/s^2$. PHA can be correlated to earthquake intensity and with peak vertical acceleration (PVA) although, PHA is a parameter that does not provides information neither of the frequency content nor the duration of motion. The simplified procedure for liquefaction evaluation developed by Seed and Idriss (1971) relates the maximum shear stress to the PHA but it is also required a scaling factor to include additional information about the magnitude of the ground motion.

2. Peak horizontal velocity (PHV) [cm/s]

It also characterizes ground-motion amplitude. This peak type intensity measure is defined by the maximum absolute velocity of the ground motion signal. PHV is more likely to characterize ground-motion accurately at intermediate frequencies because it is less sensitive to the higher frequency components [Kramer \(1996\)](#).

3. Predominant Period (T_p) [s]

A spectral parameter that provides a useful representation of the frequency content. It is defined as the period of vibration corresponding to the maximum value of the Fourier amplitude spectrum. Although radically different frequency content motions can have the same T_p value.

4. Mean Period (T_m) [s]

[Rathje et al. \(1998\)](#) proposed the mean period (T_m) as it better represents the overall frequency content of a ground motion and can be estimated more reliably with empirical ground motion data compared to T_p . It is defined as:

$$T_m = \frac{\sum_i^n C_i^2 \frac{1}{f_i}}{\sum_i^n C_i^2} \text{ for } 0.25Hz \leq f_i \leq 20Hz \quad (\text{C.2})$$

5. Period of equivalent harmonic wave ($T_{V/A}$) [s]

In general, PGA and PGV ratio increases with increasing magnitude and source-to-site distance ([Kramer, 1996](#)). As an alternative to T_p and T_m , [Green and Cameron \(2003\)](#) used the PGA and PGV values of a given ground motion to calculate the period corresponding to the intersection of the constant spectral acceleration and velocity regions of a 5% damped Newmark-Hall type spectrum. $T_{V/A}$ is computed by:

$$T_{V/A} = 2\pi \frac{\alpha_V(\xi = 5\%) PGV}{\alpha_A(\xi = 5\%) PGA} \text{ where } \frac{\alpha_V(\xi = 5\%)}{\alpha_A(\xi = 5\%)} = \frac{1.65}{2.12} \quad (\text{C.3})$$

α_V and α_A are the Newmark-Hall median spectrum amplification factors for horizontal motions corresponding to the constant velocity and constant acceleration regions of 5% damped response spectra. An interesting aspect, is the closer relation of this IM with the amplification of soft soil sites. To analyze this aspect, [Green and Cameron \(2003\)](#) presented a quadratic fit to the PGA/PHA ratio and the $T_{V/A}/T_s$ ratio, where T_s is the

fundamental elastic period of the soil deposit. Analogous to damped SDOF oscillators, as the $T_{V/A}/T_s$ ratio approaches 1 (i.e., resonance), the dynamic response of the profiles increase, resulting in an increase in the PGA/PHA ratio.

6. Arias Intensity (I_A) [m/s]

According to Arias (1970), the orthogonal component of horizontal acceleration is proportional to the sum of the total energies per unit weight stored in the oscillators of a population of undamped linear oscillators, uniformly distributed with respect to their natural frequencies, at the moment the earthquake ends. I_A integrates the root-mean-square acceleration over the entire duration.

$$I_{Arias} = \frac{\pi}{2g} \int_0^{D_T} a(t)^2, dt \quad (C.4)$$

The Arias intensity is an integral component and therefore reflects the three ground motion characteristics: amplitude, frequency and duration. Kayen and Mitchell (1997) developed a procedure to evaluate liquefaction hazard using I_A to characterize both loading and soil resistance. The SPT and CPT resistances were empirically correlated to the intensity measure and the liquefaction initiation potential was expressed by a factor of safety. The Arias intensity procedure benefits from the fact that only one piece of ground motion information is required as compared to the cyclic stress method that requires two (Kramer and Mitchell, 2006).

7. Cumulative absolute velocity (CAV) [m/s]

Similar to I_A , (Reed and Kassawara, 1990) proposed CAV as another time integral intensity measure of the acceleration throughout the earthquake shaking. Because of that, it includes the effect of the amplitude and the frequency. It is defined as the area under the absolute accelerogram:

$$CAV = \int_0^{D_T} |a(t)| dt \quad (C.5)$$

8. Cumulative absolute velocity $5cm/s^2$ (CAV_5) [m/s]

The cumulative absolute velocity after application of $5cm/s^2$ threshold acceleration is a time integral modified intensity measure.

$$CAV_5 = \int_0^{D_T} \langle \chi \rangle |a(t)| dt \text{ where } \langle \chi \rangle = \begin{cases} 0 & \text{for } |a(t)| < 5cm/s^2 \\ 1 & \text{for } |a(t)| \geq 5cm/s^2 \end{cases} \quad (C.6)$$

[Kramer and Mitchell \(2006\)](#) evaluated the efficiency, sufficiency and accuracy of nearly 300 intensity measures, CAV_5 was the intensity measure that best predicted the generation of excess pore pressure, hence liquefaction potential of saturated sandy soils.

9. Cosenza & Manfredi dimensionless index (I_D) [1]

Regarding structural demand, ([Cosenza and Manfredi, 1997](#)) showed that the intensity measure that is better correlated to plastic cycles demand is the Cosenza & Manfredi dimensionless index defined as:

$$I_D = \frac{2g}{\pi} \frac{I_A}{PHA \cdot PGV} \quad (C.7)$$

10. Significant duration ($D_{5, 95}$) [s]

The duration of strong-motion acceleration is defined by [Trifunac and Brady \(1975\)](#) as the time interval during which the central 90% of the contribution to I_A takes place. Although this parameter is not sufficient, as it does not account for neither the energy nor the frequency content of the motion; it is useful to identify the primary location of the energy in specially long motions.

$$D_{5, 95} = t_{I_A}^{95} - t_{I_A}^5 \quad (C.8)$$

11. Strain Energy Density ($StED$) [Joule/ m^3]

The dissipated strain energy density (or unit energy) is a recently proposed intensity measure that accounts not only for earthquake characteristics (induced stress) but also its consequent soil deformation. It is defined as the cumulative enclosed area of the earthquake-induced shear-strain loops and is proved to have a unique relationship with excess pore water pressure. CAV_5 and the other intensity measures depend only in earthquake stress history, while seismically-induced pore pressure generates due to plastic deformation and irrecoverable volumetric strains. $StED$ incorporates both stress and strain histories. [Jafarian et al. \(2011\)](#) provided an equation obtained by regression analysis:

$$\log(StED) = 2.502(M_w - 4.9) - 4.803\log(R_{clstd}) - 0.023\sigma'_{v0} \quad (C.9)$$

where $StED$ is the imparted strain energy density in $kJoule/m^3$, $R_{clst, d}$ is the closest distance from source in km, M_w is the moment magnitude and σ'_{v_0} is the effective overburden pressure in kPa. However, estimation of $StED$ for a particular soil deposit is difficult and needs a great numerical effort.

C.3 Anderson criteria

[Anderson \(2004\)](#) proposed a similarity score based on 10 criteria that compare two signals in terms of different intensity measures e.g., duration, amplitude, spectral shape and energy. Additionally, the comparison is made for different frequency bands. In the present study, as the criteria is used for signal motions issued after a numerical analysis, the frequency bands have been modified: i.e. the highest frequency evaluated is 15Hz (and not 50Hz, as originally suggested). The spacing of the frequency bands is approximately logarithmic which increases the weight on the lower frequencies, of higher importance for the response of large structures. The criteria and frequency bands used in this study are shown in tables [C.1](#) and [C.2](#), respectively.

Number	Symbol	Similarity of:
C1	SDa	Arias duration
C2	SDe	Energy duration
C3	SIa	Arias Intensity
C4	SIv	Energy Integral
C5	Spga	Peak Acceleration
C6	Spgv	Peak Velocity
C7	Spgd	Peak Displacement
C8	Ssa	Response Spectra
C9	Sfs	Fourier Spectra
C10	C*	Cross Correlation

Table C.1 – Anderson criteria for accelerogram similarity ([Anderson, 2004](#))

As some intensity measures need the velocity and displacement time histories, a trapezoidal integration rule is applied to the acceleration. However, if these vectors can be obtained directly from the numerical analysis, its use is preferable in order to avoid integration drifting. Afterwards, all the three vectors are band pass filtered and the 10 IM are evaluated. Finally, the similarity is given by equation [C.10](#). The use of this function has several advantages. For instance, it permits to have values between 0 and 10 which is a comfortable range; additionally, it is symmetrical though it has the same score whether motion 1 is bigger than motion 2 or vice versa. However, the main advantage is that it penalizes severely differences of a factor greater

Band	Frequency limits [Hz]
B1	0.05 - 0.1
B2	0.1 - 0.2
B3	0.2 - 0.5
B4	0.5 - 1.0
B5	1.0 - 2.0
B6	2.0 - 5.0
B7	5.0 - 15.0
B8	0.05 - 15.0

Table C.2 – Frequency bands used for Anderson criteria. Modified from (Anderson, 2004)

than 2.5 which “should not be considered useful fits for engineering applications” (Anderson, 2004). On the other hand, small differences have less effect; for example, when the difference is half the value of the smaller IM , the score is 8. Two alternatives were proposed by the author to define the final score : $S1$ defined as the average of all 10 scores in each of the 9 frequency bands; or, $S2$, the average of all scores evaluated without band pass filtering. The former is preferable as it gives more importance to low frequencies and can provide more information of the differences between the motions.

$$S_i(IM_1, IM_2) = 10 \exp \left\{ - \left[\frac{(IM_1 - IM_2)}{\min(IM_1, IM_2)} \right]^2 \right\} \quad (C.10)$$

C.4 Coherency

An alternative measure to compare two signals is the coherency which describes the similarity between the motions in the frequency domain, as follows:

$$\gamma_{jk}(\omega) = \frac{S_{jk}(\omega)}{\sqrt{S_{jj}(\omega) \cdot S_{kk}(\omega)}} \quad (C.11)$$

where the smoothed cross spectrum ($S_{jk}(\omega)$) and autospectra $S_{jj}(\omega)$ and $S_{kk}(\omega)$ are the Fourier transforms of the cross-covariance (C_{jk}) and the autocovariances (C_{jj} and C_{kk}), respectively. The coherency describes the degree of positive or negative correlation between the amplitudes and phase angles. A value of 1 indicates full coherence, i.e. perfect correlation. The modulus of the coherency is called the lagged coherency ($|\gamma|$). $|\gamma|$ is often used to evaluate the local spatial variation due to heterogeneity in the soil deposit while isolating the wave passage effect. Several empirical and semi-empirical models have been developed to relate the spatial coherency

from data recorded at dense instrument arrays (Zerva and Zervas, 2002; Zentner, 2013, among others)

C.5 Ground motion database

The ground motions were selected based on 2 main criteria. First, a wide range of characteristics: i.e. $6.2 < M_w < 7.7$; $10 < R < 28\text{km}$; $300 < V_{s30} < 800\text{m/s}$. Second, the number of standard deviations a specific ground motion parameter (or intensity measure, IM) is above the predicted mean, called ε , had to be greater than 0.4. Special attention was given to avoid bias in structural response, thus, the median response spectra of the 25 ground motion records scaled based on the five different IMs were verified to be very similar.

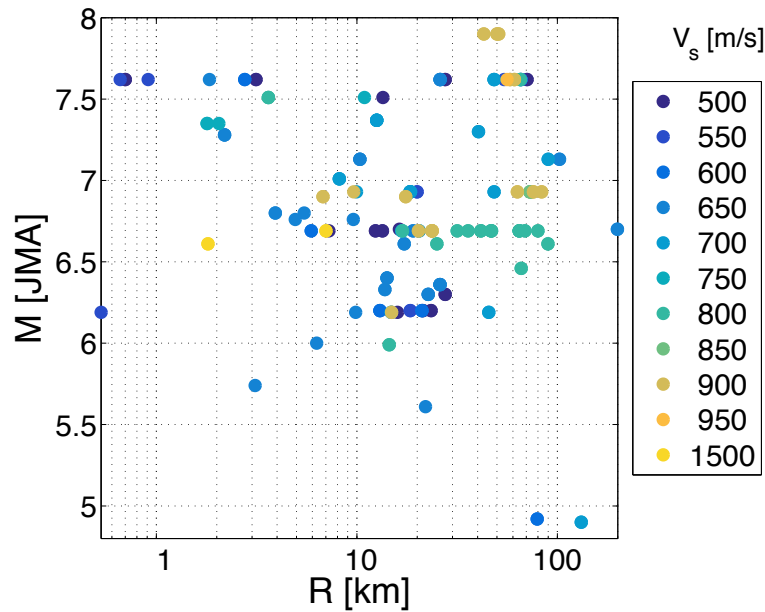


Figure C.3 – Magnitude, Distance and Shear-wave velocity

Table C.3 – Selected Ground motion records from NGA database

#	Event	Year	RSN*	M_w	R^\dagger [km]	V_{s30} [m/s]	I_A [m/s]	D_{5-95} [s]
1	Helena Montana-01	1935	1	6.0	2.07	593.35	0.1	2.5
2	Parkfield	1966	33	6.19	15.96	527.92	0.5	5.5
3	San Fernando	1971	59	6.61	89.37	813.48	0.0	10.4
4	San Fernando	1971	72	6.61	19.45	600.06	0.3	13.0
5	San Fernando	1971	73	6.61	17.22	670.84	0.2	11.8

Continued on next page

#	Event	Year	RSN*	M_w	R^\dagger [km]	V_{s30} [m/s]	I_A [m/s]	D_{5-95} [s]
6	San Fernando	1971	77	6.61	0.0	2016.13	8.9	7.3
7	Gazli USSR	1976	126	6.8	3.92	259.59	5.7	7.0
8	Tabas Iran	1978	143	7.35	1.79	766.77	11.8	16.5
9	Coyote Lake	1979	150	5.74	0.42	663.31	0.8	3.5
10	Victoria Mexico	1980	265	6.33	13.8	471.53	2.0	8.2
11	Irpinia Italy-01	1980	286	6.9	17.51	496.46	0.2	27.0
12	Irpinia Italy-01	1980	292	6.9	6.78	382.0	1.4	15.2
13	Coalinga-01	1983	369	6.36	25.98	648.09	0.3	13.6
14	Morgan Hill	1984	451	6.19	0.18	561.43	3.9	4.1
15	Morgan Hill	1984	454	6.19	14.83	729.65	0.1	8.6
16	Morgan Hill	1984	455	6.19	14.9	1428.14	0.1	9.5
17	Morgan Hill	1984	459	6.19	9.85	663.31	0.9	7.3
18	Morgan Hill	1984	476	6.19	45.47	713.59	0.1	9.1
19	Nahanni Canada	1985	495	6.76	2.48	605.04	3.9	7.5
20	Nahanni Canada	1985	496	6.76	0.0	605.04	0.9	7.3
21	Whittier Narrows-01	1987	663	5.99	14.5	680.37	0.3	9.8
22	Loma Prieta	1989	755	6.93	19.97	561.43	1.5	15.7
23	Loma Prieta	1989	763	6.93	9.19	729.65	0.9	5.0
24	Loma Prieta	1989	765	6.93	8.84	1428.14	1.7	6.5
25	Loma Prieta	1989	781	6.93	48.24	586.08	0.1	13.4
26	Loma Prieta	1989	788	6.93	72.9	895.36	0.1	12.1
27	Loma Prieta	1989	789	6.93	83.37	1315.92	0.1	10.6
28	Loma Prieta	1989	795	6.93	75.96	1249.86	0.1	11.9
29	Loma Prieta	1989	797	6.93	74.04	873.1	0.1	14.2
30	Loma Prieta	1989	804	6.93	63.03	1020.62	0.1	12.1
31	Loma Prieta	1989	809	6.93	12.15	713.59	1.6	9.0
32	Loma Prieta	1989	810	6.93	12.04	713.59	2.7	9.7
33	Cape Mendocino	1992	828	7.01	0.0	422.17	3.8	17.7
34	Landers	1992	879	7.28	2.19	1369.0	7.0	13.8
35	Big Bear-01	1992	925	6.46	59.74	509.1	0.1	25.4
36	Northridge-01	1994	943	6.69	65.84	501.75	0.1	13.2
37	Northridge-01	1994	946	6.69	46.65	572.57	0.0	15.2

Continued on next page

#	Event	Year	RSN*	M_w	R^\dagger [km]	V_{s30} [m/s]	I_A [m/s]	D_{5-95} [s]
38	Northridge-01	1994	952	6.69	12.39	545.66	3.0	7.7
39	Northridge-01	1994	957	6.69	15.87	581.93	0.3	11.6
40	Northridge-01	1994	989	6.69	9.87	740.05	0.7	9.0
41	Northridge-01	1994	1011	6.69	15.11	1222.52	0.2	8.7
42	Northridge-01	1994	1012	6.69	9.87	706.22	1.1	8.0
43	Northridge-01	1994	1013	6.69	0.0	628.99	1.8	6.5
44	Northridge-01	1994	1021	6.69	31.27	600.06	0.1	14.1
45	Northridge-01	1994	1033	6.69	46.31	485.67	0.1	17.6
46	Northridge-01	1994	1041	6.69	35.53	680.37	0.3	10.8
47	Northridge-01	1994	1050	6.69	4.92	2016.13	0.9	4.3
48	Northridge-01	1994	1052	6.69	5.26	508.08	1.8	10.1
49	Northridge-01	1994	1060	6.69	79.83	509.1	0.1	15.4
50	Northridge-01	1994	1074	6.69	41.26	421.0	0.1	15.9
51	Northridge-01	1994	1078	6.69	1.69	715.12	0.9	8.3
52	Northridge-01	1994	1080	6.69	0.0	557.42	4.1	6.7
53	Northridge-01	1994	1091	6.69	23.1	996.43	0.4	8.3
54	Northridge-01	1994	1096	6.69	64.46	662.7	0.1	18.4
55	Kozani Greece-01	1995	1126	6.4	14.13	649.67	0.3	8.6
56	Kocaeli Turkey	1999	1148	7.51	10.56	523.0	0.3	11.1
57	Kocaeli Turkey	1999	1161	7.51	7.57	792.0	0.5	8.2
58	Kocaeli Turkey	1999	1165	7.51	3.62	811.0	0.8	15.1
59	Chi-Chi Taiwan	1999	1197	7.62	3.12	542.61	5.9	8.7
60	Chi-Chi Taiwan	1999	1227	7.62	0.7	553.43	1.1	32.0
61	Chi-Chi Taiwan	1999	1234	7.62	27.57	665.2	1.0	31.4
62	Chi-Chi Taiwan	1999	1257	7.62	52.46	1525.85	0.2	25.9
63	Chi-Chi Taiwan	1999	1347	7.62	57.69	996.51	0.1	23.3
64	Chi-Chi Taiwan	1999	1472	7.62	54.28	558.76	0.3	31.8
65	Chi-Chi Taiwan	1999	1485	7.62	26.0	704.64	1.4	11.3
66	Chi-Chi Taiwan	1999	1492	7.62	0.0	579.1	2.9	16.7
67	Chi-Chi Taiwan	1999	1510	7.62	0.89	573.02	3.0	31.2
68	Chi-Chi Taiwan	1999	1511	7.62	2.74	614.98	3.7	29.5
69	Chi-Chi Taiwan	1999	1518	7.62	55.14	999.66	0.1	22.7

Continued on next page

#	Event	Year	RSN*	M_w	R^\dagger [km]	V_{s30} [m/s]	I_A [m/s]	D_{5-95} [s]
70	Chi-Chi Taiwan	1999	1549	7.62	1.83	511.18	9.3	30.8
71	Chi-Chi Taiwan	1999	1555	7.62	70.61	537.92	0.3	21.7
72	Chi-Chi Taiwan	1999	1577	7.62	62.67	704.96	0.1	36.7
73	Chi-Chi Taiwan	1999	1585	7.62	43.99	728.01	0.0	35.5
74	Chi-Chi Taiwan	1999	1587	7.62	62.11	845.34	0.1	34.6
75	Manjil Iran	1990	1633	7.37	12.55	723.95	7.5	29.1
76	Sierra Madre	1991	1642	5.61	17.79	680.37	0.4	3.7
77	Hector Mine	1999	1763	7.13	89.98	724.89	0.0	23.3
78	Hector Mine	1999	1764	7.13	102.4	480.22	0.0	27.0
79	Hector Mine	1999	1787	7.13	10.35	726.0	1.9	11.7
80	Anza-02	2001	1949	4.92	76.93	581.0	0.0	7.5
81	Gilroy	2002	2032	4.9	129.58	597.34	0.0	8.1
82	Nenana Mountain Alaska	2002	2091	6.7	199.27	424.9	0.0	21.7
83	Denali Alaska	2002	2107	7.9	49.94	399.35	0.2	24.3
84	Denali Alaska	2002	2111	7.9	42.99	341.56	0.1	23.1
85	Chi-Chi Taiwan-03	1999	2461	6.2	23.44	542.61	0.3	13.8
86	Chi-Chi Taiwan-03	1999	2495	6.2	21.34	496.21	1.8	5.2
87	Chi-Chi Taiwan-03	1999	2626	6.2	18.47	573.02	0.2	8.9
88	Chi-Chi Taiwan-03	1999	2627	6.2	13.04	614.98	1.0	12.5
89	Chi-Chi Taiwan-03	1999	2661	6.2	21.11	652.85	0.3	10.0
90	Chi-Chi Taiwan-06	1999	3300	6.3	27.57	553.43	0.3	12.6
91	Chi-Chi Taiwan-06	1999	3507	6.3	22.69	511.18	0.7	13.9

*Record sequence number at the NGA database (<http://ngawest2.berkeley.edu/>)

† Joyner-Boore source-to-site distance.

Bibliography

- Abrahamson, N. A., Silva, W. J., and Kamai, R. (2013). Update of the AS08 ground-motion prediction equations based on the NGA-West2 data set. PEER Report 2013/04, Pacific Earthquake Engineering Research Center.
- Anderson, D., Shin, S., and Kramer, S. (2011). Nonlinear, effective-stress ground motion response analyses following AASHTO specifications for LRFD seismic bridge design. *Transportation Research Record: Journal of the Transportation Research Board*, 2251:144–154, doi:10.3141/2251-15.
- Anderson, J. (2004). Quantitative measure of the goodness-of-fit of synthetic seismograms. *13th World Conference on Earthquake Engineering*, 243.
- Arias, A. (1970). *Seismic Design of Nuclear Power Plants*, chapter A mesure of earthquake intensity, pages 438–483. MIT Press, Cambridge, Massachusetts. Hansen, Robert J. (editor).
- Asaoka, A. and Matsuo, M. (1983). A simplified procedure for probability based $\phi_u=0$ stability analysis. *Soils and Foundations*, 23(1):8–18.
- Assimaki, D., Li, W., Steidl, J., and Schmedes, J. (2008). Quantifying nonlinearity susceptibility via site-response modeling uncertainty at three sites in the Los Angeles basin. *Bulletin of the Seismological Society of America*, 98(5):2364–2390, doi:10.1785/0120080031.
- Assimaki, D., Pecker, A., Popescu, R., and Prevost, J. (2003). Effects of spatial variability of soil properties on surface ground motion. *Journal of Earthquake Engineering*, 7(sup001):1–44, doi:10.1080/13632460309350472.
- Aubry, D., Chouvet, D., Modaressi, A., and Modaressi, H. (1985). Gefdyn 5, logiciel d’analyse du comportement statique et dynamique des sols par elements finis avec prise en compte du couplage sol-eau-air.
- Aubry, D., Hujeux, J., Lassoudiere, F., and Meimon, Y. (1982). A double memory model with multiple mechanisms for cyclic soil behavior. In *International Symposium on Numerical Modeling in Geomechanics*, pages 3–13, Balkema.

- Aubry, D. and Modaressi, A. (1996). *GEFDyn - manuel scientifique*. Ecole Centrale Paris, France: LMSSMat.
- Aubry, D. and Modaressi, H. (1985). Seismic wave propagation in soils including non-linear and pore pressure effects. In *Recent Advances in Earthquake Engineering and Structural Dynamics*, pages 209–224, France. Ouest Editions. Edited by V. Davidovici.
- Aubry, D. and Modaressi, H. (1989). Un modele de sols satures en dynamique non lineaire. *Revue Française de Geotechnique*, 46:43–75.
- Baker, J. W. (2007). Quantitative classification of near-fault ground motions using wavelet analysis. *Bulletin of the Seismological Society of America*, 97(5):1486–1501, doi:10.1785/0120060255.
- Banerjee, S., Carlin, B., and Gelfand, A. (2003). *Hierarchical Modeling and Analysis for Spatial Data*. Chapman and Hall/CRC.
- Bartlett, M. and Besag, J. (1969). Correlation Properties of Some Nearest-Neighbor Models. *Bulletin of the International Statistical Institute*, 43(2):191–193.
- Bazzurro, P., Sjoberg, B., Luco, N., Silva, W., and Darragh, R. (2004). Effects of strong motion processing procedures on time histories, elastic and inelastic spectra. In *Invited Workshop on Strong-Motion Record Processing*, page 19, Richmond, Calif, USA. The Consortium of Organizations for Strong-Motion Observation Systems (COSMOS).
- Been, K. and Jefferies, M. (1985). A state parameter for sands. *Géotechnique*, 35(2):99–112, doi:10.1680/geot.1985.35.2.99.
- Beresnev, I. and Wen, K. (1996). Nonlinear site response: a reality? *Bulletin of the Seismological Society of America*, 86(6):1964–1978.
- Besag, J. (1972). Nearest-Neighbour Systems and the Auto-Logistic Model for Binary Data. *Journal of the Royal Statistical Society*, 34(1):75–83.
- Biarez, J. and Hicher, P. (1994). *Elementary mechanics of soil behaviour, saturated and remolded soils*. Balkema, Amsterdam, Netherlands.
- Bielak, J. and Christiano, P. (1984). On the effective seismic input for non-linear soil-structure interaction systems. *Earthquake Engineering and Structural Dynamics*, 12(1):107–119, doi:10.1002/eqe.4290120108.

- Bielak, J., Loukakis, K., Hisada, Y., and Yoshimura, C. (2003). Domain reduction method for three-dimensional earthquake modeling in localized regions, part I: Theory. *Bulletin of the Seismological Society of America*, 93(2):817–824, doi:10.1785/0120010252.
- Biot, M. (1941). General theory of three-dimensional consolidation. *Journal of Applied Physics*, 12(2):155–165.
- Bird, J. and Bommer, J. (2004). Earthquake losses due to ground failure. *Engineering Geology*, 75(2):147–179, doi:10.1016/j.enggeo.2004.05.006.
- Bird, J., Bommer, J., Crowley, H., and Pinho, R. (2006). Modelling liquefaction-induced building damage in earthquake loss estimation. *Soil Dynamics and Earthquake Engineering*, 26(1):15–30, doi:10.1016/j.soildyn.2005.10.002.
- Boatwright, J. and Fletcher, J. B. (1984). The partition of radiated energy between p and s waves. *Bulletin of the Seismological Society of America*, 74(2):361–376.
- Bonilla, F., Archuleta, R. J., and Lavallee, D. (2005). Hysteretic and Dilatant Behavior of Cohesionless Soils and Their Effects on nonlinear Site Response : Field Data Observations and Modeling. *Bulletin of the Seismological Society of America*, 95(6):2373–2395.
- Bonilla, F., Tsuda, K., Pulido, N., Régnier, J., and Laurendeau, A. (2011a). Nonlinear site response evidence of K-NET and KiK-net records from the 2011 off the Pacific coast of Tohoku Earthquake. *Earth Planets Space*, 63(7):785–789.
- Bonilla, L., Gelis, C., and Regnier, J. (2011b). The challenge of nonlinear site response: field data observations and numerical simulations. In *4th IASPEI / IAEE International Symposium: Effects of Surface Geology on Seismic Motion*, page 13, University of California Santa Barbara.
- Boore, D. (2005). On pads and filters: Processing Strong-Motion Data. *Bulletin of the Seismological Society of America*, 95(2):745–750.
- Boore, D., Stephens, C., and Joyner, W. (2002). Comments on baseline correction of digital strong-motion data: Examples from the 1999 Hector mine California earthquake. *Bulletin of Seismological Society of America*, 92(4):1543–1560.
- Boulanger, R., Idriss, I., Stewart, D., Hashash, Y., and Schmidt, B. (1998). Drainage capacity of stone columns or gravel drains for mitigating liquefaction. In Dakoulas, P., Yegian, M., and Holtz, R. D., editors, *Geotechnical Earthquake Engineering and Soil Dynamics III*, volume 1, pages 678–690, Seattle, Washington. ASCE. Geotechnical Special Publication No. 75.

- Bradley, B., Dhakal, R., MacRae, G., and Cubrinovski, M. (2010). Prediction of spatially distributed seismic demands in specific structures: Ground motion and structural response. *Earthquake Engineering and Structural Dynamics*, 39(5):501–520.
- Bradley, B. A., Araki, K., Ishii, T., and Saitoh, K. (2013). Effect of lattice-shaped ground improvement geometry on seismic response of liquefiable soil deposits via 3-D seismic effective stress analysis. *Soil Dynamics and Earthquake Engineering*, 48(1):35–47.
- Brennan, A. J., Thusyanthan, N. I., and Madabhushi, S. P. (2005). Evaluation of shear modulus and damping in dynamic centrifuge tests. *Journal of Geotechnical and Geoenvironmental Engineering*, 131(12):1488–1497.
- Bruggeman, D. (1935). Berechnung Verschiedenez Physikalischer Konstanten Von Heterogenen Substanzen. *Ann. Phys. Lpz.*, 5(24):636. in German.
- Brunini, V. E., Schuh, C. A., and Carter, W. C. (2011). Percolation of diffusionally evolved two-phase systems. *Physical Review E*, 83(2), doi:10.1103/physreve.83.021119.
- Budiman, J. S., Mohammadi, J., and Bandi, S. (1995). Effect of Large Inclusions on Liquefaction of Sand. *Geotech. Spec. Publ.*, 56(1):48–63.
- Bunde, A. and Kantelhardt, J. W. (2005). Diffusion and conduction in percolation systems. In *Diffusion in Condensed Matter*, pages 895–914. Springer Science Business Media.
- Butterworth, S. (1930). On the theory of filter amplifiers. *Experimental Wireless and the Wireless Engineer*, 7(1):536–541.
- Byrne, P., Park, S.-S., Beaty, M., Sharp, M., Gonzalez, L., and Abdoun, T. (2004). Numerical modeling of liquefaction and comparison with centrifuge tests. *Canadian Geotechnical Journal*, 41(2):193–211.
- Camoës, J. (2014). Non-linear soil behavior and its influence on soil pile interaction. Master’s thesis, Laboratoire MSSMat, Ecole Centrale Paris, Châtenay-Malabry, France. Advisor: Arezou Modaressi.
- Caragea, P. C. and Kaiser, M. S. (2009). Autologistic models with interpretable parameters. *Journal of Agricultural, Biological, and Environmental Statistics*, 14(3):281–300, doi:10.1198/jabes.2009.07032.
- Carrilho Gomes, R. and Lopes, I. F. (2014). How the response spectrum of non-liquefied loose-to-medium sand deposits is affected by the groundwater level. *Computers and Geotechnics*, 57(1):53–64, doi:10.1016/j.compgeo.2014.01.006.

- Carrilho Gomes, R., Santos, J., Modaressi-Farahmand Razavi, A., and Lopez-Caballero, F. (2015). Validation of a strategy to predict secant shear modulus and damping of soils with an elastoplastic model. *KSCE Journal of Civil Engineering*, pages 1–14, doi:10.1007/s12205-015-0516-8. Online.
- CEN (2004). *Eurocode 7, Geotechnical design Part 1: General rules*, EN1997-1 part 1: general rules, seismic actions and rules for buildings. European Committee for Standardization, Brussels, Belgium.
- Chakraborty, P., Jafari-Mehrabadi, A., and Popescu, R. (2004). Effects of Low Permeability Soil Layers on Seismic Stability of Submarine Slopes. In *Proceedings of the 57th Canadian Geotechnical Conference*, Quebec, Canada. On CD.
- Chakraborty, P. and Popescu, R. (2012). Numerical simulation of centrifuge tests on homogenous and heterogeneous soil models. *Computers and Geotechnics*, 41(1):95–105.
- Chakraborty, P., Popescu, R., and Phillips, R. (2010). Liquefaction of heterogeneous sand: Centrifuge study. *Geotechnical testing journal*, 33(4):1–11.
- Chakraborty, A. and Okaya, D. (1995). Frequency-time decomposition of seismic data using wavelet-based methods. *Geophysics*, 60(6):1906–1916.
- Chandra, J., Gueguen, P., Steidl, J. H., and Bonilla, L. (2015). In Situ Assessment of the G- Curve for Characterizing the Nonlinear Response of Soil: Application to the Garner Valley Downhole Array and the Wildlife Liquefaction Array. *Bulletin of the Seismological Society of America*, 105(2):993–1010, doi:10.1785/0120140209.
- Chen, Q., Seifried, A., Andrade, J. E., and Baker, J. W. (2012). Characterization of random fields and their impact on the mechanics of geosystems at multiple scales. *International Journal for Numerical and Analytical Methods in Geomechanics*, 36:140–165, doi:10.1002/nag.999.
- Chen, Y. (2008). *Percolation and Homogenization theories for heterogeneous materials*. PhD thesis, Massachusetts institute of technology, Massachusetts, USA.
- Cherubini, C., Giasi, I., and Rethati, L. (1993). The coefficient of variation of some geotechnical parameters. In Li, K. and Lo, S.-C., editors, *Probabilistic Methods in Geotechnical Engineering*, pages 179–183, Rotterdam. A.A. Balkema.
- Chin, B. and Aki, K. (1991). Simultaneous study of the source, path, and site effects on strong ground motion during the 1989 Loma Prieta earthquake: a preliminary result on pervasive nonlinear site effects. *Bulletin of the Seismological Society of America*, 81(5):1859–1884.

- Ching, J., Hu, Y.-G., and Phoon, K.-K. (2015). On the Use of Spatially Averaged Shear Strength for the Bearing Capacity of a Shallow Foundation. In Haukaas, T., editor, *12th International Conference on Applications of Statistics and Probability in Civil Engineering (ICASP12)*, Vancouver, Canada. Paper No. 532.
- Chiou, B. S. and Youngs, R. R. (2008). An nga model for the average horizontal component of peak ground motion and response spectra. *Earthquake Spectra*, 24(1):173–215.
- Coelho, P., Haigh, S., Madabhushi, S., and O'Brien, T. (2004). Centrifuge modeling of the use of densification as a liquefaction resistance measure for bridge foundations. In *13th World Conference on Earthquake Engineering*, page 15, Vancouver, B.C., Canada.
- Cosenza, E. and Manfredi, G. (1997). *Seismic Design Methodologies for the Next Generation of Codes*, chapter The improvement of the seismic-resistant design for existing and new structures using damage concept, pages 119–129. Balkema, fajfar and krawinkler edition.
- COSMOS (2012). Virtual Data Center. Online; accessed 10/09/2015.
- Costa D'Aguiar, S., Modaressi-Farahmand-Razavi, A., Dos Santos, J., and Lopez-Caballero, F. (2011). Elastoplastic constitutive modelling of soil structure interfaces under monotonic and cyclic loading. *Computers and Geotechnics*, 38(4):430–447.
- Cox, B. R. (2006). *Development of a direct test method for dynamically assessing the liquefaction resistance of soils in situ*. PhD thesis, The University of Texas, Austin, Texas.
- Curtis, A., Gerstoft, P., Sato, H., Snieder, R., and Wapenaar, K. (2006). Seismic interferometry : turning noise into signal. *The Leading Edge*, 25(9):1082–1092, doi:10.1190/1.2349814.
- Darendeli, M. B. (2001). *Development of a new family of normalized modulus reduction and material damping curves*. PhD thesis, The University of Texas, Austin, Texas.
- Dasgupta, R. and Clark, R. A. (1998). Estimation of Q from surface seismic reflection data. *Geophysics*, 63:2120–2128.
- Dashti, S., Bray, J. D., Pestana, J. M., Riemer, M. R., and Wilson, D. (2010). Mechanisms of seismically-induced settlement of buildings with shallow foundations on liquefiable soil. *Journal of Geotechnical Geoenvironmental Engineering*, 136(1):151–164.
- De Martin, F. (2010). *Influence of the Nonlinear Behavior of Soft Soils on Strong Ground Motions*. PhD thesis, Ecole Centrale Paris, Paris, France.

- DeJong, J., Soga, K., Kavazanjian, E., Burns, S., van Paassen, L., Fragaszy, R., Al Qabany, A., Aydilek, A., Bang, S., Burbank, M., Caslake, L., Chen, C., Cheng, X., Chu, J., Ciurli, S., Fauriel, S., Filet, A., Hamdan, N., Hata, T., Inagaki, Y., Jefferis, S., Kuo, M., Laloui, L., Larrahondo, J., Manning, D., Martinez, B., Mortensen, B., Nelson, D., Palomino, A., Renforth, P., Santamarina, J., Seagren, E., Tanyu, B., Tsesarsky, M., and Weaver, T. (2013). Bio-and chemo-mechanical processes in geotechnical engineering. *Geotechnique*, 63(4):287–301.
- Dickenson, S. and Seed, R. (1996). Nonlinear dynamic response of soft and deep cohesive soil deposits. In *Proceedings of the international workshop on site response subjected to strong earthquake motions*, volume 2, pages 67–81, Yokosuka, Japan.
- Dickinson, B. W. and Gavin, H. P. (2011). Parametric statistical generalization of uniform-hazard earthquake ground motions. *Journal of Structural Engineering*, 137(3):410–422, doi:10.1061/(asce)st.1943-541x.0000330.
- Dobry, R., Ladd, R., Yokel, F., Chung, R., and Powell, D. (1982). Prediction of pore water pressure buildup and liquefaction of sands during earthquakes by the cyclic strain method. *NBS Building Science Series 138*, page 150.
- El Mohtar, C. S., Bobet, A., Santagata, M. C., Drnevich, V. P., and Johnston, C. T. (2013). Liquefaction mitigation using bentonite suspensions. *Journal of Geotechnical Geoenvironmental Engineering*, 139(8):1369–1380, doi:10.1061/(asce)gt.1943-5606.0000865.
- EPRI (1993). Guidelines for determining design basis ground motions. Technical report, Electric Power Research Institute. EPRI TR-102293.
- Failmezger, A. (2001). Discussions on Factor of safety and reliability in geotechnical engineering. *Journal of Geotechnical and Geoenvironmental Engineering*, 127(8):703–704, doi:10.1061/(ASCE)1090-0241.
- Fenton, G. and Griffiths, D. (2002). Probabilistic foundation settlement on spatially random soil. *Journal of Geotechnical and Geoenvironmental Engineering*, 128(5):381–390.
- Fenton, G. and Griffiths, D. (2008). *Risk assessment in geotechnical engineering*. John Wiley & Sons Inc., Chichester, 2 edition.
- Fenton, G. A. and Vanmarcke, E. H. (1998). Spatial variation in liquefaction risk. *Géotechnique*, 48(6):819–831.
- Fiegel, G. and Kutter, B. (1994). Liquefaction mechanism for layered soils. *Journal of geotechnical engineering*, 120(4):737–755.

- Field, E., Johnson, P., Beresnev, I., and Zeng, Y. (1997). Nonlinear ground-motion amplification by sediments during the 1994 Northridge earthquake. *Nature*, 390(December):599–602, doi:10.1038/37586.
- Foerster, E. and Modaressi, H. (2007a). A diagonal consistent mass matrix for earthquake site response simulations. In *4th International Conference on Earthquake Geotechnical Engineering (ICEGE)*, Thessaloniki, Greece. Paper: 1242.
- Foerster, E. and Modaressi, H. (2007b). Nonlinear numerical methods for earthquake site response analysis II- case studies. *Bulletin of Earthquake Engineering*, 5(3):325–345.
- Frary, M. and Schuh, C. a. (2005). Connectivity and percolation behaviour of grain boundary networks in three dimensions. *Philosophical Magazine*, 85(11):1123–1143, doi:10.1080/14786430412331323564.
- Garzón, L. X., Caicedo, B., Sanchez-Silva, M., and Phoon, K. (2014). Physical modeling of soil uncertainty. In Gaudin, C. and White, D., editors, *8th International Conference on Physical Modelling in Geotechnics 2014 (ICPMG2014)*, volume 2, pages 1259–1265, Perth, Australia. CRC Press.
- GEFDyn (2009). Géomecanique Eléments Finis DYNamique. Online; accessed 14/10/2015.
- Ghosh, B. and Madabhushi, S. P. G. (2003). Effects of Localized Soil Inhomogeneity in Modifying Seismic Soil-Structure Interaction. In *Proceedings of the 16th ASCE Engineering Mechanics Conference*, Seattle, WA.
- Gingery, J., Elgamal, A., and Bray, J. (2014). Response Spectra at Liquefaction Sites during Shallow Crustal Earthquakes. *Earthquake Spectra*, doi:10.1193/101813EQS272M. In press.
- Graizer, V. (2012). Effect of Low-Pass Filtering and Re-Sampling on Spectral and Peak Ground Acceleration in Strong- Motion Records. In *15th World Conference on Earthquake Engineering WCEE*, Lisboa, Portugal.
- Green, R. and Cameron, W. (2003). The influence of ground motion characteristics on site response coefficients. In *Pacific conference on earthquake engineering*, page 19, University of Canterbury, Christchurch, New Zealand. New Zealand Society for Earthquake Engineering. Paper No. 90 on CD.
- Griffiths, D. and Fenton, G. (2001). Bearing capacity of spatially random soil: The undrained clay Prandtl problem revisited. *Géotechnique*, 51(4):351–359.

- Griffiths, D. V., Fenton, G., and Manoharan, N. (2002). Bearing capacity of rough rigid strip footing on cohesive soil: probabilistic study. *Journal of Geotechnical and Geoenvironmental Engineering*, 128(9):743–755, doi:10.1061/(ASCE)1090-0241(2002)128:9(743).
- Gueddouda, M., Lamara, M., Abou-bekr, N., and Taibi, S. (2010). Hydraulic behaviour of dune sand bentonite mixtures under confining stress. *Geomechanics and Engineering*, 2(3):213–227, doi:10.12989/gae.2010.2.3.213.
- Guerreiro, P., Kontoe, S., and Taborda, D. (2012). Comparative study of stiffness reduction and damping curves. In *15th World Conference on Earthquake Engineering WCEE*, pages 2–11, Lisboa, Portugal.
- Hardin, B. (1978). The nature of stress-strain behavior for soils. In *Special Conference on Earthq. Engrg. and Soil Dyn*, volume 1, pages 3–89, Pasadena, California.
- Harr, M. (1977). *Mechanics of particulate media: a probabilistic approach*. McGraw-Hill, New York.
- Hartvigsen, A. (2007). Influence of pore pressures in liquefiable soils on elastic response spectra. Master's thesis, University of Washington, Seattle.
- Hashin, Z. and Shtrikman, S. (1962). A variational approach to the theory of the effective magnetic permeability of multiphase materials. *Journal of Applied Physics*, 33(10):3125, doi:10.1063/1.1728579.
- Hauge, P. S. (1981). Measurements of attenuation from vertical seismic profiles. *Geophysics*, 46:1548–1558.
- Hausler, E. and Sitar, N. (2002). Performance of improved ground. In *Annual Meeting Research Digest*, volume 16, page 4, University of California, Berkeley. Pacific Earthquake Engineering Research Center.
- HAZUS-MH MR3 (2003). *Multi-hazard Loss Estimation Methodology*. Federal Emergency Management Agency, Washington, DC.
- Helton, J., Johnson, J., Sallaberry, C., and Storlie, C. (2006). Survey of sampling-based methods for uncertainty and sensitivity analysis. *Reliability engineering and system safety*, 91(10):1175–1209.
- Hill, D. P., Reasenberg, P. a., Michael, a., Arabaz, W. J., Beroza, G., Brumbaugh, D., Brune, J. N., Castro, R., Davis, S., Depolo, D., Ellsworth, W. L., Gomberg, J., Harmsen, S., House, L., Jackson, S. M., Johnston, M. J., Jones, L., Keller, R., Malone, S., Munguia, L., Nava, S., Pechmann, J. C., Sanford, a., Simpson, R. W., Smith, R. B., Stark, M., Stickney, M., Vidal, a., Walter, S., Wong,

- V., and Zollweg, J. (1993). Seismicity remotely triggered by the magnitude 7.3 landers, California, earthquake. *Science*, 260(5114):1617–1623, doi:10.1126/science.260.5114.1617.
- Honjo, Y. (1985). *Dam Filters: Physical Behavior, Probability of Malfunctioning and Design Criteria*. PhD thesis, Massachusetts Institute of Technology, Department of Civil Engineering, Massachusetts.
- Honjo, Y. and Otake, Y. (2013). A simple method to assess the effect of soil spatial variability on the performance of a shallow foundation. In Withiam, J. L., Phoon, K.-K., and Hussein, M. H., editors, *Foundation Engineering on the Face of Uncertainty*, pages 385–402. ASCE. Geotechnical Special Publication No. 229 Honoring Fred. H. Kulhway.
- Huber, M. (2013). *Soil variability and its consequences in geotechnical engineering*. PhD thesis, Institut für Geotechnik der Universität Stuttgart, Germany.
- Hughes, J., Haran, M., and Caragea, P. (2011). Autologistic models for binary data on a lattice. *Environmetrics*, 22(7):857–871, doi:10.1002/env.1102.
- Hughes, T. (2000). *The Finite Element Method, Linear Static and Dynamic Finite Element Analysis*. Dover, Mineola, New York.
- Hujeux, J. (1985). Une loi de comportement pour le chargement cyclique des sols. In *Génie Parasismique*, pages 278–302, France. Presses ENPC. Edited by V. Davidovici.
- Huyse, L. and Walters, R. (2001). Random field solutions including boundary condition uncertainty for the steady-state generalized burgers equation. Technical report, NASA, Hampton, Virginia.
- Iai, S., Morita, T., Kameoka, T., Matsunaga, Y., and Abiko, K. (1995). Response of a dense sand deposit during 1993 Kushiro-Oki Earthquake. *Soils and Foundations*, 35(1):115–131, doi:10.3208/sandf1972.35.115.
- Idriss, I. (1990). Influence of local site conditions on earthquake ground motions. In *Proc. of IV U.S. Nat. Conf. on Earthquake Engineering*, volume 1, pages 55–57, Palm Springs, California.
- Idriss, I. (1991). Earthquake ground motions at soft soil sites. In *Second International Conference on Recent Advances in Geotechnical Earthquake Engineering and Soil Dynamics*, volume 3, St. Louis, Missouri.
- Idriss, I. M. and Sun, J. I. (1992). *SHAKE91: User's Manual*.
- Iervolino, I. and Cornell, C. (2005). Record selection for nonlinear seismic analysis of structures. *Earthquake Spectra*, 21(3):685–713.

- Ishihara, K. (1993). Liquefaction and flow failure during earthquakes. *Geotechnique*, 43(3):351–415.
- Ishihara, K. (1996). *Soil behaviour in earthquake geotechnics*. Clarendon Press, Oxford University Press, Oxford, UK.
- Iwan, W. and Chen, X. (1995). Important near-field ground motion data from the Landers earthquake. In *Proceedings of the 10th European Conference on Earthquake Engineering*, pages 229–234, Vienna, Austria.
- Jafarian, Y., Abdollahi, A., Vakili, R., Baziar, M., and Noorzad, A. (2011). On the efficiency and predictability of strain energy for the evaluation of liquefaction potential: A numerical study. *Computers and Geotechnics*, 38(6):800–808, doi:10.1016/j.compgeo.2011.06.001.
- Jones, A., Kramer, S., and Arduino, P. (2002). Estimation of uncertainty in geotechnical properties for performance-based earthquake engineering. PEER Report 2002/16, Pacific Earthquake Engineering Research Center, University of California, Berkeley.
- Journel, A. and Huijbregts, C. (1978). *Mining geostatistics*. Academic Press, London.
- Kasama, K., Whittle, A., and Zen, K. (2012). Effect of spatial variability on the bearing capacity of cement-treated ground. *Soils and Foundations*, 52(4):600–619.
- Katona MG, Z. O. (1985). A unified set of single step algorithms Part 3: the Beta-m method, a generalization of the Newmark scheme. *International Journal of Numerical Methods in Engineering*, 21(7):1345–1359.
- Kawase, H. (2011). Strong ground motion characteristics and their damage impact to structures during the off pacific coast of tohoku earthquake of march 11, 2011; how extraordinary was this m9.0 earthquake? In *4th IASPEI / IAEE International Symposium: Effects of Surface Geology on Seismic Motion*, page 13, University of California Santa Barbara.
- Kayen, R. and Mitchell, J. (1997). Assessment of liquefaction potential during earthquakes by arias intensity. *Journal of Geotechnical and Geoenvironmental Engineering*, 123(12):1162–1174, doi:10.1061/(ASCE)1090-0241(1997)123:12(1162).
- Kirkpatrick, S. (1973). Percolation and conduction. *Reviews of modern physics*, 5(4):574–588.
- Kokusho, T. (1980). Cyclic triaxial test of dynamic soil properties for wide strain range. *Soils and Foundations*, 20(2):45–60.
- Kokusho, T. and Kojima, T. (2002). Mechanism for postliquefaction water film generation in layered sand. *Journal of Geotechnical and Geoenvironmental Engineering*, 128(2):129–137.

- Koltermann, C. and Gorelick, S. (1996). Heterogeneity in sedimentary deposits: A review of structure-imitating, process-imitating and descriptive approaches. *Water Resources Research*, 32(9):2617–2658, doi:10.1029/96WR00025.
- Konrad, J.-M. and Dubeau, S. (2002). Cyclic strength of stratified soil samples. In *Proceedings of the 55th Canadian Geotechnical Conference: Ground and Water: Theory to Practice*, pages 89–94, Niagara Falls, Canada.
- Kontoe, S., Zdravkovic, L., and Potts, D. (2008). An assessment of time integration schemes for dynamic geotechnical problems. *Computers and geotechnics*, 35(2):253–264.
- Koplik, J. (1991). Homogenization and effective medium methods for transport in disordered granular systems. In Bideau, D. and Dodds, J., editors, *Physics of granular media*, page 215, New York, USA. Nova Science Publishers.
- Kordjani, M. (1995). *Caractérisation et modélisation du comportement en petites déformations des sols sur des chemins de sollicitation monotone et cyclique*. PhD thesis, Ecole Centrale Paris, Paris, France.
- Koutsourelakis, S., Prévost, J., and Deodatis, G. (2002). Risk assessment of an interacting structure-soil system due to liquefaction. *Earthquake Engineering and Structural Dynamics*, 31(4):851–879, doi:10.1002/eqe.125.
- Kramer, S. (1996). *Geotechnical earthquake engineering*. Prentice-Hall, New Jersey, United States of America, 1st edition.
- Kramer, S., Hartvigsen, A., Sideras, S., and Ozener, P. (2011). Site response modeling in liquefiable soil deposits. In *4th IASPEI / IAEE International Symposium: Effects of Surface Geology on Seismic Motion*, page 13, University of California Santa Barbara.
- Kramer, S. and Mitchell, R. (2006). Ground motion intensity measures for liquefaction hazard evaluation. *Earthquake Spectra*, 22(2):413–438.
- Kramer, S. L., Asl, B. A., Ozener, P., and Sideras, S. S. (2015). *Perspectives on Earthquake Geotechnical Engineering*, volume 37 of *Geotechnical, Geological and Earthquake Engineering*, chapter Effects of liquefaction on ground surface motions, pages 285–309. Springer International Publishing.
- Kuhl, D. and Crisfield, M. A. (1999). Energy-conserving and decaying algorithms in non-linear structural dynamics. *International Journal for Numerical Methods in Engineering*, 45(5):569–599, doi:10.1002/(SICI)1097-0207(19990620)45:5<569::AID-NME595>3.0.CO;2-A.

- Ladd, R. S., Dobry, R., Dutko, P., Yokel, F. Y., and Chung, R. M. (1989). Pore-Water Pressure Buildup in Clean Sands Because of Cyclic Straining. *Geotechnical Testing Journal*, 12(1):77–86.
- Lambert, S., Rocher-Lacoste, F., and Le Kouby, A. (2012). Soil-cement columns, an alternative soil improvement method. In Denies, N., editor, *ISSMGE - TC 211 International Symposium on Ground Improvement*, volume 3, pages 179–188, Brussels, Belgium.
- Li, J., Tian, Y., and Cassidy, M. (2015). Failure mechanism and bearing capacity of footings buried at various depths in spatially random soil. *Journal of Geotechnical and Geoenvironmental Engineering*, 141(2):1–11.
- Lopez-Caballero, F. (2003). *Influence du Comportement Non Linéaire du Sol sur les Mouvements Sismiques Induits dans des Géo-Structures*. PhD thesis, Laboratoire MSS-Mat, Ecole Centrale Paris, Paris, France.
- Lopez-Caballero, F. and Modaressi, A. (2011a). Identification des paramètres du modèle de l'ECP: Barrage de MATEMALE. Technical report, Laboratoire MSS-Mat, Ecole Centrale Paris. Projet CODHYBAR 2.
- Lopez-Caballero, F. and Modaressi, A. (2011b). Numerical analysis: Specification and validation of used numerical methods. FP7-SME-2010-1-262161, PREMISERI project, Paris, France.
- Lopez-Caballero, F. and Modaressi-Farahmand-Razavi, A. (2010). Assessment of variability and uncertainties effects on the seismic response of a liquefiable soil profile. *Soil Dynamics and Earthquake Engineering*, 30(7):600–613.
- Lopez-Caballero, F. and Modaressi-Farahmand-Razavi, A. (2013). Numerical simulation of mitigation of liquefaction seismic risk by preloading and its effects on the performance of structures. *Soil dynamics and Earthquake engineering*, 49(1):27–38.
- Lopez-Caballero, F., Modaressi-Farahmand-Razavi, A., and Modaressi, H. (2007). Nonlinear numerical method for earthquake site response analysis i — elastoplastic cyclic model and parameter identification strategy. *Bulletin of Earthquake Engineering*, 5(3):303–323, doi:10.1007/s10518-007-9032-7.
- Maharjan, M. and Takahashi, A. (2012). Liquefaction Centrifuge Modeling in Non-homogeneous Soil Deposits. In *15 WCEE*, page 10, Lisboa, Portugal.
- Masing, G. (1926). Eigenspannungen und Verfestigung beim Messing. In *2nd International Congress on Applied Mechanics*, pages 332–335.

- McLachlan, D., Blaskzkiewics, M., and Newnham, R. (1990). Electrical resistivity of composites. *Journal of the American Ceramics Society*, 73(8):2187–2203.
- Menq, F. (2003). *Dynamic Properties of Sandy and Gravelly Soils*. PhD thesis, University of Texas, Austin, TX, USA.
- Mitchell, J., Cooke, H., and Schaeffer, J. (1998). Design considerations in ground improvement for seismic risk mitigation. In Dakoulas, P., Yegian, M., and Holtz, R. D., editors, *Geotechnical Earthquake Engineering and Soil Dynamics III*, volume 1, pages 580–613, Seattle, Washington. ASCE. Geotechnical Special Publication No. 75.
- Modaressi, A. (2003). *Modélisation des milieux poreux sous chargements complexes*. Institut National Polytechnique de Grenoble, Grenoble, France. Dossier d’Habilitation à Diriger des Recherches.
- Modaressi, H. (1987). *Modélisation numérique de la propagation des ondes dans les milieux poreux anélastiques*. PhD thesis, Laboratoire MSSMat, Ecole Centrale Paris, Châtenay-Malabry, France. Advisor: Denis Aubry.
- Modaressi, H. and Benzenati, I. (1994). Paraxial approximation for poroelastic media. *Soil Dynamics and Earthquake Engineering*, 13(2):117–129.
- Modaressi, H. and Foerster, E. (2000). *CyberQuake Version 2.0 User’s Guide*. BRGM, 45060 Orleans, Cedex 2, France. BP 6009.
- Mollova, G. (2007). Effects of digital filtering in data processing of seismic acceleration records. *EURASIP Journal on Advances in Signal Processing*, 2007(1):9, doi:10.1155/2007/29502. Article ID 29502.
- Montoya-Noguera, S. and Lopez-Caballero, F. (2015). Numerical modeling of discrete spatial heterogeneity in seismic risk analysis: Application to treated ground soil foundation. *GeoRisk: Assessment and Management of Risk for Engineered Systems and Geohazards*, doi:10.1080/17499518.2015.1058957. Online.
- Montoya-Noguera, S. and Lopez-Caballero, F. (2016). Effect of coupling excess pore pressure and deformation on nonlinear seismic soil response. *Acta Geotechnica*, 11(1):191–207, doi:10.1007/s11440-014-0355-7.
- Mukabi, J. (1994). Internal reports of IIS. Technical report, University of Tokyo. Personal communications with [Tatsuoka et al. \(1995\)](#).

- Mylonakis, G. and Gazetas, G. (2000). Seismic soil–structure interaction : beneficial or detrimental? *Journal of Earthquake Engineering*, 4(3):277–301, doi:10.1080/13632460009350372.
- Nakagawa, K. and Soga, K. (1995). Nonlinear cyclic stress-strain relations of soils. In *Third International Conference on Recent Advances in Geotechnical Earthquake Engineering and Soil Dynamics*, pages 57–60, St Louis, USA.
- Nobahar, A. (2003). *Effects of soil spatial variability on soil-structure interaction*. PhD thesis, Memorial University of Newfoundland, Canada.
- Nobahar, A. and Popescu, R. (2000). Spatial variability of soil properties – effects on foundation design. In *Proceedings of 53rd Canadian geotechnical conference*, volume 2, pages 1139–1144, Montreal, Quebec.
- Otake, Y. and Honjo, Y. (2015). A simplified procedure to evaluate the effect of soil variability on geotechnical structures. In Oka, Murakami, Uzuoka, and Kimoto, editors, *Computer Methods and Recent Advances in Geomechanics (IACMAG)*, pages 1265–1270, London. Taylor & Francis Group.
- Paice, G., Griffiths, D., and Fenton, G. (1994). Influence of spatially random soil stiffness on foundation settlements. In Yeung, A. T. and Félio, G. Y., editors, *Vertical and Horizontal Deformations of Foundations and Embankments*, pages 628–639. American Society of Civil Engineers (ASCE). Geotechnical Special Publication (GSP) No. 40.
- Paice, G., Griffiths, D., and Fenton, G. (1996). Finite element modeling of settlements on spatially random soil. *Journal of Geotechnical Engineering*, 122(9):777–779, doi:10.1061/(asce)0733-9410(1996)122:9(777).
- PEER (2013). NGA database. Online; accessed 10/09/2015.
- Penzien, J. and Watabe, M. (1974). Characteristics of 3-dimensional earthquake ground motions. *Earthquake Engineering & Structural Dynamics*, 3(4):365–373, doi:10.1002/eqe.4290030407.
- Phoon, K., editor (2008). *Reliability-Based Design in Geotechnical Engineering: Computations and Applications*. Taylor & Francis, New York, 2 edition.
- Phoon, K. and Kulhawy, F. (1996). On quantifying inherent soil variability. In Shackelford, C. D., Nelson, P. P., and Roth, M. J. S., editors, *Uncertainty in the Geologic Environment: from Theory to Practice*, pages 326–340, New York. ASCE. Geotechnical Special Publication No. 58.
- Phoon, K., Quek, S., Chow, Y., and Lee, S. (1990). Reliability analysis of pile settlement. *Journal of Geotechnical Engineering*, 116(11):1717–1735.

- Phoon, K.-K. and Kulhawy, F. (1999). Evaluation of geotechnical property variability. *Canadian Geotechnical Journal*, 36(4):625–639, doi:10.1139/t99-039.
- Pitilakis, K. and Anastasiadis, A. (1998). Soil and site characterization for seismic response analysis. In ECEE, editor, *XI European Conference on Earthquake Engineering*, page 24, Paris, France. Invited Lecture.
- Popescu, R. (1995). *Stochastic variability of soil properties: data analysis, digital simulation, effects on system behaviour*. PhD thesis, Princeton University, Princeton, NJ.
- Popescu, R., Deodatis, G., and Nobahar, A. (2005a). Effects of random heterogeneity of soil properties on bearing capacity. *Probabilistic Engineering Mechanics*, 20(4):324–341.
- Popescu, R., Prevost, J. H., and Deodatis, G. (1997). Effects of spatial variability on soil liquefaction: some design recommendations. *Géotechnique*, 47(5):1019–1036.
- Popescu, R., Prevost, J. H., and Deodatis, G. (1998a). Characteristic percentile of soil strength for dynamic analyses. In Dakoulas, P., Yegian, M., and Holtz, R. D., editors, *Geotechnical Earthquake Engineering and Soil Dynamics III*, volume 1, pages 1461–1471, Seattle, Washington. ASCE. Geotechnical Special Publication No. 75.
- Popescu, R., Prevost, J. H., and Deodatis, G. (1998b). Spatial Variability of Soil Properties: Two Case Studies. In Dakoulas, P., Yegian, M., and Holtz, R. D., editors, *Geotechnical Earthquake Engineering and Soil Dynamics III*, pages 568–579, Seattle, Washington. ASCE. Geotechnical Special Publication No. 75.
- Popescu, R., Prevost, J. H., and Deodatis, G. (2005b). 3D effects in seismic liquefaction of stochastically variable soil deposits. *Géotechnique*, 55(1):21–31.
- Popescu, R., Prévost, J. H., Deodatis, G., and Chakraborty, P. (2006). Dynamics of nonlinear porous media with applications to soil liquefaction. *Soil dynamics and earthquake engineering*, 26(6):648–665.
- Prakash, V., Powel, G., and Campbell, S. (1993). *DRAIN-2DX Base program description and user guide: version 1.10*. Dept. of Civil Engineering, University of California, Berkeley. UCB/SEMM-1993/17.
- Prandtl, L. (1921). Über die Eindringungsfestigkeit (Harte) plastischer Baustoffe und die Festigkeit von Schneiden. *Zeitschrift für angewandte Mathematik und Mechanik*, 1(1):15–20.

- Preisig, M. and Jeremic, B. (2005). Nonlinear finite element analysis of dynamic soil-foundation-structure interaction. Technical report, Department of Civil and Environmental Engineering University of California, Davis. SFSI Draft report.
- Raghunandan, M. and Liel, A. (2013). Effect of ground motion duration on earthquake-induced structural collapse. *Structural Safety*, 41:119–133.
- Rahman, M. and Yeh, C. (1999). Variability of seismic response of soils using stochastic finite element method. *Soil dynamics and Earthquake Engineering*, 18(1):229–245.
- Rathje, E. M., Abrahamson, N. A., and Bray, J. D. (1998). Simplified Frequency Content Estimates of Earthquake Ground Motions. *Journal of Geotechnical and Geoenvironmental Engineering*, 124(2):150–159, doi:10.1061/(ASCE)1090-0241(1998)124:2(150).
- Reed, J. W. and Kassawara, R. P. (1990). A criterion for determining exceedance of the operating basis earthquake. *Nuclear Engineering and Design*, 123(2-3):387–396, doi:10.1016/0029-5493(90)90259-z.
- Regnier, J. (2013). *Seismic site-response variability : from site-classification to soil non-linear behaviour*. PhD thesis, Universite Paris-Est, Paris, France.
- Régnier, J., Bonilla, L. F., Bard, P. Y., Bertrand, E., Hollender, F., Kawase, H., and Sicilia, D. (2014). PRENOLIN Project: A Benchmark on Numerical Simulation of 1D Non-Linear Site Effect. Preliminary Results from the Verification Phase on Idealistic Cases. *Abstract and presentation for the Seismological Society of America Annual Meeting*. PRENOLIN participants: D. Assimaki, D. Boldini, S. Iai, S. Kramer, E. Foerster, C. Gélis, G. Gazetas, J. Gingery, Y. Hashash, P. Moczo, S. Foti, G. Lanzo, F. Lopez-Caballero, D. Roten, K. Pitilakis, F. DeMartin, B. Jeremic, A. Nieto-Ferro, M.P. Santisi, and D. Mercerat.
- Reine, C., Van Der Baan, M., and Clark, R. (2009). The robustness of seismic attenuation measurements using fixed- and variable-window time-frequency transforms. *Geophysics*, 74(2):WA123–WA135.
- Rioul, O. and Vetterli, M. (1991). Wavelets and signal processing. *IEEE Signal Processing Magazine*, 9(LCAV-ARTICLE-1991-005):14–38.
- Roman, H. E., Bunde, A., and Dieterich, W. (1986). Conductivity of dispersed ionic conductors: A percolation model with two critical points. *Physical Review B*, 34(5):3439–3445, doi:10.1103/physrevb.34.3439.

- Roscoe, K. H. and Pooroshasb, H. B. (1963). A fundamental principle of similarity in model tests for earth pressure problems. In *Proc. of 2nd Asian Regional Conference on Soil Mechanics*, volume 1, pages 134–140, Tokyo.
- Ruiz, S. and Saragoni, G. (2009). Free vibration of soils during large earthquakes. *Soil Dynamics and Earthquake Engineering*, 29(1):1–16.
- Saez, E. (2009). *Dynamic non-linear soil structure interaction*. PhD thesis, Ecole Centrale Paris, France.
- Saez, E., Lopez-Caballero, F., and Modaressi-Farahmand-Razavi, A. (2013). Inelastic dynamic soil-structure interaction effects on moment-resisting frame buildings. *Engineering structures*, 51(1):166–177.
- Sahimi, M. (2003). *Heterogeneous materials 1: Linear transport and optical properties*. Springer, New York.
- Saim, R. (1997). *Dès comportements repères des grains sans colle à un exemple de sol réel*. PhD thesis, École Centrale Paris, France.
- Schnabel, P., Lysmer, J., and Seed, H. (1972). SHAKE: A computer program for earthquake response analysis of horizontally layered sites. Report No. EERC 72-12, Earthquake Engineering Research Center.
- Seed, H. and Idriss, I. (1971). Simplified procedure for evaluating soil liquefaction potential. *Journal of the Soil Mechanics and Foundations Division*, 107(SM9):1249–1274.
- Seed, H., Murarka, J., Lysmer, J., and Idriss, I. (1976). Relationships between maximum acceleration, maximum velocity, distance from source and local site conditions for moderately strong earthquakes. *Bulletin Seismological Society of America*, 66(4):1323–1342.
- Seed, H., Wong, R., Idriss, I., and Tokimatsu, K. (1986). Moduli and damping factors for dynamic analyses of cohesionless soils. *Journal of Geotechnical Engineering*, 112(11):1016–1032.
- Shinozuka, M. and Ohtomo, K. (1989). Spatial severity of liquefaction. In *Proceedings of the second US-Japan workshop in liquefaction, large ground deformation and their effects on lifelines*, pages 193–206, New York. NCEER.
- Snieder, R. and Safak, E. (2006). Extracting the Building Response Using Seismic Interferometry: Theory and Application to the Millikan Library in Pasadena, California. *Bulletin of the Seismological Society of America*, 96(2):586–598, doi:10.1785/0120050109.

- Sorrentino, L., Kunnath, S., Monti, G., and Scalora, G. (2008). Seismically induced one-sided rocking response of unreinforced masonry facades. *Engineering Structures*, 30(8):2140–2153.
- Stockwell, R. G., Mansinha, L., and Lowe, R. P. (1996). Localization of the complex spectrum: The S transform. *IEEE Transactions on Signal Processing*, 44:998–1001.
- Stokoe, K. and Richart, F. (1973). Shear Moduli of Soils, In-Situ and From Laboratory Tests. In WCEE, editor, *5th World conference in earthquake engineering*, pages 356–359, Rome, Italy.
- Tatsuoka, F. (2001). Impacts on geotechnical engineering of several recent findings from laboratory stress-strain tests on geomaterials. Technical report, University of Tokyo, Geotechnical Engineering Laboratory.
- Tatsuoka, F., Lo Presti, D., and Kohata, Y. (1995). Deformation characteristics of soils and soft rocks under monotonic and cyclic loads and their relationships. In Prakash, editor, *Third Int. Conf. on Recent Advances in Geotechnical Earthquake Engineering and Soil Dynamics*, volume 2, pages 851–879, St Louis, MO, USA.
- Terzaghi, K. (1943). *Theoretical Soil Mechanics*. John Wiley & Sons.
- Trifunac, M. and Brady, A. (1975). A study on the duration of strong earthquake ground motion. *Bulletin of the Seismological Society of America*, 65(3):581–626.
- van Gelder, P. (2000). *Statistical methods for the risk-based design of civil structures*. PhD thesis, Delft University of Technology, Netherlands.
- Van Paassen, L. (2011). Bio-mediated ground improvement: From laboratory experiment to pilot applications. In Han, J. and Alzamora, D. E., editors, *GeoFrontiers 2011: Advances in Geotechnical Engineering*, pages 4099–4108, Dallas, Texas, United States. ASCE. Geotechnical Special Publication No. 211.
- Vanmarcke, E. (1977). Probabilistic modeling of soil profiles. *Journal of the Geotechnical Engineering Division*, 103(11):1227–1246.
- Vanmarcke, E. (1983). *Random fields: analysis and synthesis*. MIT Press, Cambridge.
- Vechio, F. and Emara, M. (1992). Shear deformation in reinforced concrete frames. *ACI Structural journal*, 89(1):46–56.
- Vucetic, M. and Dobry, R. (1991). Effect of soil plasticity on cyclic response. *Journal of Geotechnical Engineering*, 117(1):89–107.

- Wair, B. R., DeJong, J. T., and Shantz, T. (2012). Guidelines for estimation of shear wave velocity profiles. PEER Report 2012/08, Pacific Earthquake Engineering Research Center, University of California, Berkeley.
- Wang, L. (1996). Processing of near-field earthquake accelerograms. Report No. EERL 96-04, Earthquake Engineering Research Laboratory, Pasadena, California.
- Webster, R. and Oliver, M. (2007). *Geostatistics for environmental scientists*. John Wiley & Sons Inc., Chichester, 2 edition.
- Whittle, P. (1963). Stochastic processes in several dimensions. *Bulletin of the International Statistical Institute*, 40:974–994.
- Wiener, O. (1912). Die theorie des Mischkorpers fur das feld des stationaren Stromung. Erste Abhandlung die Mittelswertsatze fur Kraft, Polarisation un Energie. (german) [The theory of composites for the field of steady flow. First treatment of mean value estimates for force, polarization and energy]. *Abhandlungen der mathematisch-physischen Klasse der Koniglich Sachsischen Gesellschaft der Wizzenschaften*, 32(6):509–604.
- Withers, M., Aster, R., Young, C., Beiriger, J., Harris, M., and Moore, S. (1998). A comparison of select trigger algorithms for automated global seismic phase and event detection. *Bulletin of the Seismological Society of America*, 88(1):95–106.
- Wu, C. and Peng, Z. (2011). Temporal changes of site response during the 2011 M w 9.0 off the Pacific coast of Tohoku Earthquake. *Earth, Planets and Space*, 63(7):791–795, doi:10.5047/eps.2011.06.011.
- Wu, C., Peng, Z., and Assimaki, D. (2009). Temporal Changes in Site Response Associated with the Strong Ground Motion of the 2004 Mw 6.6 Mid-Niigata Earthquake Sequences in Japan. *Bulletin of the Seismological Society of America*, 99(6):3487–3495, doi:10.1785/0120090108. Short Note.
- Yoshida, N. (2013). Applicability of total stress seismic ground response analysis under large earthquakes. In *COMPADYN2013: 4th ECCOMAS Thematic Conference on Computational methods in structural Dynamics and earthquake engineering*, page 13, Kos Island, Greece.
- Yoshida, N. and Iai, S. (1998). Nonlinear site response and its evaluation and prediction. In *2nd International Symposium on the Effect of Surface Geology on Seismic Motion*, pages 71–90, Yokosuka, Japan.
- Yoshida, N. and Towhata, I. (2003). *YUSAYUSA-2 and SIMMDL-2, theory and practice (version 2.1)*. Tohoku Gakuin University and University of Tokyo, Japan. first published in 1991.

- Youngs, R. (2004). Software validation report for shake04. Technical report, Geomatrix Consultants.
- Yu, G., Anderson, J., and Siddharthan, R. (1993). On the characteristics of nonlinear soil response. *Bulletin of the Seismological Society of America*, 83(1):218–244.
- Zentner, I. (2013). Simulation of non-stationary conditional ground motion fields in the time domain. *Georisk: Assessment and Management of Risk for Engineered Systems and Geohazards*, 7(1):37–48, doi:10.1080/17499518.2013.763572.
- Zerva, A. and Zervas, V. (2002). Spatial variation of seismic ground motions: An overview. *Application Mechanics ASME*, 55(3):271–297.
- Zienkiewicz, O., Chan, A., Pastor, M., Schrefler, B., and Shiomi, T. (1999). *Computational Geomechanics with Special Reference to Earthquake Engineering*, volume 2. John Wiley & Sons, Baffins Lane, Chichester, England, 4th edition.
- Zienkiewicz, O. and Shiomi, T. (1984). Dynamic behavior of saturated porous media: the generalised biot formulation and its numerical solution. *International Journal for Numerical and Analytical Methods in Geomechanics*, 8(1):71–96.
- Zienkiewicz, O. and Taylor, R. (1991). *The Finite element method, solid and fluid mechanics, dynamics and non-linearity*, volume 2. McGraw-Hill Book Company, London, 4th edition.